Interfacial Interactions of Faceted Organic Crystals
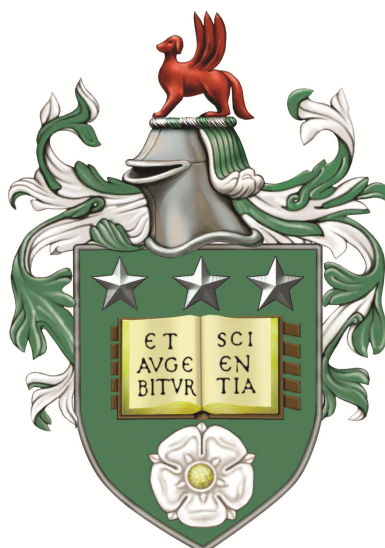# – An in-silico study with Atomic Force Microscopy

Alexandru Aurelian Moldovan

Submitted in accordance with the requirements for the degree of

Doctor of Philosophy

The University of Leeds

School of Chemical and Process Engineering

February 2020

Intellectual Property Statement

The candidate confirms that the work submitted is his own and that appropriate credit has been given where reference has been made to the work of others.

This copy has been supplied on the understanding that it is copyright material and that no quotation from the thesis may be published without proper acknowledgement.

The right of Alexandru Aurelian Moldovan to be identified as Author of this work has been asserted by him in accordance with the Copyright, Designs and Patents Act 1988.

Acknowledgements

Many thanks are given to my supervisory team consisting of, Simon Connell for his guidance and expertise throughout my PhD as well as endless patience with my obsession for complex graphs, Robert Hammond who has always eloquently counselled me on matters of computational modelling, and finally Professor Andrew Bayly who grounded the project and brought it back to a practice perspective. Also, I would like to thank Vasuki Ramachandran for her support and direction at the start of my PhD.

A special thanks to Professor Sven Schroeder for adopting me into his research group and allowing a great collaboration with many synchrotron trips to flourish. And from that research group, I would like to thank Beth W., Thoko, Beth E., Arturs, Anu, Abdul, and James for always offering engaging discussions and being welcoming throughout my PhD.

I want to express my deepest gratitude to my industrial collaborators, Radoslav Penchev (Pfizer) for his exceptional contributions and continuous enthusiasm to the project, and Andrew Maloney (CCDC) who always imparted great wisdom and support when it was most needed. Exceptional thanks to Diane Cochrane, Andrew Scott, and Robert Simpson for their help and support with all things microscopy.

To my colleagues of the CP3 CDT, I would like to thank you all for making my time at Leeds so memorable. In particular, I would like to thank Tom, Jakub, and Ben for their endless support, constant pestering and idle chit chat about all things science and philosophical. Without you three, I would not have achieved as much as I have. As part of the CDT collaborations and discussions are the most valuable aspects and for that, I have Rob, Mo, Laura, Jono, Lewis, Rosi, Jonny, Elliot and Bradley to thank.

I want to thank my friends for their continuous support and always putting up with my constant explanations of my project, in particulate Ryan and Chris for always motivating me to keep going. A special thanks are extended to the Brown family for making my PhD journey a fun one and reminding me that other things happen outside the project. My most enormous gratitude to Isla and Skye for helping me through the stresses of the last couple of months of writing.

And finally, the biggest thanks goes to my family for always being a great motivator and fantastic support team. In particular, my mother for being the unmovable rock and primary inspiration in my life.

Abstract

As the most popular form of drug delivery, solid form formulations, such as tablets, are utilised throughout the world, and their development is crucial to delivering new medicines to market. However, the solid form drug product does not only require focus on its active pharmaceutical ingredient (API) but also its interactions with other ingredients (excipients) within the formulation. The compatibility between the API and excipients plays a critical role in the final drug product performance. Currently, drug products are being developed using a trial and error approach to determine the best formulation. The ability to pre-screen API-Excipient particle interactions would allow formulators to make a more informed decision on the experimental studies to be carried out, thus reducing the development time and resources required to get a molecule from discovery to product.

This body of work presents two methodologies for assessing the inter-particulate interactions between faceted organic crystals, such as those used for drug product formulations. Previous studies have utilised single probe molecules to computationally calculate the interactions between the probe and surface, in order to relate those to the inter-particulate forces. Within this project, an in-silico methodology has been developed which calculates interactions of opposing crystal slabs, taking into account approach distance, atomic roughness induced steric repulsions, displacements and rotation. Maps of the interaction space were produced allowing identification of the mechanism of surface interaction, all a marked improvement on single molecular probe methods. This development could aid pre-screening efforts, and inform solid-state and formulation scientists, of the impact the surface chemistry can have interactions.

Atomic force microscopy adhesion data has previously been shown to correlate well with formulation performance. In this study, the facet specific interactions were measured for the first time and shown to agree with the in silico method. It was found, not unexpectedly, that micro-surface roughness controlled surface adhesion, although in silico measurements showed conversely that atomic roughness increased surface adhesion.

The materials analysed were Paracetamol Form I (Para), α - L-Glutamic acid (LGA) and β - D-Mannitol due to their varying crystal morphology, surface chemistry, and ease with which it can be crystallised. Multiple paracetamol facets were used for adhesive measurements, and a cleaning study was carried out determining

the most effective protocol of cleaning paracetamol surfaces from a topographical and surface chemistry point of view.

For the in-silico approach, a molecular mechanics (MM) workflow has been developed and an accompanying analysis tool, allowing high-throughput analysis. It was found that Para shows higher cohesive behaviour in the presence of DMAN compared to LGA due to the higher interactions between the hydrophilic surfaces of DMAN. Surface roughness was found to be inversely correlated to the interaction energy, except for a few cases where higher roughness equated to more energy due to the slabs interlocking. Facets $(10\bar{1})$ and $(11\bar{1})$ of Para were found to be the most interactive across Para and DMAN/LGA substrate facets respectively. Finally, a strong case has been made for using energy distributions to describe facet interactions, over conventional use of the lowest interaction energy.

Experimentally, for the first time, the adhesion between faceted organic crystals was measured. Small crystals were mounted onto the end of AFM cantilevers, and with the orientation of the substrate crystals (also faceted) adjusted, the two crystals were brought into contact. Forces were measured for the fully indexed Para crystal giving a ranking of most interactive facets $Para/Para : F_{10\bar{1}} >> F_{101} > F_{11\bar{1}}$. Similarly to the in-silico results, the $(10\bar{1})$ was found to be the most adhesive for Para/Para systems followed by the (101) and $(11\bar{1})$. As with the in-silico Para was found to be more cohesive in the presence of DMAN and more adhesive with LGA, showing a correlation with the model.

The cohesive/adhesive balance analysis and interactive probe ranking were within agreement between the experimental and computation technique, thus validating the model and increasing confidence that it can be used to assist in pre-screening API-Excipient interactions.

Contents

List of Tables

List of Figures

CHAPTER 1

Introduction and Motivations

"The saddest aspect of life right now is that science gathers knowledge faster than society gathers wisdom - Isaac Asimov"

Within this chapter, a basic introduction to the background of the project, research aims, and objectives as well as an outline of the literature review shall be given.

1.1 Pharmaceutical Discovery / Development

Historically, the discovery and development of pharmaceutical products have been a time and resource-intensive process due to the complexity of the multivariable systems. Typically an Active Pharmaceutical Ingredient(API), the component in the formulation responsible for the pharmacological efficacy, requires 12 years [1, 2] to translate from discovery to market. Drug formulations come in many forms, ranging from inhalation, liquid, and solid dosage, each with their advantages. For example, an inhalation formulation is more suitable for respiratory illnesses that require the direct administration to the area of inflammation [3]. This type of formulation has its manufacturing requirements dependent on the delivery system.

1.1.1 Formulations

Once an API has been chosen for development, the appropriate formulation type is chosen. The most popular formulation is the solid oral form, making up over 70% [4] of drug product worldwide. Its popularity stems from advantages offered to both the patient and manufacturer, namely an easy to handle and, relatively, low-cost manufacturing product that offers the patient a convenient administration route [5].

A typical formulation consists of an API and a list of excipients (EXP) to enable the drug to be manufactured and offer the desired performance. Excipients are used to modify both physical and chemical properties of the drug formulations, such as binders, bulking, and wetting agents[6, 7, 8]. The solubility and dissolution rates are the key performance properties related to the bioavailability of the drug.

1.1.2 Solid-State Form

All solid-state drugs can be subdivided into multicomponent and single (anhydrous) component systems. Single components exist as the pure API. Multicomponent include solvates (also hydrates), cocrystals and salts[9, 10, 11]. Solid form solvates are crystals structures which contain trapped solvent within their crystal lattice. Thus hydrates are a type of solvate due to the trapped solvent being water. Cocrystals are stoichiometric multicomponent systems consisting of an API and a cocrystal (coformer) that exhibits solid-state behaviour at ambient temperature. Salts are a different type of multicomponent system, while the solvates, hydrates and cocrystals are formed of two or more constituents, and these are neutral in charge[12]. Salts are by nature ionically held together in a crystal structure with the constituents undergoing proton transfer [11].

Different crystalline material of the same single or multicomponent system are called polymorphs [13]. Polymorphism, which is exhibited in the crystalline struc-

ture that contains rigid molecules, is known as packing polymorphism, due to the lack of conformational changes in the molecules. Conformational polymorphism occurs due to different conformers of the same molecule. There can only be one thermodynamically stable polymorph, thus lowest in free energy, at a given set of environmental conditions (temperature, pressure, humidity, etc.), the rest would be considered metastable polymorphs. The impact of polymorphism is significant within pharmaceutical formulations and in particular manufacturing due to the changing of Physico-chemical properties of the crystalline state and thus the formulation [7, 13, 14, 15]. Therefore, solid form screenings are heavily regulated and form a large part of the development period. The effect of crystal form changes on the physical and chemical properties are shown in Table 1.1.

Table 1.1: Properties which can be affected by solid form variation [12]

Chemical	Physical	Mechanical	Surface	Thermo-dynamics	Kinetic
Chemical Stability/ Reactivity	Stability	Compactability	Surface-Free Energy	Solubility	Dissolution
Photo Chemical Reactivity	Hygrosco-picity	Hardness	Stickiness	FreeEnergy of Fusion	Nucleation and crystal growth rate
	Morphology	Powder Flow	Interaction tension	Melting Point	Solid-State reaction rate
	Density	Tabletting	Surface Area	Heat of Fusion	
	Colour	Tensile Strength		Vapour Pressure	
	Refractive index	Cleavage			

The most important characteristics of any pharmaceutical product is the solubility of the API, within liquid systems akin to the human stomach, which is inherently linked to the chemical structure. Beyond this, the dissolution rate of the formulation impacts the effectiveness of the drug, which is inherently affected by the size, shape, and other characteristics of the particles [16]. Reduction in particle size leads to an increase in surface area and thus increased dissolution rate [17, 18, 19], except in the case of porous particles which are more influenced by their internal pores than exterior surface area. Comparisons between measured surface areas of particles allow for some explanations of differing product performances, but this does not fully explain some variations that might occur due to surface properties. Why some surfaces are more hydrophobic than others, or why some have a higher propensity to adhesion. To gain an understanding of this, one must look at the surface energetics [17, 19, 20].

1.1.3 Pharmaceutical Computational Design

A quality by design (QbD) method has been implemented across the process of pharmaceutical development and manufacturing in order to reduce the number of failed candidates and batches. This is due to the complexity of the formulations, caused by variations in solid form of the API and the compatibility of the excipients [21]. Computational methodologies have been introduced as part of QbD to help understand the fundamental science at each stage of the pharmaceutical process. A multiscale modelling approach, across multiple time and length scales, can be taken to develop parts of the design and manufacturing process[22]. Figure 1.1 shows the different computational methods used across a range of length scales, which will be explored in further detail in Chapter 2.4.
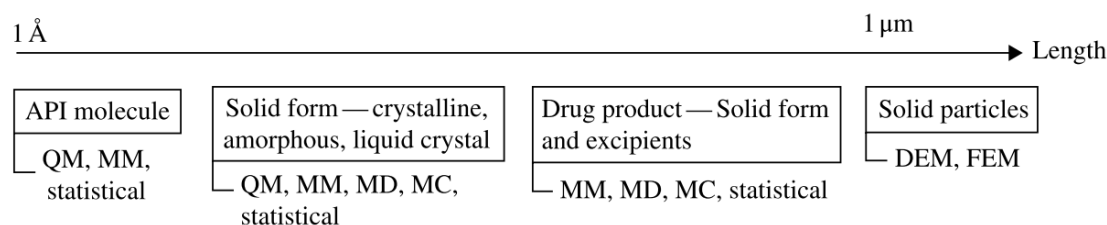
Figure 1.1: Schematic showing multiscale modelling landscape in solid-sate chemistry. Described above as QM (Quantum Mechanics) MM (Molecular Mechanics); MD (Molecular Dynamics) and MC (Monte Carlo); DEM (Discreet Elemental Methods) and FEM (Finite Elemental Methods); Statistical is described as a knowledge-based methods utilising datasets[23].

The main focus of this project will be placed on inter-particular interactions between API-EXPs and how these can impact the behaviour of drug products. As such, molecular mechanics (MM) will take precedence as the most important point of discussion. Several studies have shown the value of calculating the interactions between surfaces, adsorbed molecules and the type of insight that can be gained from such simulations [24, 25, 26, 27].

1.1.4 Surfaces and Their Properties

The experimental studies of surfaces have always been challenging, from ensuring a representative surface to controlling environmental factors. Measuring surface area, energy, and chemical composition can be made possible with the use of several instruments and techniques. Particle sizing by laser diffraction allows for the measurements of the particle size distribution (PSD),which is a basic property used for anticipating the powder behaviour. Surface energy measurements using inverted gas chromatography (IGC)[17] determines the adsorption of a probe molecule to a surface, whereas surface force apparatus (SFA) [28] and atomic force microscopy (AFM)

[29] measure the surface-surface physical interaction. Measuring the contact angle between a liquid and solid describes the ability of a liquid to wet a surface; hence the interaction of water (or any other liquid) with a surface, as such gives a measure of hydrophobicity or hydrophilicity. Finally, X-ray photoelectron spectroscopy (XPS)[30] can offer an insight into the chemical surface composition, although, currently this method has shown limited use on organic crystals due to the sensitive nature the materials and high energy X-Ray used.

As this work focuses primarily on understanding and measuring the interacting forces between two surfaces, we require an experimental method capable of measuring the force of interaction between two surfaces. The classic and most quantitative technique for this type of measurement in the Surface Force Apparatus, but this can only handle mica surfaces in a crossed cylindrical configuration. AFM offers the only viable possibility of measuring the forces between particles.

Previous studies have successfully shown the use of AFM in measuring cohesive and adhesive forces, which are described as the forces between alike (homogeneous) and different (heterogeneous) particles, respectively[31, 32, 33, 34]. While particle-particle interactions can be measured with AFM, there is a lack of studies investigating the surface interactions across the facets of two organic crystals coming together. With compounds having different surface properties due to their exposed chemical termination groups[35, 36], understanding how these facets interact is crucial in modifying the crystal habit and drug product for optimised performance.

1.2   Project Aims, Objectives and Outline

The interactions between the active pharmaceutical ingredient (API) and the excipients used in solid form formulations, such as tablets, play a critical role in the final drug product performance. Understanding the forces that cause the two particles to aggregate can be of important significance, we currently only understand the interaction down to the macro scale where capillary and van der Waals interactions are dominating. Whilst we can say these forces dominate, pinpointing the exact chemical and physical composition which cause these has not been trivial or thoroughly examined. Studies that have focused on the inter-particular interactions have not fully accounted for any facet-specificity and thus do not account for the anisotropic nature of organic crystals and their chemistry. Gaining such information, by either in-silico or experimental studies would benefit further research into understanding how surfaces chemistry of organic crystals can impact particle interactions.

The ability to pre-screen API-Excipient particle interactions via in-silico methods would allow formulators to make a more informed decision on the experimental studies to be carried out, thus reducing the development time and resources required to get a molecule from discovery to product. However, as with any computational model, this must be validated with experimental data.

This project aims to probe the interactions between specific organic crystal surfaces using Molecular Mechanics and Atomic Force Microscopy. This will allow us to identify the impact of surface chemistry onto inter-particulate interactions.

The project has two objectives:

Firstly, to design a computational framework for calculating, at the atomistic level, the interaction energy between two surfaces coming together using molecular mechanics and to gain a molecular-level understanding of what causes different combinations of API-EXP to have specific adhesive properties. In order to compare in-silico results with experimental measurements and thus validate the model, a ranking system between the various API and excipients shall be developed to encapsulate the cohesive-adhesive nature of the systems.

Secondly, to develop an experimental methodology for ranking API-EXP compatibility based on their adhesion properties. The crystal surfaces will also require characterisation, in order to account for any physical (topographical) contributions towards the inter-particulate interactions. This work will be carried out using AFM functionalised probes.

1.2.1   Thesis Outline

This section describes the structure of the thesis and briefly summarises the content of each chapter and its contribution towards achieving the objectives and reaching

the aims of the project.
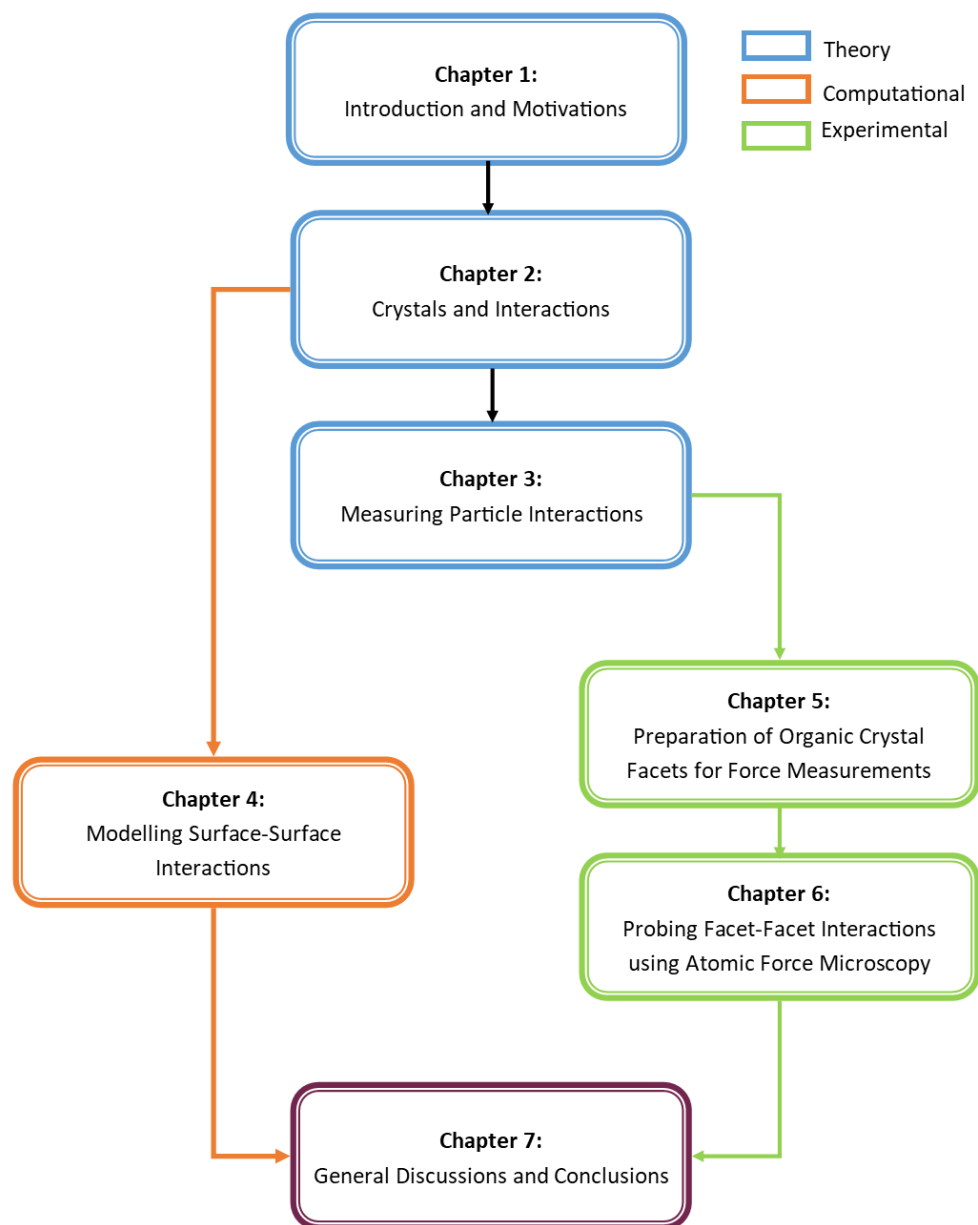
Figure 1.2: Thesis outline. Illustrating the transition from theory (blue) to in-silico (orange) and experimental (green) work flows

Figure 1.2 shows the overall structure of the thesis with the initial chapters focusing on a review of the theory required to carry out the work and brief introduction to the literature review. The objectives of the project form two workflows, experimental (green) and computational (orange). Each chapter is presented as standalone pieces of work, containing a literature review of the state of the art, methodology, results and discussions. Chapter 7 ties together the two workflows and concludes all findings.

Chapter 1: Motivations and background are presented to contextualise the work and outline the structure.

Chapter 2: Fundamental theory and necessary literature review of the material required for the in-silico approach and principles of crystallography, interactions, and facets.

Chapter 3: Approaches to experimentally measuring surface interactions and fundamental theory required for atomic force microscopy.

Chapter 4: In-silico approach - describing morphology prediction, calculating surface-surface interactions, the impact of surface properties and a given an example for a set of excipients with an API. A rank of the most adhesive facets is given.

Chapter 5: Cleaning study demonstrating a methodology for cleaning organic crystal facets to remove surface contaminants

Chapter 6: Experimental approach - describing the methodology of preparing crystal probes and measurements of facet-facet interactions with an assessment of the impact surface roughness can have on the adhesive properties. A rank of the most adhesive facets is given.

Chapter 7: Compares the experimental and in-silico ranks, as well as individual facet contributions to assess the validity of the model and conclude the findings of the project.

CHAPTER 2

Crystals And Interactions

"Science is about knowing; engineering is about doing - Henry Petroski"

This chapter will focus on the fundamental theory and literature review associated with crystals, interactions, and the in-silico aspect of those.

2.1   Crystallography

Crystalline solids are comprised of 3D repeating motifs of atoms or molecules in a lattice. The repetition of the motifs is described by the symmetry operators which create the final unit cell (smallest repeating unit). A unit cell can be described by six parameters, which comprise of lengths (**a,b,c**) and three inter-axial angles $(\boldsymbol{\alpha}, \boldsymbol{\beta}, \boldsymbol{\gamma})$[37].
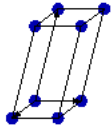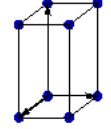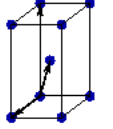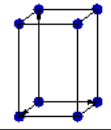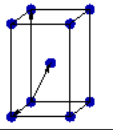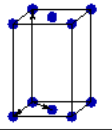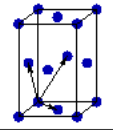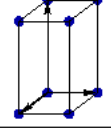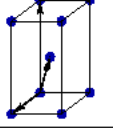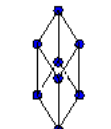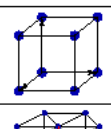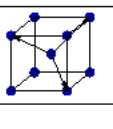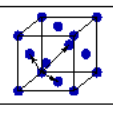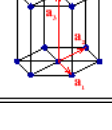
Bravais lattice	Parameters	Simple (P)	Volume centered (I)	Base centered (C)	Face centered (F)
Triclinic	$a_1 \neq a_2 \neq a_3$ $\alpha_{12} \neq \alpha_{23} \neq \alpha_{31}$				
Monoclinic	$a_1 \neq a_2 \neq a_3$ $\alpha_{23} = \alpha_{31} = 90°$ $\alpha_{12} \neq 90°$				
Orthorhombic	$a_1 \neq a_2 \neq a_3$ $\alpha_{12} = \alpha_{23} = \alpha_{31} = 90°$				
Tetragonal	$a_1 = a_2 \neq a_3$ $\alpha_{12} = \alpha_{23} = \alpha_{31} = 90°$				
Trigonal	$a_1 = a_2 = a_3$ $\alpha_{12} = \alpha_{23} = \alpha_{31} < 120°$				
Cubic	$a_1 = a_2 = a_3$ $\alpha_{12} = \alpha_{23} = \alpha_{31} = 90°$				
Hexagonal	$a_1 = a_2 \neq a_3$ $\alpha_{12} = 120°$ $\alpha_{23} = \alpha_{31} = 90°$				

Figure 2.1: Bravais lattice types in a three-dimensional representation [Source:[18]]

Extra points on the face or body of the lattice produce the 14 Bravais lattice types over the seven systems noted in Figure 2.1. The symmetry from the unit cell has an impact on the final structure of the crystal affecting growth rates, crystal habit, surface chemistry and mechanical properties. It is possible to refine the crystal system further using the symmetry operators that are used to describe the rotation, translation, mirror and inversion of the lattice to give a full 3D arrangement of the atoms in space, thus giving the space group [18].

The space groups are, in essence, instructions of how to repeat the motif. The 230 possible space groups are based on the normal symmetry operators; rotational, translational, screw, and glide plane which are multiplied by the number of Bravais

lattice types.

2.1.1 Miller Indices

The faces of a crystal can be described and numbered in terms of their axial intercepts. By using the law of rational indices[38, 39], the Miller indices (hkl) of a crystal and lattice can be expressed. In essence, they are describing the orientation of the plane.

The standard notation for Miller indices are as follows:

(hkl) – Round brackets are used to describe a specific plane or crystal facet

{hkl} – Curly brackets are used for a set of planes related by symmetry known as forms

[hkl]– Square brackets are used to describe a vector

<hkl> - Pointed brackets are used to denote direction related by symmetry

2.1.2 Crystal Packing Energetics

A molecular-based crystal is constructed from molecules that are packed densely into a lattice. The binding energy of the lattice is a result of the intermolecular interactions between molecules holding the lattice into a rigid state[40]. An understanding of the intermolecular bonds is crucial due to the direct impact on the physicochemical properties of the crystal. Factors affecting the intermolecular bonding of a system can be associated with [41]:

- The strength of interactions

- The distance between bodies interacting

- Molecular size and shape

- Directionality

The intermolecular bonding types include van der Waals, hydrogen bonding and electrostatic forces. Van der Waals (VdW) bonds are described as distance-dependent, weak attractive forces between two bodies[42]. The VdW interactions can be further classified into three types of forces that are Keesom forces (permanent dipoles), Debye forces (between the permanent and induced dipole), and London force (instantaneously induced dipoles). Hydrogen bonding (HB) is relatively strong directional dipole-dipole induced interaction occurring between the electronegative atom that with a lone pair of electrons and a hydrogen atom that is

attached to an electronegative atom[43]. Electrostatic forces are described as interactions between partially charged bodies and can typically be modelled as coulombic interactions. A detailed explanation of these interactions is given in section 2.4.

It is important to highlight the difference between intramolecular and intermolecular contributions. Intramolecular interactions correspond to the typically covalent bond occurring between atoms that are part of different molecules, whereas intermolecular interactions are occurring between atoms that are part of molecules and are typically weaker such as VdW. The link between the two is vital to understanding the potential energy landscape of molecular crystals and polymorphism. Molecules may adopt energetically favourable conformations (reach energy minima) in the crystal lattice (conformation) to improve packing efficiency and have a higher total potential energy contribution from intermolecular interactions.

Crystal structures can be mathematically described with atom-atom intermolecular potentials, which describe the attractive and repulsive forces between atoms, and it is possible to calculate the intra- and intermolecular interaction responsible for crystal packing energy. The lattice energy is a summation of all intermolecular energies in a 3D crystal and is calculated via pairwise summation between a central atom from a molecule to all surrounding molecules to a distance that the energies become negligible (> 18 Å). When n are the atoms in a central molecule, and each of the surrounding molecules (N) whose atoms are n', the lattice energy can be calculated using equation 2.1. Assuming vacuum, 0 K temperature[44].

$$E_{latt} = \frac{1}{2} \sum_{k=1}^{N} \sum_{i=1}^{n} \sum_{j=1}^{n'} V_{kij} \tag{2.1}$$

Where, V_{kij} is the interaction energy between central atom i and adjacent atoms j in the k surrounding molecule. As the interactions occur between two bodies, a factor of $\frac{1}{2}$ is used to account for duplication. The atom-atom interaction pair (V_{kij}) consists of attractive dispersive and short-range repulsions that are described by Lennard-Jones (6-12) (See section 2.4.4.4) potentials with an electrostatic component:

$$V_{kij} = \frac{A}{r^{12}} - \frac{B}{r^6} + \frac{q_i q_j}{r} \tag{2.2}$$

A and B are described as empirical atom-atom potentials, which are obtained from *ab initio* or experimental work. Validations of lattice energies are routinely carried out by comparing E_{latt} with the enthalpy of sublimation (ΔH_{sub}). Sublimation is defined as the direct transition from a solid phase to a gas phase without transition through the liquid phase[45],, therefore, a comparison can be made with the lattice energy, which is the energy required to hold the crystal lattice. The experimentally determined lattice energy (V_{Exp}) can be described with equation 2.3, where

the *2RT* represents the correction for vibration contribution towards the lattice due to differences between the gas and solid phase[44].

$$V_{Exp} = -\Delta H_{sub} - 2RT \tag{2.3}$$

2.2 Crystal Morphology

The external shape of a crystal is referred to as the habit. The crystal habit has a significant influence on the manufacturing of pharmaceutical products, affecting processing units such as filtering, blending, mixing, surface wetting, etc. The crystal habit is traditionally described using qualitative terms such as plate-like, prismatic and needle-like. A more quantitative approach is applying the miller indices to describe the external shape of a crystal; this is referred to as the morphology. Crystals can exhibit the same morphological forms but different habits. The choice of solvents or thermodynamic variations can cause such effects. The morphology of the crystal is determined by the relative growth rates of the various facets[23, 44]. With the smallest facets being the most energetically favourable and thus fastest growing. Figure 2.2 shows a crystal of the same morphological form but a different habit. Two of the most common and highly utilised methods of predicting morphologies are based on the geometrical nature of the unit cell and the chemistry of the system.
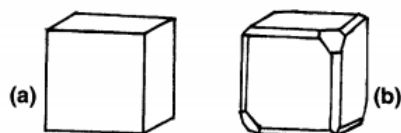
Figure 2.2: Diagram showing two different habits with the same morphology due to difference in relative growth rates [Source:[45]]

Gibbs and Wulff[46, 47] first pioneered
the predictions of the crystal shapes, by relating the energetics of the crystal growth to the minimised surface energy of the equilibrium form. Bravais[48] law states that the larger the interplanar distance (d_{hkl}), the larger the crystal facet (hkl), which was inversely proportional to the growth rate of the facet due to the lower surface energy. Friedel[49] experimentally proved this theory, with a few exceptions that were later explained by Donnay and Harker[50] who postulated that the anomalies were due to crystal symmetry related to the space groups present in the crystallographic structure. Thus, the Bravais-Friedel-Donnay-Harder (BFDH) can predict the crystal shape using interplanar distance (example for cubic systems in Equation 2.4), space group and lattice parameters.

$$d_{hkl} = a \left(\frac{1}{h^2 + k^2 + l^2} \right)^{\frac{1}{2}} \tag{2.4}$$

While using BFDH morphology to show the most important miller form, it is based purely on geometrical properties and takes no chemistry into account. The attachment energy model was proposed by Hartman and Perdok[51] to determine

the crystal morphology from the intermolecular bonding at the surface of the crystal. Attachment energy (E_{Att}) is described as the energy released on the addition of a growth slice to the surface of a crystal[52]. Equation 2.5 relates the lattice energy (E_{Latt}) to the slice energy (E_{Slice}), which is defined as the energy released upon a formation of a slice thickness d_{hkl}[44].

$$E_{Latt} = E_{Slice} + E_{Att} \tag{2.5}$$

The attachment energy of a facet is proportional to its size, with the lowest energy facet having the slowest growth rates and thus largest area. To quantify the number of broken surface bonds, the anisotropy factor[53, 54] can be calculated (Equation 2.6) to provide a measure of how satisfied the intermolecular bonds are at the surface when compared to those in the bulk[55].

$$\epsilon_{hkl} = \frac{E_{hkl}^{Slice}}{E_{Latt}} \tag{2.6}$$

2.3   Crystal Surfaces

Crystal properties are a product of their bulk and surface structures; it is important to ascertain which parts of the structures give rise to crystal strength, porosity, density and whether any surface features, physical or chemical have any influence on these properties. During crystallisation, the most stable surfaces, within a given solvent, are exhibited. Higher energy surfaces can be exposed by cleaving the crystal, typically occurring during particle reduction processes such as milling.

Determining the molecular terminal groups present on a particular facet is essential in understanding the interaction with external components as they directly influence the surface energy. This can be determined by experimental and computational methods. The surface free energy can be described as the energy arising from breaking internal bonds to form a new surface of the same material[56] as described in Equation 2.7

$$\Delta G = \gamma \Delta A \tag{2.7}$$

Where ΔG is the work required for a new surface to form at a specific temperature, with γ being the surface free energy, and ΔA is the increment of new surface area. The total surface energy (E_S) is described in Equation 2.8, $\frac{\Delta \gamma}{\Delta T}$ is the temperature-dependent coefficient of surface energy [45].

$$E_S = \gamma - T\frac{\Delta \gamma}{\Delta T} \tag{2.8}$$

One of the limitations of the attachment models discussed previously is the exclusion of solvent and what affects it has on the surface energy as it assumed the solvent affects every facet equally and thus, not change the habit. The surface energy for a given facet in vacuum γ_{hkl} can be estimated by taking into account the unit cell volume (V_{Cell}), the number of asymmetric units (Z), attachment energy (E_{Att}) and the interplanar distance (d_{hkl}) as shown in Equation 2.9, where N_A is Avogadro's number.

Equation 2.9 shows how the specific surface energy of a facet can be calculated by accounting for the energy released when attaching a layer of molecules equivalent to a d_{hkl} to a surface. The volume and number of molecules are used to normalise for the size of the slab thus only accounting the energetic change.[25]

$$\gamma_{hkl} = \frac{ZE_{Att}d_{hkl}}{2V_{Cell}N_A} \tag{2.9}$$

2.3.1 Surface Topology

Within an ideal system, a surface would be comprised of repeating units formed in a perfect pattern, representing the bulk. However, in a real system, defects are present both on the surface and the bulk. These defects have various causes ranging from thermodynamics, kinetics and impurities. Surface features are manifested as terraces, kinks, adatom, and vacancies.

These are all present at an atomistic resolution. However, their effects can affect macroscopic properties. For example, there will be a stronger interaction between incoming molecules with a kink than a terrace. The increased interaction originates from the increased points of contact and surface area. Figure 2.3[57] shows a diagram incorporating all the different types of defects.
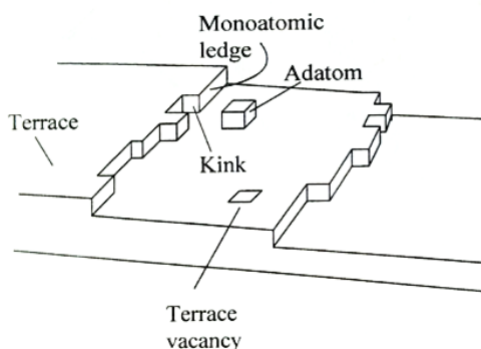
Figure 2.3: Schematic representing different surface features present on a crystal surface [Source:[57]]

2.3.2 Surface Relaxation

Surface relaxation occurs when the intermolecular bonds on the surface are unsatisfied as there are no possible interactions with the vacuum. As such the energy of the top layer gets redistributes towards the bulk and reduce the interplanar distance between the surface molecule and bulk[58]. Figure 2.4[59] shows a simplistic diagram of this occurrence, with the top layer having a smaller interplanar distance $(d_{1-2} < d_{bulk})$. The surface relaxation will affect the intermolecular forces/distances that are modelled on the system. It has been previously shown that the relaxation of inorganic and metallic surfaces has a significant energetical difference compared to the bulk. However, this has not been extensively studied for organic materials due to the difficulty in analysing surface chemistry and subsequent topography[60, 61]. While briefly discussed in this study, it is important to consider when modelling surfaces.
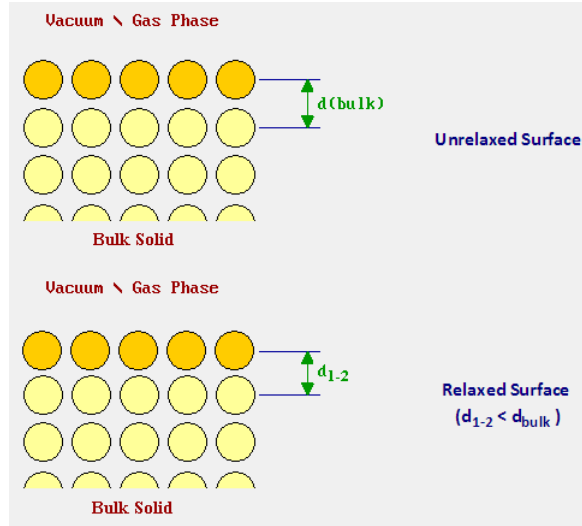
Figure 2.4: Simplistic Diagram showing the relaxation of a surface and the reduction in interplanar distance of the surface (d_{1-2}) compared to the bulk (d_{bulk})[Source:[59]]

2.3.3   Liquid-Solid Interfacial Interactions - Wetting Energy

The wetting energy is used to describe the cohesive and adhesive forces between a solvent interacting with a surface. The adhesive forces are the interactions between the solvent and surface while the cohesive is the solvent to solvent interactions. These forces are described using Young's equation of interfacial tension (γ) between solid-liquid-gas as a function of contact angle (θ_c) as seen in Equation 2.10[62]. Figure 2.5[63] shows the corresponding terms labelled. When the contact angle is zero degrees the surface is said to be perfectly wetting, and at 180° the surface represents a non-wetting condition and can be called strongly hydrophobic.

$$\gamma_{SG} = \gamma_{SL} + \gamma_{LG}cos\theta_c \tag{2.10}$$

Contact angle measurements have formed a routine part of surface analysis in the lab, with the use of high-speed cameras, macro-lenses and drop dispensers to ensure high accuracy of the reading. However, the modelling of wetting energetics is more of a complex problem. Several studies have attempted to accurately model the interaction between solvent and surfaces using quantum mechanical (QM) calculations by implementing continuum solvation models such as the conductor-like screening model(COSMO) to incorporate solvation effects into QM calculations[64, 65, 66]. While these show promise, it is outside the scope of this project to delve into detail regarding the QM calculations.
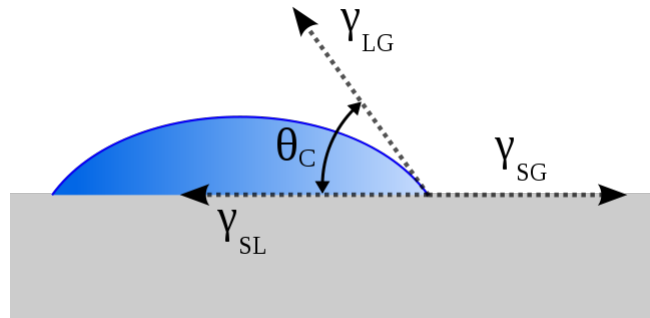
Figure 2.5: Diagram showing the different interfacial tensions and contact angle when discussing solvents to surface interactions [Source:[63]]

2.4   Interactions Between Bodies

The interactions between bodies occur due to a range of forces, and this section aims to illustrate the different contributions which will ultimately result in varying particle behaviours within formulations. Gaining an idea of the component forces responsible for the cohesion and adhesion of powders allows for more efficient drug product design, as the materials properties can then be tuned to achieve the desired performance.

2.4.1   Capillary Forces

Manufacturing of pharmaceutical powders typically requires several particle sizing steps (reduction or enlargement) to ensure adequate packing or weight. During granulation, which is used to increase particle sizes by agglomerating particles together, a certain level of liquid will be present on the macroscopic surface. If a high enough concentration of solvent is reached on the surface of a particle a mobile liquid bridge can form between two particles, linking them together; this is referred to as a pendulum state. Figure 2.6[67] is a schematic showing a pendulum liquid bridge where R is the radius of two identical spheres that are separated $2s$ apart. The liquid bridge has a contact angle θ at the surface and a half-angle $\hat{\beta}$. The buoyance and gravitational forces are assumed to be negligible. The capillary force F_L is the sum of the surface tension force F_S acting the gas-liquid interface and the pressure deficit force F_P, which relates to the difference in pressure between the liquid internal and external.

$$F_L = F_S + F_P \tag{2.11}$$
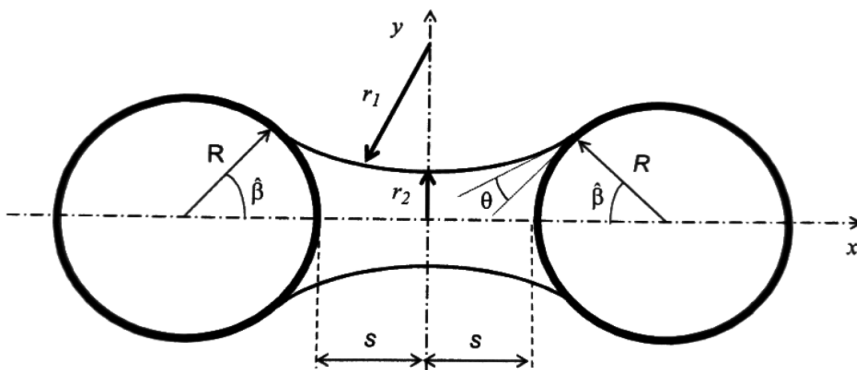
Figure 2.6: Pendulum liquid bridge between two spheres [Source:[67]]

The liquid bridge is approximated to have two principle radii r_1 (radius of bridge surface in the plane of the figure) and r_2 (radius of the next neck in the plane of

symmetry). Based on Fisher *et al.*[68] determination of the axial surface tension force F_S, and pressure deficit force F_P acting at the plane of symmetry ($s = 0$):

$$F_S = 2\pi r_2 \gamma_L \tag{2.12}$$

$$F_P = \pi r_2^2 \Delta P \tag{2.13}$$

Where γ_L is the surface tension of the liquid-gas interface and ΔP is the hydrostatic pressure (pressure difference between the inside of the liquid bridge and the ouside atmosphere). At $\theta = 0$, during perfect wetting, the hydrostatic pressure within the liquid bridge is determined using Laplace Equation[69]:

$$\Delta P = \gamma_L \left[\frac{1}{r_1} - \frac{1}{r_2} \right] \tag{2.14}$$

Substituting equation 2.13 into 2.14:

$$F_L = \pi r_2 \gamma_L \left(\frac{r_1 + r_2}{r_1} \right) \tag{2.15}$$

Applying trigonometry:

$$r_1 = R(\frac{1}{\cos}\hat{\beta} - 1) \tag{2.16}$$

$$r_2 = R(1 + \tan\hat{\beta} - \frac{1}{\cos}\hat{\beta}) \tag{2.17}$$

Substituting equations 2.16 and 2.17 into 2.15 gives the most basic form of the capillary force:

$$F_L = \frac{2\pi r_2 \gamma_L}{1 + \tan(\frac{\hat{\beta}}{2})} \tag{2.18}$$

Equations 2.16 and 2.17 assume the separation between particles is zero, however, this is not true for real particles where roughness causes a separation between the two particles. As such the two equations can be adjusted to include the half distance separation (s) :

$$r_1 = R((1 + \frac{s}{R})\frac{1}{\cos}\hat{\beta} - 1) \tag{2.19}$$

$$r_2 = R(1 + (1 + \frac{s}{R})\tan\hat{\beta} - (1 + \frac{s}{R})\frac{1}{\cos}\hat{\beta}) \tag{2.20}$$

Illustrating that a small separation between the surface can have a significant impact on the overall capillary force.

Liquid bridges can be measured by altering the amount of liquid present on a surface and measuring the forces required to separate the surfaces. The amount of liquid present on the surface can be related to the relative humidity (RH) of

the system. The RH can have a prominent effect on the force required to separate two bodies (pull-off force). The impact of RH on the adhesion forces has been documented throughout many studies[29, 70, 71, 72, 73]. For instance, work carried out by Jian et. al. showed an increase in pull-off force for graphene when %RH > 40, as illustrated in Figure 2.7[72].
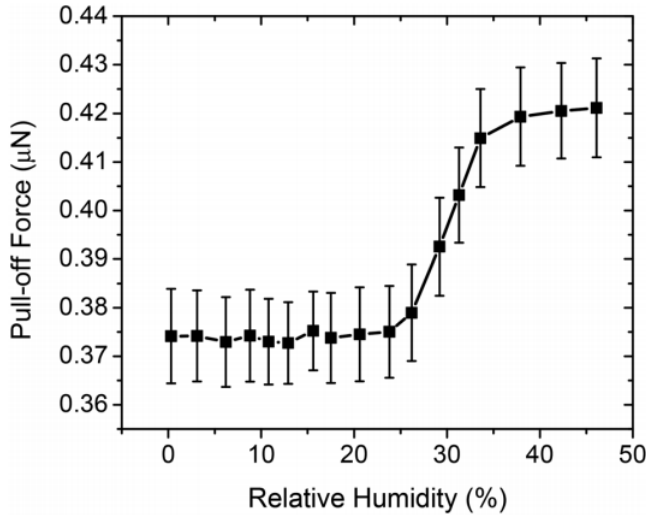
Figure 2.7: Graph of the pull-off force required to separate two bodies (graphene - SiO_2) as a function of relative humidity [Source:[72]]

2.4.2 Coulombic Forces

Typically reserved for ionic systems, coulombic forces also exist between partially charged species in organic crystals. The coulombic force between two charged atoms or ions is a relatively strong physical force and can be described using the inverse-square law where the electric field E_1 at a distance r away from charge Q_1 is given by[74]:

$$E_1 = \frac{Q_1}{4\pi\epsilon_0\epsilon r^2}Vm^{-1} \tag{2.21}$$

Where ϵ is the dielectric constant for the medium, as this field acts on a second charge Q_2 as a function of r:

$$F(r) = Q_2E_1 = \frac{Q_2Q_1}{4\pi\epsilon_0\epsilon r^2}N \tag{2.22}$$

2.4.3 Hydrogen Bonding

Hydrogen atoms are covalently bonded to an electronegative atom (O,F or N) causing it to be electron deficient and thus partially positively charged. These conditions

allow for a second weaker bond to be formed between the hydrogen atom and another electronegative atom in the direction of its lone pair electron orbital, forming an X-H...Y bonding configuration.

2.4.4 Van der Waals

Van der Waals forces can be further categorised into three types:

- Dipole-Dipole: Molecules that hold permanent dipoles that interact with other permanent dipoles.

- Dipole - Induced Dipole: The permanent dipole induces a dipole onto a non-polar atom or molecule.

- Dispersion Forces: Due to fluctuation in charges between atoms or molecules a displacement of central charge takes place and thus at a certain time a dipole will exist and induce a dipole in another atom or molecule.

2.4.4.1 Dipole - Dipole (Keesom)

Polar compounds consist of charged atoms separated by an intermolecular distance. The distance between the two charged groups gives rise to a dipole. Such charged groups can be found throughout much of organic chemistry. Typically electronegativity plays a crucial role in directing the flow of electrons from one atom to another. Similar to the coulombic forces, the equation to describe the dipole-dipole interactions is shown in Equation 2.23, where w is the interaction energy between two dipoles u_1 and u_2 at a distance r apart [75].

$$w(r) = -\frac{2u_2^2 u_1^2}{3(4\pi\epsilon_0\epsilon)^2 r^6} \qquad (2.23)$$

2.4.4.2 Dipole - Induced Dipole (Debye)

When a polar molecule is within proximity of a secondary non-polar molecule, a dipole will be induced within the second molecule altering the electron distribution, polarising the atom. Equation 2.24 describes the magnitude of the induced dipole μ:

$$\mu^* = \alpha\epsilon \qquad (2.24)$$

Where α is the polarisability of a molecule, the electronegativity of the atom determines polarisability thus the larger the polarising atom, the less electronegative

and as such less polarising. As the shape and symmetry of the electrical field are important, so is the position of the second molecule. The interaction energy w is dependent on the magnitude of dipole of molecule two (μ_2) and the polarisability of the first one (α_1).

$$w(r) = \frac{u_2^2 \alpha_1 + u_1^2 \alpha_2}{(4\pi\epsilon_0\epsilon)^2 r^6} \tag{2.25}$$

The interaction energy is inversely proportional to the sixth power of the distance $\frac{1}{r^6}$ and as such is one of the components of the van der Waals type forces. Substituting α with $\frac{u_2}{3k_bT}$, k_b being the Boltzmann constant and T temperature, we arrive at the final form of Equation 2.26[76, 75]:

$$w(r) = \frac{u_2^2 u_1^2}{3(4\pi\epsilon_0\epsilon)^2 k_b T r^6} \tag{2.26}$$

2.4.4.3 Dispersion Interaction (London)

The London dispersion forces are some of the weakest intermolecular forces that occur between two molecular groups that are formally neutral charge, but are always present and as such one of the most important when considering crystals systems being held together by intermolecular interactions. These interactions originate from quantum mechanics and occur when the movement of electron clouds between non-polar atoms occurs, at any instant there exists a finite dipole thus inducing a dipole moment in a neighbouring atom. Equation 2.27[77] describes the interaction energy w with I_1 and I_2 being the ionisation energies of the two atoms.

$$w(r) = -\frac{3}{4} \frac{\alpha_1 \alpha_2}{(4\pi\epsilon_0)^2 r^6} \frac{I_1 I_2}{(I_1 + I_2)} \tag{2.27}$$

2.4.4.4 Predicting Van der Waals using Lennard-Jones Potentials

Lennard-Jones (LJ) potentials are used to describe the attractive and repulsive forces experienced by two bodies as a function of distance (r), shown in Equation 2.28. The depth of the potential well is given with ϵ, which is the interaction between the two bodies, with σ being the separation distance between the two at zero potential.

$$w(r) = 4\epsilon \left[\left(\frac{\sigma}{r}\right)^{12} - \left(\frac{\sigma}{r}\right)^6 \right] \tag{2.28}$$

The equation can be further simplified with A and B to describe the repulsive and attractive terms respectively by substituting $A = 4\epsilon\sigma^{12}$ and $B = 4\epsilon\sigma^6$ into Equation 2.28:

$$w(r) = \frac{A}{r^{12}} - \frac{B}{r^6} \tag{2.29}$$
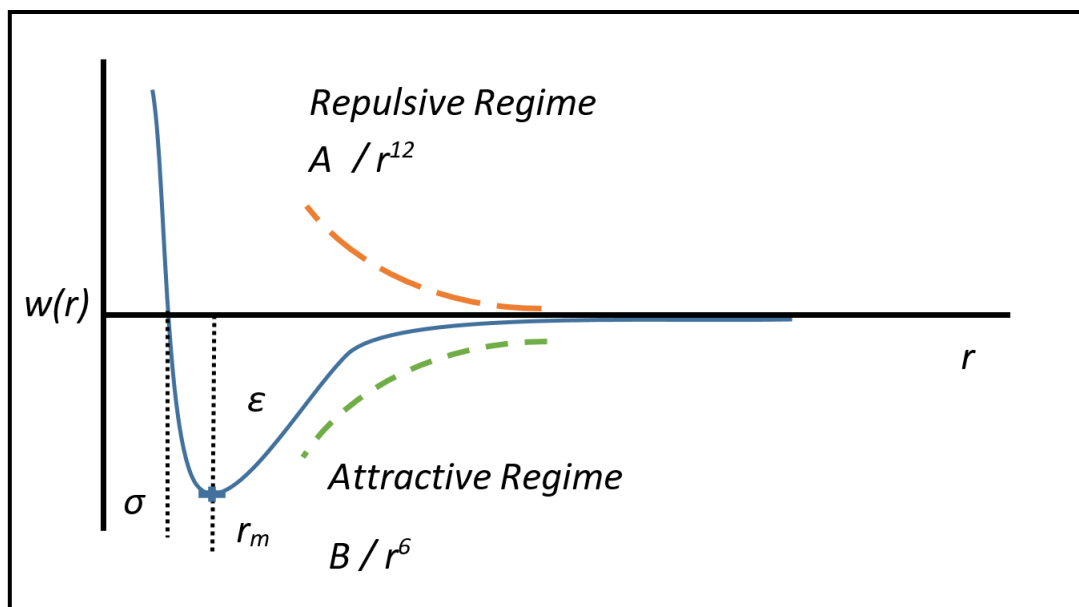
Figure 2.8: Lennard-Jones potential graph showing the repulsive force (orange) and attractive force (green) when two bodies are approaching each other.

The graph in Figure 2.8 shows the interaction energy plot as a function of distance to model van der Waals interaction using LJ potentials. The powers of 12 and 6 are used to illustrate the fall off of the force as distance increases, thus only being "felt" by the bodies at close range. Another set of potentials that could be used are called Buckingham potentials which was initially proposed as an improvement on the L-J potential. However, they are typically not used to model organic crystals as the set of potentials does not adequately model small interatomic distances as the nuclei of two atoms can overlap [78].

2.4.5   Forcefield General Form

Force fields are used to describe atom-atom interactions and contain the terms A and B seen in Equation 2.29. The total energy (U_{Tot}) [79] of the system can be calculated by summing the bonded and non-bonded interactions, these include; bond stretching $(E_{Stretch})$, bending (E_{Bend}), torsion $(E_{Torsion})$, van der Waals (E_{VdW}), and electrostatic (E_{Elec}). A basic forcefield[44, 79] would be described as :

$$U_{Tot} = E_{Stretch} + E_{Bend} + E_{Torsion} + E_{vdW} + E_{Elec} \qquad (2.30)$$

25

$$U_{Tot} = \sum^{nBonds} \left(\frac{k_n}{2} \right) (r_{ij} - r_0)^2 + \sum^{nBondPairs} \left(\frac{k_n}{2} \right) (\sigma_n - \sigma_0)^2 +$$

$$\sum^{nTorsions} \left(\frac{k_n}{2} \right) (1 + \cos(m\vartheta_n + \vartheta)) + \sum_{i=1}^{nVdW} \sum_{j=1}^{nVdW} \left[\frac{A_{ij}}{r_{ij}^{12}} - \frac{B_{ij}}{r_{ij}^{6}} \right] + \quad (2.31)$$

$$\sum_{i=1}^{nElec} \sum_{j=i-1}^{nElec} \left[\frac{C}{\epsilon} - \frac{Q_i Q_j}{r_{ij}} \right]$$

Where, r_{ij} is the actual distance between two atom pairs, r_0 is the standard bond length for the particular bond, k_n is the force constant of the bond, σ_n and σ_0 are the actual angle and standard angle respectively, and C is a conversion constant for energy into kcal/mol, which is the standard unit used to describe energy.

2.5 Modelling Organic Crystals

Molecular modelling has had a large impact on our understanding of the fundamental properties of matter, the atomic and molecular scale, with a lot of the fundamental theories highlighted above being used in a range of fields, from biological to materials and pharmaceuticals[80, 81, 82]. This project will be focused on modelling solid-state organic surfaces and in particular, their interactions with other organic surfaces. Extensive work has been carried out in successfully modelling the crystal bulk as well as a surface for a range of organics. From QM [83] through to MD[84] surface interactions have been a challenge for many due to the complexity of the system.

Extensive work has been carried out towards the use of computational methods and forcefields required for simulating organic crystals. A few notable papers have emerged that relate the crystallographic structure to their physical properties. A recent study by Rosbottom *et al*[85] demonstrated a framework for modelling the structure, morphology and surfaces of para-aminobenzoic acid (pABA). The crystal morphology was predicted within very close approximation to the experimentally grown crystals as seen in Figure 2.9.
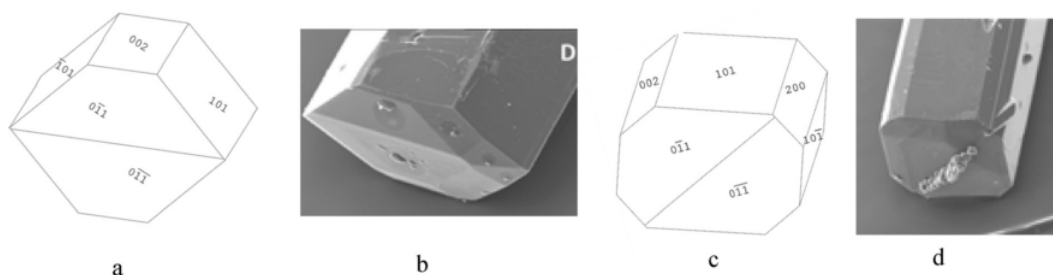
Figure 2.9: a and c) are sketches of the morphological predictions using attachment energy model for α-pABA. b and d) are experimentally grown single crystals of α-pABA using slow evaporative method in ethyl acetate [Source:[85]]
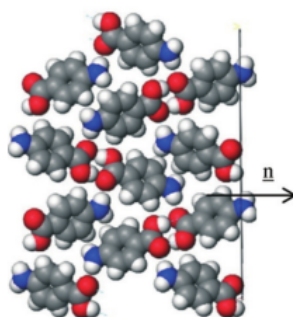
Figure 2.10: Space fill diagram showing the surface chemistry of facet (10$\bar{1}$) for α-pABA [Source:[85]]

From the predicted morphology, the paper goes to further analyse the inter-

27

molecular interactions that occur at the surface during addition of a growth slice. Interaction strengths were compared and the functional groups that were responsible for them. Figure 2.10[85] shows the structure of the $(10\bar{1})$ of α-pABA. It was found that hydrogen bonding across the COOH group was the strongest interaction which caused the higher growth rate compared to the other facets. The ability to gain such a detailed insight into an organic crystal is valuable to understand the surface properties and how surfaces can be modified to change the physical properties of the particulate.

Discussions and reviews of the current literature regarding the current approach to surface interactions is given in the introduction to Chapter 4 in order to offer more context to the results discussed in said chapter.

2.6 Conclusions

This chapter has highlighted the fundamental knowledge required for understanding crystals and the forces that occur within and between them. The predictive capabilities of such systems and forces have been given where appropriate; it is obvious that it is not a full detailed explanation of all computational modelling, however, relevant details have been covered. While the surfaces of crystals have been previously investigated with a degree of success describing the surface chemistry and how it could possibly impact the interaction with other systems. There is still a lack of understanding on how two facets would interact with each other as direct facet-facet calculations have not been carried out extensively. Understanding what effect surface chemistry has on those and subsequent impact to the inter-particular interaction is crucial for effective drug product design.

This project is focused on understanding how different surface chemistries impacts facet-facet interactions and predicting them using in-silico methods. The aim is to generate a ranking system for the most adhesive API/Excipients systems with facet specificity. This would impact pharmaceutical formulations by reducing the number of trials required during the development stage in order to find compatible excipients. While an in-silico tool would be useful; it would require being validated using experimental methods, which will be discussed in the next chapter.

CHAPTER 3

Measuring Particle Interactions

"No amount of experimentation can ever prove me right; a single experiment can prove me wrong - Albert Einstein"

This chapter describes techniques used for assessing the interactions that occur at the surface of crystalline materials and covering fundamental atomic force microscopy theory.

3.1 Techniques for Measuring Particle-Particle Interactions

Interacting particles will exhibit multiple-length scale forces. Complimentary techniques are typically used to understand the complexity of the system. This section will focus on existing methods of measuring particle-particle interactions. Three techniques have been highlighted due to their ability to measure forces between two surfaces.

3.1.1 Surface Force Apparatus (SFA)

The instrument is comprised of two smooth mica crossed cylinders that are brought together through the translation of a piezoelectric drive to which one mica surface is mounted. The second mica is mounted to a spring with a known spring constant (k)[28, 47]. The separation between surfaces is measured using optical interferometry. As the distance between the two surfaces is adjusted, the deflection of the spring (x) is measured and converted to force using Hooke's Law[86]. Figure 3.1[87] illustrates the construction of SFA.

$$F = -kx \tag{3.1}$$

The distances can be measured to angstroms resolution allowing short-range forces to be calculated. Due to the relatively large area of contact, long-range intermolecular forces can be studied. Studies in biological[87], polymeric and solid-solvent interfaces have been successfully carried out using SFA[88].

The benefits of SFA include high precision, and known contact area which can be accurately calculated using well-understood contact mechanics; as opposing cross cylinders are geometrically equivalent to a sphere on a flat plane. However, the need for cross-cylinder geometries and the use of mica surfaces, which can only be utilised to a depth of nanometres to preserve the transparency, pose severe limitations compared to the benefits. For this reason, it is only suitable for a number of systems that allow for light to pass through unimpeded and can be coated onto a cylindrical geometries.

3.1.2 Total Internal Reflectance Microscopy (TIRM)

A technique developed over the last 20 years that utilises light scattering to determine the potential energy between two interacting surfaces[89]. TIRM uses a transparent plate and a single microscopic sphere immersed in liquid. Light is scattered by the sphere when illuminated by an evanescent wave through the plate. The
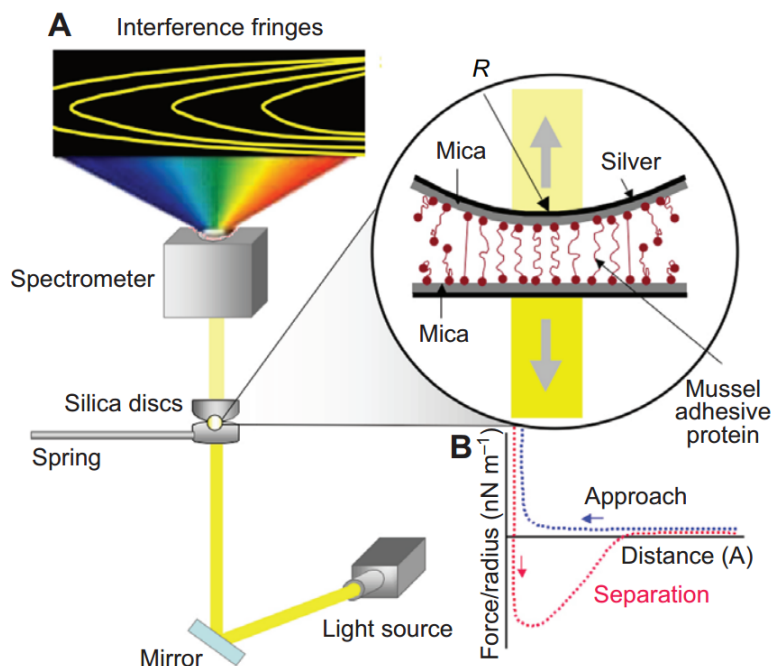
Figure 3.1: Diagram showing surface force apparatus design as used in biological studies [Source:[87]]

intensity of light is correlated to the distance between two objects. Potential energy is determined using the equilibrium distribution of separation distances sampled by Brownian motion[89, 90]. A schematic showing the workings of TIRM is illustrated in Figure 3.2[90].

The non-invasive nature of TIRM allows for $<$pN forces to be measured without any damage to the sample. TIRM has been widely used for colloidal[89], biological and materials studies, which have been applied on liquid-liquid[91], liquid-solid[88], and solid-solid[90, 92] interactions. The technique is, however, only usable under fluid environments prohibiting studies that require to be carried out in air.

3.1.3 Inverse Gas Chromatography (IGC)

The technique is based on the distribution of components that are separated between two phases, stationary and mobile. In typical gas chromatography (GC) the mobile phase is an inert gas used to carry vaporised materials (the sample) over the stationary phase, typically a polymer lined on the inside of a column[20]. A schematic view of the instrumental setup shown in Figure 3.3. The single column is used to separate and characterise multiple gases/vapours that are pumped through. Inverted gas chromatography is, as the name implies, the inverse of GC where a single gas/vapour probe molecule (adsorbate) is used in a column packed of solid material of the sample being analysed.
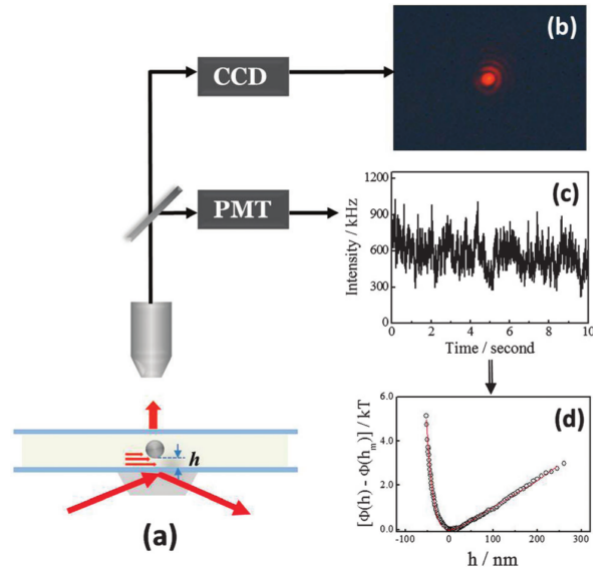
Figure 3.2: (a) Schematic of a typical TIRM setup: a Brownian colloidal particle moves in the evanescent field generated by total internal reflection at the glass–liquid surface and the scattering intensity from the particle is collected by an objective and recorded by a photomultiplier tube (PMT). Typically recorded scattering intensity from the Brownian motion of the particles as a function of time. (d) Measured interaction potential of the particle [Source:[90]].
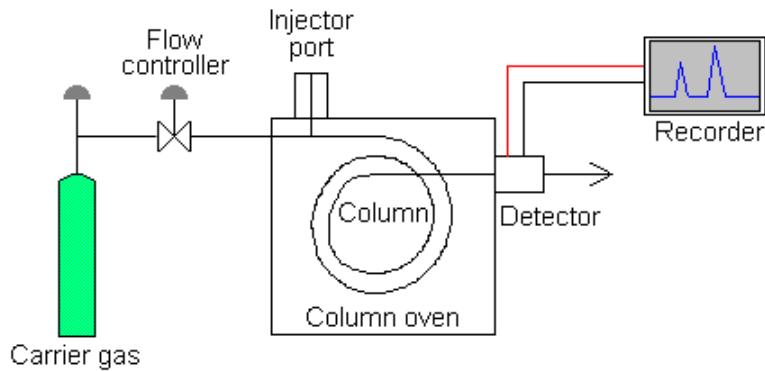
Figure 3.3: Schematic showing the basic instrumental set up of Inverted Gas Chromatography. Source: [93]

The distribution of solute between the stationary and mobile phase corresponds to the solute-free energy minimum. A partition coefficient (K_R), describing the ratio between solute and immiscible solvent at equilibrium can be calculated, which is correlated to the mass (m_s), surface area (σ) of the solid and the retention volume V_N (volume of carrier gas required to elute adsorbate). Both K_R and as such V_N can be related to the strength of the interaction between the adsorbent and stationary phase[20].

$$K_R = \frac{C_s}{C_M} = \frac{V_N}{\sigma m_s} \qquad (3.2)$$

IGC can be used to take into account the different components associated with interacting forces such as dispersion forces and Debye forces[94]. This is carried out by using a range of molecular probes. For dispersive forces, "dispersive probes" are used (decane, nonane and octane) and for any charged forces, "polar probes" are utilised (Ethyl acetate and chloroform). The list of possible probes is extensive and can be useful to distinguish the difference in interactions from one adsorbent to another with the stationary phase [17]. Several studies have been carried out using IGC on powder-based API(s) with a few showing correlation to modelling of molecule-surface calculations[24, 95, 96, 97]. Others have reported the lack of correlation between IGC and other surface sensitive techniques such as atomic force microscopy (AFM)[33, 72].

A study which investigated the adhesive properties of five inhalation APIs and three excipients using an AFM colloidal method (explained in a future section) and IGC found no correlation between the two methods [33]. However, a higher correlation was found between the AFM data and performance testing used for benchmarking. This is not to suggest that IGC cannot be used, as the study could have used a larger range of molecular probes, but it does indicate that IGC does not provide a complete description of surface interactions [3]. This can be attributed to the complexity of two surfaces interacting and the lack of ability to measure the surface energy of just one of these surfaces by IGC. Other limitation relative to this project would include the lack of control over packing and calculation of the surface area (calculated using BET adsorption model [94]) of the columns which would offer no information to facet specific energetics.

3.2 Atomic Force Microscopy (AFM)

The atomic force microscope was first invented by Binnig *et al*[98] in the 1980s and forms part of a series of scanning probe microscopes. AFM was primarily used for topographical imaging of non-conductive surfaces at an atomistic resolution.

3.2.1 General Overview

A schematic of a typical AFM is shown in Figure 3.4[99]. The sample is scanned by a tip, which is attached to a cantilever with a known spring constant (k). A constant force is kept between the tip and the sample by monitoring the deflection of the tip with the use of a laser diode and photodiode (known as an optical lever) reflecting from the surface of the cantilever. In most cases, the sample is moved against the tip in the xyz directions using a piezoelectric motor, but it is also possible to move the tip with a stationary sample. A feedback loop is created between the cantilever deflection and z displacement of the sample. The fundamentals of AFM relies on Hooke's Law, as seen in Equation 3.1 where the force (F) of the tip interacting with the sample is determined by knowing the spring constant (k) and the deflection of the spring (x).
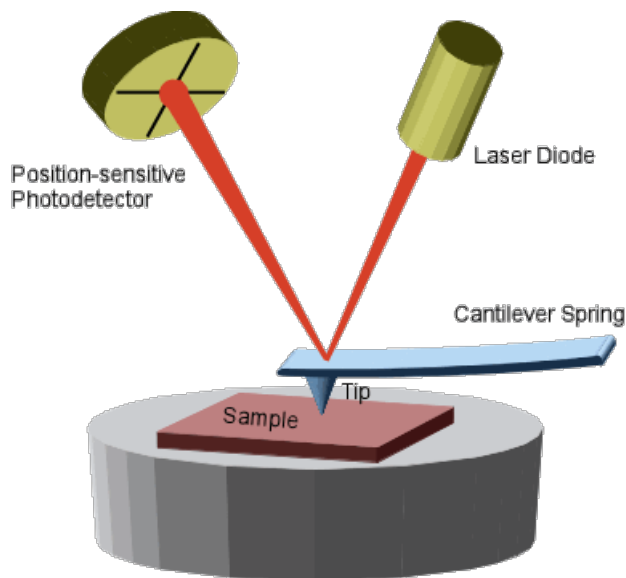
Figure 3.4: Illustration showing the instrumental set up of a typical atomic force microscope [Source:[99]]

3.2.2 Force Measurements

The force measurements are carried out by measuring the cantilever deflection (x) as a function of the position of the piezo Z_P normal to the surface of the sample. A force vs distance plot as seen in Figure 3.5 can be achieved by calculating the force

(F) and plotting it vs the tip-sample separation (D), which is calculated by adding the deflection of the piezo potion, as shown in Equation 3.3.

$$D = x + Z_P \tag{3.3}$$
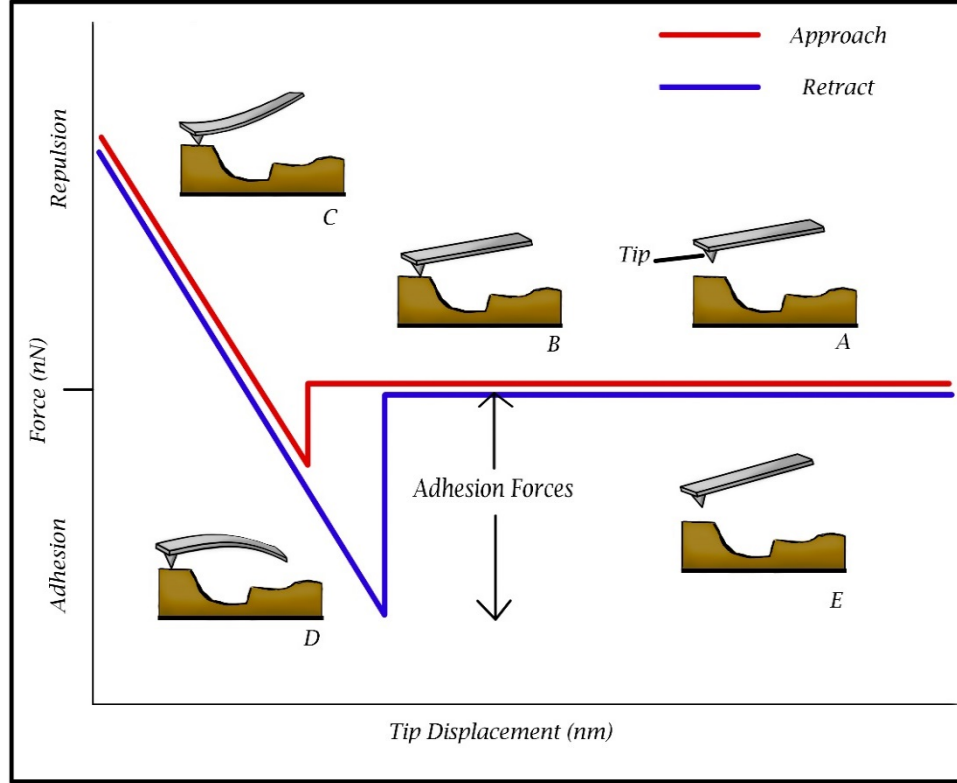
Figure 3.5: Graph of force-vs-displacement curve illustrating contact and different stages, with the tip approaching (red) and retracting (blue) a) There is no deflection. b) As tip approaches, the attractive forces acting between the substrate and tip cause the cantilever to deflect and the tip to make contact with the surface. c) Cantilever bends as force is exerted and thus deflection increases. d) The cantilever is retracted from the surface. However, adhesive forces prevent detachment of the tip and cause a bending deflection. e) Cantilever returns to the original state.

As the tip approaches the surface, dominating attractive forces pulling the tip down to achieve contact. Further displacement towards the sample causes the cantilever to bend upwards, representing repulsive interaction. At a pre-determined force level, or trigger set point, the piezo reverses direction and retracts away from the surface and pulls off the surface. The "pull-off" force is related to the adhesion force (F_{ad}) of the tip-surface interface. As a force (F) is applied to the end of the cantilever bending causes the reflected laser beam to move through an angle twice, the change of the endslope dx/dX. X is the horizontal component of the cantilever when it is not bending and x being the deflection of the cantilever at its end. The endslope in cantilevers with rectangular cross-section of length L, thickness t, and
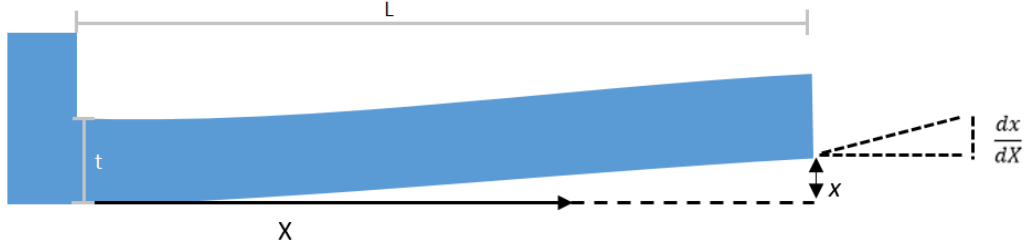
Figure 3.6: Side view schematic of cantilever under applied force where X is the horizontal position with reference to the base of the cantilever and x being the defection of the cantilever at the end.Thickness, and length are denoted with L and t, with the width (w) being perpendicular to the page plane.

width w is described in Equation 3.4.

$$\frac{dx}{dX} = \frac{6FL^2}{Ewt^3} \tag{3.4}$$

Where E is Young's modulus of the cantilever. The deflection of the cantilever is proportional to the endslope, as seen in Figue 3.6.

The movement of the optical beam is proportional to the endslope of the cantilever [29]. The deflection can be defined by Equation 3.5 under equilibrium conditions; where the speed of the cantilever is below its resonance frequency.

$$x = \frac{4FL^3}{Ewt^3} = \frac{2}{3}L\frac{dx}{dX} \tag{3.5}$$

During tip retraction, the energy (W) required to bend the cantilever must equal the F_{ad} in order for pull-off to occur. This is assumed under no sample deformation:

$$W = \frac{F_{ad}^2}{2k} \tag{3.6}$$

As the force-distance curve is inferred from the current change (ΔI_{pd}) on the photodiode as the laser moves across the surface vs the position of the piezo electric motor, a conversion must be made using the zero distance and the sensitivity of the spring. These are both inferred from the curve itself and in particular the linear part of the force curve as seen in part c) of Figure 3.5. The zero distance is defined as the point of contact between the tip and sample. The slope sensitivity is the linear repulsion region past the zero point contact. The gradient $\Delta I_{pd}/\Delta x$ is measured and defined as the deflection sensitivity. The spring constant calibration is carried out using the deflection sensitivity measured and thermal tune method proposed by Hutter and Bechhofer[100].

As a brief overview, the thermal tune method measures the deflection signal whilst the cantilever is suspended from the surface at thermal equilibrium. Random impulses (Brownian motion) are detected over a period of time. The function is then

Fourier transformed in order to obtain a Power Spectra Density (PSD). Taking the integral of the resonant peak yields the power related to that resonance. Describing the cantilever as a harmonic oscillator by the total energy of the system, and in particular, the potential energy can be described in equilibrium, Equation 3.7.

$$\frac{1}{2}m\omega_0^2 x^2 = \frac{1}{2}k_B T \tag{3.7}$$

Where, T is temperature, k_B Boltzman's constant (1.385 x $10^{-23} J/K$), m the effective mass and finally ω_0 is the resonant angular frequency. The spring constant (k) is determined by simplifying the displacement (x) and temperature and using the power (P) of the resonance peak as seen in Equation 3.8.

$$k = (k_B T)/x^2 = (k_B T)/P \tag{3.8}$$

Some of the limitations of using force curves extend to their dependency on the cantilever, as any damage or alternation would cause the calibration to be invalid. However, being able to measure forces with a resolution of pN and sensitivity of pm makes AFM ideal for measuring forces between surface planes. Assuming one can mount a surface plane onto a cantilever.

3.2.3 Colloidal Probes

The colloidal technique was first developed by Ducker *et al*[101] where a solid silica sphere was glued to the end of a cantilever. The smooth surface and easily defined sphere radius mean the surface forces could be analysed quantitatively because of the symmetrical nature of the geometry as well as a plethora of models that can be used to describe the forces between a sphere and flat plane, some of which will be covered in the next section.

Spheres could be coated in different chemicals and powders to allow for a range of interactions to be measured. During the glueing process, traditionally an epoxy-based adhesive would be used that contains an evaporative solvent. Typically after a colloid had been glued, it would be leftover 24hrs to ensure no solvent was present as it could contaminate the surface of the sample.

The advantage of using a colloidal probe, besides the ability to probe with specific functional groups, is the ease in which these can be functionalised and thus an array of chemical probes can be used to understand the surface chemistry of a facet. However, coating said probes with powders does introduce a physical and chemical uncertainty to all the measurements, as the geometry of the probe is no longer a smooth sphere, but coated in many asperities. Investigating, the surface chemistry impact on these measurements would only yield data describing the average surface

as no surface chemistry can be elucidated from the colloidal probe surface. Further discussions and literature examples have been given in Section 6.1.

3.2.4 Derjaguin Approximation

The material and geometric properties of the tip-sample can affect the forces measured. By using the Derjaguin approximation[102] the influence on the two arbitrary geometries $U(D)$ is reduced to simple planar surfaces. This is achieved by relating the energy per unit area between two planar surfaces U_A with a width gap x_w between the two arbitrary geometries U and a separation distance D as described in Equation 3.9, where dA is the cross-sectional area of the real geometries.
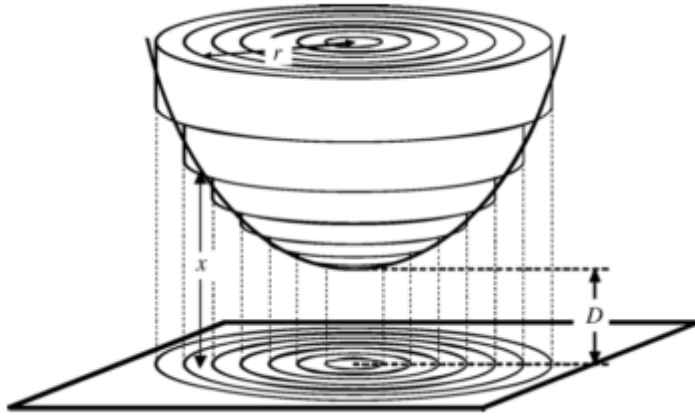
Figure 3.7: Schematic showing the Derjaguin approximation where x is width gap between the planar surfaces, D is the separation distance and r is the radial distance for the planer surface [Source:[29]]

$$U(D) = \int U_A(x_w)dA \tag{3.9}$$

This can be related to the force (F) experienced between two arbitrary shaped surfaces as f is the force per unit area:

$$F(D) = \int f(x_w)dA \tag{3.10}$$

Using colloidal probes with a spherical component, the radius of the sphere can be taken into account. Figure 3.7 shows the Derjaguin approximation on a sphere, and the final derivation is shown below in Equation 3.11, where R is the radius of curvature.

$$U(D) = 2\pi R \int_D^\infty U_A(x_w)dx_w \tag{3.11}$$

3.2.5 Contact Regimes

Material properties such as elasticity can affect the contact between the tip and sample due to deformation occurring at the interface, as such contact can be made but is not stable as the surface can deform, so a true zero point is difficult to define. Three major contact regimes have been developed to represent the interactions between two bodies in contact in different situations. The deformation is related to Young's modulus; which describes the elasticity of the sample and will be noted as δ from here on in.

3.2.5.1 Hertz

The model assumes a linearly elastic sphere indenting into an elastic planar surface[103]. The deformation (δ) of a sample can be related to the contact region radius a in Equation 3.12.

$$\delta = \frac{a^2}{R} = \left(\frac{F^2}{RE_{Tot}^2}\right)^{1/3} \tag{3.12}$$

Where R is the radius of the tip in contact with a flat surface. F is the force exerted by the tip onto the surface, E_{Tot} is the reduced Young's modules that are defined by Equation 3.13 with k_s being the stiffness of the sample. The adhesion and surface forces are neglected within the Hertz model.

$$E_{Tot} = \frac{2a}{3k_s} \tag{3.13}$$

3.2.5.2 Johnson-Kendall-Roberts (JKR)

The JKR model assumes both bodies are elastic, similar to the Hertz model, but it takes into account the adhesion within the contact regions[104](adhesion from outside the contact area is ignored). JKR is applicable to soft samples with high adhesion. The sample deformation is described by Equation 3.14.

$$\delta = \frac{a^2}{R} - \frac{2}{3}\sqrt{\frac{6\pi W a}{E_{Tot}}} \tag{3.14}$$

Where W is the adhesion work per unit area, and the force of adhesion (F_{ad}) can be taken into account using Equation 3.15

$$F_{ad} = \frac{3\pi RW}{2} \tag{3.15}$$

3.2.5.3 Derjaguin-Muller-Toporov (DMT)

The DMT model assumes an elastic sphere against a rigid plane. The model includes vdW and adhesion force outside the contact region [105]. This model can be applied to stiff samples with low adhesion. The sample deformation is described by Equation 3.16[29].

$$\delta = \frac{a^2}{R} = \left(\frac{F^2 + 2\pi RW}{\sqrt[3]{RE_{Tot}^2}} \right)^{\frac{1}{3}} \tag{3.16}$$

The adhesion force between the sphere and sample is modelled similar to JKR:

$$F_{ad} = 2\pi RW \tag{3.17}$$

It should be noted that the above models do not take into account the surface roughness of the bodies. All methods assume smooth spherical bodies, the impact of morphology and surface roughness are acknowledged and have been previously investigated[106]. Regardless of these limitations, these models have been used in a number of applications.

3.3 Conclusions

Throughout this chapter, experimental methods have been highlighted that would allow for the measurement of two surfaces interacting. Comparative techniques such as SFA, TIRM, and IGC have been described in order to offer a balanced view of possible experimental routes. However, due to a lack of surface specificity, physical limitations, and geometrical constraints, such methods proved inferior when compared with AFM.

An overview of how AFM works and the underlying physics behind how forces are measured has been given. The contact regimes that model how surfaces behave based on their elasticity and adhesive properties have also been described. A more in-depth description of the current technology, regarding the measurements of surface-surface forces, is given in Chapter 6 in order to offer more contextual relevancy.

AFM has been used as the main experimental component in this research. This study focuses on the functionalisation of the cantilever to create facet specific probes using APIs which are then utilised to identify surface properties that impact inter-particular interactions. The forces between API-EXP crystals have been measured and ranked against one another. The AFM data will be compared to the surface-surface interactions calculated by the in-silico methodology developed.

CHAPTER 4

Modelling Surface-Surface Interactions

*"Shall I refuse my dinner because I do not fully understand the process of digestion?
- Oliver Heaviside"*

This chapter focuses on the computational aspects of facet-facet interactions by reviewing state of the art, describing the methodology and analysing the results from the developed model.

Introduction
Literature review and chapter outline

Crystal and Morphology Calculations
Preparation of crystal structures and morphologies for Surface-Surface Interaction Model

Methodology
Crystal structure and morphology calculations

Results
Crystal geometry, lattice energy and predicted morphologies

Surface-Surface Interaction Model
Calculating inter-particular forces between organic crystal facets and association to surface properties

Methodology
Model construction, running, convergence, and data analysis

Results
Cohesive/Adhesive balance, facet-specific interactions, impact of surface chemistry, probability of interaction

General Discussions
Improvement from previous studies, surface chemistry, and predicting average particle interaction energy

Conclusions
Summary of chapter

Figure 4.1: Outline of Chapter 4

4.1 Introduction

The understanding of how surfaces interact with one another can offer an insight into the behaviour of particles within large systems. The ability to simulate these interactions allows us to explain mechanisms and reasons for their occurrences.

A practical outcome of understanding the chemistry of surface interactions at an atomistic level would be to guide formulation development. Models have been developed to investigate surface energies by using molecular probes [25, 107, 108]. Most include the use of a grid-search method where a surface with a grid is defined, and interaction energies are calculated between probe (molecule or cluster) as it moves across the grid.

Correlations have been observed between computational predictions of particle-particle interactions and experimental data [24], by utilising a program called "Syst-Search" [107, 109], which allows direct probing of specific crystal surfaces with a single molecule. SystSearch creates a slab of a specific facet over which a grid is built, and a probe molecule is placed. The probe molecule has six degrees of movement, three translational (x, y, z) and three rotational $(\theta\gamma\delta)$. The interactions between probe-slab are calculated at every position and rotation. Figure 4.2 shows how the systematic search is set up and run. Whilst promising, a few limitations were found, but the programmed performed well at predicting solvent-surface interactions, which is more indicative of its set up [25, 110].
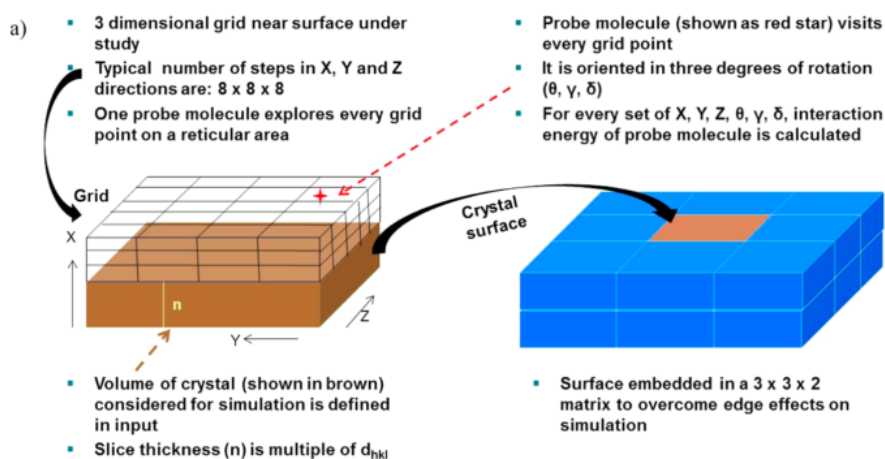
Figure 4.2: a) Shows the computational method for creating the slab and grid above the slab. b) Shows the six degree of freedom of the probe (P) in relation to the surface (S)[Source:[24]]

Ramachandran et al.[24] utilised the SystSearch tool to investigate the cohesive-adhesive balance (CAB) between APIs and excipients used for inhalation formulations. The de-agglomeration of cohesive powders was measured using dry powder laser diffraction analysis by exposing agglomerated particles to different pressures till they de-agglomerated, the pressure at which this occurred converted to the force

47

of de-agglomeration. A correlation was found between the predicted probe-surface interactions and de-agglomeration data, as seen in Figure4.3, fluticasone propionate (FP) ranked the highest cohesive, energetic interaction. However, discrepancies were identified regarding the calculations carried out for α-lactose monohydrate (LMH) where adhesion values between LMH and the other APIs did not agree with the experimental measurements. The difference was linked to the H-bonding from LMH not being correctly simulated. This highlights that more research needs to be done to improve the prediction of H-bond and electrostatic dominated surfaces.

Such a model has conformational limitations as the probe molecule and slab are kept rigid, and only one molecule can be added at a time. It is possible to get an overview of the interactions by using the molecular probe. However, it does not represent a surface due to the lack of intermolecular interactions that would be present from the rest of the slab both in the lateral planes and the bulk. SystSearch has shown to be a promising starting point, but the inability to generate two slabs for surface-surface calculations means it is not suitable for this study.

(a)   (b)
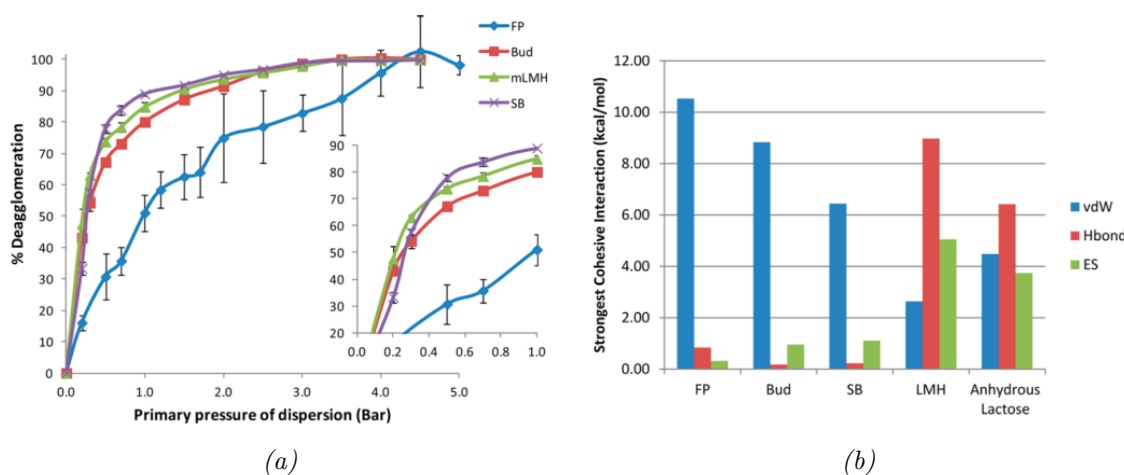
Figure 4.3: Two plots are showing the experimental a) de-agglomeration of the particles and b) probe-molecular slab interaction. A) De-agglomeration data carried out by laser diffraction analysis on a range of APIs fluticasone propionate (FP), budesonide (Bud), and salbutamol base (SB)) and the commonly used excipient, α-lactose monohydrate (LMH) showing the cohesive interactions with FP having the highest. B) Component energetics making up the interactions between probe and surface via SystSearch, showing the highest cohesive interactions, (excluding LMH) FP shows the highest cohesion followed by Bud and SB [Source:[24]].

Work by Pencheva, Hammond *et al*[108, 109] has shown the use of a systematic grid search method for two nano-clusters of organic material, ascorbic acid and aspirin. This promising work identified the corners and edges of a crystalline nano-clusters as highly energetic binding sites. Even with limitations such as assuming pristine, non-relaxed, zero-roughness surfaces, it highlights the importance of understanding the inter-particle interactions. While the edges are the most energetically

favourable sites of interactions, this does not explain interactions seen in inhalation formulations or granules where the facets of the crystals are in direct contact, and in some cases showing a higher affinity for certain facets[111].

The thickness of each nano-cluster was not large enough to achieve stable cluster energy, indicating that larger systems were required to get convergence. As the clusters were relatively small, their depth did not allow for the representation of interactions contributing from the bulk of the surface, thus not representing a large percentage of atoms that could contribute to the overall adhesion of the two surfaces.

The study presented in this thesis focuses on the design of a computational framework to calculate the molecular interactions between two surfaces. This chapter aims to describe the model developed, demonstrate its use on a combination of excipients, and describe how the surface chemistry and topology can impact the CAB between API and excipients. Moreover, the facet specificity and difference in surface chemistry will be explored in order to quantify the impact of functional groups on the final interaction energy.

The surfaces which the model will use have been predicted from their published crystal structures. Paracetamol has been chosen as the API due to its prismatic nature and extensive available literature. The excipients chosen were, D-Mannitol and L-Glutamic acid due to their differences in both morphology and types of functional groups present.

The outline for this chapter has been given in Figure 4.1, where the surface simulation will be described separately to the developed framework.

Contributions

"The candidate confirms that the work submitted is his own and that appropriate credit has been given where reference has been made to the work of others. It is to be noted that the project started with an early version of code developed by the industrial sponsor, Pfizer, where Rasolav Penchev was the main contributor. A script developed at the Cambridge Crystallographic Data Centre (CCDC) has been used in order to analyse surface descriptors, as published by Bryant *et al* [112]"

4.2 Crystal and Morphology Calculations

In order to calculate the facet-facet interactions between systems, their surfaces had to first be calculated. Starting with a crystal structure and calculating the lattice energy allows for the energetics of the system to be accounted for. These are then used to predict the morphology and subsequently, the most stable facets of the particles.

4.2.1 Methodology

This section covers the computational methodologies used for calculating the lattice energy, particle morphology.

Reported crystal structures of paracetamol(PARA), α-L-glutamic acid(LGA), β-D-mannitol(DMAN) were selected from the Cambridge Structural Database (CSD). The refcodes for PARA, DMAN and LGA are HXACAN28[113], DMANTL07[114], and LGLUAC03 [115] respectively. These were chosen due to the excellent fit to experimental data, as measured by the relatively low R-factor when fitted to the proposed structure. Dreiding was selected as the forcefield (FF) of choice due to its generic application to all organics and explicit description of H-Bond interactions, lending itself to quantify the impact of H-bonds within systems better. Due to the nature of the model, a single forcefield had to be used to describe different systems. While other generic forcefields exist that describe organic molecules, Materials Studios (MS) has only a limited number and Dreiding was the best-described FF available.

Crystal calculations were carried out in order to predict the possible morphologies of the systems. A lattice energy minimisation was performed for two reasons. Firstly, to ensure the crystal structure used was adequately describing the system in question; secondly, to carry out an energy normalisation across all systems using the same forcefield, effectively allowing for relative comparisons across multiple chemistries.

The energy normalisation was required as a single forcefield (FF) was used to describe multiple systems. The preferred protocol for carrying out FF based calculations is to use a specialised FF for the system types (Momany, Williams for an amino acid-based system) or to fit a FF to a system using quantum mechanics based calculations or even machine learning methodologies [116, 117]. As SSIM calculates interaction energy between heterogeneous systems, using a specialised/fitted FF would yield biased results. Therefore, a generic FF that contains a diverse list of atom types has been chosen (i.e. Dreiding).

BIOVIA's Materials Studio (MS) 17.1 [118] was used for calculating the lattice energy and morphology. MOPAC 2015 [119] was used to calculate the atomic charges

for every molecular structure.

4.2.1.1 Crystal Structure Optimisation and Morphology Prediction

Crystal structures were energy minimised using the Forcite module (part of MS), keeping all the atoms bar the hydrogens rigid, and allowing the cell to relax. The SMART algorithm was selected for minimisation. The molecule was kept rigid in order to ensure un-realistic conformations were not reached. By allowing the cell to relax, the structure is allowed to relax to the FF used and as such all structures start from an energetically favourable position and no energy tension is carried over to the surface-surface calculations.

The hydrogens were the only type of atoms to be optimised as the structures were determined using single-crystal X-ray diffraction; thus, the hydrogen positions were predicted as opposed to measured. Changes in the unit cell were monitored to ensure they remained within sensible dimensions.

The lattice energy of the system was checked in comparison to the enthalpy of sublimation to ensure the system was modelled within 5 kcal/mol. While the comparison of the lattice parameters and the lattice energy do not yield perfect replicas of the real system, they do offer a sanity check for the representation of the modelled system against the real world.

Crystal morphologies were calculated using the Morphology module in MS. Calculations were carried out using Dreiding FF. The smallest interplanar spacing was set to 0.8 Å d_{hkl} and only stable surfaces were generated. The surface termination was determined by the most stable surface when shifting the slicing (lowest attachment energy). Calculations were carried out using the attachment energy model (see description in section 2.2).

All structures were treated with the same protocol to ensure consistency. MOPAC was used to calculated atomic charges. Ewald was used for the electrostatics summation method with a width of 0.5 Å and a limiting radius of 18.5 Å.

4.2.2 Results Paracetamol, L-Glutamic Acid & D-Mannitol Structures

Table 4.1 shows the data before and after geometry optimisation for Paracetamol(Para), β-D-Mannitol (DMAN), and α-L-Glutamic Acid (LGA). As unit cells were optimised, it is important to understand what is changing and how these changes are reflected in the cell parameter values. While the heavy atoms in the molecules were kept rigid, implying there were no conformational changes (except for the H atoms), the molecules did move in order to minimise the energy. To accommodate this movement, the unit cell must expand or contract to contain the

molecules to their lowest energy. Para form I polymorph is a monoclinic system (see Figure 2.1). DMAN and LGA are orthorhombic, which plays a crucial role in how the system can relax. With orthorhombic systems, there should be no changes in the angles after optimisation as they should still be equal to 90°.

Table 4.1: Cell parameters of Para, LGA and DMAN before and after geometry optimisation.

Lattice Parameter	Paracetamol	D-Mannitol	L-Glutamic Acid
a Å	7.077	8.694	10.282
b Å	9.173	16.902	8.779
c Å	11.574	5.549	7.068
α^o	90	90	90
β^o	97.9	90	90
γ^o	90	90	90
Optimised [% Diff]			
a Å	7.437 [5.1]	8.858 [1.8]	10.643 [3.4]
b Å	9.365 [2.1]	16.213 [4.3]	8.849 [0.8]
c Å	11.394 [1.6]	5.804 [4.4]	7.406 [4.6]
α^o	90 [0]	90 [0]	90 [0]
β^o	97.95 [0.5]	90 [0]	90 [0]
γ^o	90 [0]	90 [0]	90 [0]

Para exhibited the greatest percentage change in the *a* parameter, changing from 7.077 Å to 7.437 Å equating to a 5.1 % change. Parameters *b* and *c* changed very little, 2.1 % and 1.6 % respectively, which indicates the lattice has undergone a relatively small change. The changes of lattice length of Para are reflected in the change of β angle.

Unlike Para, DMAN did not exceed 4.4 % change along any axis. However, the lattice did have a more significant overall change with 1.8 %, 4.3 %, and 4.4 % along the lattice lengths (a,b and c). Indicating that the molecules were not in an energetically optimal position, when using Dreiding FF. The changes for LGA tell a similar story where two of the lengths *a* and *b* have a relative change of 3.4 % and 4.6 % respectively. It is also worth noting that the cell angles have no change(for DMAN and LGA).

Most importantly, these differences could be improved if one were to use a fitted forcefield for each compound. However, as described previously, this is not reasonable for this project.

Further comparisons (as seen in Table 4.2) of the lattice energy with the enthalpy of sublimation (ΔH_{Sub}) indicates a satisfactory agreement between computational and experimental data in order to conserve the crystallographic data. At the time

of writing there was limited polymorph specific ΔH_{Sub} data; only Para was found to have published polymorphic specific enthalpy data. The ΔH_{Sub} of LGA and DMAN were not polymorph specific; therefore, the data has been considered as an approximation.

All systems are in good agreement with experimental values. Para being the closest with a lattice energy of -26.08 kcal/mol compared to the 28.18 kcal/mol ΔH_{Sub}. DMAN exhibited a higher deviation of 8 kcal/mol. LGA shows the highest deviation between the E_{Latt} and ΔH_{Sub} where the values are -57.16 kcal/mol and 45.48 kcal/mol respectively. However, once corrected for the difference between intra-molecular energy associated with the neutral and zwitterionic states [120], the difference is lower as ΔH_{Sub} becomes 63.68 kcal/mol.

Table 4.2: Lattice energies for Para, LGA and DMAN compared to literature values. ‡ Polymorph specific data could not be found as such it is assumed ΔH_{Sub} (kcal/mol) is for the stable form. ∗ Corrected value for zwitterion of LGA [120]

System	E_{Latt}	ΔH_{Sub}^{298}	Reference
Paracetamol (Form I)	-26.08	28.18	[121]
β-D-Mannitol	-40.52	48.23‡	[122]
α-L-Glutamic Acid	-57.16	45.48 (63.68)‡*	[120, 123]

The molecular structure, unit cell and crystal packing parameters, for Para (a-c), DMAN (d-f) and LGA (g-h), are all shown in Figure 4.4. It is possible to illustrate the likely interaction sites for a molecule using the "Full Interaction Maps" in Mercury, which shows all possible interactions based on the CSD-database [124].

In Figure 4.4a, the blue colour indicates regions where H-Donors are likely to be present. Red and orange are indicative of H-acceptor and aromatic groups, respectively. From this, it can be seen that the OH (hydroxyl) and NH (amide) groups act as both proton donor and acceptors. These functional groups allow for hydrogen bonding (HB) to occur between molecules within the unit cell, as seen in 4.4b, where Z = 4 and Z' = 1. The network of HB occurs across planes parallel to the *a* axis, and due to the interpenetration of the layers a zig-zag pattern forms (Figure 4.4c) which would indicate the crystal is difficult to compress.

Both excipients, DMAN and LGA, share the same number of asymmetric units with Z = 4 and Z' = 1 as well as the same space group of $P2_12_12_1$. However, due to the nature of DMAN as a sugar alcohol, it only contains OH functional groups which act as both HB-acceptor/donor as seen in Figure 4.4d. Figures 4.4e and 4.4f further illustrate the degree of HB within DMAN firstly within the unit cell and then how this exhibited within the packing of the crystal (the view is along the *c* axis).

While LGA has fewer hydroxyl groups(Figure 4.4g), it does have a protonation
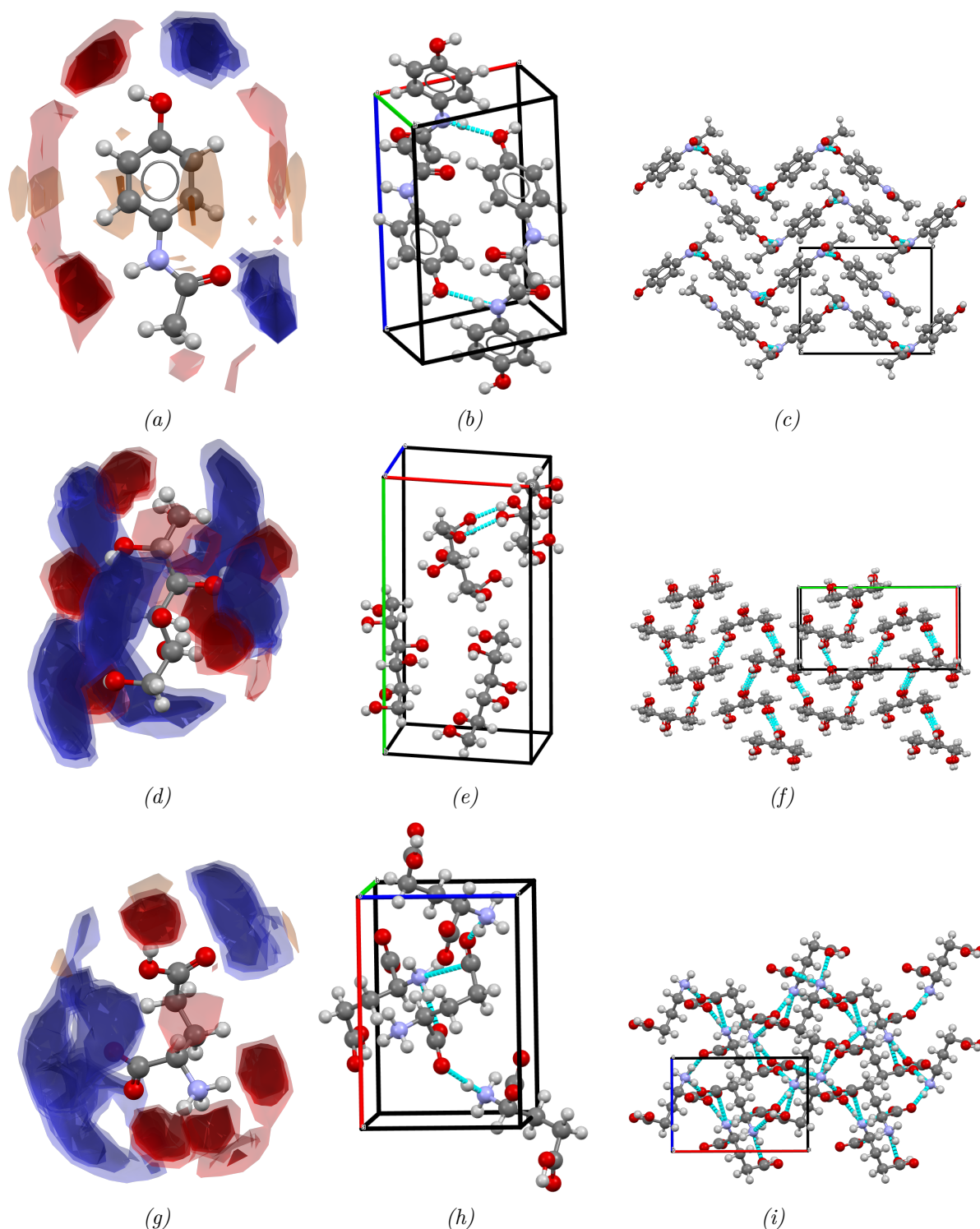
Figure 4.4: Illustrations of the molecular structure, unit cell and crystal packing of Para (a-c), DMAN(d-f) and LGA (g-i). A, D, G) Molecular structure illustrating the sites where possible H-bonding (HB) would occur due to H-donor/acceptor atoms, blue and red, respectively. B, E, H) Unit cells showing how the molecules from the different asymmetric units arrange, blue lines represent HB. C, F, I) A multiple of 2x2x2 unit cells showing the crystal packing of the structures across a particular axis, blue lines represent HB.

site due to its acidic nature which occurs at the primary ammonium group giving a charged NH_3^+ which donates the proton to the COO^- group to adjacent molecules (intermolecular bonding). Similarly to DMAN, LGA exhibits a high degree of HB networks across the crystal planes which can be seen in Figures 4.4h and 4.4i, where the planes are interlocked with HB.

The orientation of molecules within the unit cell is crucial to the final arrangement within the crystal and thus morphology. Slight variations in conformation can propagate and affect the way the crystal grows and what surface chemistry is exhibited on each facet.

4.2.3 Morphology Prediction

The morphologies of all systems were calculated using the attachment energy model, as described in Section 2.2 and 4.2.1.1. The calculated morphologies do not take into account any solvent effects or growing conditions, which can have an impact on the ratios between facets and in some cases, even their presence altogether. As such, some variation is inherently present when comparing to experimental observations. Typical differences will include facets with small surface areas and the presence of highly active facets.
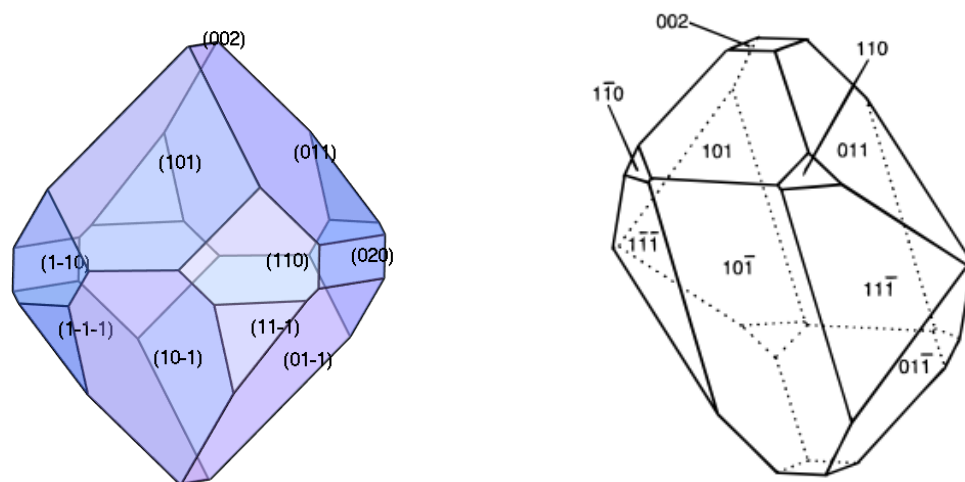
Figure 4.5: Predicted crystal morphology (left) of Para compared to observed morphology (right) [Source [125]]

Para exhibits a prismatic shape (in Figure 4.5) with over seven unique forms predicted. Table 4.3 shows the different forms, their multiplicity (number of equivalent facets that exist), d-spacing (d_{hkl}), attachment energy (E_{att}) as well as slice energy (kcal/mol), anisotropy factor, and finally the representative total facet area (%).

The fastest-growing faces, and thus the ones with the smallest % area, are ones with the greatest E_{att}. For Para, form {002} has the greatest absolute value of E_{att} at -17.90 kcal/mol and thus the smallest area of 0.075 %. However, the form

Table 4.3: Morphology data for Paracetamol

hkl	Multiplicity	d_{hkl} (Å)	Attachment Energy (kcal/mol)	Slice Energy (kcal/mol)	Anisotropy Factor %	Total Facet Area %
{01 1}	4	7.206	-11.49	-15.76	60.43	46.528
{10 1}	2	5.811	-11.95	-15.30	58.67	18.368
{10-1}	2	6.600	-13.31	-13.94	53.45	14.911
{02 0}	2	4.682	-13.45	-13.80	52.91	4.065
{11 0}	4	5.789	-14.23	-13.02	49.92	11.191
{11-1}	4	5.395	-14.57	-12.68	48.62	4.861
{00 2}	2	5.642	-17.90	-9.35	35.85	0.075

{11$\bar{1}$} has an E_{att} of -14.57 kcal/mol but an area of 4.861 % which is higher than {020} with an area of 4.065 % and E_{att} of -13.45 kcal/mol. The multiplicity of these forms causes the disparity between the % area and E_{att}. Hence, there are four facets of {11$\bar{1}$} form compared to the two {020}. Therefore, E_{att} is described for a single facet, whereas the % total area is for all equivalent facets. The predicted morphology is in agreement with literature both experimentally[125] and ab initio [126]determined morphologies. The major difference is the {020} facet which has been predicted but does not appear within the literature.

Table 4.4: Morphology data for DMAN

hkl	Multiplicity	d_{hkl}(Å)	Attachment Energy (kcal/mol)	Slice Energy(kcal/mol)	% Total Facet Area
{ 1 1 0}	4	7.852	-9.56	-30.96	51.382
{ 0 2 0}	2	8.300	-9.07	-31.45	27.392
{ 0 1 1}	4	5.476	-19.46	-21.06	21.187
{ 1 0 1}	4	4.862	-22.92	-17.60	0.040

Facets for DMAN and LGA have been tabulated in Tables 4.4 and 4.5. The most

(a) *Observed DMAN crystal fully indexed.[Source:[127]]*

(b) *Predicted morphology.*
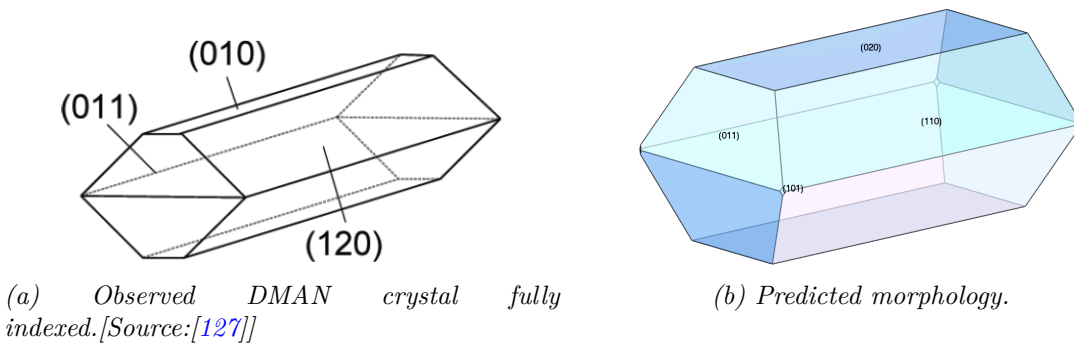
Figure 4.6: Observed DMAN crystal (a) compared to predicted morphology(b).

dominant (calculated) forms for both excipients are the {110}, with a multiplicity of 4 and fractional total facet area of approximately 52 %.

The calculated morphology of DMAN is compared to experimentally observed crystals in Figure 4.6 [127] . Forms {011} and {020} are accurately predicted. Forms {020} (predicted) and {010} (measured) are the same surfaces but with different d_{hkl}, where the latter is half the size of the predicted (d_{hkl} - 8.300 Å). The only difference is of the {110} (predicted) compared to {120} (measured).DELETED

With this in mind, when looking at LGA, there are a few more differences between predicted and observed structures in literature. When comparing observed morphology from light microscopes, it is possible to see the resemblance between measured and predicted as seen in Figure 4.7[108]. However, when compared to indexed crystals, the same facets do not appear (Figure 4.7). This disparity is exaggerated due to the morphology of LGA being very heavily dependant on the growth conditions as seen in literature [128].
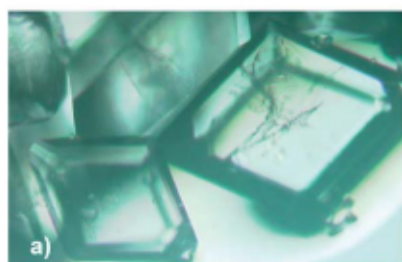
(a) $\alpha - LGA$ grown crystals. Source:[108]   *(b) Observed fully indexed crystal Source:[128]*
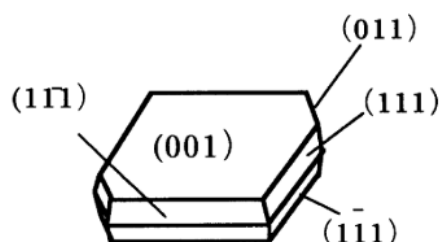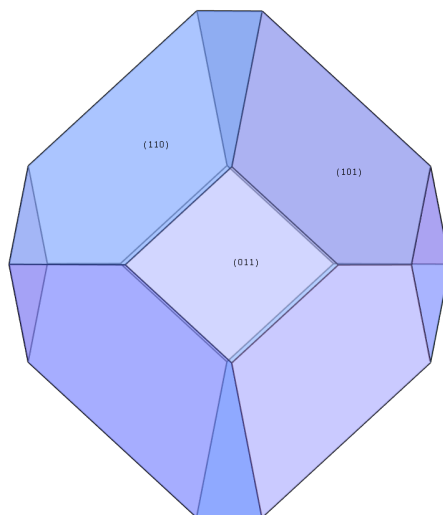
(c) Predicted crystal morphology of LGA

Figure 4.7: Observed crystal morphology of LGA (a-b) compared to predicted morphology (c)

Morphologies of Para, LGA and DMAN have been predicted with varying levels of success. Further improvements could be made by using specific FFs for the

Table 4.5: Morphology data for LGA

hkl	Multiplicity	d_{hkl}(Å)	Attachment Energy (kcal/mol)	Slice Energy(kcal/mol)	% Total Facet Area
{ 1 1 0}	4	6.804	-18.96	-38.20	52.818
{ 1 0 1}	4	6.079	-21.85	-35.31	32.340
{ 0 1 1}	4	5.678	-23.98	-33.19	14.843

systems in question. However, doing as such would make it challenging to justify the energetics calculated when using a generic FF for multicomponent calculations. The surface chemistry of a selection of facets will be discussed in the following section, where individual facet-facet interactions are addressed.

4.3   Surface-Surface Interaction Model (SSIM)

This section covers the computational methodologies used for surface generation and surface-surface interactions model. The surface-surface interaction model (SSIM) is a script which operates as a framework that uses existing software (Materials Studio) to calculate atom interactions for a pair of predicted surfaces. Details of how the model is constructed and run are given. The final part of this section covers the analysis tool developed to assist in data analysis and interpretation. Both code bases have been made available for use through code repositories (gitlab.com/AlexAMC/SSIM & gitlab.com/AlexAMC/SSIMTool). The version of the model used for this body of work can also be found in the Appendix A.

SSIM is designed to calculate the atomic level intermolecular interactions between two surfaces (i.e. not coarse-grained approach), determining the distribution of energies that the two surfaces can exhibit. Every unique XY position - within a given resolution - is explored and its energy minimum in the z-axis calculated. Interaction energies can be split into their constituent components (H-Bond, Van der Waals and Electrostatic), in order to determine the source of the interactions and the relevant functional group as determined by the surface chemistry.

Before disclosing the details of how the model is constructed and energies calculated, it is important to outline a higher abstraction of the model routine for clarity. Surface slabs were constructed using the Materials Studio Morphology module (giving most stable surface slices). All atoms and planes were rotated in the XY plane with the use of the Materials Studio API in order to ensure correct alignment. Slabs were positioned with a separation distance of zero and moved apart, calculating the interaction energy at each step until the minimum was reached. The interaction energy was calculated by a summation of atom-atom interactions between the atoms in the reticular unit cell of the probing surface and the entire substrate layer, thus giving values per area. The probing surface was scanned across the substrate and rotated giving three translational and one rotational (along z-axis) movements.

4.3.1   Construction

The "construction phase" of the code base deals with the construction, alignment, and contains the application of molecular slabs,

Molecular slabs representing surfaces, identified from the morphology predictions were constructed to a set thickness based on the convergence criteria of the system. In the case of paracetamol, a slab thickness of 36 Å was used (see section 4.3.3). The orientation of the plane was set to U along X, V in XY plane for all surfaces to ensure that origins were in the same plane and they aligned during construction, essentially setting all surfaces to the same plane even though their planes are derived

from the given Miller indices.

The probing layer will be described as L_P and substrate layer as L_S from here on in. Figure 4.8 shows the construction and alignment of the slabs. The two-dimensionally periodic slabs were converted into supercells (large slabs with no periodicity). Due to differences in lattice parameters between L_P and L_S, L_P is required to have other molecules around the unit cell in order to detect collisions between the slabs. For example, if a given probing surface has a reticular area half the size of the substrate, it is possible that the probe would interlock with the surface in unfavourable conformation if the planes were infinite. As such, by adding reticular unit cells around the centre, it is possible to detect any steric hindrance from the edge of the surface. However, calculations are carried out per unit area using only one L_P unit-cell of complete molecules to probe the substrate. To achieve this, the unit cell parameters (U_P and V_P) of L_P were multiplied by three, with the central unit cell (L_P_Centre) being the one of interest as highlighted blue in Figure 4.8.

Using the desired area of L_S, as determined by energy convergence testing (see 4.3.3), the cell parameters U_S and V_S were multiplied by the minimum of repeating units to achieve the stated area and also approximate a square. Equation 4.1 shows the integer multiplication factor x_d for each unit cell dimension (U_S and V_S). Calculating an approximately square slab reduces edge effects caused by the size bias where some unit cells had high aspect ratios. Both the reticular area of the unit cell and that of the slab are recorded.

$$x_d = \left\lceil \frac{\sqrt{A_{Set}}}{L_d} \right\rceil \tag{4.1}$$

Constraints were used in order to reduce the number of pairwise calculations. "Fixed" atoms have no contribution to the total energy of the system when calculated with other fixed atoms. Calculations between unfixed - fixed atoms are computed normally, thus only the probing unit cell is required to be unfixed in order to calculate the interaction energy.

Atoms from L_P and L_S were all fixed upon initial construction, except for those present in L_P_Centre. Atoms in the top of L_P were labelled as L_P_Top for use in collisions detection (highlighted green in 4.8).

L_P and L_S were both placed in a non-periodic environment with their origins overlapped. L_P was then flipped horizontally around its centre of geometry in order to ensure the top of both slabs were interacting.

The centroids of the two slabs were calculated, as seen in Figure 4.8. L_P was displaced based on the distances between the centroids resulting in the two slabs being separated and facing one another. The displacement amount $D_{L_P-L_S}$ was

calculated using Equation (4.2), where x_{sep} is the desired separation between the top of the two slabs; T_P and T_S are the thicknesses of a repetitive unit cell.

$$D_{L_P-L_S} = x_{Sep} + \left(\frac{T_P}{2} + \frac{T_S}{2} \right) \tag{4.2}$$

To ensure L_P was directly over the centre of L_S, and thus reducing edge effects, the calculated centroids in the top d-spacing of the slabs were aligned in the XY plane. When increasing the thickness of the slabs, it was found the centre of geometry of the slabs would oscillate with every addition. The oscillation was caused by the non-symmetrical addition of each layer when increasing the slab thickness. To achieve consistent alignment during convergence testing, the top d-spacing of the slab was used.

The XY grid on which L_P moves was constructed by taking the largest vectors of $U_P, U_S, V_P,$ and V_S from the two slabs. The larger grid resolved the size differences of the two-unit cells.

It is important to note that the thickness of the surface is measured from a plane, as such might not represent the caps of the surface which would typically add 1-2 Å onto the thickness of the slab. This omittance of the caps within the measurement of thickness is to be expected as it would be unreasonable to measure the thickness of a
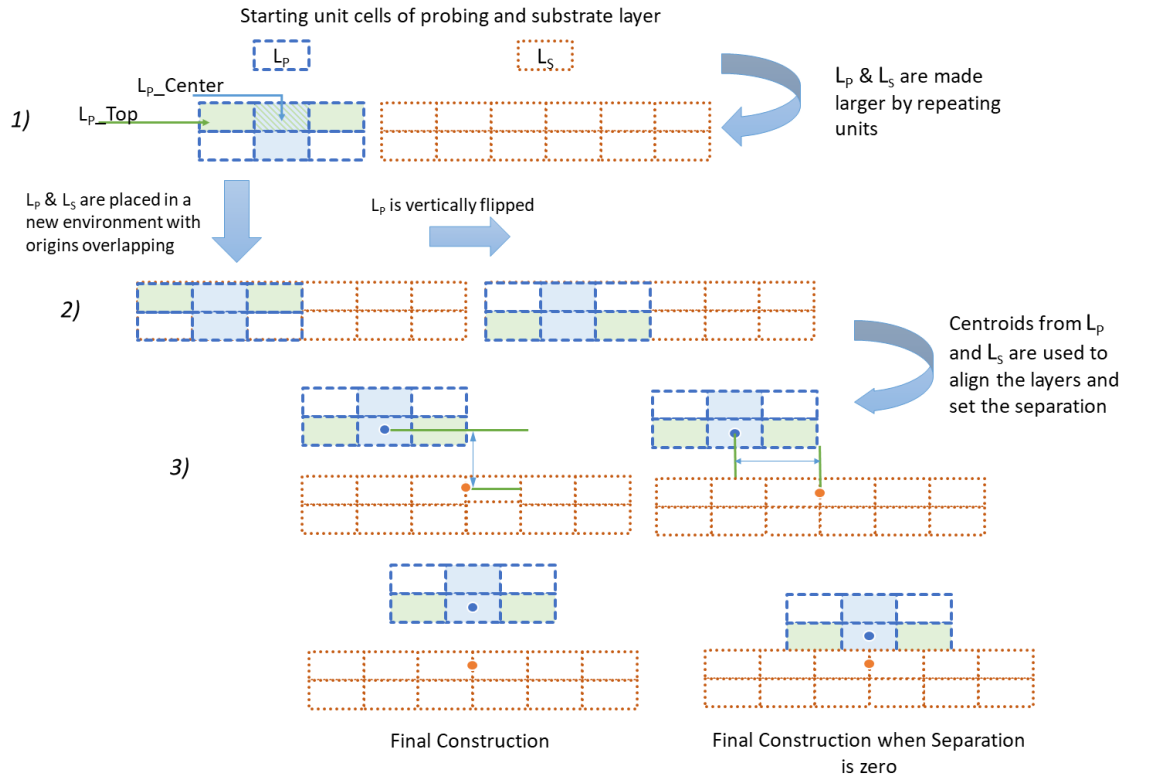
Figure 4.8: Diagram illustrating the three steps required to construct the probing (L_P - blue) and substrate (L_S - orange) layers.

surface from one atom point to another when the surface topology (on an atomistic scale) is rough.

4.3.2   Running

This section will focus on describing how the model ran and calculated the interaction energy for each XYR position.

Once the slabs were constructed, the energy of L_P was calculated in isolation with L_P_Center unfixed and L_P_Top fixed. Note - As previously described, the fixed term refers to the exclusion of atom-atom terms in the energy summation. The isolated environment allows for the internal slab energies to be calculated (E_P and E_S), which was then used to calculate the interaction energy between the two slabs, as shown in Equation 4.3. The system energy (E_{sys}) was calculated at every z-step during the scanning phase.

$$E_{int} = E_{sys} - (E_P + E_S) \tag{4.3}$$

A "separation" approach has been used in order to calculate the E_{int} minimum. The two slabs L_P and L_S start at a separation of 0 Å. Figure 4.9 illustrates the functions used to map out the surface energy landscape between the two slabs.

In the initial state, the atoms in L_P_Centre were fixed while those in L_P_Top unfixed. This allows for any collisions to be detected between the two slabs. The energy minimum search was then performed in the Z-direction, utilising the steepest descent style methodology (described further on).

Once the energy minima were found, the XYZ positions were stored. This was done due to the time requirements of running the Forcite Module in MS. When fixing/unfixing atoms, Forcite takes ~ 2.0 seconds to run. However, if the atoms have not been changed since the previous run, it takes ~ 0.2 seconds to run (time-based on four cores). As such, all energy minima are found while L_P_Centre and L_P_Top are set to collision detection.

Upon finding the minimum in the z-direction for every XY position in the grid with collision detection, the L_P_Centre and L_P_Top fixations are swapped (unfixed/fixed). All previously stored positions were then restored and the energy of the system calculated with the unfixed L_P_Centre. By calculating E_{int} between L_P_Centre and L_S, edge effects were reduced, and the slab thickness was taken into account. After the energies have been calculated, L_P rotates to the next R position; if all R positions have been calculated, the data is saved, and run is terminated.

Step sizes (in the z-direction) are computed dynamically in order to find the energy minimum for E_{int}. This allows for a minimum number of steps to be taken in order to reach the minima. Equation 4.4 describes how the step size (δZ) is
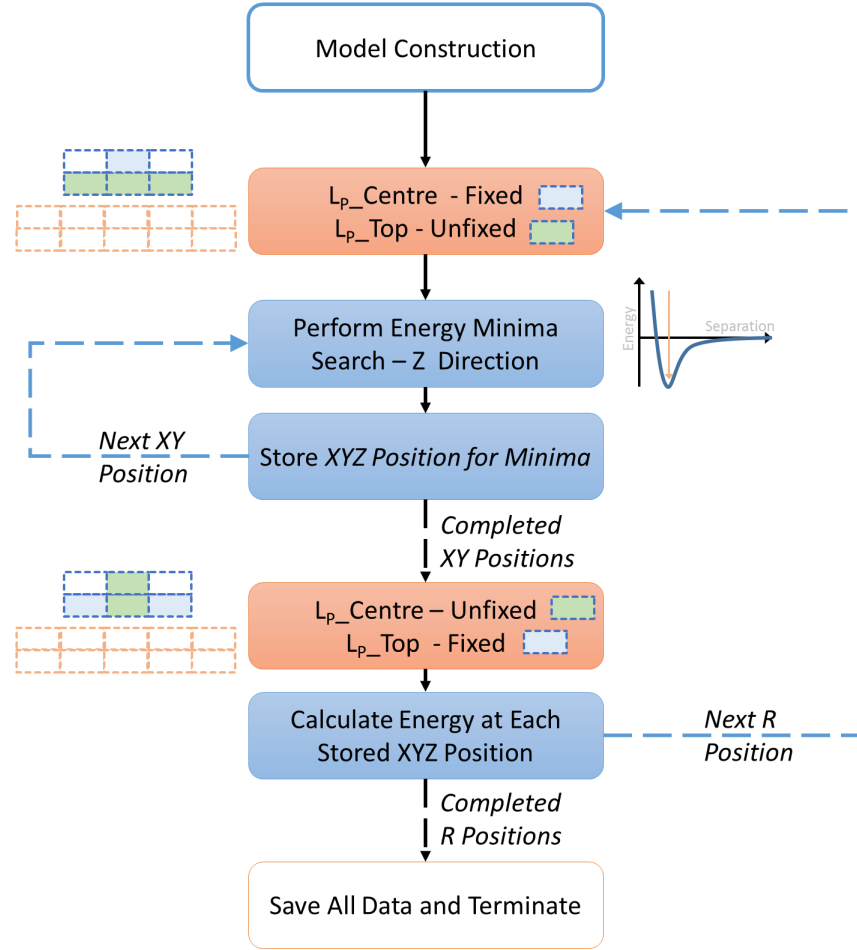
Figure 4.9: Flow chart illustrating how SSIM computes the surface-surface interactions. The time required is reduced by carrying out energy minima searches with L_P_Top atoms. Once all XY positions have been scanned, the energy from L_P_Centre to L_S is calculated from stored positions. This is then repeated for every R position.

calculated by taking the energy difference between steps into account (δE_{int}) and using a size constant (S) to control to smallest possible step size. Run termination occurs when $\delta E_{int} < 0.001\ kcal/mol$ and the $\delta Z < 0.001\ \mathring{A}$.

Note: the first three steps of the separation were taken at 0.5 $\mathring{A}$ in order to account for the surface termination of the layers. Due to atomistic surface roughness, the starting position of the slabs could have the atoms overlapped in such a way that upon separation E_{int} becomes less positive, but then as the atoms from L_P move through the top of L_S, E_{int} becomes positive again. Essentially a local minimum is present as illustrated in Figure 4.10 at point 2.

$$\delta Z_i = S \log \left(\left| \frac{\delta E_{int}}{\delta Z_{i-1}} 10^3 \right| \right) \qquad (4.4)$$

An algorithm has been developed with the help of Thomas Hardcastle (University
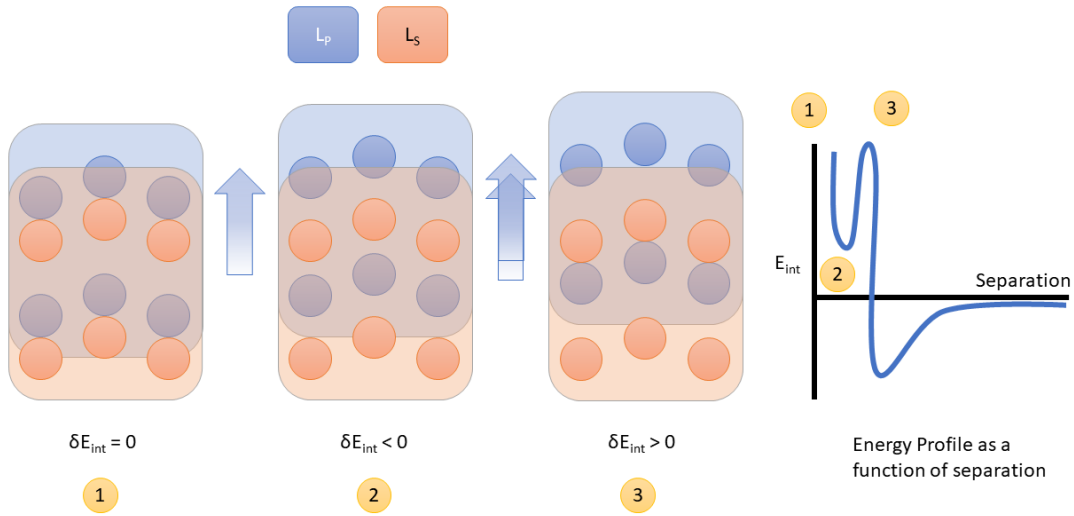
Figure 4.10: Diagram illustrating the overlapping that occurs when separating two layers from overlapped centre of geometries. As L_P (blue box) separates (1) from L_S (orange box) the energy (E_{int}) reduces and a local minima is created once the layer moves again (2).

of Leeds), where two cases can be accounted for in the layer separation. Figure 4.11a shows the possible cases. In the first case where the minimum is overshot whilst the δE_{int} from point $a \Rightarrow b$ is < 0. The following step size taken between $b \Rightarrow c$ will yield a $\delta E_{int} > 0$, the algorithm will go back to position b and will take a step size of 0.001 Å - this is treated as a "scouting" step. If $\delta E_{int} > 0$, the energy position on the right of E_{int} minimum. Whereas, if $\delta E_{int} < 0$ it is to the left and normal step sizes are resumed. In the given example, because the energy minimum has been passed, the layer moves back to position a. From this position, another step is taken with a new step size calculated by halving the size constant (S) and thus making a smaller step size than in step 1. Figure 4.11b shows the flow of conditions required to move to different positions. For the second case, the movement from $g \Rightarrow f$ gives $E_{int} > 0$ and thus a small step is taken $e \Rightarrow g$ of 0.001 Å. As the "scouting" step calculates that $E_{int} < 0$, normal descent resumes.

4.3.3   Convergence

This section describes the energy convergence carried out in order to determine the required size for slabs. The limiting radius, area, and thickness are all varied sequentially in order to converge to a stable size slab. The probe slab only changes in thickness due to the fixed unit cells described earlier.

Due to a lack of periodic boundaries, an oscillation can be seen while increasing
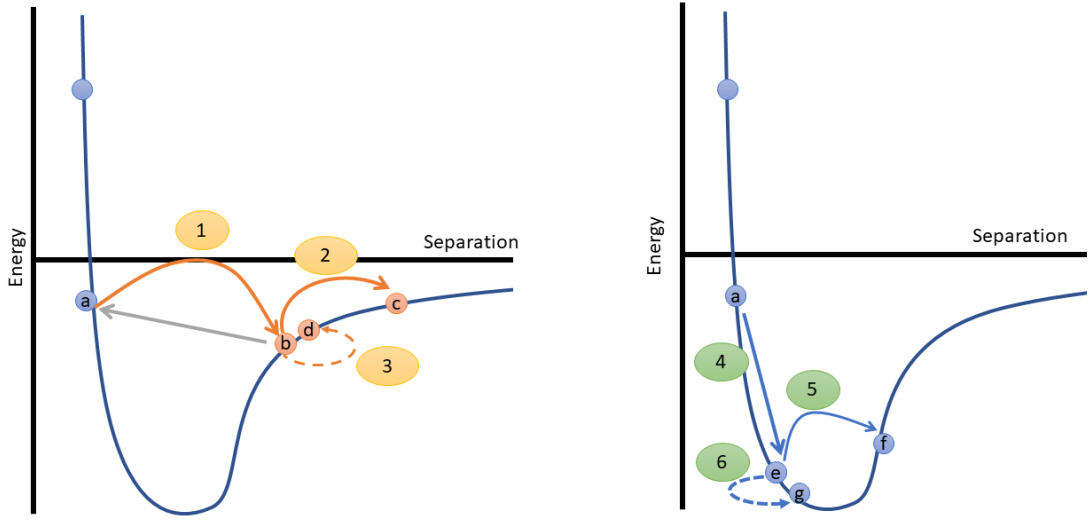
(a) Case 1 and case 2
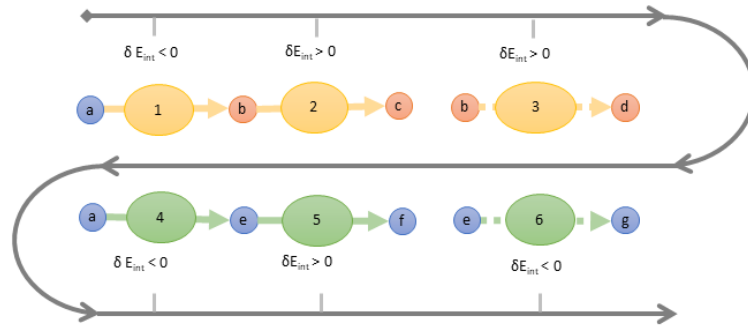
(b) Flow chart

Figure 4.11: Separation steepest descent algorithm. Case 1 shows the situation where the step size is largely overshot. Case 2 illustrates the situation where the step size is overshot next to the minima.

the limiting radius of the pairwise atom interactions. The oscillation is caused by the electrostatic contribution to the total energy. This would typically be remedied by the use of Ewald summation. However, without periodic conditions, this is not possible. For this reason, a large limiting radius has been chosen. Based on Figure 4.12, 80 Å was deemed satisfactory due to the energy plateau of the interaction and electrostatic energy.

In order to ensure the sizes of L_P and L_S were large enough to account for all meaningful energetic contributions, the areas and thicknesses were increased to convergence.

Initially, L_P was kept at a constant thickness of one d_{hkl} while the area of L_S was changed from 985 $Å^2$ to 10,905 $Å^2$ by incrementally increasing the number of
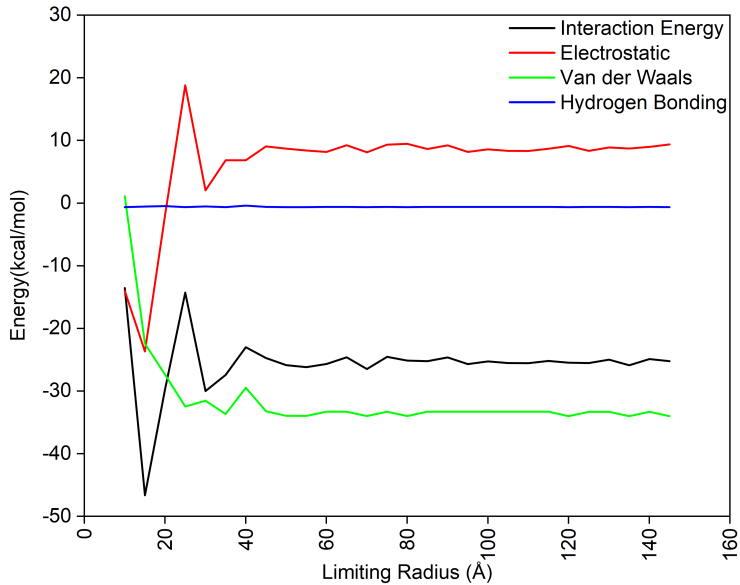
Figure 4.12: Limiting radius of atom pairwise calculations. Showing the convergence point of all energy components.

repeating units using U_S and V_S parameters. Figure 4.13a shows the minimum size of L_S converging at approximately 3,500 Å^2. The dataset was fit with an exponential decay (R^2 0.99986) to describe the decrease of interaction energy as a function of the distance between two atoms.

With the selected area, the thickness of L_S was increased while L_P was kept constant. This tested the minimum depth required for L_S. Figure 4.13b shows oscillation from the fit that can be attributed to the electrostatics. As all calculations were carried out in direct space (no Ewald summation) it is no surprise the electrostatic components fluctuate, this effect is system dependent. The thickness of L_S was set to 35 Å, and L_P thickness was varied, as shown in Figure 4.13c. A thickness of 35 Å was selected for both probe and substrate layers, based on convergence data shown.

The final test for the convergence was carried out by changing L_P with L_S. As all parameters were converged the energy distributions between the swapped surfaces were essentially identical, as seen in Figure 4.13d. A small difference in energy does exist. However, this is caused by the distance between the two layers not being identical. SSIM uses geometric centroids to align the two layers. When the probe is swapped with the substrate, the slabs do not have the exact same size or the same centroid position. A small variation such as 0.01 Å in the *xy* vectors can have a noticeable impact on the final energy calculated. Figure 4.13d shows a 0.6 *kcal/mol* difference between the two probing surfaces of Para(011) and LGA(110), thus accounting for 2.6 % of difference between the two, which can be deemed an

66

(a) L_S area convergence

(b) L_S thickness convergence

(c) L_P thickness convergence

(d) Energy distribution with swapped probing surfaces
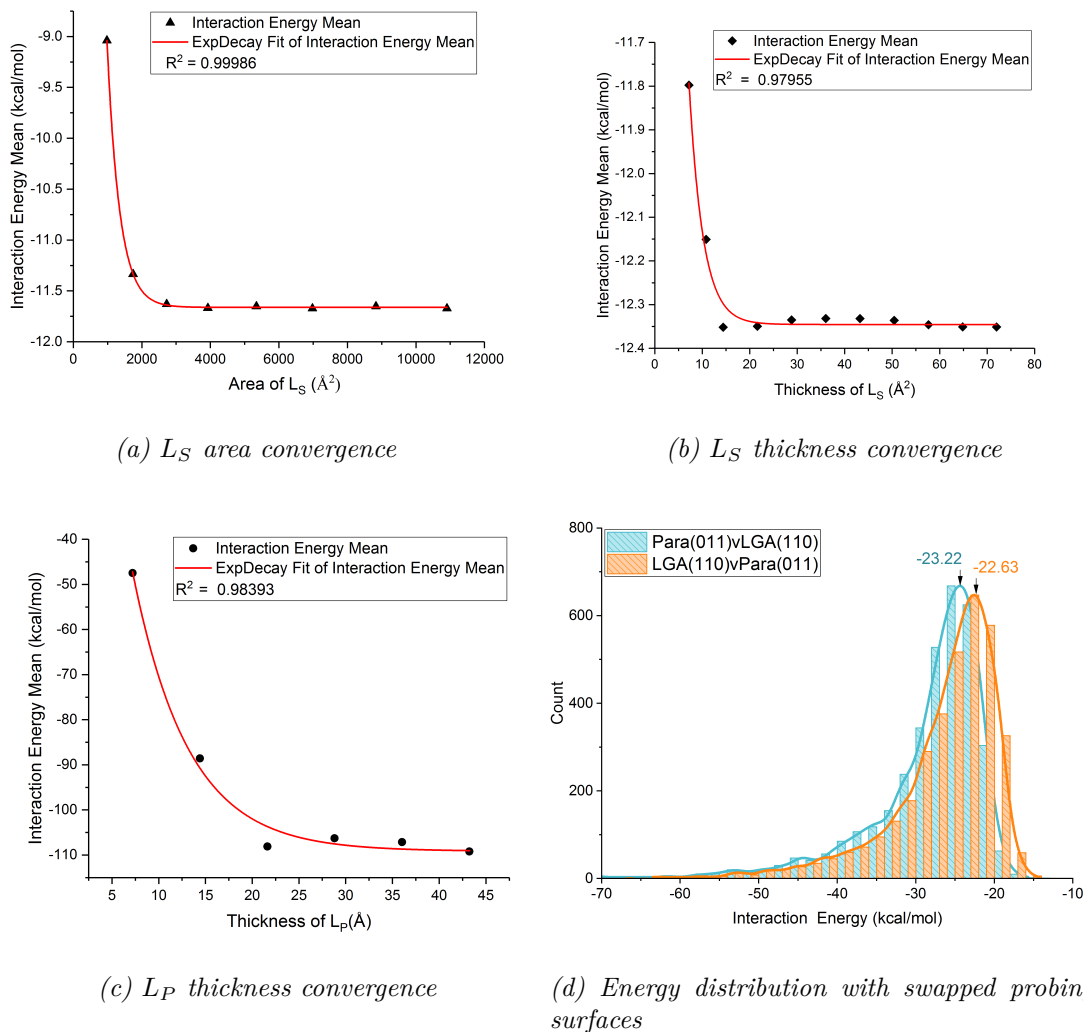
Figure 4.13: Convergence data for SSIM model with Paracetamol system.

acceptable variation considering the number of computational resources saved by not calculating both states of probe vs substrate.

As such, based on the limiting radius, convergence, and swapping test, the model is optimised to calculate the surface-surface interactions for systems comparable to paracetamol, systems that are of similar molecular size include similar functional groups and are single-component organic crystals.

4.3.4   Analysis Tool (ssim_tool)

The Surface-Surface Interaction Model - Tool (*ssim_tool*) has been developed to automate the data analysis of the SSIM output. Energy differences can be compared across a range of parameters. Cohesive/adhesive balance plots can be generated to get a snapshot overview of the average interactions between binary systems. Facet-Facet interactions can be directly compared to determine the most interactive facet. Moreover, surface energy mapping allows for a direct correlation between grid

position and energy contribution. The tool is written in Python 3.6 and is designed to be used with Jupyter Notebooks 3.6[129], utilising libraries such as pandas[130], matplotlib[131], and seaborn[132].

Main output files are inputted to the analysis program, which reads the file names. From the name a facet combination and unit area is determined (i.e. Para(011)_109vs LGA(110)_120.pl.out, 011/110 and 109/120 are recorded). This is then cross-referenced with a supplied morphology file containing all stable miller planes and their associated % surface area coverage.

In order to normalise to the unit cell size, every energy minimum calculated is divided by the smallest unit area of the two facets interacting. Conversion of $kcal/mol$ to mJ/m^2 was carried out using Equation 4.5, where ka and kb are the conversion factors for $\mathring{A}^2$ to m^2 (10^{20}) and $kcal$ to mJ (4.184×10^6) respectively. N_A is given as Avogadro constant.

$$\frac{kcal}{mol\mathring{A}^2} \times \frac{k_a k_b}{N_A} = \frac{mJ}{m^2} \tag{4.5}$$

From the supplied morphology file, the fractional surface areas are multiplied between the two facets giving the probability of the two surfaces colliding based on their sizes. This value is used to multiply against the energy minima at each point, giving a *"expected interaction energy"*. This shows the likelihood of the two surfaces interacting based on their energies a surface area.

To get an overview of the whole dataset cohesive/adhesive balance (CAB) plots are generated. In order to compute these, all datasets are taken into account for a specific probing surface. CAB allows us to describe whether the inter-particulate forces are dominated by adhesion or cohesion. However, in some instances, specific facets may exhibit different affinity when compared to the entire system, which highlights the heterogeneity of surface chemistry across crystal facets.

The CAB plot is constructed to determine if cohesive or adhesive forces dominate the particular probing facet. The linear relationship where $E_{Coh} = E_{Adh}$ describes the forces being balanced and is shown as the black identity line in Figure 4.14. To calculate the E_{Coh} and E_{Adh} for each probe the independent facet-facet interaction averages (median or mean) are computed, and the average of this aggregated is then used to give the (x, y) coordinates on the CAB plot. For example, to calculate the cohesive component, a probing surface is selected (Para(011)), averages from all energies against other paracetamol surfaces Para(011, 101, 10$\bar{1}$, 11$\bar{1}$) are calculated An average value of these averages is then calculated which forms the y component of the dataset. This process is then repeated for every surface. In order to get the adhesive energy, the same protocol is implemented, keeping the probing surface as paracetamol for every facet, finding the average interaction en-
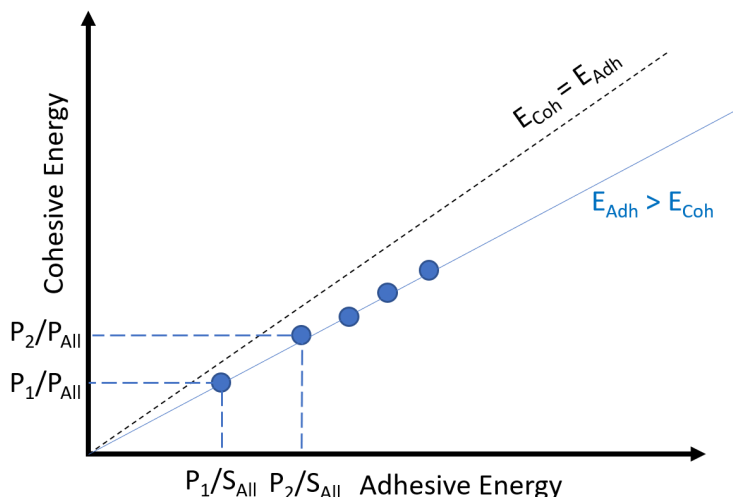
Figure 4.14: Schematic of a Cohesive/Adhesive Balance (CAB) plot. In the case of the cohesive energy (Y-axis), the blue dots represent the average energy of individual probes (P_1, $P_2...P_n$) calculated against all other probes (P_{All}), comparatively the adhesive axis (X-axis) the averages are of the individual probes against all substrate facets (S_all). The overall linear fit of the blue dots indicates the system has a higher affinity to adhesive energy than cohesive.

ergy against all other excipient facets. For example, the adhesive forces between Para-LGA, utilising the same selected Para surface, the average interaction value for Para(011) - LGA(101),LGA(110),LGA(011) are taken, and this is repeated for all Para probes.Equation 4.6 illustrates how every CAB point is calculated where p is the number of probes and s substrates.

By calculating the averages of averages, we eliminate the bias imposed by surfaces with larger unit cells and thus more data points due to their larger grid size. Thus, all facet-facet interactions have an equal contribution to the final E_{Coh} and E_{Adh} components.

$$E_{Coh}, E_{Adh} = \frac{1}{ps} \sum_{i=1,j=1}^{i=p,j=s} \bar{E_{i,j}} \tag{4.6}$$

4.3.5 Summary

This methodology section has described how the crystallographic information was used in conjunction with atomistic modelling to calculate a theoretical morphology for paracetamol, L-Glutamic acid, and D-Mannitol.

An in-depth description has been given of the model developed to calculate the interaction between two surfaces. Showing how the model is constructed, how it runs and the convergence parameters for single-component organic crystals such as paracetamol. A big advantage to this approach is the analysis method and its ease of

use when compared to more traditional MD methods. A bespoke analysis package (ssim_tool) has been described and has been made available under GNU GPLv3 licence (gitlab.com/AlexAMC/SSIMTool).

4.4 Surface-Surface Interaction Model Results

The purpose of the surface-surface interaction model (SSIM) is to predict the behaviour of faceted organic crystals interacting cohesively (like materials) and adhering (different materials). To achieve this, interactions at the atomistic scale are calculated across all possible direct space with four degrees of freedom. SSIM does not account for defects, roughness, surface features or solvent effects. SSIM is used to calculate how the individual surface chemistries between two facets can impact their affinity for one another.

Taking into account every possible geometrical configuration (with the exception of tilt) between two surfaces, the model replicates conditions in mixing, granulation or blending environments, where crystals are coming into contact from every direction with one another. Gathering energy distribution data gives a representation of how the functional groups on the surface affect inter-particular interactions in general, and not just for a specific location and distance between two surfaces where the energy is strongest.

SSIM generates a high dimensional dataset where the extraction and representation of the data are essential in understanding how the systems interact. This section explores how the data can be analysed and represented for Para, DMAN and LGA. Due to the level of precision and flexibility of the dataset, the following set of analyses are deemed "basic interpretations" and are not a reflection of the limitations of SSIM, but represent what time has allowed to be explored during this project.

4.4.1 Overview

Three data types are immediately accessible from SSIM. Firstly, positional data - where x, y, z, r positions are mapped with their appropriate energy minima. Secondly, collated positional data allows energy distributions to be drawn to analyse how each contributes to the overall surface-surface interaction. Finally, using the energy distribution from each facet-pair interaction, it is possible to construct a Cohesive-Adhesive Balance (CAB) plot to quantitatively describe the adhesive/cohesive nature of the overall system (with all facets).

4.4.2 Cohesive-Adhesive Balance

Data from all Para-Para, Para-DMAN, and Para-LGA calculations have been compiled into one CAB plot to show the overall behaviour of the systems. Figure 4.15 shows the balance between E_{Coh} and E_{Adh} for Para in the presence of LGA(blue) and DMAN(orange). Gradients and R^2 are tabulated in Table 4.6 to illustrate the

magnitude of energy and goodness of fit. Moreover, all data points are tabulated with their associated standard error (SE) to illustrate the spread within the probe-specific data set; thus if a single substrate has higher interaction energy, the SE is higher.
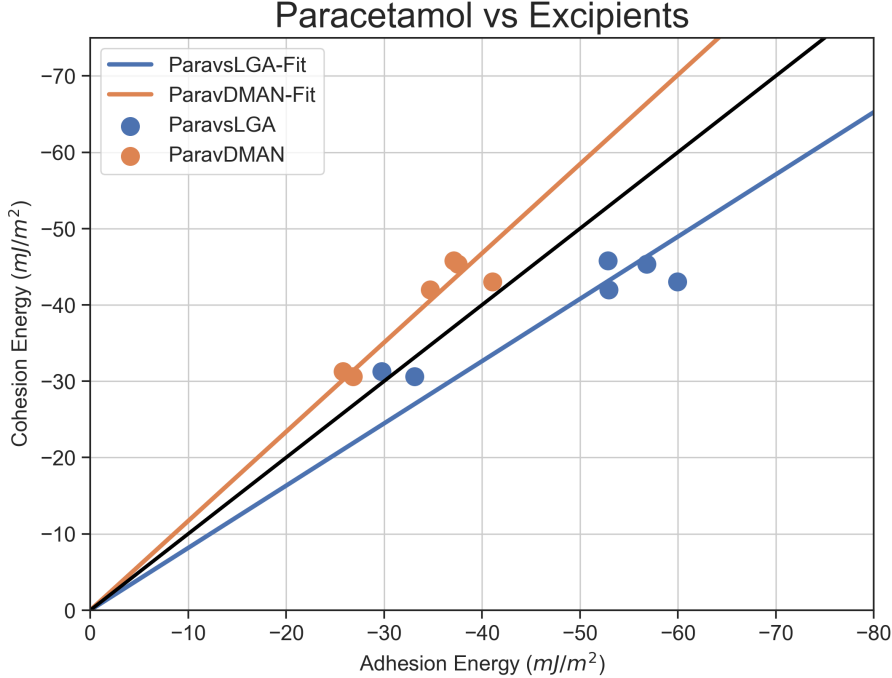
Figure 4.15: Cohesive-Adhesive Balance (CAB) plot of Paracetamol in the presence of excipients L-Glutamic Acid (blue) and D-Mannitol (orange). Blackline illustrates the state of equilibrium between E_{Coh} and E_{Adh}. Lines of best fit are used to illustrate the overall system behaviour towards excipients.

Para exhibits an overall affinity to interact with itself when in the presence of DMAN. However, with a gradient of 1.169 (orange line in Figure 4.15), it exhibits only a marginal preference for cohesive interactions cohesive properties but is still stronger than adhesive interactions. The relatively high R^2 of 0.8476 indicates that most facets behave similarly to the rest of the system, i.e. have a higher E_{Coh} affinity.

In contrast, Para has a higher affinity to LGA than itself. With most of the data points below the equilibrium line (black line in Figure 4.15). The gradient is calculated to be 0.816, which is roughly (0.184 abs) the same difference as Para-DMAN (0.169 abs) on the opposite side of the equilibrium line. With an R^2 of 0.5535 the fit is poorer than for Para-DMAN. It is apparent that the system does not have homogenous interactions towards LGA with one data point (related to the Para(020) facet) being on the opposite side of the equilibrium line and thus showing the facet has higher cohesive energy than adhesive. The values E_{Coh} and E_{Adh} for Para(020) are -31.31 and -29.76 mJ/m^2 respectively. These similarities are associated with the surface topography and chemistry of each facet, properties

Table 4.6: Tabulated fit data showing the gradient and R^2 of Para vs DMAN and LGA

Systems	**Gradient**	R^2	**Para Probe**	E_{Adh} (mJ/m^2)	E_{Adh} SE (mJ/m^2)	E_{Coh} (mJ/m^2)	E_{Coh} SE (mJ/m^2)
ParavLGA	0.816	0.5535	$11\bar{1}$	-59.958	2.900	-43.055	3.684
			101	-56.823	2.586	-45.323	3.840
			110	-52.915	2.458	-41.959	3.397
			$10\bar{1}$	-52.837	3.869	-45.780	3.909
			011	-33.106	1.426	-30.604	1.743
			020	-29.758	1.763	-31.305	2.199
ParavDMAN	1.169	0.8476	$11\bar{1}$	-41.056	29.818	-43.055	3.684
			101	-37.528	27.556	-45.323	3.840
			$10\bar{1}$	-37.089	27.290	-45.780	3.909
			110	-34.681	26.493	-41.959	3.397
			011	-26.848	12.931	-30.604	1.743
			020	-25.801	9.181	-31.305	2.199

which will be discussed in subsequent sections.

Table 4.6 shows that the Para probing facet with most E_{Adh} is $(11\bar{1})$ followed by (101), (110), and $(10\bar{1})$ with the last swapping between DMAN and LGA. The ranking for the energy of adhesion is as follows:

$$LGA : (11\bar{1}) > (101) > (110), (10\bar{1}) >> (011) > (020)$$

$$DMAN : (11\bar{1}) > (101), (10\bar{1}) > (110) >> (011) > (020)$$

Interestingly, facets (020) and (011) both show the least amount of E_{Adh} by a considerable amount compared to the top two competing surfaces ($\sim$-30 mJ/m^2 difference) for both LGA and DMAN. It is to be noted, as shown in Figure 4.5, facets (011) and (020) are the largest and (second) smallest facets, respectively. The smaller facets are more surface-active due to fewer intermolecular bonds being satisfied(low anisotropy factor). Table 4.3 shows the anisotropy factor for each facet, with $(11\bar{1})$ having the lowest at 48.62 % correlating with the strongest E_{Adh} and of the highest E_{Coh}. However, (110) and (020) are the second and third most active surfaces with an anisotropy factor of 49.92 % and 52.91 % respectively but their E_{Adh} , and therefore calculated rank, are comparatively lower in energy. This behaviour suggests that there are other factors at play as opposed to just the unsatisfied intermolecular interactions at the surface of the facet.

Cohesively speaking, Para-Para interactions, are strongest amongst $(10\bar{1})$ probes. The ranking for the energy of Para/Para cohesion is as follows:

$$(10\bar{1}), (101) > (11\bar{1}) > (110) >> (020) > (011)$$

Again, this does not follow the ranking based on the anisotropy factor. Which has been used previously by other studies to identify surfaces that are more likely to be attractive to other particles [55, 133]

A note on the standard error (SE) for E_{Adh} and E_{Coh}. The larger errors are indicative of a larger distribution of energy between facet-facet interactions. The reason why DMAN has a substantially larger SE than LGA will be explored in Section 4.4.4.2 where specific facet-facets interactions are discussed. The distributions of all these surfaces were composed of 105,480 energy minima for Para/DMAN, 87,300 for Para/LGA and finally 102,780 for Para/Para interactions.

4.4.3 Cohesive Interactions

Using the SSIM data, it is possible to generate facet-facet specific interactions energies using ssim_tool. Plotting distributions of all energy minima calculated for specific facets gives an idea of which facets are most interactive and what range of energetics exist within the system.

In order to visualise all the facets, these distributions are plotted vertically in "violin plots". It is essentially a means of efficiently displaying a large quantity of comparative statistical distributions. They are vertically plotted histograms which visually shows the full spread of interaction energies measured, from the average position out to the low probability min and max values. The violin plot for each facet is then placed side by side on the same scale for direct comparison.

Figure 4.16 shows the different energy distributions across all facet pairs of Para-Para. Total interaction energy (blue) is plotted alongside van der Waals (orange) in order to illustrate what proportion of the total energy is composed of VdW interactions. VdW accounts for a large proportion due to the systems in question being neutrally charged and having relatively large slabs.

The intensity of each peak has been normalised as such its position is more important than its relative size. All facets have been sorted in order of the greatest average minimum energy. For Para vs Para, the correlation is still the same as seen in the CAB plots, with $(10\bar{1})$ being the strongest probing facet followed by (101).

Whilst some distributions exhibit Gaussian behaviour, and a majority are asymmetric distributions with a negative skew. This means that using a mean to describe the systems is not applicable; as such, the median is used to describe averages.

Figure 4.17 shows the top five interactions between Para-Para surfaces, only showing the electrostatic (ES) and Van der Waals(VdW) components of the total energy. The ES appears to have a normal distribution whilst VdW exhibits an asymmetric distribution more indicative of the total energy. This again is not a surprise as it makes up a significant proportion of the final energy. However, the ES
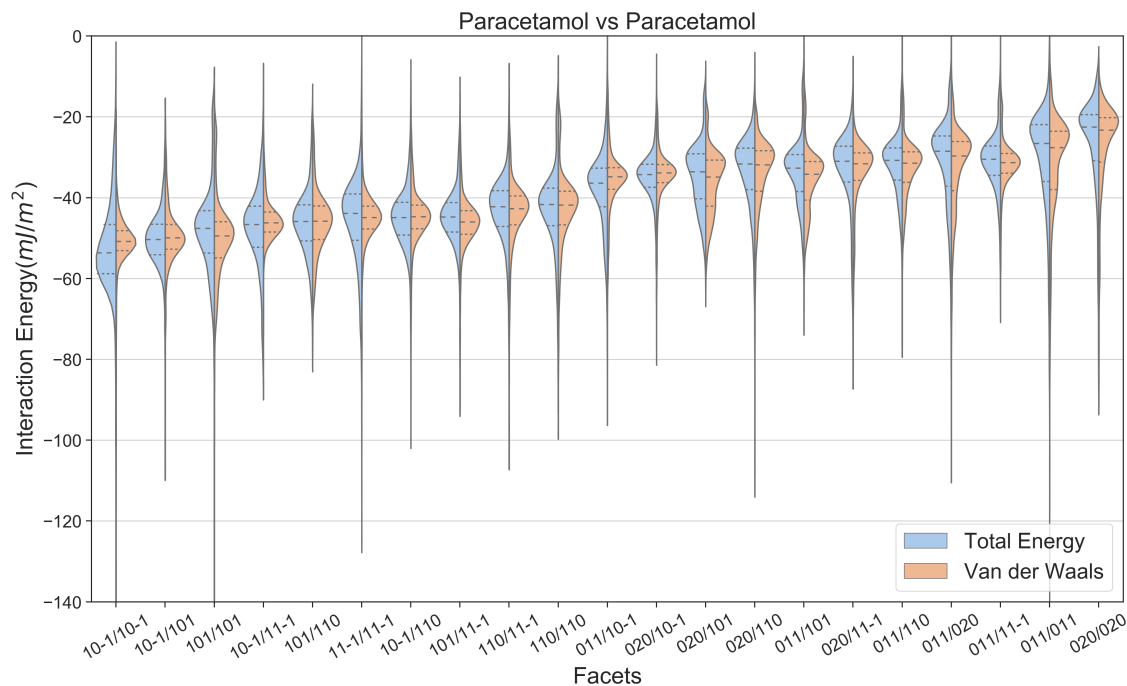
Figure 4.16: Violin plot of all Paracetamol vs Paracetamol facet-facet interactions as distributions. Vertically plotted kernel density estimates plots where the total energy (blue) is plotted along with the Van der Waals energy (orange) component. The order of distributions is sorted based on median values. Dashed lines represent the mean and quartiles of the distributions.

component does show repulsive (positive values) energy. This suggests the bulk long-range VdW overcomes the repulsive ES interactions when it optimises the separation between slabs.

The large "tails" of the distributions are associated with the interlocking aspects of the surfaces. In particular with homogenous surfaces such as $10\bar{1}/10\bar{1}$ where the surface topology is the same, and thus channels can interlock, resulting in few positions where the interaction is much stronger.

Figure 4.18a shows the facet-facet interactions for facets $(10\bar{1})/(10\bar{1})$ between Paracetamol. The heat map represents each grid positions with the colour associated energy minimum for that grid position. The energy at $(4,3)$ is -120.50 mJ/m^2 which is significantly higher compared to -28.89 mJ/m^2 at $(0,6)$. As the layers displace, the surface topology is complimentary and thus will align, and interlock at specific points causing the strong energy. Rotating the probing surface by 45°, as seen in Figure 4.18b, shows a much more uniform surface. Plotting the average interaction energy as a function of probe rotation illustrates the uniqueness of these positions. Figure 4.18c shows how the average interaction energy changes with the strongest being found at a rotation of 0°, due to the alignment of the identical opposing lattice, thus higher contact and closer interlocking between the surfaces.

The single spike in energy associated with the position and rotation indicate
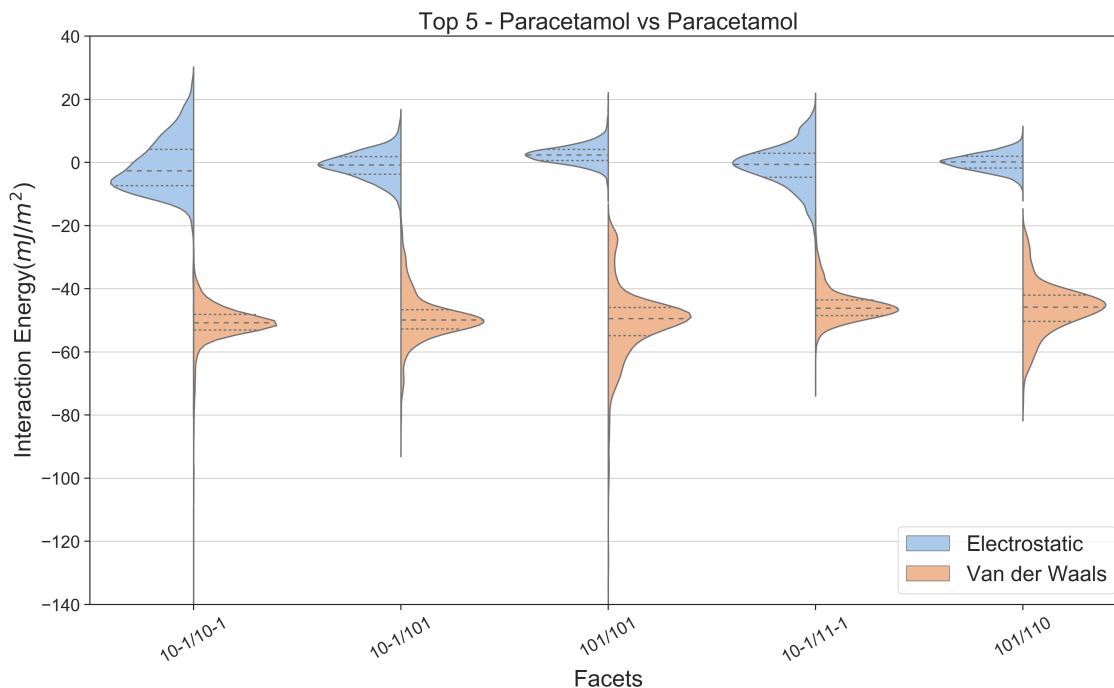
Figure 4.17: Violin plot of top five Para-Para facet-facet interactions as distributions. The component energies of the total interaction energy are displayed as electrostatic (blue) and Van der Waals (orange)

that functional groups and their relative position on the surface have a significant impact on energy minimum. Figure 4.19a the average % contributions by the different energy components (VdW, ES and HB),shows VdW dominates with typically $\geq 85\%$ of the total energy. The contribution of HB can be associated with specific functional groups, although this only makes up a maximum of 2 % in just under half of the surface-surface interactions. It is worth emphasising that not all surfaces are created equally. By that, it is meant that some will have the ability to contribute to HB interaction whilst others will not. Therefore, surface topology and available functional groups play an essential role in the total interaction energy.

The topology can be responsible for a few outliers to the data set. Figure 4.19b illustrates an artefact of the model, which only occurs in homogenous surfaces (like surfaces). The total energy (mJ/m^2) is plotted against the displacement of L_P required to reach the energy minimum for all grids points between two slabs. The density of these energies and displacements are depicted in the top and right positioned histograms. Each point represents one position in the x, y, r grid.

Figure 4.19b shows how at one position , out of approximately 5,000,the energy is $-300mJ/m^2$. Drastically different from the average energy of the facet pair interaction at $-60mJ/m^2$. Using the heat map in Figure 4.18a, it is possible to pinpoint the exact position where the outlier exists. Figure 4.20 shows the structure of the two layers, where the energy minimum is $-300mJ/m^2$. Viewing along the $x-axis$

(a) Rotation = 0°

(b) Rotation = 45°

(c) Average energy as a function of rotation of L_P.
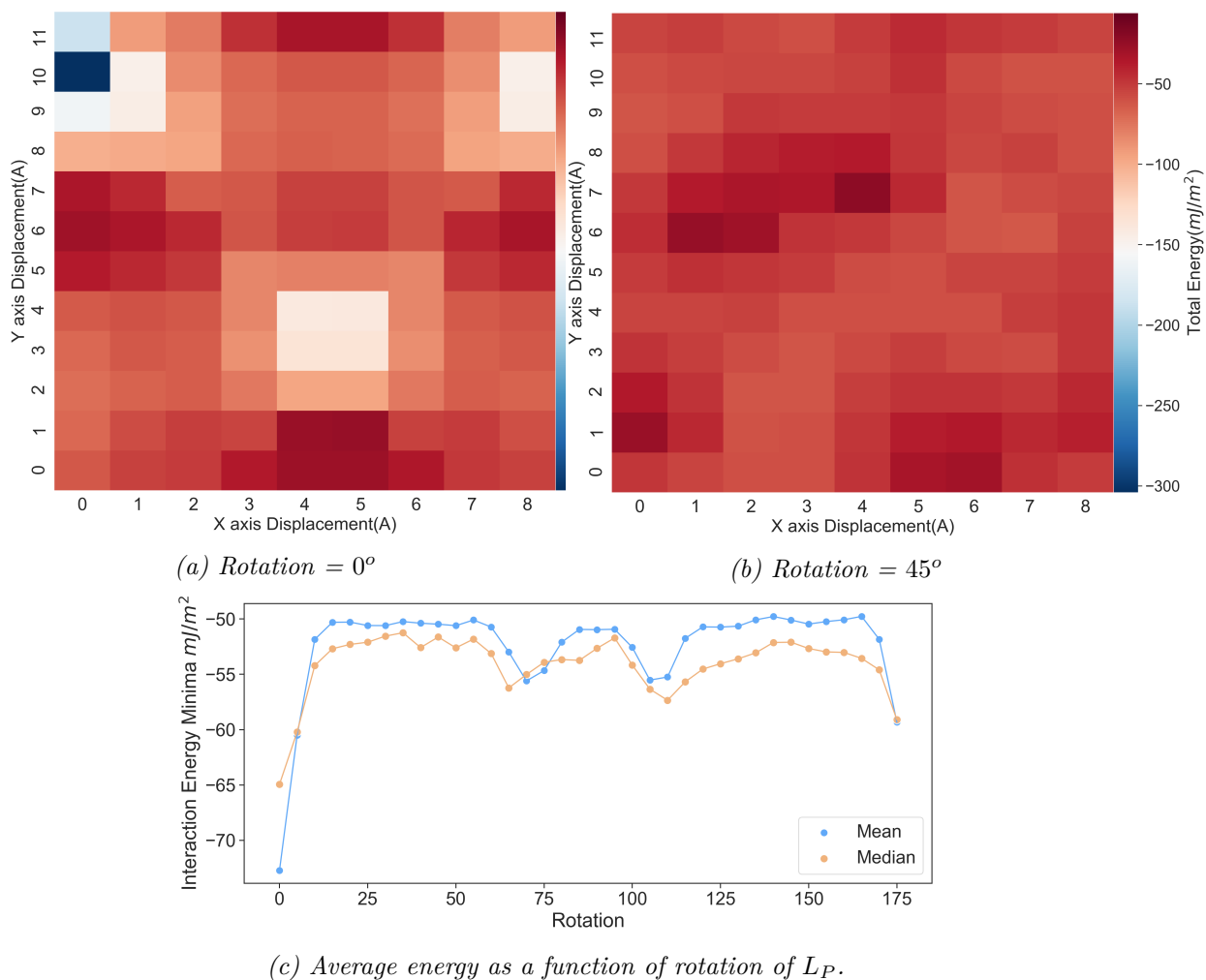
Figure 4.18: Minima energy distribution for x, y spatial points on the scanning at rotation 0 and 45 for Para-Para $(10\bar{1})/(10\bar{1})$

(Figure 4.20a), the continuation of bulk from the substrate is apparent. Blue highlights show the aromatic chain, in the substrate, aligned with the (yellow highlights) probe, which is a continuation of the aromatic chains. A closer look at the interface shows the dimer formed between the carboxylic groups of the layers. Figure 4.20b illustrates how the symmetry of the opposing surfaces creates a mirror plane for the functional groups. Instead of forming S-shaped pattern across the $x-axis$, the interface creates a circle where the carboxyl groups interact.

This interaction is improbable in the real world when mixing faceted crystals. However, previous models for calculating surface-surface interactions have used the strongest energy minimum to determine the likelihood of two surfaces interacting. Using SSIM allows the probing of all possible positions and thus a better description of the likely energies between two facets.

Intuitively, one would expect the total energy to be stronger the closer two surfaces are together. However, the heterogeneous interactions in Figure 4.19c show
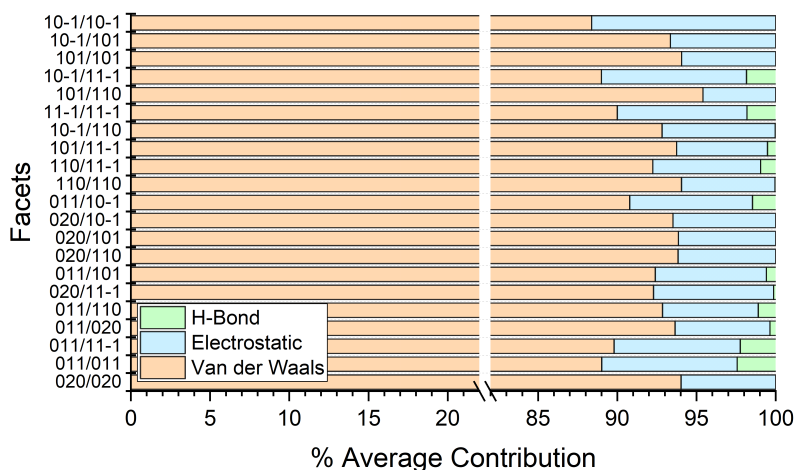
(a) Average contribution % from each component energy towards the total interaction energy for specific facet-facet interactions of Para-Para
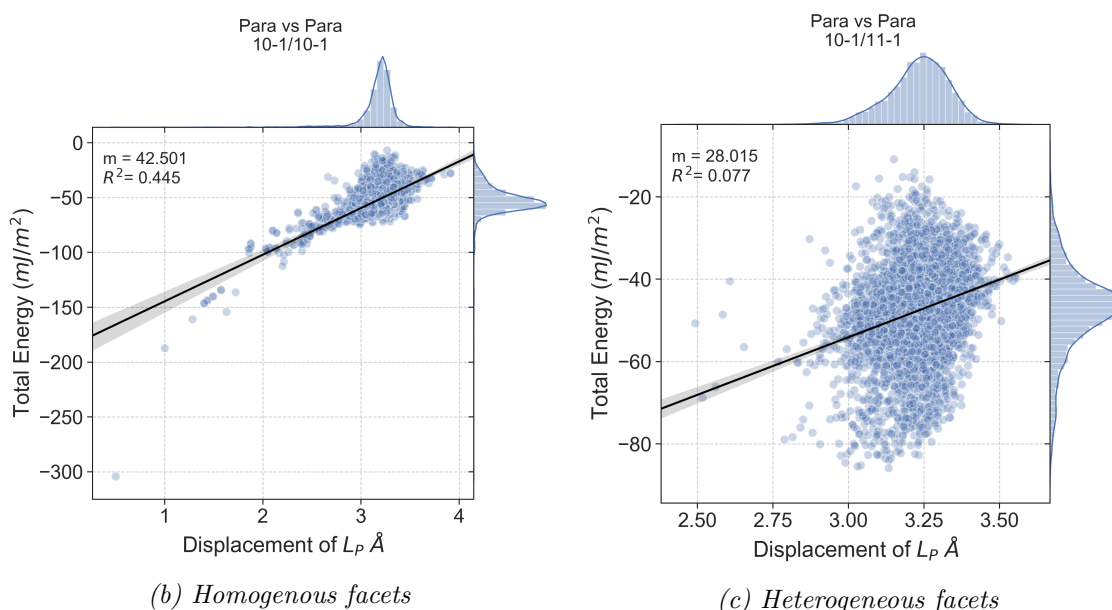
(b) Homogenous facets

(c) Heterogeneous facets

Figure 4.19: a) Shows the contribution from different energy components that make up the total energy of the minimum calculated. b) & c) Illustrate the distribution of energy minimum for homogenous (b) and heterogenous (c) surface pairs. The vertical distribution on the right hand size shows where the density of energy lays, whereas the top horizontal distributions highlights the density of the displacements for L_P. A linear regression (black line) is fitted across the whole dataset to check for any linear correlation between the two.

.

that is not necessarily the case. In some facet pairs, the interactions are dominated by the compatibility of functional groups. Analysing the linear regressions of the plots in 4.19, comparing the R^2 of each plot can indicate the existence of a linear relationship between energy and distance. In the heterogeneous case, the R^2 is 0.077, showing a weak correlation between the two parameters. However, for the homogenous facets, the R^2 is 0.45, which while still not high, it has a stronger correlation. This attribute can also be seen for heterogenous facets (plots can be found in Appendix A.1). It is therefore suggested that in cases where the R^2 is relatively low ≤ 0.3, SSI(surface-surface interactions) are dominated by the functional groups

(a) Along x axis

(b) Along y axis
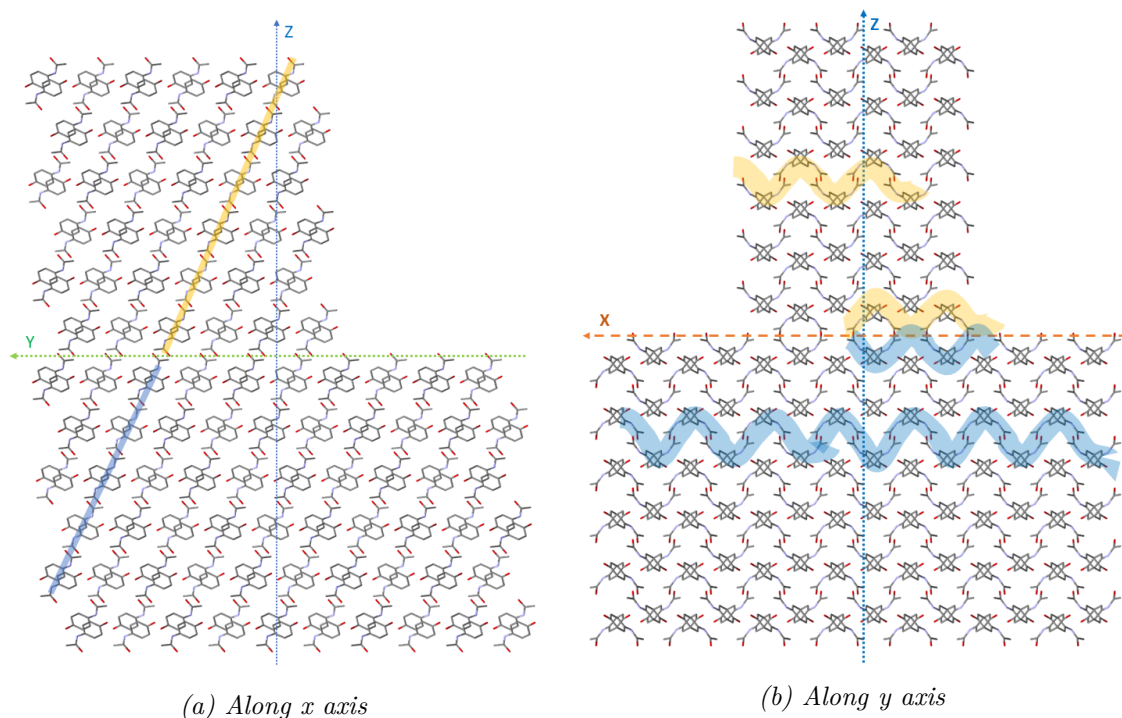
Figure 4.20: Position of Para-Para $(10\bar{1})vs(10\bar{1})$ *at points (0,10,0 of* x, y, r*) as highlighted in 4.18. a) Shows* L_P *interacting with* L_S *along the x-axis. Highlighted in blue are the aromatic ring chains within* L_S *aligned with the same groups in* L_P *(yellow). b) View along the y-axis, showing the mirror symmetry of the two slabs along the x-axis. Both figures illustrate how the single position can exhibit a continuation of the lattice from the bulk.*

present.

4.4.3.1   Impact of Surface Chemistry

Investigating the effects of surface chemistry on such diverse datasets poses many challenges. Due to the nature of the systems, it is not a simple interaction that could be described by "Facet A and facet B have OH groups; therefore the OH groups are contributing the largest amount to the total energy". Such a naive approach is invalidated due to the complex nature of how these interactions occur. The "density" of these functional groups, their orientation and accessibility can impact their contribution towards the total energy. In order to deconvolve these interactions, a multivariate linear regression analysis has been implemented. The linear regression used to describe the data set shall be called the model from here on in.

Five total surface descriptors have been selected to encapsulate the different properties of the surface. The density of H-bond donor (Dons) and acceptor (Accs) atoms, as well as aromatic(Aroms) atoms, have been computed using a script developed by M. Byrant et al. [112]. "Dons" describe atoms where the charge is positive, whereas acceptor describes more electronegative groups. The remaining two descriptors are for surface topology. Where, root-mean-square deviation of the surface

(a) *Linear regression performance*

(b) *Contributing surface properties*
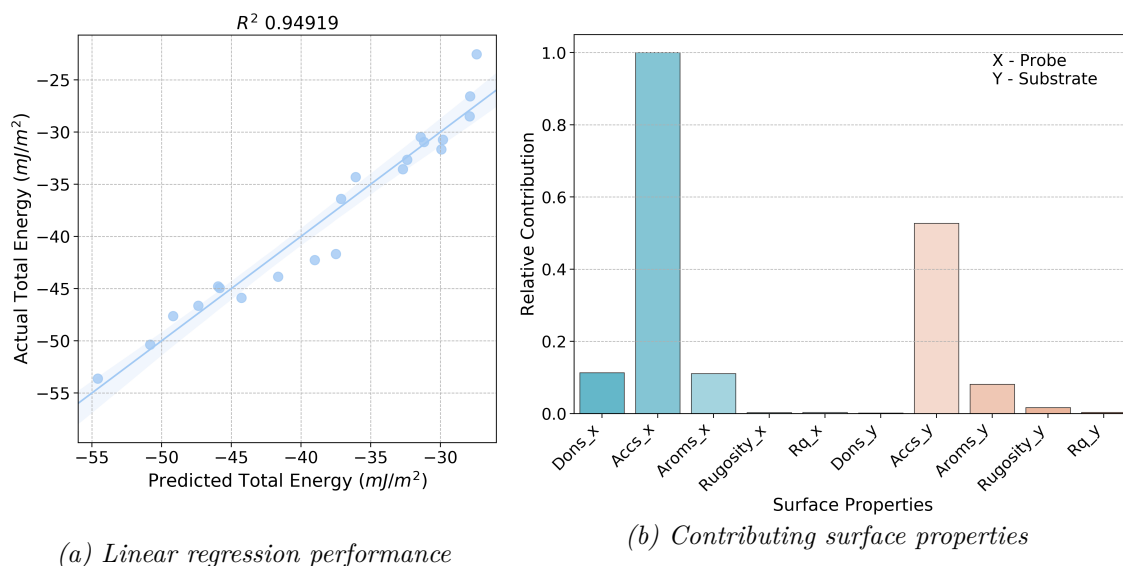
Figure 4.21: Results from multivarite linear regression model for Para-Para. a) Shows the performance of the model where the predicted values are plotted against SSIM computed values. b) Surface descriptors used and their relative contributions to the model.

(R_Q) and rugosity are used to describe the deviation from the normal and roughness of the surface, respectively. Rugosity is defined as the $Area_{True}/Area_{Projected}$, thus takes into account the highest deviations as well as the frequency of those.

The interaction represents the surfaces coming into contact, hence a set of descriptors for each surface was used (suffixed as '_x' and '_y', for probe and substrate respectively). The median interaction energy for each facet combination is used as the target for the model. Surface descriptors were normalised before fitting.

Using the Para-Para data set and the ten descriptors mentioned above, the model can predict 94.9% of total energies ($R^2 = 0.949$) as shown in Figure 4.21a. The coefficient of each descriptor is taken as an indication of the contribution of that factor to the interaction energy.

The largest contribution comes from the presence of HB acceptor (Accs) groups, followed by aromatics (Aroms) and HB donors (Dons) equally. Interestingly the R_Q makes no contribution and rugosity only a small amount. This could be due to the lack of diversity between the facets. Most of the surface roughness is similar for all paracetamol facets. It is expected that the surface properties of the probe and substrate should have equal contributions; however, this is not the case. If Dons exist on the substrate and on the probe, they can have a noticeable contribution. As the Accs_x are binding to Dons_y, the model already accounts for this contribution by taking into account the Acc_x; thus, contributions that would exist from Dons_y are already accounted for.

Table 4.7 shows the surface descriptors for each facet of paracetamol. The ranking calculated in Section 4.4.2 is used to order the rows of the table. The most

cohesive surface, facet $(10\bar{1})$, shows to have the lowest density of Dons groups but the highest Accs and Aroms.

(a) Para(10$\bar{1}$)

(b) Para(101)

(c) Para(11$\bar{1}$)

(d) Para(110)

(e) Para(020)

(f) Para(011)
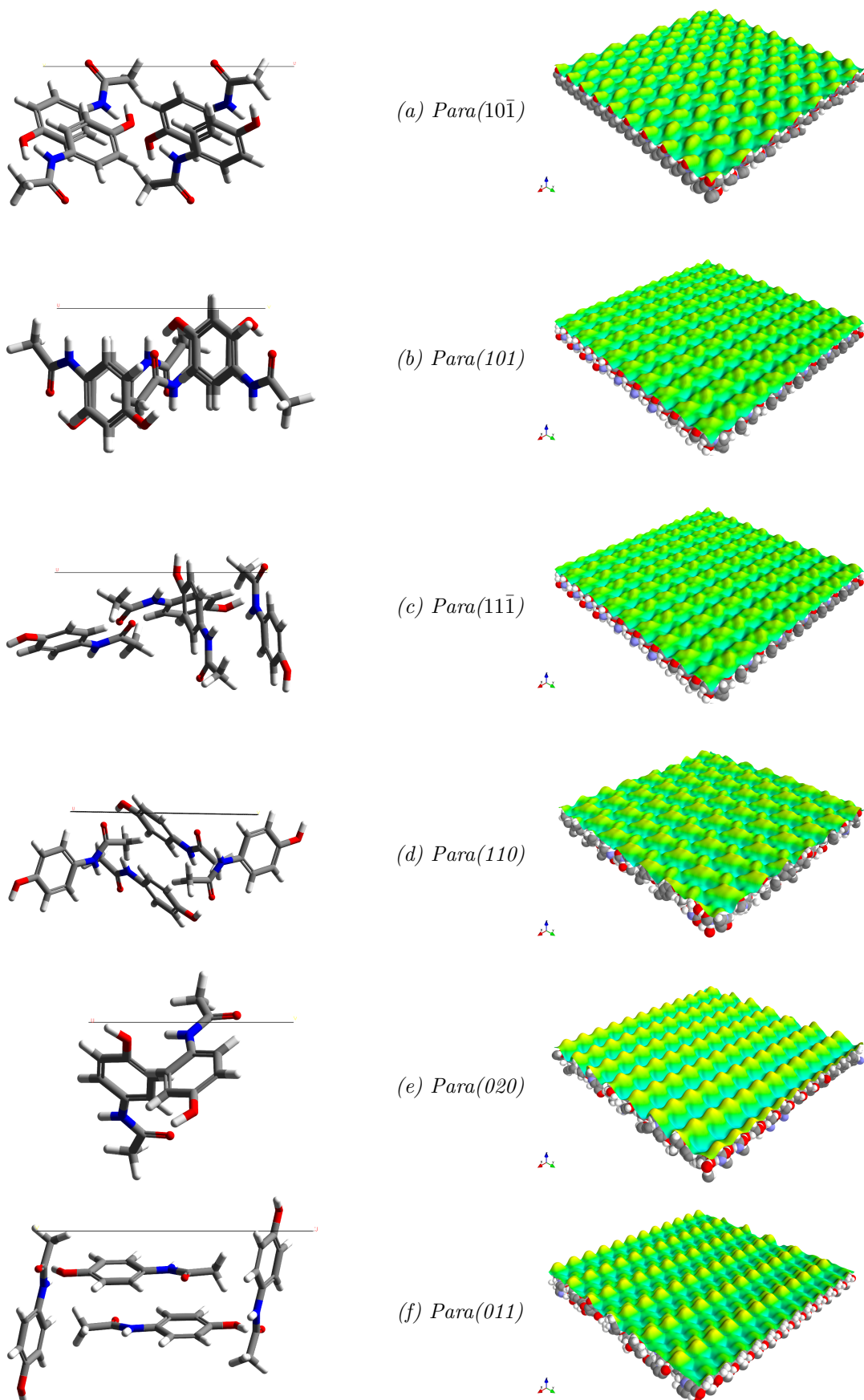
Figure 4.22: Unit surfaces showing the surface chemistry and slabs to illustrate topology. Surfaces were generated using a tool supplied by Cambridge Crystallographic Data Center (CCDC) [112]]

All facets of paracetamol have been visualised to examine the functional groups and topology of the atomistic surfaces (Figure 4.22). Facet $(10\bar{1})$ has two carbonyl groups perpendicular and four aromatic rings off-axis to the surface. Facets $(11\bar{1})$ and (020) both have protruding carbonyl groups, but they do not allow for easy interactions with other groups due to either steric hindrance (020) or other groups sticking out further from the surface $(11\bar{1})$.

The tabulated surface descriptors and generated slabs show that (020) has the highest roughness with an R_Q of 4.97 Å and a rugosity of 1.42. As expected, the roughness decreased the interaction energy of the facet. In the case of (020), the peaks of the surface are methyl groups which are comparatively less interactive than the other functional groups (OH, NH or CO). The orientation of the protruding functional groups has an impact on the ranking of the facets. For example, both OH groups in (101) are orientated with the hydrogens pointing towards the bulk and thus the more electronegative oxygen pointing perpendicular to the surface. On the other hand, (011) and (020) have the hydrogens pointing away from the surface. These orientations are not taken into account in the surface descriptors. Descriptors are classified based on the atom type and not directionality.

Table 4.7: Surface descriptors for the different facets of Paracetamol

System	hkl	Dons	Accs	Aroms	Rugosity	Rq
Paracetamol	10-1	0.0092	0.0185	0.1017	1.29	2.97
	101	0.0158	0.0158	0.0701	1.20	2.43
	$11\bar{1}$	0.0142	0.0176	0.0922	1.23	3.54
	110	0.0116	0.0152	0.0540	1.29	3.44
	020	0.0132	0.0126	0.0192	1.42	4.97
	011	0.0153	0.0195	0.0671	1.31	3.39

4.4.4 Adhesive Interactions

The adhesive interactions are described as those between Paracetamol (Para) and D-Mannitol (DMAN), or L-Glutamic Acid (LGA). Based on the CAB plot in Figure 4.15, it is possible to see that Para has a greater affinity towards LGA than DMAN, as Para-DMAN is dominated predominantly by cohesive interaction. This section aims to understand what causes the adhesive surface-surface interactions (SSI) and how the surface chemistry of each system and facet contributes to these.

4.4.4.1 Overall Interactions
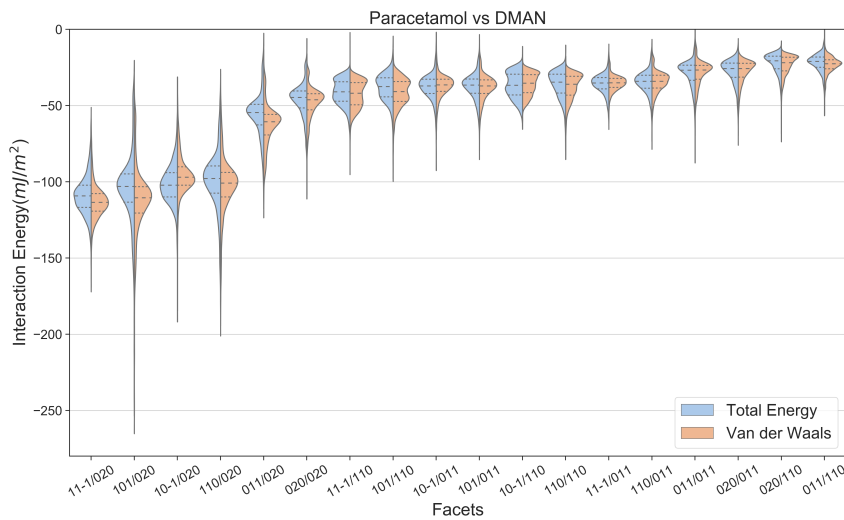
(a)
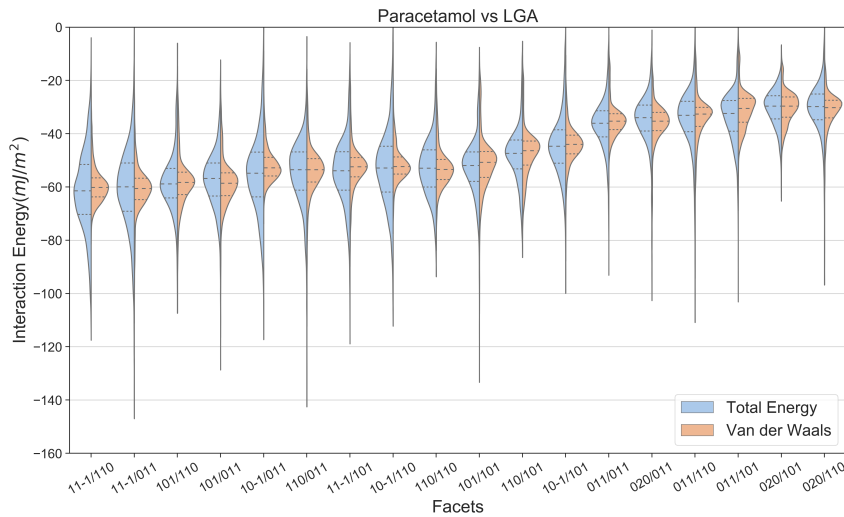
(b)

Figure 4.23: All facet pair interactions of Para with DMAN (a), and LGA (b), showing the total energy (blue) and Van der Waals (orange) contribution.

The higher cohesive nature of Para in the presence of DMAN is indicated initially by Table 4.6 in Section 4.4.2, where the values for E_{Adh} are lower than those for E_{Coh}. However, as previously mentioned, the standard error (SE) of these values,

for each probing facet, represents the range of interaction energy. E_{Adh} SE values for Para-DMAN are much higher than those for Para-LGA, with a range of 9.18 - 29.82 mJ/m^2 and 1.43 - 3.87 mJ/m^2 respectively. The large energy range suggests that either, the surface chemistry of each facet is so diverse that it causes a large range of energy across single facet-facet interactions, or the different DMAN facets are very distinct, resulting in a wide range of energies being calculated for a single Para probe - alternatively, a combination of the two.

Figure 4.23a suggests both scenarios could be valid, with the latter having a more significant impact. Para(11$\bar{1}$) has (on average) the strongest interaction energy with DMAN, but in this case, the strongest singular SSI between Para(11$\bar{1}$)-DMAN(020). However, this is based on the median energy of these facet pairs. The strongest singular point of interaction exists between Para(101) and DMAN(020). All Para probes exhibit the strongest interaction with DMAN(020). The energy difference between the top four strongest SSI and the rest is large (60 mJ/m^2), which skews the average when considering all probe-substrate pair interactions.

However, facet pairs such as Para(11$\bar{1}$)-DMAN(110), Para(101)-DMAN(110),and Para(10$\bar{1}$)-DMAN(110) show a wider bimodal distribution of energy. Implying that the surface properties of individual facets cause a difference. These facet subsets will be further investigated in the next section. Observing all facet pair interactions, it is possible to see how certain facets cause a higher adhesive balance than cohesive. As previously highlighted, the (020) facet of DMAN has higher energies even when compared to the Para cohesive energies. However, all energies must be taken into account when investigating all facets; thus, Para-DMAN is predominantly cohesive. Nonetheless, Para has a high affinity for facet DMAN(020).

Analysing the LGA data does not show as large of a difference as previously seen. The most considerable variation in average energies between facets is (30 mJ/m^2). The order of most interactive surfaces of LGA is (110), (011), and finally (101). The distribution of VdW energy appears to be more aligned with the total energy distribution, indicating that the vast majority of the energy is from VdW, as seen for Para-Para.

As with DMAN, it is interesting to see that energy outliers still exist in these distributions (indicated by the long tail in Para(11$\bar{1}$)vLGA(011)). Further analysis was conducted to identify what is causing these outliers and how the surface chemistry could be impacting them.

The top five interacting surfaces from the DMAN and LGA systems are shown side by side in Figure 4.24. The total energy has been split into its components showing the ES (blue) and VdW (orange) contributions. The top four facets interacting with DMAN have a stronger VdW contribution than the ones in LGA. However, the ES for DMAN appears to be predominantly positive in four of the five
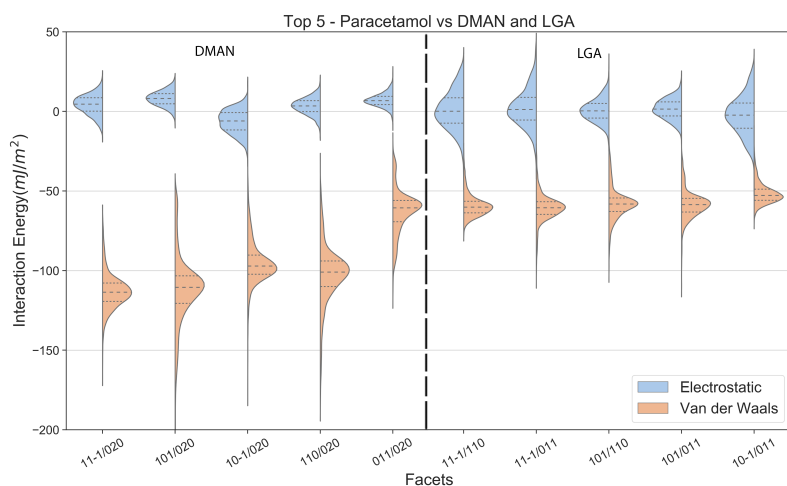
Figure 4.24: Top five strongest interacting surfaces (based on median of distributions) for Para vs DMAN and LGA. Showing the contributing of electrostatic (blue) and Van der Waals (orange) energies.

cases. In contrast with the LGA facets, where the ES distributions are Gaussian, and the average is around 0 mJ/m^2.

Although some asymmetric distributions are present for facets such as the Para($11\bar{1}$)-LGA(110), these differences suggest that the surface chemistry or topology in DMAN has a significant impact on the energies calculated. Less ES contributions were observed despite the presence of partially charged states for the COO^- group and NH_3^+ as previously described in Section 4.2.2.

4.4.4.2 Facet Specific Chemistry

Identifying the effects of the facet chemistry and structure on the interaction energy is important in understanding where the energy can be enhanced or repressed by changing facet features.

D-Manntiol

(a) DMAN(110)

(b) DMAN(020)

(c) DMAN(011)
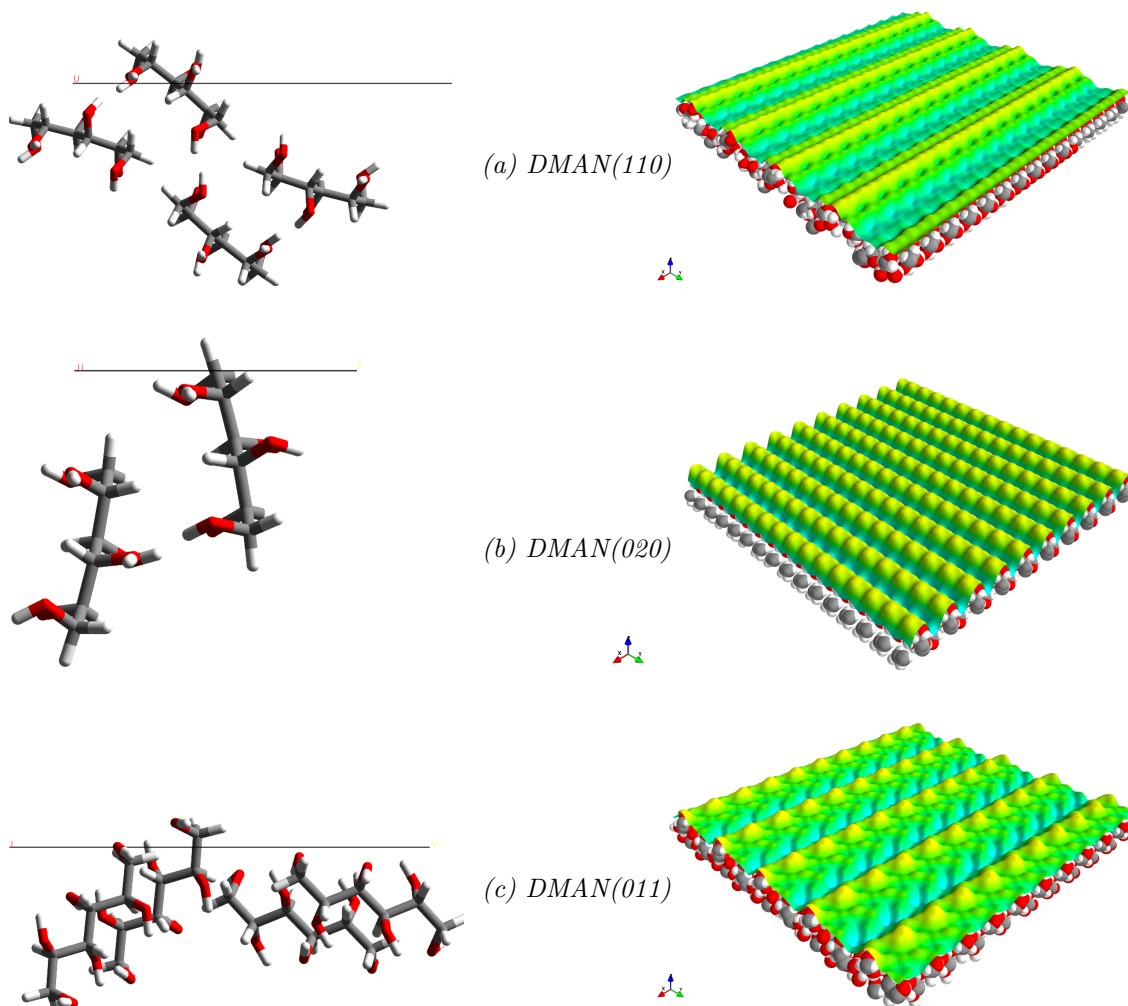
Figure 4.25: Unit surface and slabs of DMAN facets.

The surface chemistry and topology of DMAN are shown in Figure 4.25. As DMAN contains only OH functional groups, the orientation of these dictate if the facet is HB-donor or HB-acceptor. The most significant differences are in facets (110) and (020). DMAN(110) contains OH groups perpendicular to the surface, but the molecule protruding the surface is at a 45° to normal of the surface (Figure 4.25a, thus the depth of the surface and in turn, the roughness is not large (when compared to other facets). While there are hydroxyl groups on the surface, due
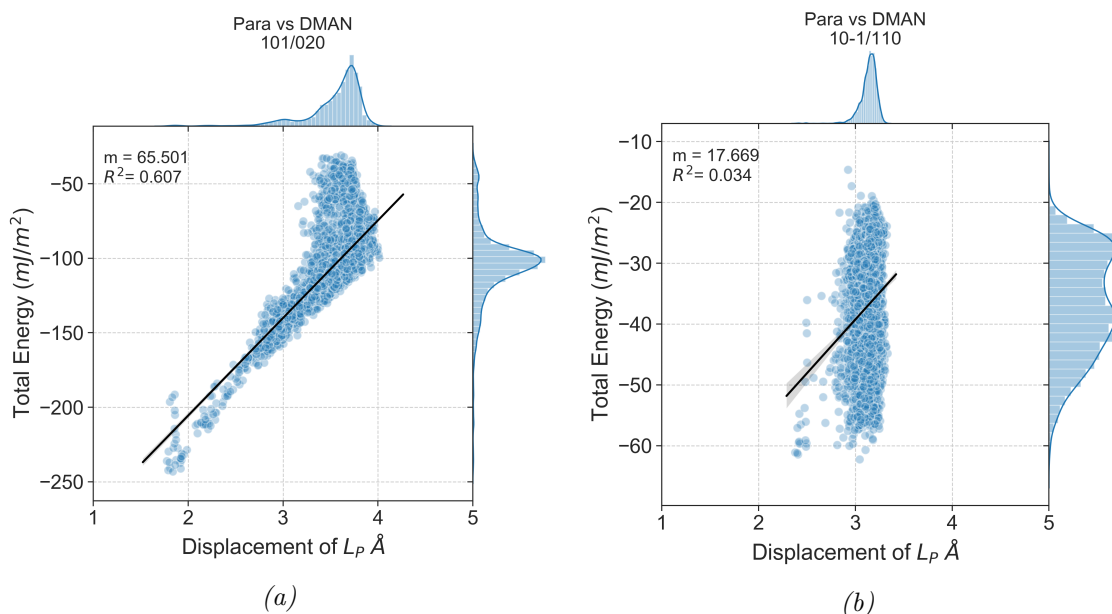
*Figure 4.26: Both graphs show all calculated energy minima for Para(101)-DMAN(020)**(a)** and Para(10\bar{1})-DMAN(110) **(b)**. Histograms top and right show the distribution of the displacement and energy for the facet pairs.*

to the steric hindrance of the methyl group, interactions with those electronegative groups are less probable. On the other hand, facet (020) (Figure 4.25b) has molecules protruding perpendicular to the surface. Causing a considerable depth to the surface and increased roughness. Due to the orientation of the molecule, both HB-donor and HB-acceptor atoms are available on the surface. This makes the (020) more susceptible to interlocking in the high depth surface channels where HB can occur and other electrostatic interactions with the probing Para surfaces.

It is possible to identify whether topology or surface chemistry is dominating the SSI based on the energy-displacement graphs shown in Figure 4.26.

In the case of Para(101)-DMAN(020) in Figure 4.26a, there is a strong positive correlation ($R^2 = 0.607$) between the displacement and total energy of the facet pair. This indicates the topology has a large impact on energy. On the other hand, the distribution in Figure 4.26b, where the energy change is large, but the displacement is predominantly around 3 Å, indicates that the topology has minimal impact and thus most of the contributions come from the functional groups.

Figure 4.27 shows spatial mapping of the energy at different rotations for (101)/(020). The plot in Figure 4.27d shows how the energy changes as L_P rotates around the z-axis. The mean (blue) is more sensitive to outliers and as such any deviation between that and the median suggests an asymmetric energy distribution and thus range in energy. The strongest average energies occurs at rotation of 0° and 35° shown in Figures 4.27a and 4.27b. The strongest energy points appear in a line which is indicative of the channels created by the two surfaces when they have come into

Para(101) vs DMAN(020)

(a) 0° Rotation Total Energy

(b) 35° Rotation Total Energy

(c) 0° Rotation HB Energy

(d) Average total energy at different rotations
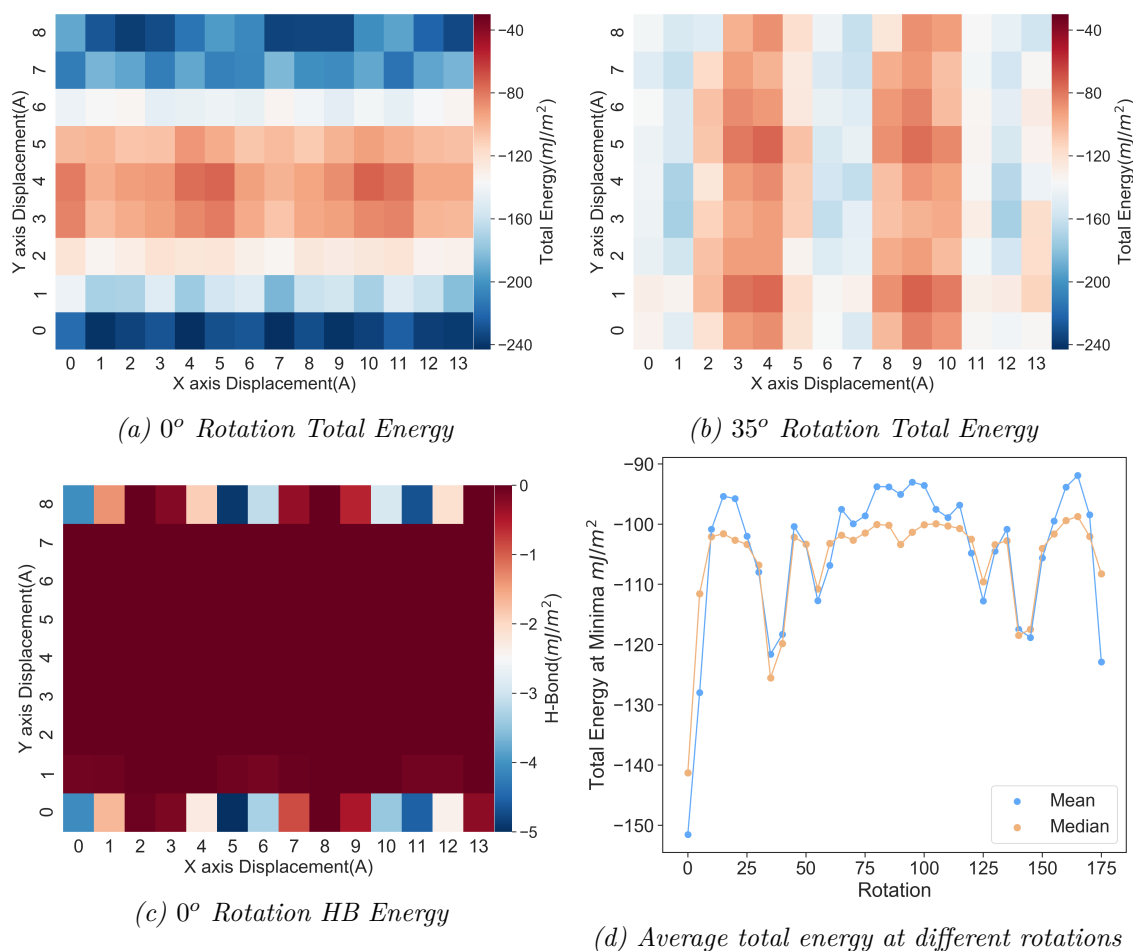
Figure 4.27: Example of high energy positions between heterogeneous systems and surfaces. Figure shows all minima positions and energy for Para(101)-DMAN(020) at different rotations. a) Total energy at rotation 0° showing the effects of the channels of the (020) surface. b) Total energy at a 35° rotation where another channel can be seen with a lower energy. c) Shows the contribution from HB towards the 0° rotation structure. d) The median and mean are shown for the to surface as the rotation is changed from 0 − 175° in 5° steps

contact and are interlocking. A rotation of 35° results in an energy channel rotation of 90°, which means there is more than one topological channel that can be formed between the two surfaces. Analysing the plot in Figure 4.27c, HB contributions are visible and correlate with the formation of channels.

The plots in Figure 4.28, for $(10\bar{1})/(110)$ do not exhibit formation of energy channels. The plot showing average energy change with rotation (4.28d shows 90° to have, on average, the strongest interaction energy. However, the mean and median energy fluctuates throughout the rotation, which explains the bimodal distribution seen in Figure 4.23a. Extracting the VdW component (4.28a) shows the regions of strong interactions. Analysing the ES (4.28b) and HB (4.28c) show specific regions of electrostatic and hydrogen bond interactions overlapping. As Para$(10\bar{1})$ contains only HB-acceptor groups, these act as a probe for detecting HB interactions. The

Para(10$\bar{1}$) vs DMAN(110)

(a) VdW Energy at 90° *(b) ES Energy at* 90° *(c) HB Energy at* 90°

(d)
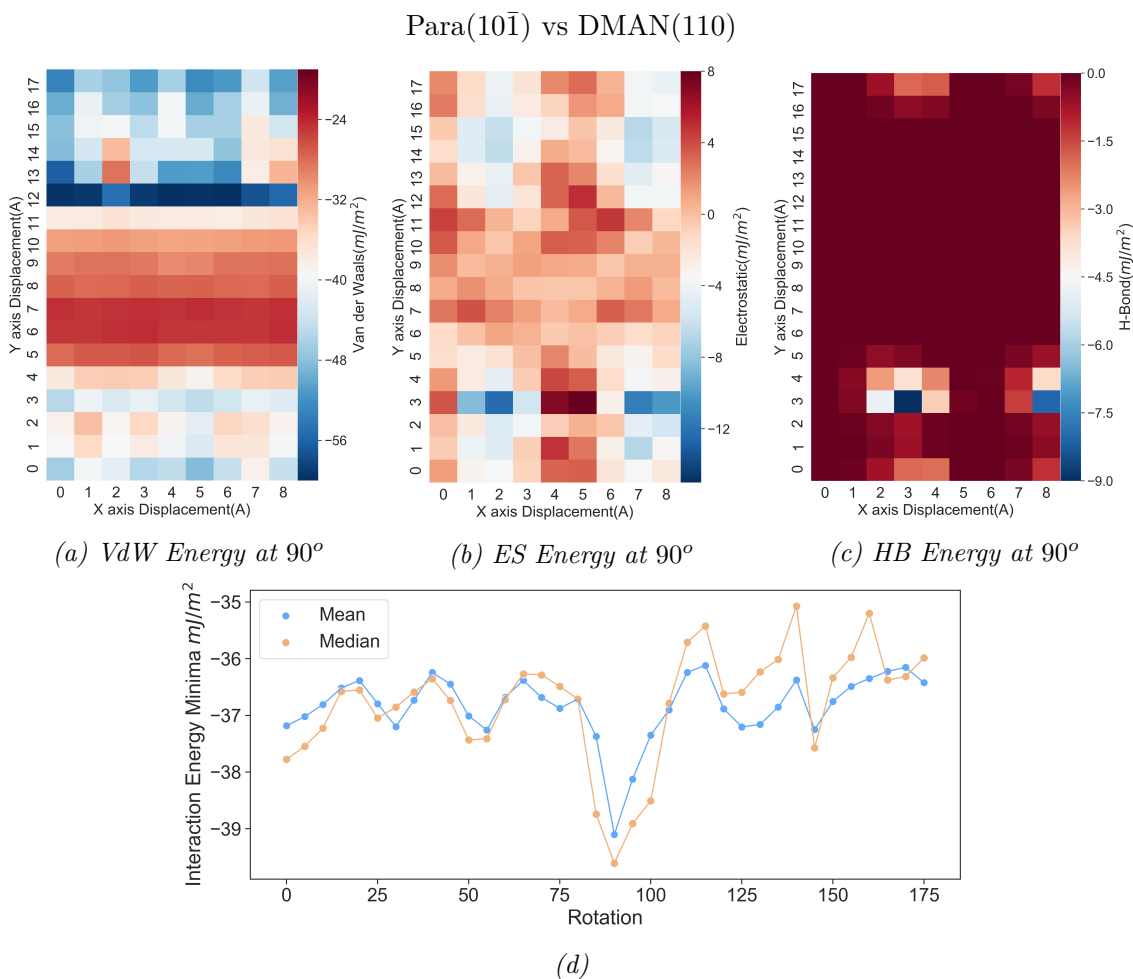
Figure 4.28: Example of functional groups contributing to specific interactions and how the contributing energies can be analysed (Para(10$\bar{1}$)-DMAN(110)). All spatial plots are set to a rotation of 90°*. A), b) and c) show the VdW , ES and HB respectively, indicating positions where energies overlap. d) Plot of mean (blue) and median (orange) for the energy at every rotation.*

distance of 5 Å between the two points of strong HB correlates with the distance between the two HB-donor groups on DMAN(110) which exist on the edge of the unit surface cell. This indicates that SSIM is over calculating some of the positions of the lattice; however, it does so across all rotations and thus does not significantly impact the frequency of energies.

L-Glutamic Acid

Distinguishing features in LGA can also be found across the different facets, even though the energy does not differ as greatly as for DMAN(Figure 4.23b). LGA offers more interesting facet terminations, as shown in Figure 4.29. Due to the presence of the carboxylic acid COOH and carboxylate COO^- groups on the LGA facets, it is expected they will engage in more ES interactions. Facet (011) is the only one with clearly exposed NH_3^+ groups on the surface (4.29c), is the strongest interacting

facet with the LGA(110) facet in Figure 4.24. Similarly to DMAN, the angles of protruding molecules greatly impacts the roughness of the surfaces. Due to the lack of gaps between the molecules, both horizontally and vertically, (011) has the smallest roughness. This implies the topology has little impact, and the majority of the difference in energy contributions come from the functional groups.

Facet (110) (4.29b) has two carboxylic acid groups present on the unit surface with the inverse of each being present on the surface (i.e.OH and C=O). Unlike (011), vertical and horizontal gaps exist between molecules causing for a rougher surface. As the valleys are hosts to the COO⁻ groups; it is thus expected that the topography and functional groups would impact energies from this surface.

Finally, LGA(101) (4.29a) appears to be similar to (110) with the carboxylic and carboxylate groups, however, lacking the presence of the primary ammonium group as it is in the depth of the surface. Although, (101) has a larger surface roughness which would contribute to higher displacement-based energy contributions.

(a) LGA(101)

(b) LGA(110)

(c) LGA(011)
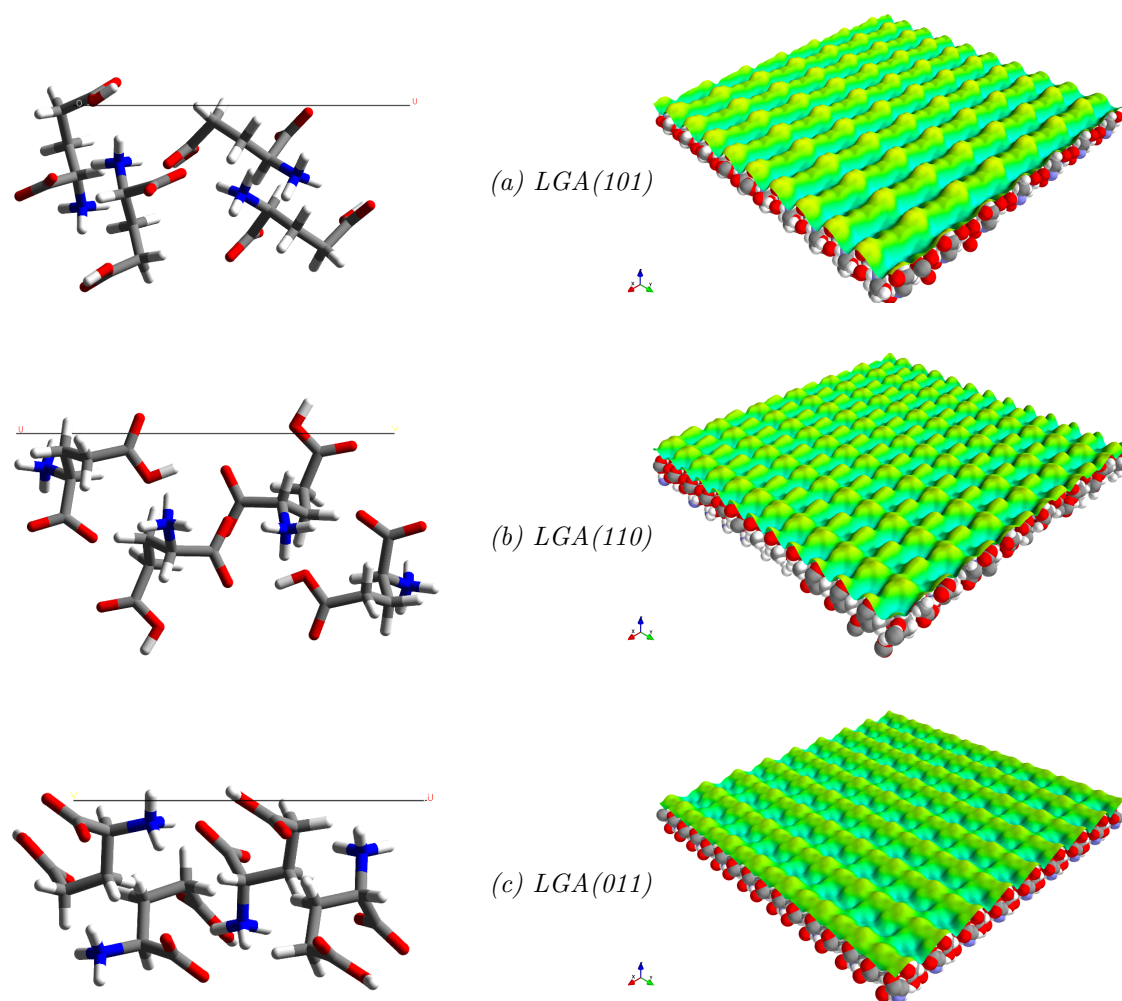
Figure 4.29: Unit surfaces and slabs of the different LGA facets. Surface generated utilising script developed by CCDC [112]

Para(11$\bar{1}$) vs LGA(011)

(a) H-Bond and displacemnt of L_P at 40°

(b)
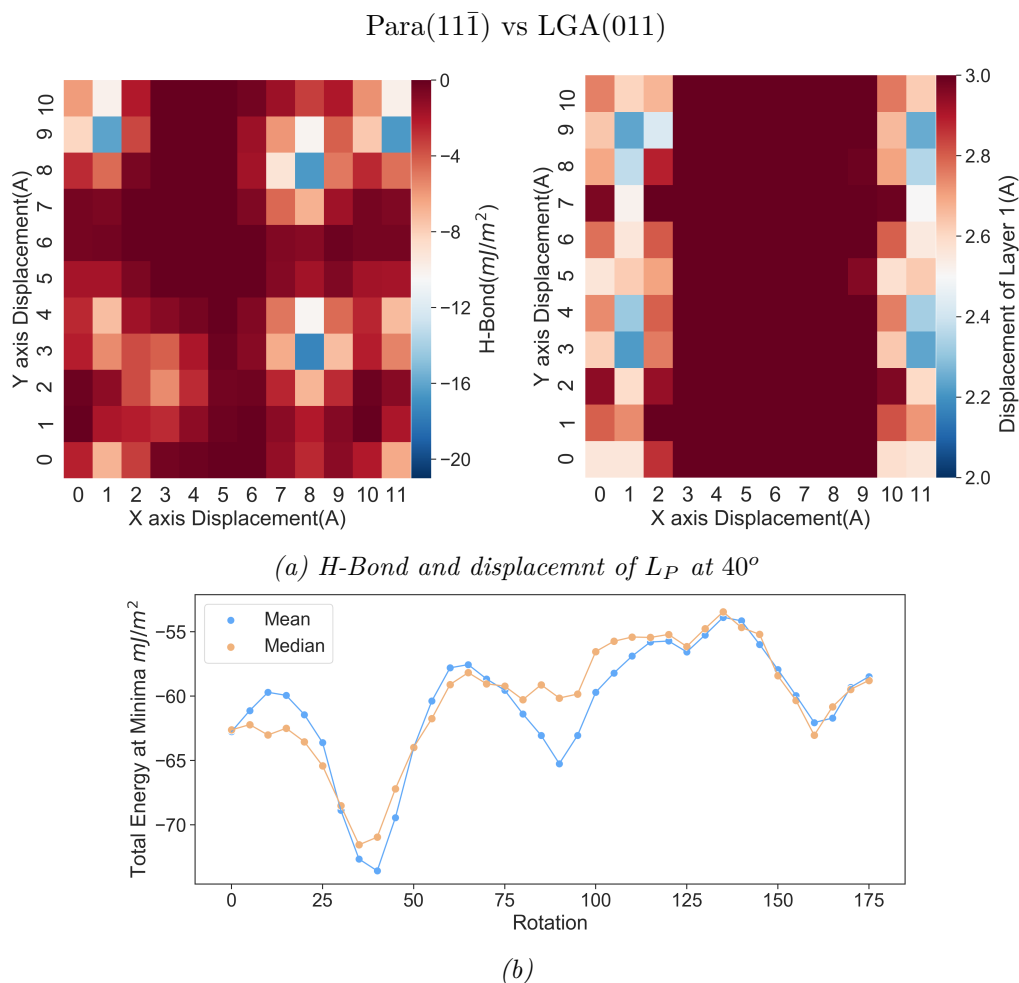
Figure 4.30: a) H-Bond and displacement of L_P plots for every minimum position on the grid at a rotation of 40° for Para(11$\bar{1}$)-LGA(011). b) Average energy for all minima as every measured rotation.

Analysing the data for the two most interacting facets (011) and (110), we can start to understand what role the surface chemistry and topology play for interactions of Para with LGA. Figure 4.30a shows the spatial orientation of interactions at a rotation of 40° for Para(11$\bar{1}$)-LGA(011). As indicated by the rotational plot (4.30b) the strongest interaction energy is calculated at 40°.

Unlike DMAN, (11$\bar{1}$) and (011) do not form the same type of interlocking channels, due to the lower depth of the surface in LGA. However, strong interaction occurs due to the presence of partially negatively charged groups on the surface of (011) and OH on the surface of (11$\bar{1}$) (4.22c). An HB value of 18 mJ/m^2 at position (8,3), which is considerably high contribution compared to other HB interactions of the explored facets. The approximate 3 Å distance between points (8,8) and (11,9) is the distance between COOH and adjacent (but lower position) of COO$^-$ observable in Figure 4.29c. Furthermore, a height difference of -1 Å is shown in the displacement map in position (11,9), supporting that is the lower carboxylate group

that is causing predominant interactions.

Para(11$\bar{1}$) vs LGA(110)
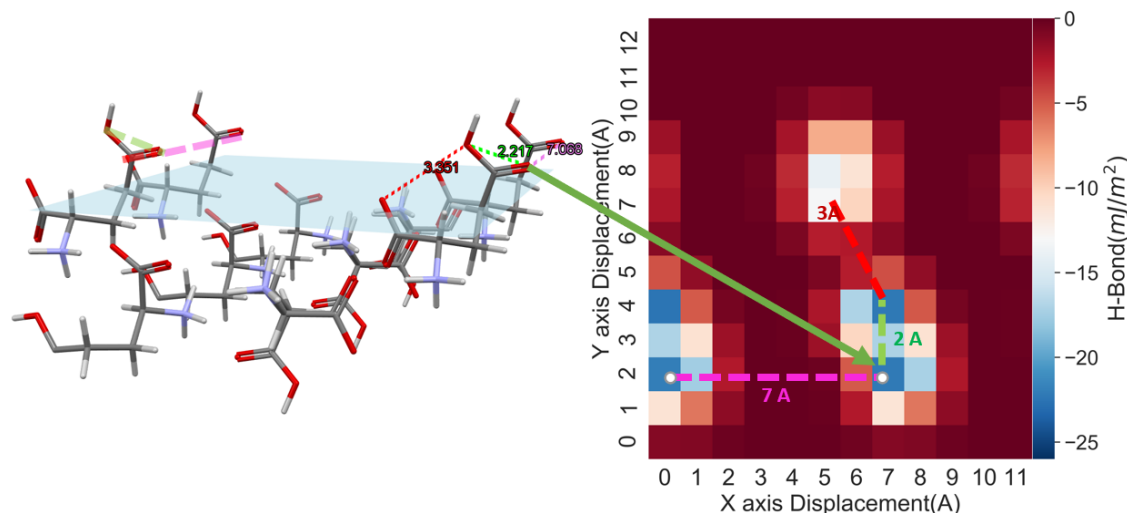
(a) H-Bond at 170° and spatial mapping onto two unit cells.
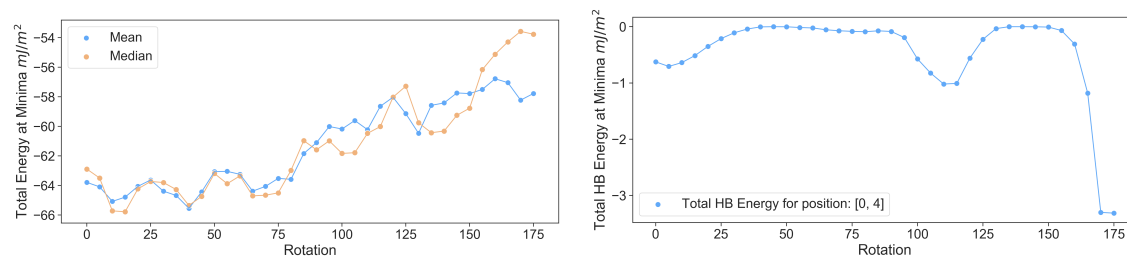
(b)

Figure 4.31: a) Mapping distances between functional groups using HB energy and spatial maps. b)left) Average total energy of every minima at difference rotations. right) HB energy minima for position (0,4) at every rotation

Due to the HB probing nature of Para(11$\bar{1}$), we can also investigate the LGA(110) facet in the same detail. Figure 4.31 shows that the facet pair does not engage in specific channel interlocking at set rotations, but the HB-accepts and donors of LGA have a large impact on the interactions. Assessing the weakest energy interaction at 170° (4.31b), with the largest difference between the median and mean (indicative of singular position high energy interactions), the HB interactions are assessed (4.31a). Tracking one position (0,4) for any HB energy changes shows that the rotation does indeed affect the position of where interactions would occur.

Position (7,2) is related to the C=O of the carboxylic acid group, which is 2 Å separated from its neighbouring OH group. Interestingly both groups are interacting, suggesting that the probing group is both HB-donor and HB-acceptor. Furthermore, 3 Å away at position (5,7) sits the CO$^-$ of the carboxylate group which a lower HB energy. The lower energy is due to the lower position of the COO$^-$ group in the surface, as the two cannot interlock properly to grant as much

access as the COOH group. Moving from the original starting position (7,2), it is possible to see a repeating structure appearing 7 Å away to the position (0,2). When mapped onto the molecular structure, it is obvious this is the carboxylic acid group again, which further indicates that SSIM is over-calculating grid sizes in a specific vector. In this case, the U vector.

Analysing these 3-dimensional data structures uncovers some of the surface chemistry and topological contributors for individual facets.

4.4.4.3 Impact of Surface Chemistry

Based on the analysis carried out in Section 4.4.3.1, the excipient surface descriptors have been calculated, linear models have been fitted in order to assess the impact of said descriptors and better understand the overall contributions towards system interactions. The models have been individually calculated, as opposed to collating all the data together (LGA and DMAN), in order to describe different system types initially. It is unreasonable to expect a linear model to accurately describe three separate surface types with only one data set for each surface type (i.e. DMAN only contains OH functional groups and LGA is the only one that contains partially charged groups). In order to generate a more accurate generic statistical model, one must first acquire a larger dataset and secondly use more sophisticated models such as machine learning algorithms [134, 135].

Table 4.8 contains all the excipient surface descriptors used for the models. As discussed in the previous section, DMAN(020) has the highest roughness, followed by DMAN(011) and LGA(101) based on the combination of Rq and rugosity. As DMAN only contains OH functional groups, and these act as both donors and acceptors, hence the descriptor values are equal. Further improvements could be made to take into account the directionality of the O−H bond in order to determine if the functional group can donate a proton. As neither system contains aromatic rings, the values for these are zero. When comparing the values in the table with reported surfaces in figures for DMAN (4.25) and LGA(4.29), it is clear that it is a

Table 4.8: Excipient surface descriptors

System	hkl	Dons	Accs	Aroms	Rugosity	Rq
DMAN	020	0.0361	0.0361	0.000	1.76	6.88
	011	0.0408	0.0408	0.000	1.29	4.15
	110	0.0475	0.0475	0.000	1.17	3.58
LGA	110	0.0160	0.0333	0.000	1.36	3.34
	101	0.0218	0.0448	0.000	1.37	4.06
	011	0.0177	0.0360	0.000	1.20	2.89

(a) Para vs DMAN

(b) Para vs LGA
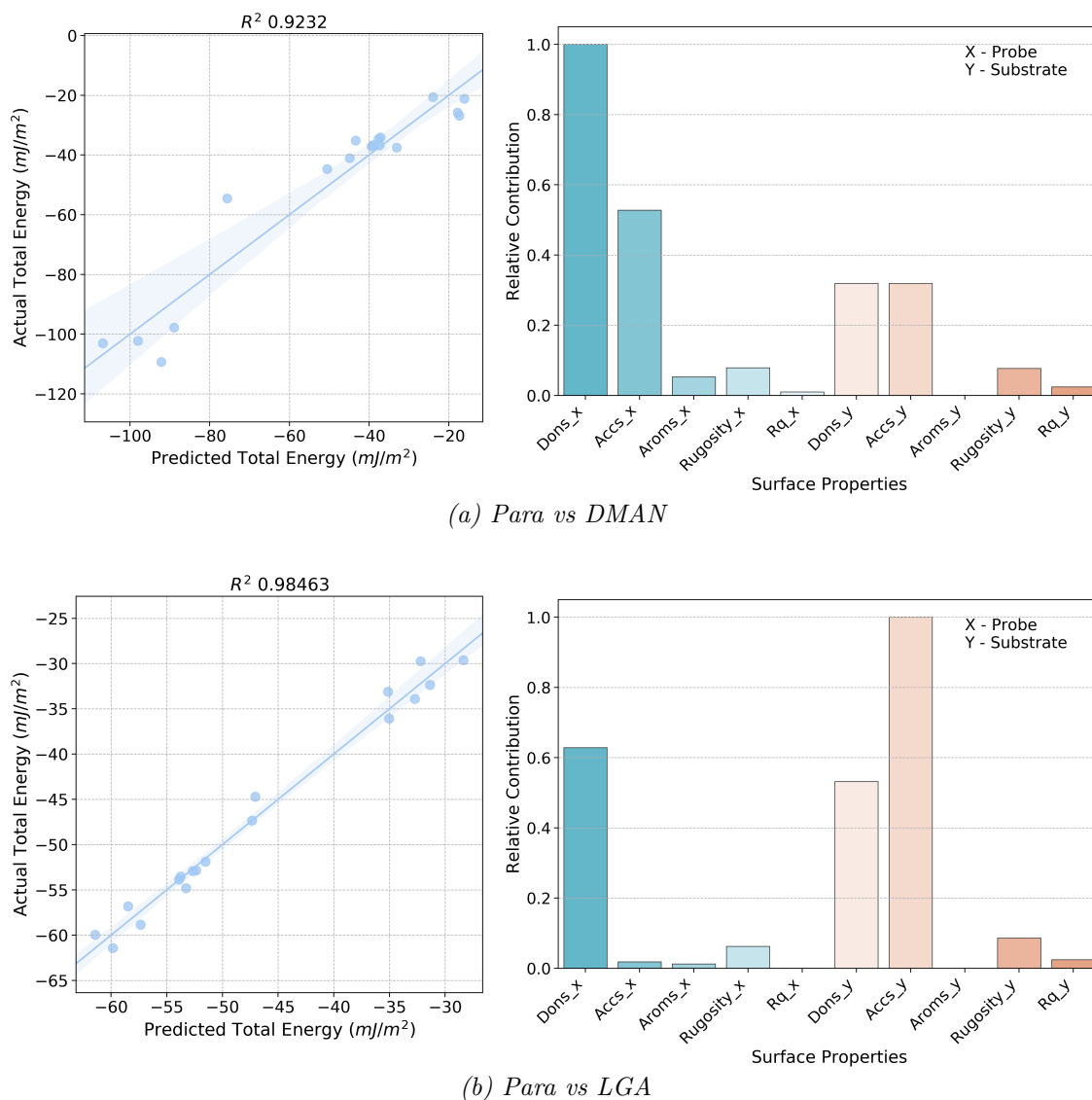
Figure 4.32: Linear regression models for analysing the contribution of surface properties towards interaction energy for Para-DMAN (a) Para-LGA (b). left) Model performance indicator, actual calculated total energy against predicted total energy, with R^2 (top) . right) Surface properties and their relatively contributions towards the linear model.

satisfactory numerical descriptor of said surfaces.

The Para-DMAN model in Figure 4.32a shows a good fit $R^2 = 0.9232$. The graph of predicted vs actual calculated total energy shows that the model successfully captures weaker interactions in the region of (-50 - -20 mJ/m^2). However, stronger interactions are less successfully captured, due to the four facet pairs of DMAN(020) substrate having much higher interaction energy, thus causing the overall data set to be split into two due to the abrupt change in energy.

The model allocates the largest contribution to be from the HB donor from the probe (Dons_x), followed by the HB acceptor groups from the probe (Accs_x). As previously stated, the hydroxyl groups in DMAN act as both Dons_x and Accs_y, thus the contributions from both are equal. While the contributions are equal from
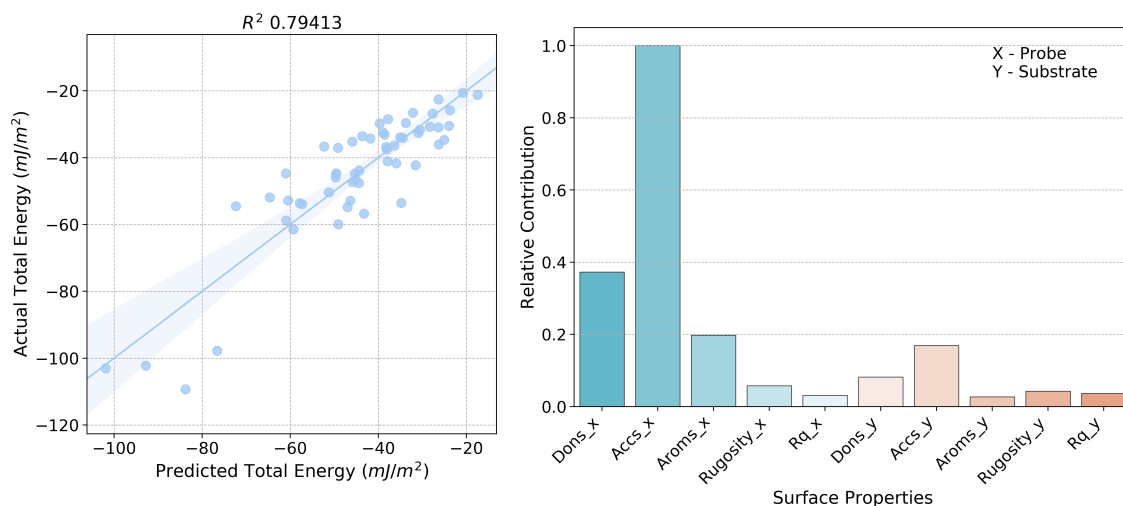
*(a) Linear regression model trained on cohesive and adhesive data - **including** Rugosity and R_q*
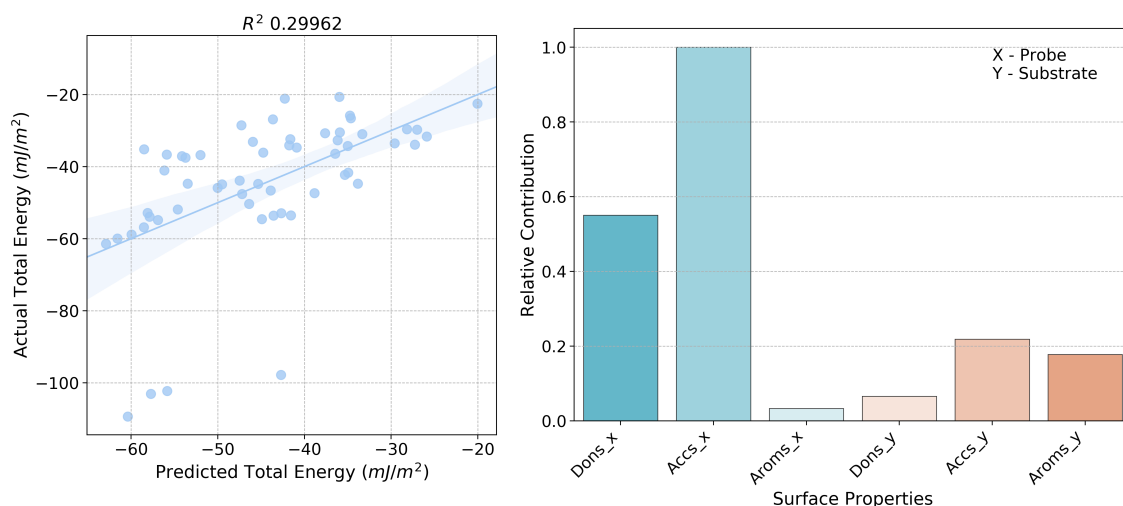
*(b) Linear regression model trained on cohesive and adhesive data - **excluding** Rugosity and R_q*

Figure 4.33: Linear regression models illustrating the impact of surface roughness, utilising all three datasets (Para, DMAN, and LGA).

the two substrate groups, the levels of contribution are unexpectedly low. This could be due to the nature of interactions being predominately driven by VdW or an artefact of using a linear model. When describing independent variables, these typically are just that. Independent. However, one can imagine a situation where Dons_x and Accs_y are interacting, and the model accounts only for Dons_x having a contribution, especially when the density of Accs_y and Dons_y are equal. Interestingly, the rugosity of both probe and substrate have an equal impact on the predicted energy. However, the Rq of DMAN has a higher contribution compared to Para. This suggests that the roughness of two systems plays a role in the energy calculated; however, the larger deviation of the Rq for DMAN has a higher impact than that of Para. This confirms observations made regarding the surface roughness

of DMAN(020) in earlier discussions.

Figure 4.32b shows the correlation of the linear model (Para-LGA) to have a better fit $R^2 = 0.98463$. This is in part due to the uniformity of the energies across all facets, as seen in Figure 4.23b. The most contributing surface properties are the presence of Accs_y functional groups, and these include the COO$^-$ and COOH functional groups. Further supporting the surface analysis carried out in the previous section. The Dons_x have the second-highest contribution, which indicates that whilst the electronegative functional groups are important within the substrate, they also have a matching pair to interact with.

Similarly to the DMAN data, the rugosity has a more significant contribution than the Rq. However, substrate roughness has a significant contribution compared to the probe. Indicating that the roughness of the substrate is greater or has broader implications for how the surfaces interact.

The difference between rugosity and Rq, as previously commented on (Section 4.4.3.1), is based on dimensionality. Whilst they both describe an aspect of roughness, rugosity describes the 2D aspect of the roughness. When $Area_{True} > Area_{Projected}$ the factor will be larger due to either deep valleys/tall peaks or due to width of said features. Rq is the RMSD of the surface, thus, describing the deviation from the normal along a sampling line, making it a 1D descriptor. Combining the two allows the linear model to process the nature of the roughness for both dimensions.

As previously seen, many interaction energies are dominated by the separation of the two layers. The roughness impacts how close these layers can be, thus is an important descriptor. This is illustrated in Figure 4.33. When combining all the data for one linear model (Para-Para, Para-DMAN, and Para-LGA), there is a change in the performance of the model and the contributing surface properties. Including the roughness descriptors the model performs relatively well with $R^2 = 0.7941$, Figure 4.33a. As expected, the stronger interaction energies are not very well described; as the least amount of data exists for those (four data points for Para-DMAN(020)). The large contribution comes from Para is due to the wide range of surfaces.

The model drastically underperforms across the whole energy range when the roughness descriptor is removed (Figure 4.33b), which is reflected in the fit ($R^2 = 0.2996$). This highlights the importance of accounting for surface roughness. The rank of the contributing surface properties does not alter significantly between the models, Accs_x and Dons_x still being the two highest contributors.

Carrying out these type of analysis based on linear regression confirms the qualitative analysis of the surface chemistry of each facet and the comparison to interaction energies calculated. The discussed analysis method enables high throughput analysis of multiple systems. The analysis is carried out automatically using the

ssim_tool application developed, allowing for repeatable and robust analysis.

4.4.5 Probability of Interactions

All facet pair interactions have been compared in terms of energetics per unit area (mJ/m^2) in order to predict their affinity for one another and thus the likelihood of them strongly interacting on a larger scale as part of particles. However, considering only the energetics neglects parameters such as kinetics of the particles and physical representations of the facets. The former is not within the scope of this project as it would involve larger scale calculations. However, the latter can be approximated.The morphology calculations (Section 4.2.3) predict a facet percentage representation for the crystal. Smaller facets have higher interactive surfaces; however, the probability of two small facets colliding is smaller.

The values calculated for each morphology were processed, as detailed in Section 4.3.4, to give an equivalent probability of the two facets coming together(i.e. if two small surfaces were to come into contact, the probability is low). The product of interaction probability and energy gives the expected interaction energy per area
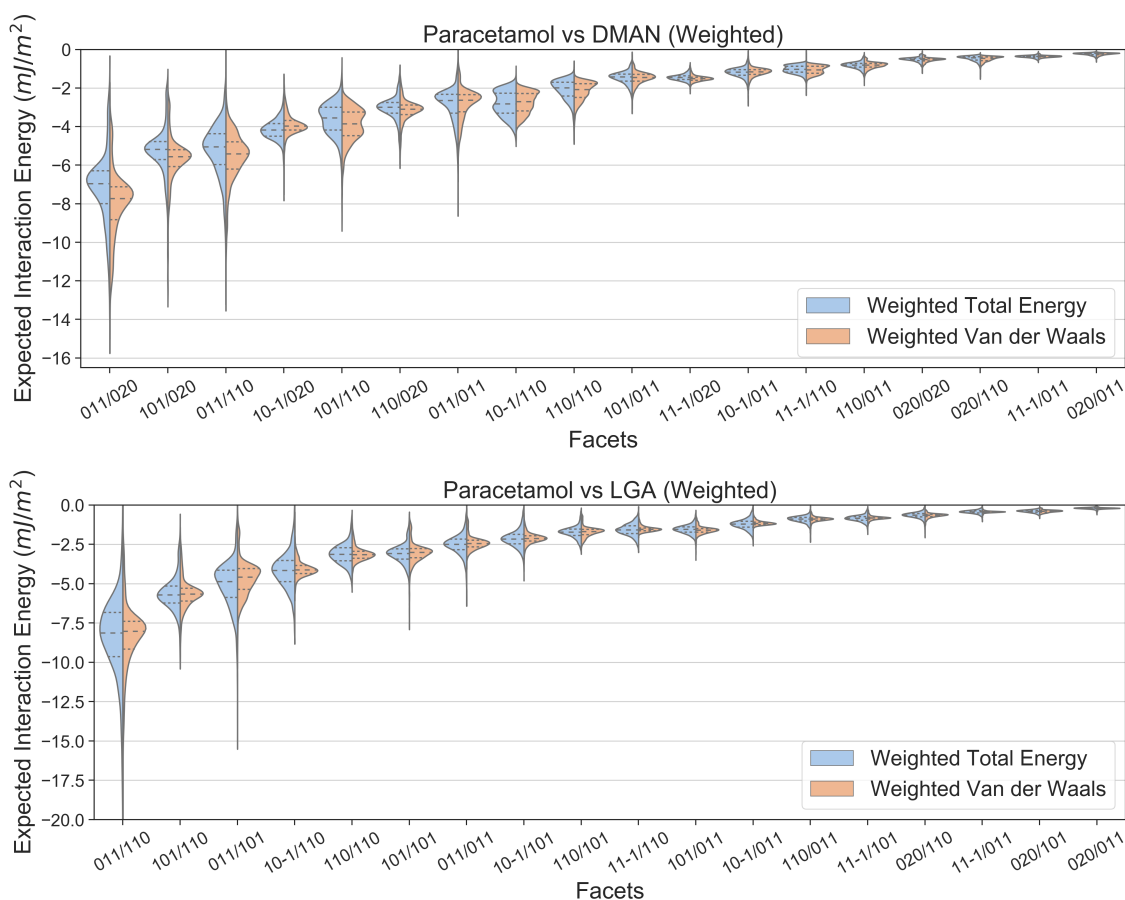
Figure 4.34: Expected interaction energy distributions for Para-DMAN and Para-LGA. Original interaction energies were individually weigheted using the % surface representation. The weighted total energy (blue) and weighted Van der Waals (orange) are shown.
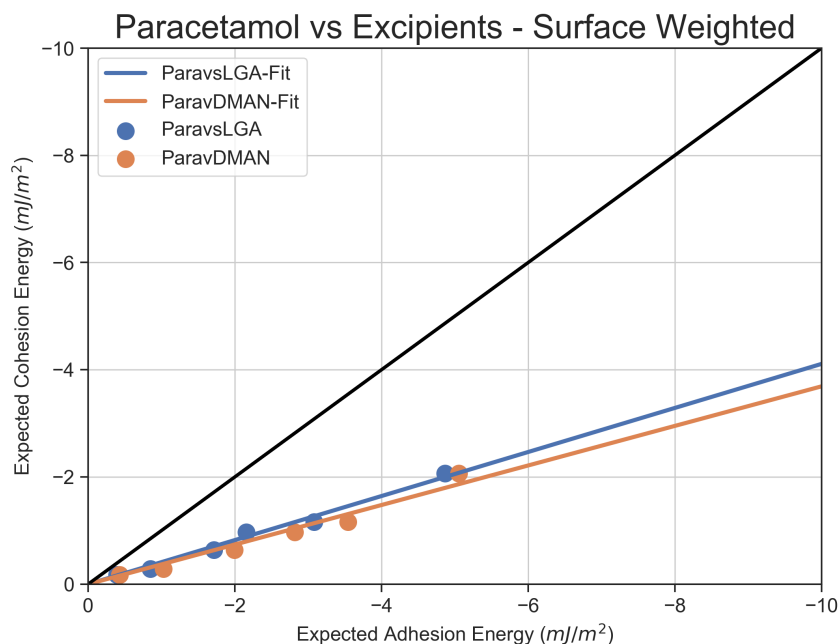
Figure 4.35: Cohesive-adhesive balance (CAB) plot for Para vs excipients (DMAN and LGA) with the expected adhesive and cohesive energies calculated using the % surface representation of each facet pair.

(EIE). As such, it is possible to account for geometric properties of the particles as opposed to just the energetics. Figure 4.34 shows the EIE for Para-DMAN and Para-LGA. The order of Para probes is the same in the presence of both excipients (except for lower energy facet pairs with small differences), with (011), (101), and ($10\bar{1}$) accounting for the top four interaction. The size of these facets are ranked in from largest to smallest, respectively (see Table 4.3).

Ranking of EIE is similar for LGA, where the largest surfaces have the highest energy. LGA (110), (101), and (110) are ordered largest surface to smallest (see Table 4.5). This expected ranking is a function of the size differences between facets. Whilst Para($11\bar{1}$)-LGA(011) have high interaction energy, their surface representations are 4.6% and 14.8%, respectively. Thus chances of these two surfaces interacting are 0.68%, and therefore their expected interaction energy is very low (ranked third-lowest).

On the other hand, instances where the surface representation is small, but the energy is significantly higher causes the EIE to be still relatively high. This is the case for Para-DMAN, where three of the top four interactions contain DMAN(020), which is half the representative size of DMAN(110), 24.4% and 51.4 % respectively. Previously discussed data from Section 4.4.4.2 detailed what caused the high interaction energy between Para and DMAN(020). This suggests a preferential facet interaction within a bulk powder, where all other facets have less of an affinity to Para, unlike (020).

Accounting for the expected interaction energy, it is possible to analyse the CAB

plot based on % surface representation of each facet. Figure 4.35 shows the large impact of accounting for the geometry of the crystals. In this situation, Para has a higher affinity to both excipients than itself. Table 4.9 offers more insight into the details of the CAB plot. Both data sets have a good fit with $R^2 = 0.9869$ and 0.9648. The gradients suggest that Para-DMAN is more adhesive than Para-LGA. This is skewed due to the larger expected adhesive energies across all facets when compared to Para-LGA.

The probing facet ranking, therefore, changes, from the originally presented values in Section 4.4.2, to a size-based rank. Both data sets share the same ranking order for Para listed below:

$$(011) >> (101) > (10\bar{1}) > (110)(11\bar{1}) > (020)$$

Based on the predicted morphology and the calculated interaction energy, therefore, it is possible to approximate the probability of two surfaces adhering together. This also allows for the identifications of facets that have truly higher energetic surfaces, where the surface representation does not completely eliminate the likelihood of strong adherence.

Table 4.9: Tabulated fit data for the expected interaction energy showing the gradient and R^2 of Para vs DMAN and LGA

Systems	**Gradient**	R^2	**Para Probe**	E_{Adh} (mJ/m^2)	E_{Adh} SE (mJ/m^2)	E_{Coh} (mJ/m^2)	E_{Coh} SE (mJ/m^2)
ParavLGA	0.4109	0.9869	011	-4.867	2.050	-2.062	0.981
			101	-3.081	1.522	-1.161	0.476
			10-1	-2.156	1.089	-0.970	0.434
			110	-1.713	0.819	-0.635	0.273
			11-1	-0.846	0.419	-0.283	0.117
			020	-0.389	0.157	-0.175	0.093
ParavDMAN	0.3690	0.96480	011	-5.054	1.561	-2.062	0.981
			101	-3.541	1.363	-1.161	0.476
			10-1	-2.817	1.088	-0.970	0.434
			110	-1.994	0.793	-0.635	0.273
			11-1	-1.025	0.398	-0.283	0.117
			020	-0.430	0.103	-0.175	0.093

4.5   General Discussion

Building upon previous methods of using single molecular probes[109, 24] and nanoclusters [120] applied to a grid search method, a novel full space probing method has been developed. Limitations of using single molecular probes to determine surface-surface interactions were solved by generating slabs where energies were calculated per unit area with a set converged slab sizes. Thus, the model accounts for interactions from the surface and surface-bulk atoms. Both single-molecule and nanoclusters methods focused on finding the strongest interaction energy and thus optimising spatial orientations. While optimising all degrees of freedom is useful for finding the most energetically optimal position, it does not represent interactions that would occur in real-world systems where entire crystals are unlikely to shift by Å in order to reach more satisfactory energy. This is after assuming that surfaces are pristine and periodic. Therefore, by calculating all possible energy minima, a statistical representation can be drawn, and more applicable information can be analysed.

Based on calculations for Paracetamol with α-L-Glutamic acid and β-D-Mannitol, it is possible to extract atomistic information at different applicable scales. Initially, spatial positions can be analysed to determine how functional groups interact in specific cases for particular facet pairs. Furthermore, these can be compared relatively to other facet pairs to determine patterns of interactions. For example, it was found that Para has a preferential interaction with DMAN(020) compared to all other possible facets. Based on positional data and surface analysis, the cause of this was determined to be surface roughness and functional groups present on the surface. While not surprising, quantifying these feature leads to a more robust understanding.

By aggregating all the facet data, it is possible to identify specific surface features which have a high impact on the interaction energy. It was demonstrated when analysing the surface chemistry of Para-LGA using multivariate linear regression. It was found that the H-Bond acceptor groups on LGA such as $C{=}O$ and COO^- have a higher impact on the interaction energy than its H-bond donor groups (NH_3^+ and OH). Moreover, the orientation of functional groups on the surface was identified as one of the reasons for drastic changes in interaction energy.

All data were collated into the Cohesive-Adhesive Balance (CAB) plots which were used to identify overall system trends, in which, it was found that Para is predominantly cohesive in the presence of DMAN but adhesive in the presence of LGA. It was possible to identify probing surfaces that did not fit the system trend. For example, Para(020) showed a more cohesive affinity in the presence of LGA, while the rest of the facets were adhesive. Finally, the data was weighted with

the percentage surface representation of each facet in order to calculate expected interaction energy and thus attempt to predict which facets are most likely to have adhered together during inter-particular interactions. SSIM allows for analysis of the functional groups, surface properties, and system dependent interactions; covering a range of applicable scales while using atomic-scale information.

The probability of interactions analysis aims to predict the likelihood of two facets interacting from a bulk perspective. A primary assumption is the correct calculation of the % surface representation of each facet from the predicted morphology. As the morphologies were predicted using the attachment energy model, it does not account for thermodynamics or solvents affects, two factors which significantly impact crystal growth and final habit of crystal[136, 137, 138, 139, 127]. However, these percentages can be adjusted to fit real-world systems. SSIM calculates the interaction energy for two surfaces of specific chemistry coming into contact. As such, the data can be recycled to predict how atomistic interactions would occur for lab measured crystals.

Previous studies have utilised the anisotropy factor, which is the % of unsatisfied intermolecular bonds on the surface of a facet, describing the most interactive facet when the factor is low [85, 55, 112]. The comparative rankings can be seen below:

$$Para/Para(SSIM) : (10\bar{1}), (101) > (11\bar{1}) > (110) >> (020) > (011)$$

$$Para/LGA(SSIM) : (11\bar{1}) > (101) > (110), (10\bar{1}) >> (011) > (020)$$

$$Para/DMAN(SSIM) : (11\bar{1}) > (101), (10\bar{1}) > (110) >> (011) > (020)$$

$$Para(Anisotropy) : (11\bar{1}), (110) > (020), (10\bar{1}) > (101) >> (011)$$

The rankings between SSIM and anisotropy support the fact that highly energetic surfaces will typically have higher interaction energies. However, it is important to note that simply ranking based on energy is not enough, as illustrated by the ranking differences for $Para(020)$ and $Para(10\bar{1})$. As SSIM accounts for the surface topography and position of functional groups, the ranking of most interactive facets is tailored for the systems in questions, and thus offers an improvement on existing methods.

4.6 Conclusion

This chapter presented a methodology for assessing the inter-particular interaction between faceted organic crystals at an atomic resolution. The surface-surface interaction model (SSIM) has been developed using a grid search method to sample all unique free space between two slabs and calculates their interaction energy at every position. Full contact between the facets was assumed at the energy minimum for the z-axis. The set of facets (forms) considered for each material was identified/evaluated using the attachment energy model which predicted stable slices surface terminations and predicted crystal morphology for Paracetamol (Para), α-L-Glutamic acid (LGA) and β-D-Mannitol (DMAN).

Cohesive-Adhesive balance plots showed that Para was more adhesive in the presence of LGA, but more cohesive when in the presence of DMAN. Practically this means that Para is more likely to agglomerate to itself in the presence of DMAN causing non-uniform granulation in a solid form formulation. By analysing the cohesive energy based on facet specific information, it was found that Para($10\bar{1}$) and Para(101) were the strongest interacting facets. This was caused by the higher density of H-bond acceptor groups on the surface, which were predicted to have a significant contribution to the interaction energy based on the multivariate linear regression model.

Surface specific data highlights the importance of considering the whole distribution of energy from facet pair interactions as opposed to strongest interaction energy, as previously done with single molecular probes and nanoclusters [120, 24]. Strongest, single position, cohesive interaction for Para has been identified as caused by the interaction of homogenous surfaces where the lattice aligns, and a continuation of lattice exists.

Analysing the surface properties of Para with all excipients showed the impact of surface roughness and available functional groups. In some cases, if the surface roughness is higher, the interaction energy is increased. It was found that the orientation of functional groups causes a large impact. In situations where the HB-donor/acceptor groups such as OH protrude with the hydrogen first, it will most likely be strongly interacting with HB - acceptor surfaces.

SSIM predicts the interaction energy between accurately generated crystal facets. When generating the predicted morphology the fractional area for each facet is calculated. Using the fractional area, it is possible to calculate the likelihood of adherence between two surfaces. Combining the geometrical representation with the calculated energetics can be used to adjust the calculated CAB values to represent the expected interaction. As each energy is calculated per unit area, it is possible to adjust the values based on real-world, observed crystals in order to adjust the

likelihood of adherence as long as the forms on the real crystal are in the predicted morphology.

In summary, a method has been developed that allowed us to determine the specific contributions of functional groups, surface roughness and spatial positioning between two organic facets, which is the first time this has been achieved. This work is novel based on its application of molecular mechanics calculations, in order to ascertain a distribution of interaction energy between two facets as well as the tool developed for it, allowing for high throughput analysis which was previously not possible using similar molecular dynamics approaches. Using these methods, it was possible to identify which functional groups of Paracetamol which had the highest contributions and also the mechanisms by which these surfaces interacted. Furthermore, the impact of atomistic surface roughness was quantifiably assessed, illustrating that in certain conditions, the roughness can either increase or decrease the interaction energy dependent on the surface geometries.

CHAPTER 5

Preparation of Organic Crystal Facets for Force Measurements

"Research is what I'm doing when I don't know what I'm doing - Wernher von Braun"

Within this chapter, a cleaning study is presented for the preparation of Paracetamol surfaces.
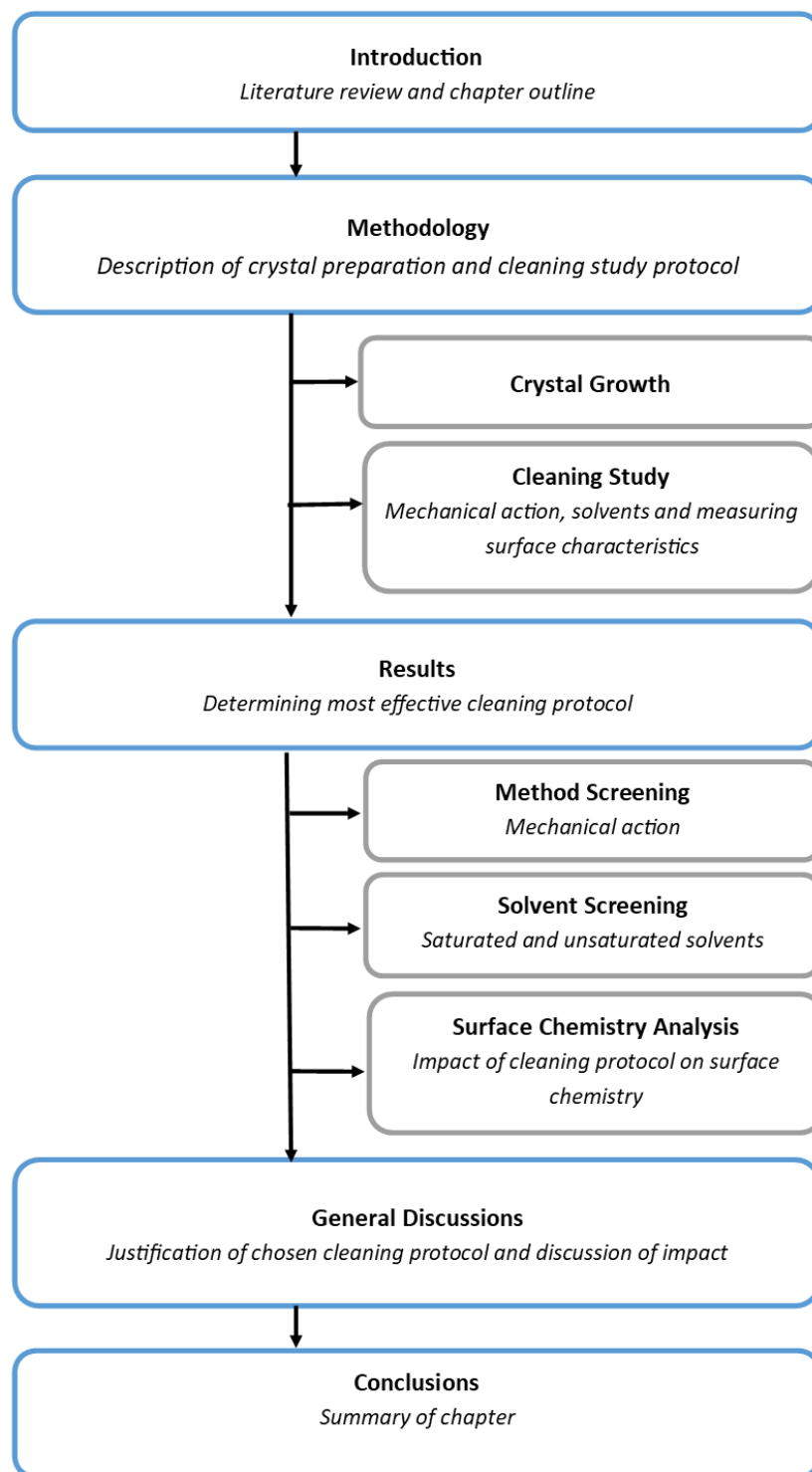
Figure 5.1: Outline of Chapter 5

5.1 Introduction

The purpose of the study described in this chapter is to identify a method of preparing paracetamol facets for surface-surface force analysis. Due to the nature of the growth conditions (stagnant flow over a long period), surface contaminants exist on the surface. Even with carefully handled samples, other crystal fragments can adhere to the surface and interfere with surface-based measurements. Contaminants on the surface can have a two-fold effect on the adhesive force, by physically and chemically altering the surface. Debris and crystal fragments cause steric repulsion due to the sensitivity of the instrument. Molecular adsorption is classed as a chemical contaminant as it changes the surface chemistry of the surface and thus the measured adhesive properties. Studies have highlighted that surface contamination occurs on nearly all materials[140, 141, 142, 143, 144, 145] .

Typical methods for surface cleaning such as heating, aggressive solvents, sputtering, and ozone cleaning do not typically work for organic crystals as they would either vaporise, etch or decompose the surface of organic crystals, none of which allow for the probing of the surface chemistry [146, 147, 148, 149, 150, 151, 152] . For example, paracetamol has a melting point of 170 ^{o}C; however, metallic crystals are typically heated ≥ 400 ^{o}C past which most organic crystals would decompose[144, 153]

The use of surfactants and organic solvents has been shown to clean more sensitive materials. However, in the presence of organic materials, these solutions can bind to the surface and create monolayers[154].

A less aggressive, non-contaminating protocol is required to ensure the facets are clean enough for measuring surface-surface interactions. The protocol must remove surface contaminants and debris, but have a minimal impact on the topography of the surface or altering chemical compositions. The use of a gas cluster ion beam has shown that it is possible to atomically clean surface with a controlled depth. The beam bombards the surface with nanoscale clusters of ion, typically argon. Whilst this technique is technically suited towards the cleaning of organic surfaces, due to the small footprint of the beam ($\approx 20nm$) the time requirements to clean a whole single crystal would be impractical[141, 155, 156, 157].

As part of a collaboration with Benjamin Tayler-Barrett (BTB, Schroeder Group, University of Leeds), surface chemistry analysis was performed using Near Ambient Pressure - X-Ray Photoelectron Spectroscopy (NAP-XPS), which was carried out at the National Synchrotron Light Source- II (NSLS-II) in Brookhaven Laboratories, USA. The measurements were carried out by the author (AM) and BTB. BTB conducted analysis of the data, details of the theory, methodology and detailed results can be found in BTB's thesis 'The Detection and Quantification of Nonyl Phenyl Ethoxylate Surfactant on Paracetamol Single Crystal Surface'[158], and will

not be repeated within this writing as it falls outside of the scope of this project.

A brief overview of NAP-XPS is given to allow for data interpretations. NAP-XPS is used to analyse the surface chemistry of materials by exposing a sample to X-rays and measuring photo emitted electrons. By measuring the kinetic energy and number of electrons that escape the sample, the chemical state of the surface can be determined. The spectra collected contain peaks that correspond to the specific electron configuration of given elements, so the chemical composition can be determined. Typically XPS requires high vacuum ($< 10^{-8}$ mbar), however, NAP-XPS allows for much lower pressures of up to 1 mbar to be used allowing for the use of gases and water vapours to stabilise charged systems. Organic crystals typically have poor conductivity and act as insulators, so when bombarded with x-rays, they tend to charge and affect the measured spectra. NAP-XPS allows for the chemical determination of organic surfaces [159, 160, 161, 162, 163, 30, 20, 164].

This cleaning study focuses on determining a suitable method for cleaning paracetamol crystals without drastically altering the topography or chemical composition of the surface. In order to investigate possible solutions, this chapter will present a rapid method (mechanical action used to clean the surface) and solvent screening with the use of optical and atomic force microscopy. Different cleaning regimes and solvents have been studied in order to select the least surface damaging protocol.

5.2   Methodology

Within this section, a brief description of the experimental design will be given along with a detailed account of the cleaning procedures and steps taken in order to assess their efficacy.

In order to reduce the surface contaminants and debris, the cleaning protocol must incorporate both mechanical and chemical cleaning methodologies. Different mechanical actions were used to determine the optimum cleaning to surface damage; a strong solvent was used for this in order to highlight any topographical impact. Chemically, a range of solvents varying in solubility, was chosen in order to assess the impact on the sensitive organic surface.

All experimental procedures were carried out in conjunction with laboratory health and safety regulations and COSSH assessments were carried out through RIVO. Paracetamol at >99% purity and all solvents at HPLC grade were purchased from Sigma-Aldrich (Irvine, UK). Silicon based AFM probes were purchased from Bruker (Coventry, UK)

5.2.1   Crystal Growth - Evaporative

Large single crystals were grown in order to isolate unique facets and allow for easy sample handling during crystal cleaning. An evaporative method was used in order to grow sufficiently large crystals.

The evaporative method was carried out by dissolving 15.65 g of paracetamol in 135 ml of absolute ethanol under agitation. The container was covered with parafilm, to ensure a limited number of airborne particulates induced nucleation, and left for 5 hours to ensure dissolution. The contents were separated into two 100 ml crystallising containers. These were covered in parafilm which were then pierced to ensure the escape of solvent. The crystallising containers were placed on a slab of polystyrene to reduce benchtop vibration. After four weeks, the crystals were harvested and placed in a desiccator for 24 hours before imaging.

5.2.2   Cleaning Study

A systematic study was carried out to determine the optimum cleaning regime for single facets of paracetamol. Initially, four different mechanical methods of cleaning were tested with the use of absolute ethanol (EtOH) to verify the type of topography damage inflicted on the surface.

Optical images and force volume scans were carried out pre- and post-cleaning with the use of a Multimode 8 Bruker atomic force microscope equipped with a J scanner.

109

5.2.2.1 Method and Solvent Screening

The mechanical actions screened were compressing, wiping, rolling and solvent jet. Once the least damaging method was identified four solvents, EtOH, methanol, water and dichloromethane were used.

Solvents were selected based on the solubility of paracetamol. Paracetamol is most soluble in methanol and least in dichloromethane (DCM). Solubility is tabulated in Table 5.1[165]. Saturated solvents were also used in order to reduce the dissolution of the surface. Due to their increased concentration of solute, the equilibrium between dissolution and re-crystallisation is more balanced, unlike pure solvent, which is in favour of dissolution driven by the difference in concentration.

All cleaning methods (except the solvent Jet methodology) were carried out using precision lens tissue (Fisher, UK). The tissue was wetted with approximately 5 ml of the solvent and used in three different methods. After each cleaning method, the crystal facet was dried using N_2 gas to reduce surface dissolution and remove residual solvent. Each method was carried out four times before drying. Figure 5.2 illustrates the different cleaning methods. A jet washer used was the WP-250 Nano Water Flosser (Waterpik, purchased from Amazon, UK).
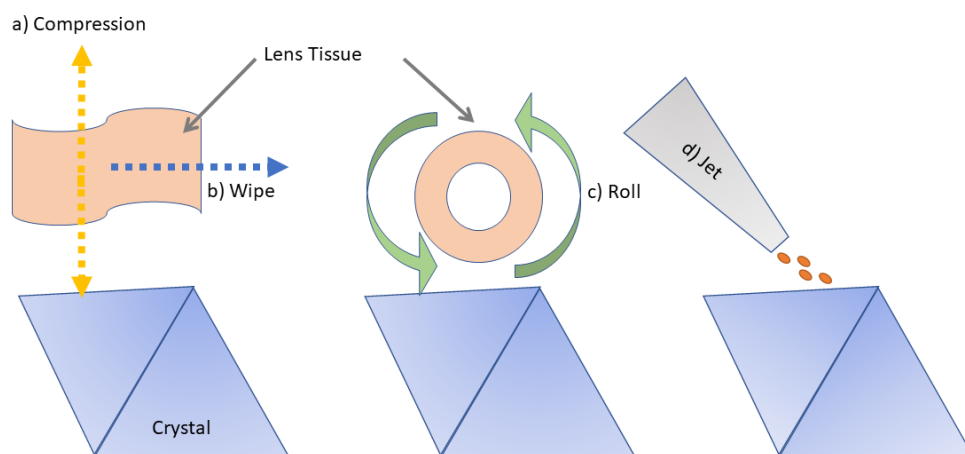
Figure 5.2: The four cleaning methods used to remove debris from the crystal surface mechanically. a) Compressing the solvent soaked lens tissue onto the surface. b) Wiping the crystal. c) Using a cylindrical lens tissue to roll across the surface. d) Pressure jet of solvent directly onto the surface.

Compression - the lens tissue was held in tension and lowered to the crystal surface, once contact had been made, it was lifted, and an untouched tissue

surface was used. - The principle mechanical action is minimal lateral force onto the crystal surface.

Wipe - the lens tissue was held in tension and using a single motion, the tissue was wiped across the surface of the crystal with only the tension applying pressure. - Maximum lateral force onto the surface of the crystal.

Roll - the lens tissue was rolled into a single-layered cylinder. This was then rolled across the surface of the crystal, with each roll being exposed to a new tissue surface. - A combination of lateral and vertical force

Jet - the jet pressure was set to the lowest setting of approximately 0.6 bar. The solvent was slowly scanned across the surface of the crystal before being dried. - The mechanical action is in essence similar to that of sputtering but with a less damaging abrasive.

Saturated solvents were prepared by adding paracetamol into 100ml of solvents, over a few hours. Additions were repeated to ensure crystals were still present in the solution. The saturated solvents were left under agitation for over 48 hours. Saturated solvents were filtered using a 0.5 μm syringe filters before use.

Table 5.1: Solvents used for cleaning and paracetamol solubility at 30° given as g of solute / kg of solvent. [165]

Solvent	Solubility g/kg
water	17.39
ethanol	232.25
methanol	371.61
dicholoromethane	0.32

5.2.2.2   Optical Microscopy

Images of the surfaces pre- and post-cleaning were taken using the long working Nikon 5x lens attached to the AFM. The camera used was the ueye stock CCD sensor part of the Bruker system. Images were calibrated using the AFM cantilever (TESPA-V2) as the reference scales. Images were processed in ImageJ [166].

5.2.2.3   AFM - Force Volume Scans

Adhesion measurements were taken as a way of assessing the change of surface adhesive properties and uniformity of the surface was pre and post-cleaning. Using AFM force spectroscopy the adhesive force between AFM cantilever (Si probe) and the crystal surface was measured. By taking a force curve measurement (Section

3.2.2) it was possible to measure the adhesive force at a particular point, moving the probe across the surface and taking multiple force curves forms the basics of FV scans. FV scans, therefore, have allowed for the collection of large data sets of forces pre- and post-cleaning.

Table 5.2: Cantilever specification for RTESPA-150-D

Thickness	1.75 μm
Length	125 μm
Width	35 μm
f_o	150 kHz
Spring Constant	6 N/m

Before every scan, the cantilever was placed under a chamber containing a deep UV (183 nm) lamp, which generated ozone. Ozone cleaning allowed the probe to be stripped of any organic material. The cantilever used was the RTESPA-150-D, specifications of which are tabulated in Table 5.2.

To place the crystal flat on the metallic stub, a putty-like substance (Rodico, Cousins UK) was used. The single crystal was placed into the putty and adjusted using carbon tipped tweezers in order to reduce damage to the crystal. During the experiment, the cantilever was calibrated via thermal tuning at the start of the day and halfway through. Relative humidity and temperature were monitored throughout the systematic study, due to a lack of fluctuation in either, they will not be reported. The temperature averaged at 22^oC and RH at 32 % . The humidity was checked in order to ensure force changes were not caused due to an increase in surface-bound water and thus capillary forces.

The scanning parameters used for all scan are tabulated in Table 5.3.

Table 5.3: Scanning parameters for Force Volume scans of RTSPA-150-D on paracetamol single crystals.

Scan size	10.00 μm	Ramp size	550.00 μm
Ramps/lines	64	FV Speed	40.00 $\mu m/s$
Trigger Threshold	12.00 nN	Velocity	6.87 $\mu m/s$

To capture a representative area of the crystals pre- and post-cleaning, FV scans were carried out on three random sites across the surface. Data were processed using NanoScope Analysis 1.8, where each height scan was flattened using a first-order polynomial fit to remove the tilt of the sample. Adhesion data was exported and plotted using a bespoke script developed in Python 3.6[129], utilising libraries such as pandas[130], matplotlib[131], and seaborn[132].

5.3 Results - Crystal Cleaning

To determine the best cleaning regime for paracetamol crystals, a systematic study has been undertaken. Initially, four different methods were tested using EtOH as a solvent. The least surface damaging method was selected and tested with several solvents both, saturated and unsaturated. Adhesion and height scans were recorded for all crystals pre and post-cleaning. The least damaging and most effective cleaning regime was subsequently investigated using NAP-XPS in order to ascertain any changes in surface chemistry resulting from the cleaning. Furthermore, the surface-sensitive measurements were used to check whether residual solvent resided on the surface.

5.3.1 Method Screening

Optical microscopy images of paracetamol surfaces are tabulated in Table 5.4, showing the surface pre- and post-cleaning. Pre-cleaned facets exhibit a variety of surface defects and contaminants. Changes in surface topography across cleaning regimes were due to different crystals being used for each protocol; thus, pre-cleaned samples were "as received" in each case.
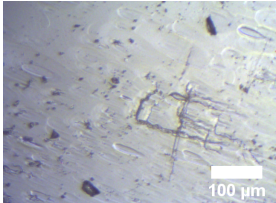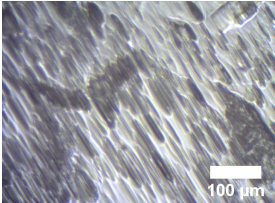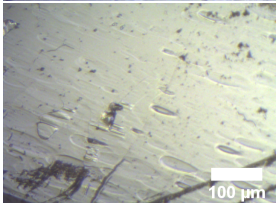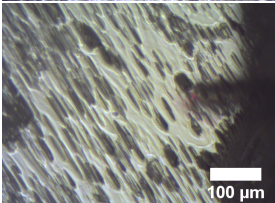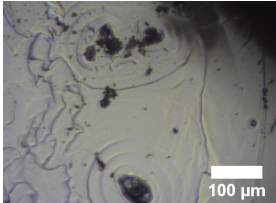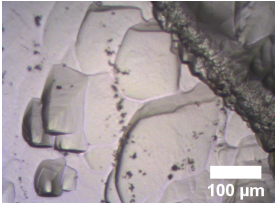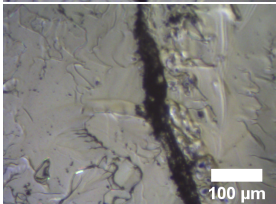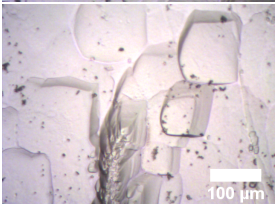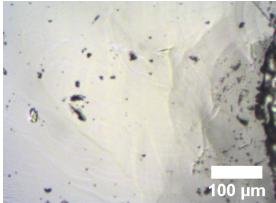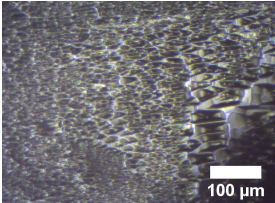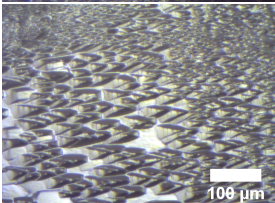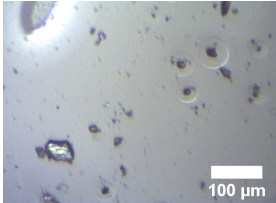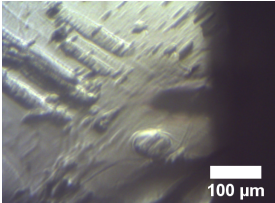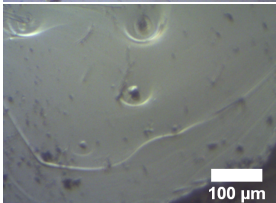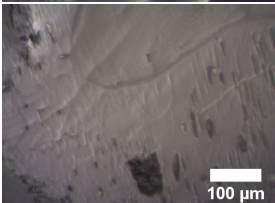
Compressing or rolling the lens tissue across the surface caused the most substantial topographical damage, where the surface was not only dissolved but irreversibly changed. These changes can be seen in the optical images and are of the 50-100 μm length scale.

Whilst the jet of solvent did not cause surface damage on the same length scale to the aforementioned methods, upon closer inspection of the optical images, it becomes apparent that the crystal surface had sustained a large amount of damage on the smaller scale, resulting in a "fuzzy" - as such, increasing the overall roughness of the surface.

Therefore, based on simply the high degree of roughening of the surfaces across multiple length scales, the three methods (compression, rolling and jet) were deemed inadequate for the principle mechanical action of cleaning regime.

In contrast, wiping the crystal surface caused the least amount of topographical damage. Evidence of dissolution and crystallisation can be seen in the optical images on the post-cleaned surface. However, no obvious damage has been caused to the surface, leading to increased roughness. Therefore the solvent screening was carried out using the wiping methodology.

Table 5.4: Optical microscope images of paracetamol surfaces cleaned with ethanol and four different methods.

Method	Pre-cleaning	Post Cleaning
Compression		
Wipe		
Roll		
Jet		

5.3.2 Solvent Screening

With the selected cleaning methodology, four solvents were screened for compatibility. The aim was to reduce the amount of surface debris and maintain the original surface topography without changing the uniformity of the surface.

5.3.2.1 Optical Images

All optical images are tabulated in Table 5.5, showing the crystal surfaces pre- and post-cleaning with the different solvents, ethanol (EtOH), methanol (MeOH), ultrapure water, and dichloromethane (DCM). The solvents tested were both unsaturated and saturated with paracetamol.

Unsaturated Solvents

The most aggressive solvents, in terms of surface dissolution, were EtOH and MeOH, showing changes in surface topography. This is to be expected as paracetamol is very soluble in both solvents, particularly MeOH. However, using water (also a polar solvent) caused smaller scale roughening indicating a reduced dissolution. DCM showed to cause no change to the facet topography, thus suggesting it is a suitable solvent.

Observed surface dissolutions correlated with the solubility data in Table 5.1, where paracetamol is most soluble in MeOH and EtOH followed by water and finally DCM.

Saturated Solvents

Saturated solvents were used in order to reduce the dissolution of the surface. Due to paracetamol's low solubility in DCM, no data was collected with saturated DCM.

Even with the use of saturated solvents, EtOH and MeOH exhibited a high degree of surface roughening, deeming these solvents unsatisfactory to remove contaminants and debris from the surface. While the saturated solvents were left to equilibrate for 48 hours, the presence of surface dissolutions indicates the solvents were not fully saturated.

However, saturated water did show significantly less topographical changes. As such, both DCM and saturated water were considered as viable solvent candidates. While the surfaces were not adequately cleaned, as some surface debris could still be visible, the use of DCM in particular drastically reduced the optically visible surface contamination.

Table 5.5: Optical microscope images of paracetamol surfaces cleaned with different solvents both un-saturated and saturated using the wipe method

Solvent	Un-Saturated		Saturated	
	Pre-cleaning	Post Cleaning	Pre-Cleaning	Post-Cleaning
Ethanol				
Methanol				
Water				
DCM				

(a) Methanol
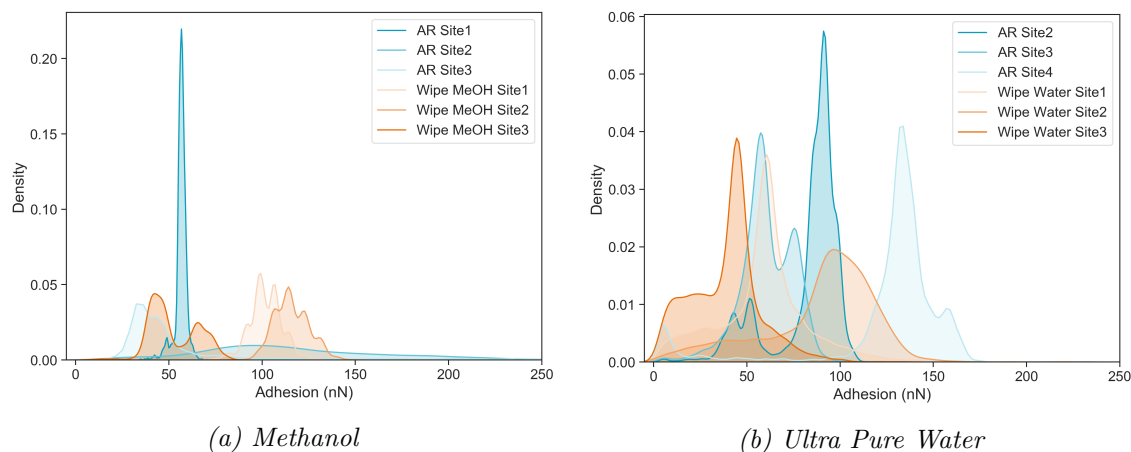
(b) Ultra Pure Water

Figure 5.3: Adhesion distributions of paracetamol samples pre-cleaning (blue), as received (AR), and post-cleaning(orange) using the wipe method with methanol (a)-MeOH) and ultra pure water (b)-Water). Each distribution represent one site scan (10x10 µm area).

5.3.2.2 Adhesive Properties

Using force volume (FV) scans, it was possible to measure the adhesive properties of the silicon cantilever to the crystal surface. The main points gathered from the FV scans was the change in adhesion distribution. By monitoring the range of distributions from pre- to post-cleaned, it was possible to assess surface uniformity. The justification being that a change towards larger adhesion distributions was caused by the change in surface topography or chemistry. Homogenous surfaces are described by a uniform distribution. Thus any solvent depositions or dissolution would be indicated by a reduction in adhesion uniformity (larger distribution).

Using the optical and height images in conjunction with the adhesion data, it was possible to determine the most effective cleaning solvent.

As an example, Figure 5.3 highlights the effect of cleaning with the use of MeOH and water. In Figure 5.3a the pre-cleaned sample (blue) shows a predominantly uniform distribution; however, once cleaned with MeOH, the adhesion distribution increased across all sites.

In contrast, Figure 5.3b illustrates a starting surface with a broad adhesion distribution (50-160 nN) and post-cleaning with water slightly increased the adhesion distribution to 0-150 nN. Illustrating that the surface was not uniform after cleaning.

Figure 5.4 shows the nanoscale effects of cleaning with saturated water. The height scans illustrate the changes caused to the surface on a smaller length scale to those seen in the optical images. Height differences as significant as 50 nm can be seen on the surface post-cleaning.

The distribution graph shows how the range of adhesion values increased post-cleaning — indicating a non-uniformity, caused by either chemical or topographical

changes. Similarly to the other polar protic solvents, the solvent appeared to dissolve the surface of the organic crystal. Therefore, saturated water was not selected as a viable cleaning solvent.

(a) Pre-Cleaning
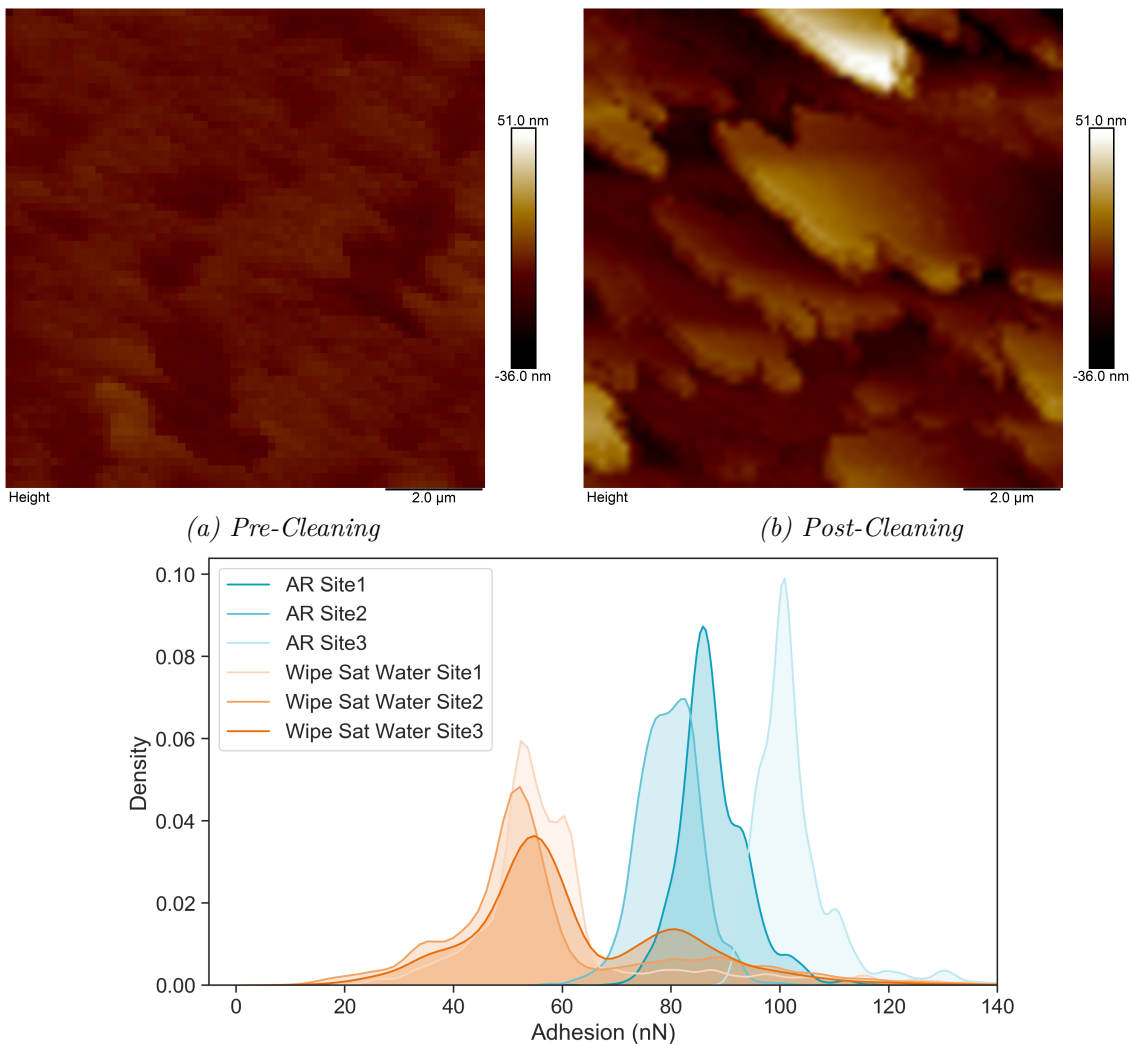
(b) Post-Cleaning

Figure 5.4: Height scans extracted from the FV for surfaces pre-(a) and post-(b) cleaning with saturated ultra pure water. c) Adhesion distribution of all sites scanned across the surfaces.

Finally, the DCM cleaned crystal is shown in Figure 5.5. The initial state of the crystal surface was smooth (small height deviations-2nm), as shown in the pre-cleaning height scan. The preservation of smoothness post-cleaning indicated that DCM was not causing any noticeable surface damage. Within the heightmap, it is possible to identify the crystal terraces.

The low resolution is due to the nature of the scanning parameters and small scale height deviations 2 nm. As the height is recorded during the FV scan, it means that while 4096 force curves were recorded, the image resolution is 64x64 pixels.

Post-cleaning, the height map illustrates that the surface was not damaged and

surface terraces can still be visible.

The uniformity of adhesion forces further evidences the lack of surface damage. The distribution shows that while the overall adhesion values have increased, the range has stayed the same if not reduced in some cases. Suggesting that the surface chemistry might have been altered as the topography has not.

Based on these results, the use of DCM with a wiping methodology has been chosen as the least aggressive method of cleaning paracetamol surfaces. Furthermore, this method was used in conducting NAP-XPS experiments to determine the surface chemistry change post-cleaning.

(a) Pre-Cleaning   *(b) Post-Cleaning*
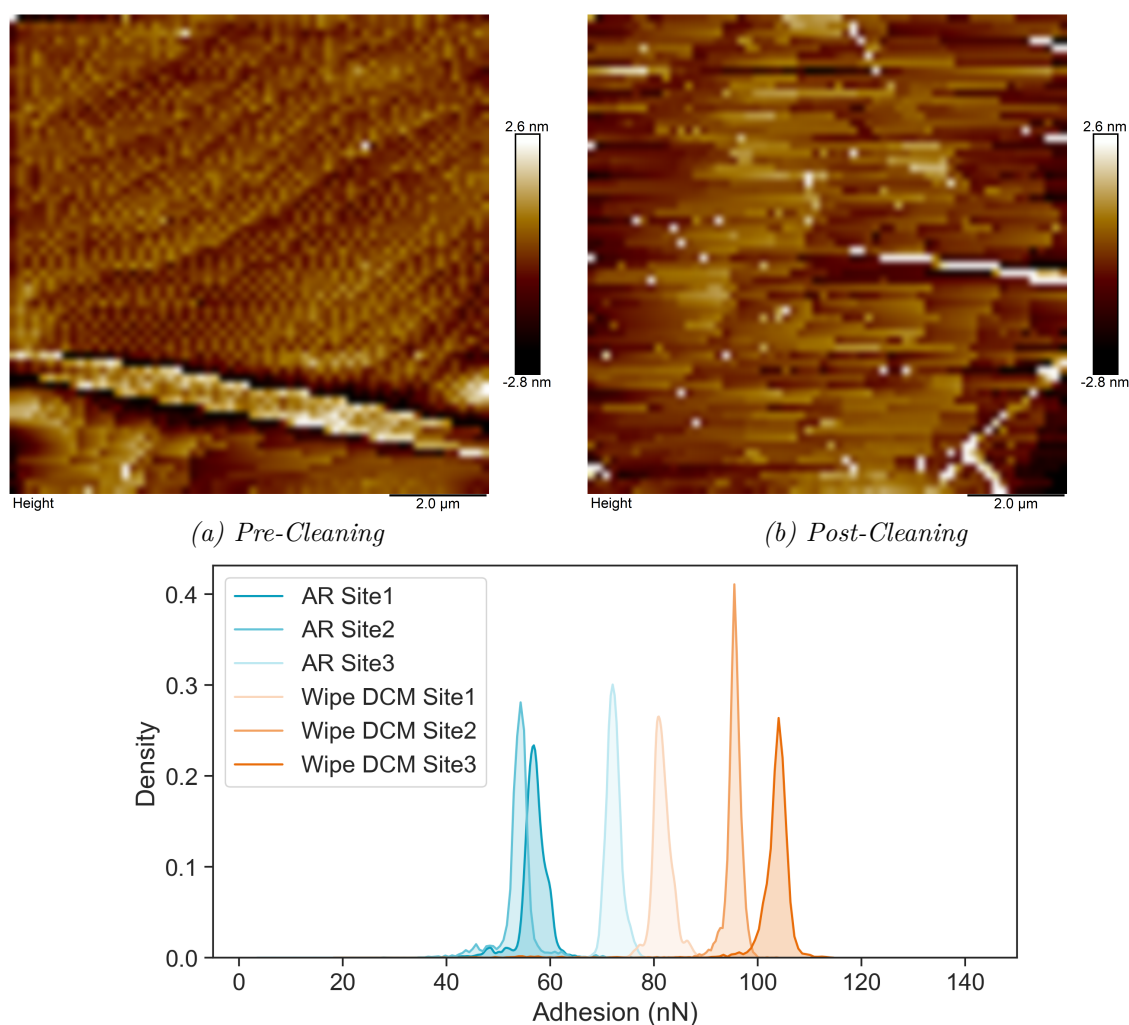
Figure 5.5: Height scans extracted from the FV for surfaces pre-(a) and post-(b) cleaning with DCM. c) Adhesion distribution of all sites scanned across the surfaces.

5.3.3 Surface Chemistry Analysis

Utilising NAP-XPS allows probing of the chemistry of a sample. With the use of variable photon energy sources such as those found at a synchrotron, it was possible to examine the surface chemistry of a specific facet of paracetamol and determine the chemical change when cleaned with DCM. As previously stated, the data was collected in collaboration but processed and analysed by Benjamin Tayler-Barrett (BTB). As such, further details such as survey and high-resolution scans, detailed spectra and other related analysis can be found in BTB's thesis [158]. The purpose of this section is to highlight the findings.

The bulk sensitive measurements (highest surface penetration) taken at 1000eV photon energy are shown in the spectra in Figure 5.6a where there is a clear reduction in carbon signal post-cleaning. The associated reduction was calculated to be 19 % of total carbon content, based on the detailed C1s spectra, it was found that the adventitious carbon was being reduced. Therefore a reduction surface contamination.

Further conformation of the surface being cleaned was found in the surface-sensitive measurement at 550 eV, where the carbon signal was reduced post-cleaning, as seen in Figure 5.6b. However, the reduction of adventitious carbon was calculated to 7 %.

The use of NAP-XPS has shown the surface has been chemically cleaned. Moreover, no Cl peaks were found in the survey spectra, indicating no trace of DCM left on the surface. Although not entirely removing contamination, it is essential to remember that more aggressive cleaning regimes dissolved and re-crystallised the surface, as such a balance must be reached.

(a) Bulk sensitive   *(b) Surface sensitive*
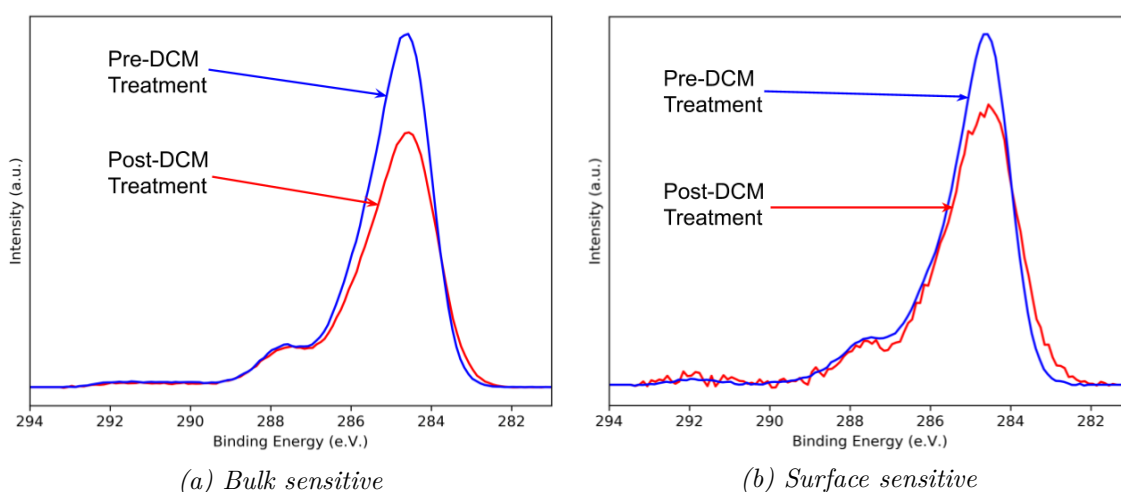
Figure 5.6: C1s orbital spectra for a single paracetamol facet pre-(blue) and post-(red) DCM cleaning. a) Bulk sensitive measurement at 1000 eV photon energy. b) Surface sensitive measurement at 550 eV.

5.4 General Discussion

Initial method screening for mechanical surface cleaning highlighted the effect of pressure and direction on the surface topography from the lens tissue movement. The wiping method was found to cause the least amount of surface roughening. Methods, such as compressing and rolling, caused too many surface defects. Whilst using a pressurised jet of solvents reduced the damage incurred compared to manual cleaning, it highlighted an uneven impact on the surface, thus causing small scale roughening. Optical images were sufficiently detailed to determine the most suitable method.

A note on surface debris. Elimination of large surface contaminants was carried out simply by the use of pressurised nitrogen gas at 2-3 bar. The surface debris mentioned in these discussions is those fixed to the surface that can be seen in the pre-cleaning images and are not dislodged by the pressurised N_2 gas.

The solvent selection was carried out using a range of solvents with varying solubility. DCM was found to be the optimum cleaning solvent. It was expected that the surface of Para would dissolve and re-crystallise under EtOH and MeOH cleaning due to the high solubility of 232.25 g/kg and 371.61 g/kg respectively. However, one would expect once saturated for the dissolving effect to subside and the surface to simply be cleaned. Based on the optical images, the former did not materialise, which is most likely caused by the solvent not being fully saturated regardless of the 48 hours spent under agitation with solute still present.

Saturated water did initially appear to be a viable solvent candidate; however, on closer inspection of the FV scans pre- and post-cleaning, it was apparent that the surface topography was being dissolved. The adhesion data showed a decrease in uniformity, indicating a topographical or chemical change in surface properties. Moreover, water had the lowest volatility from all the chosen solvents, the presence of which was detected through the measured force curves as long range attractive forces during the pull-off phase.

DCM was found to be the most effective cleaning solvent. Optically, it removed debris from the paracetamol surface, while maintaining the original topography. Adhesion data showed little change in the uniformity, with an increased measured force in some sites, suggesting removal of surface contamination. In general, in AFM adhesion studies, clean surfaces have high adhesion (are high energy) and dirty, contaminated surfaces have low adhesion (low energy)- depending on specific probe-surface combinations, such as interactions with a hydrophilic probe with hydrocarbon contamination leads to low adhesion. At the extreme, for example, a clean silicon probe in a UHV vacuum can covalently bonds itself with a Si wafer upon first contact, but not if there is a contaminating lubrication layer. The NAP-

XPS data confirmed contamination removal based on the reduction of adventitious carbon. Due to the high volatility of DCM, no trace of DCM was left on the surface as it rapidly evaporates. Making it an ideal cleaning solvent.

5.5 Conclusions

The focus of this chapter was to identify a suitable cleaning protocol for paracetamol crystals in order to prepare them for surface-surface measurements. DCM was found to be an adequate solvent when used with a mechanical wiping action. Based on macro, nano and angstrom based measurements, the solvent removed contaminants with minimal topographical or chemical damage.

Macro-scale changes were assessed using optical microscopy - showing no damage to the crystal surface. Nano-scale changes were monitored through FV scans comparing pre- and post-cleaning samples, checking for changes in surface structure and uniformity of adhesion. Angstroms scale variations were probed through NAP-XPS by analysing the changes of surface chemistry - showing contaminant removal and no trace of DCM left on the surface.

It was found that DCM did not remove all contaminants, with only a maximum of 19 % of chemical contaminants being removed. However, in the balance of surface preservation, and representative samples, it was found to be the best solvent for cleaning paracetamol crystals.

Based on all presented information, wiping single faceted crystals of paracetamol with lens tissues wetted with DCM has been chosen as the optimum protocol due to a reduction of surface contaminants whilst preserving the surface topography.

CHAPTER 6

Probing Facet-Facet Interactions using Atomic Force Microscopy

"An experiment is a question which science poses to Nature, and a measurement is the recording of Nature's answer. - Max Planck"

This chapter describes the experimental approach for measuring the facet-facet interactions, whilst including a literature review, and general discussions regarding the properties that impact these interactions.
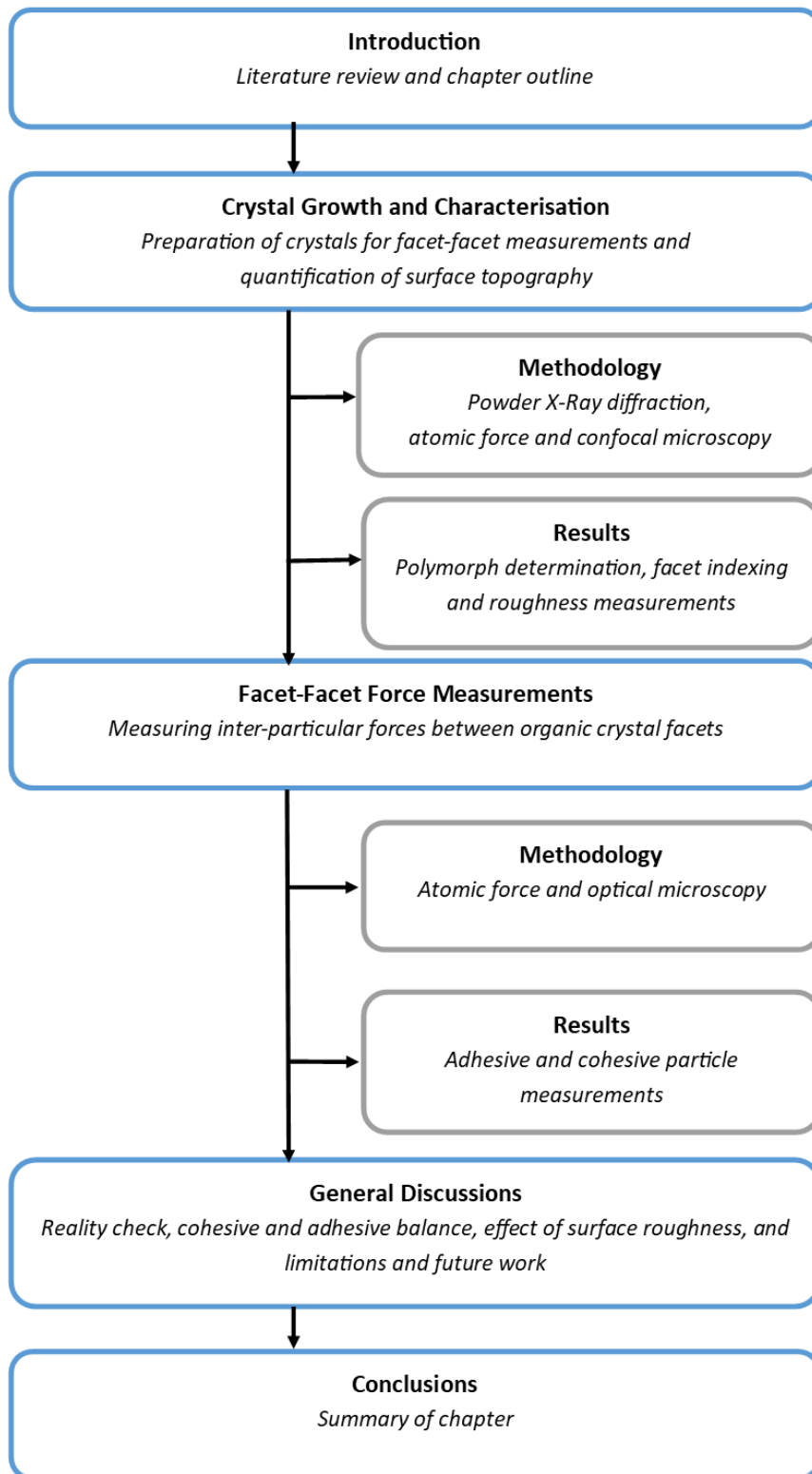
Figure 6.1: Outline of Chapter 6

6.1 Introduction

The former chapters have focused on defining what a crystal surface is (Chapter 2), how it is possible to compute its interactions with other surfaces (Chapter 4), and how to best prepare a representative surface by removing contaminants (Chapter 5). The purpose of the study described in this chapter is to validate the previously presented computational effort and gain further understanding of the facet-facet interactions between faceted organic crystals.

By measuring and quantifying the forces acting between two opposing facets, it is possible to rank preferred interactions and as such, identify facets and systems that have a higher affinity to one another. The adhesive properties between organic crystals have a large impact on product performance, in particular for inhalation drugs, as well as manufacturability of any powder-based pharmaceutical such as tablets. Inhalation drugs rely on the Cohesive/Adhesive Balance (CAB) between the API-Excipient in order to adequately deliver the API to the lungs.Briefly, CAB describes the balance of interactions between like particles (cohesive) and different particles(adhesive), a more detailed explanation of how this is calculated can be found in Section 4.4.2. During the manufacturing process, tablets are initially prepared by mixing before being compressed into their final form, interactions between powders and sticking to tablet presses can cause larger setbacks for the process.

In order to study these particle interactions, careful consideration has been given for geometries involved and representative surfaces that have been probed. As such, atomic force microscopy (AFM) has been chosen as the method of choice for this study. Other alternative methods such as surface force apparatus (SFA) and inverse gas chromatography (IGC) have not been used for reasons which have been previously discussed in Chapter 3.

Surface interactions studies using AFM have been seen throughout many fields, ranging from biological studies[168, 169, 104, 170] monitoring forces of single protein chains interacting with substrates to inorganic materials cohesively interacting[72, 171, 172, 173].

Surface roughness plays a crucial role in the measurement of adhesion forces.
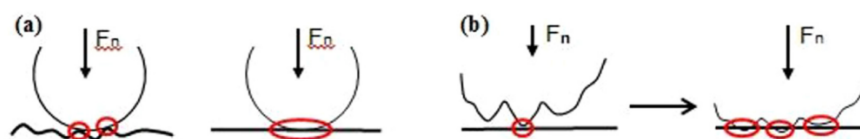
Figure 6.2: A) Increased contact area shown in red where the surface roughness is reduced over flatter samples. B) Effect of deformation on the contact area, showing an increase in area when the force is increased.[167]

Increased surface roughness of particulates leads to a decrease in the contact area between the two bodies, as shown in Figure 6.2 a)[167]. The elastic and plastic deformation of the two materials makes it difficult to accurately determine the contact area due to the change in surface topology during force exertion. Figure 6.2 b) shows how the contact area is increased when the rough surface deforms and the sample is levelled. Sindel and Zimmermann *et al*[174] showed this effect when pressing lactose colloidal probes onto lactose substrates. The impact of surface roughness and surface deformation on the force measurements has been studied by many[96, 175, 126], but has proved difficult to quantify. As such, the surface roughness has been quantified within this study at both the macro and nanoscale in order to account for the impact of surface roughness.
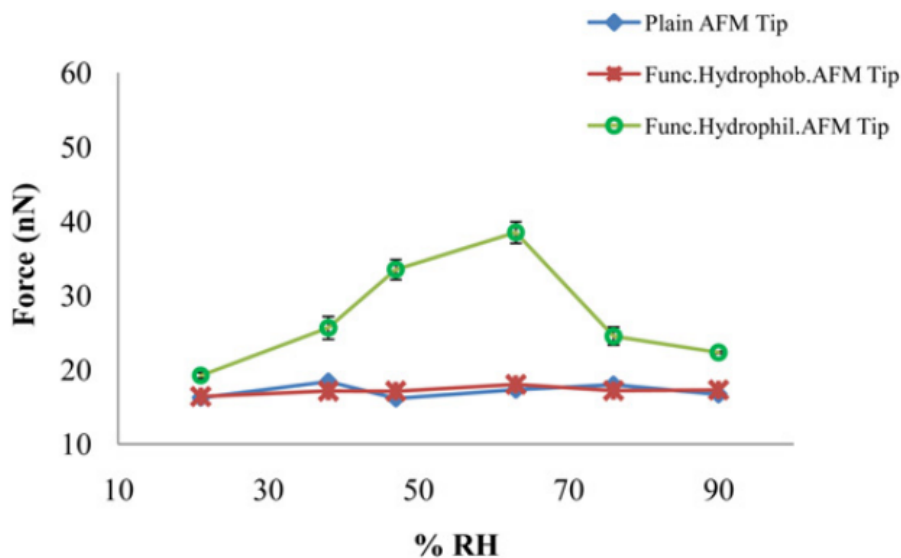
Figure 6.3: Effect of relative humidity on the adhesive force of paracetamol facet with the use of normal(SiO_2 - blue), hydrophobic (red), and hydrophilic (green) AFM probes Source [176]

The contribution of RH in the total of adhesion forces has been explained in Section 2.4.1. A more specific study investigating the impact of RH on paracetamol facets indicated that different crystal facets could exhibit higher adhesion forces based on their surface chemistry [176]. The study also investigated the chemical nature of adhesion based varying % RH; finding very small differences using normal silicon nitride AFM cantilevers, but an increase in adhesive force between 50-60% when probing with a hydrophilic tip as seen in Figure 6.3. This can be explained by the formation of liquid bridges (as described in Section 2.4.1) between surface and probe due to the deposition of water on the surface of paracetamol after 50% RH. As the relative humidity is increased, the hydrophilic properties of the surfaces causes a mono-layer of water to form on the surface.
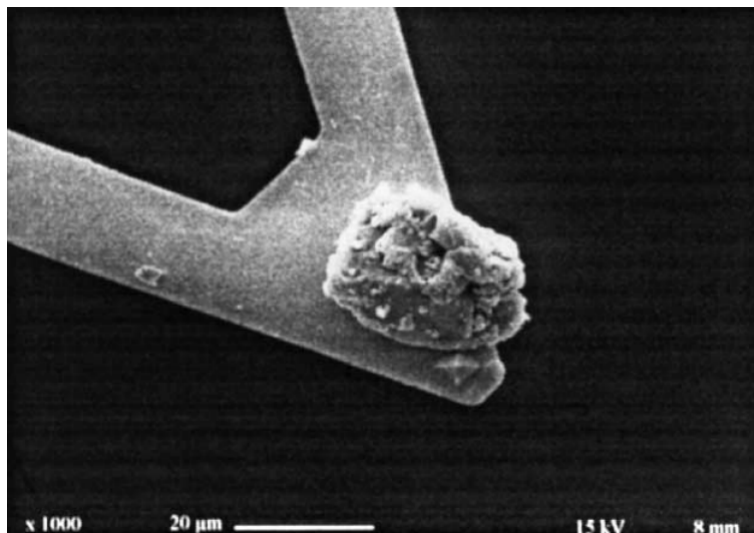
Figure 6.4: SEM image of an AFM cantilever that has been functionalised with a lactose particle Source: [174]

Cohesive-adhesive balance (CAB) studies, which look at the ratio between cohesive (API-API particles) interactions and adhesive (API-EXP particles) interactions have shown the advantages of using the colloidal probe technique. Begat et al [177] carried out force measurements between API particles and flat grown API, and excipient crystals as substrates. The ratio between the two indicated if the system was being dominated by adhesive or cohesive forces. Thus describing the powder behaviour for the given system. CAB ratio is important for formulations as the agglomeration and segregation of powders affects the fluidisation and dispersion properties of powders.

Typically, AFM colloidal studies are carried out by either dispersing micronised powder across a spherical probe, or by attaching a particle to the end of the cantilever as shown in Figure 6.4. It is important to note that the micronised powder results in an average adhesion force measurement due to the random dispersion of the powder. The single particle on the cantilever will yield adhesion information of the specific surface exposed to the substrate. As it is visible from Figure 6.4 the adhered particle has no definitive morphology, and as such, this cannot be correlated to any facet specific surface properties.

Work done by Finot *et al* [172] showed the use of a single gypsum crystal functionalised cantilever proving the feasibility of attaching a single crystal, $< 50\mu m$ size, to a cantilever with facets present, as shown in Figure 6.5. Due to the nature of the material, the group had to account for a lot of charge based interactions as the study was carried out in a solution of calcium sulphate. Forces between facets of gypsum were measured. Whilst these measurements proved the feasibility of such a study. There were a few aspects that were not taken into account that are critical regarding the adhesion force measured. The contact between the two crystals was
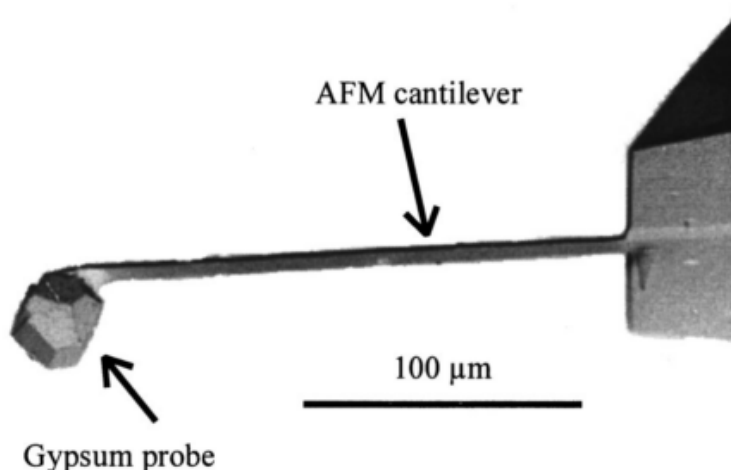
Figure 6.5: Scanning electron micrograph showing a (30 µm) gypsum crystal attached to a linear cantilever.[172]

not discussed, or the area of the probe used. Most commercial AFMs have a cantilever tilt of 7-20° [178] to ensure the tip of the cantilever and the chip of the probe do not touch the sample at the same time. The tilt can impact the measured forces by up to 20 %, as such it is normally taken into account[29].

Direct inter-particulate forces measured via AFM have been compared to those that use indirect methodologies, such as IGC. Jones et al [33] compared the drug product performance of several APIs, and excipients, to the cohesive-adhesive balance calculated by AFM and IGC. No consistent relationship was found between the formulation performance and IGC data. In contrast, the AFM determined CAB ratio correlated with the formulation performance. Jones et al[33] highlight that to expect a linear relationship between adhesion data and drug product performance is overly simplistic due to the complexity of the interactions occurring over the powders. One of these complexities is understanding the individual facets contribution to the particle-particle interactions and how their surface properties can influence these interactions.

This project aims to simply rank the adhesive-cohesive properties of single particles based on their surface chemistry. In order to achieve comparable results, the contact area must be measured, relative humidity be kept within limits, and thus values can be relatively comparable with computational data.

This study focuses on measuring the forces between paracetamol, D-mannitol, and L-glutamic acid single facets, and ranking the systems based on their adhesive forces. These systems have been chosen due to their varying crystal habit and surface chemistry anisotropy. This chapter aims to describe the methodology developed to carry out the force measurements, quantify the surface characteristic of each facet and furthermore describe how the surface properties impact the forces measured.

6.2 Methodology Crystal Growth and Characterisation

In order to carry out facet-facet measurements, small probe crystals and large substrate crystals were required. These were subsequently characterised. In this section two methodologies will be described. Firstly, the characterisation of the crystals used, and their surfaces, followed by the methods for carrying out the facet-facet force measurements.

The materials used were paracetamol (Para) (Sigma-Aldrich, UK), D-mannitol (DMAN), and L-glutamic acid(LGA) (Fisher, UK). Para was grown as both probes and substrate, whereas, DMA and LGA only as substrates. The size requirements for probes was set to $< 100 \mu m$; substrates were grown as large as possible up to 2 cm in length.

In order to grow probe crystals, a cooling method was used. By rapidly cooling the solution, it was possible to grow smaller crystals. Larger, substrate crystals were grown using the same methodology described in Section 5.2.1. Facet indexing of the substrate crystals and polymorph determinations were carried out using powder X-ray diffraction due to the large size of the crystals. Further surface topography characterisation was investigated using atomic force microscopy (AFM) to image the surfaces and measure the roughness. Probe surface area was measured using confocal microscopy.

As the Para probes have been reserved for future experiments, they have been preserved and thus not imaged using any form of damaging measurement such as scanning electron microscopy due to the possible beam damage that can be caused to organic crystals [179].

Optical and confocal microscopy was utilised to gain a macroscopic perspective of the surfaces. Optical images from the AFM were captured using the built-in camera system described in Section 5.2.2.2.

6.2.1 Cooling Growth

Cooling crystallisation was carried out in a 100 ml glass jacketed and inductively heated vessel fitted with an overhead 4-blade pitched impeller. Crystallisation was monitored by the use of turbidity and temperature probes. To 40 ml of absolute ethanol heated to 40 ^0C, 12.43 g of paracetamol was added to reach supersaturation. This mixture was set to the agitation of 300 RPM and heated to 58 ^0C. The solution was held at a constant temperature for 30 minutes to ensure full dissolution. The vessel was then cooled to 18 ^0C over 2 hours. Crystals were harvested and vacuum filtered. Samples were placed in a drying oven at 38 ^0C overnight and then stored

in a desiccator.

6.2.2 Powder X-Ray Diffraction (PXRD)

In order to carry out facet determination, using PXRD, the substrate crystals had to be mounted level with the sample holder in order for the surface of interest to be in the plane of the x-ray beam, and as such, all reflection would be caused by a specific Miller Plane. In order to hold the crystal and allow for easy manipulation, a soft putty-like substance (Rodico) was used, which was then mounted on harder clay and placed on a deep PXRD sample holder. A 6 mm beam slit was used for DMAN and LGA in order to record enough counts, as the substrate crystals were smaller.

To determine polymorphism, unused crystals were manually crushed and placed on a flat sample holder.

Measurements were carried out at ambient temperature using a Bruker D8 diffractometer with a Cu Kα ($\lambda = 1.542$ Å) source. With a 2θ range of $5 - 65^o$ the step size was set to 0.0164^o. Data was analysed and plotted in OriginPro 2019.

6.2.3 Confocal Microscopy

A Zeiss LSM 800 confocal microscope was used in order to acquire 3D representative data of the probe surface to measure the true area that would be required for the facet-facet force normalisation. An EpiPlN Apo 50x/0.95 objective was used in order to scan the sample, and image stacks were captured with 50 nm steps sizes over a range of 32 μm.

Confocal topographical profiles were processed using Gwyddion 2.54. Images were levelled by fitting a plane through three points. Projected and true surface areas were calculated by masking out the regions of the images that did not correspond with the flat surface of the facet before using the statistical quantities module.

6.2.4 Atomic Force Microscopy

The surface topography was measured using a Bruker Fast Scan AFM with MLCT-BIO cantilevers. All measurements were carried out in contact mode. Cantilevers were ozone cleaned prior to being use. The MLTC-BIO-D cantilever was used for imaging due to the low spring constant 0.03 N/m, allowing for probe crystals which were attached to the stiffer cantilevers, to be measured.

The crystal surfaces were imaged in air at ambient conditions. The Para crystals, both probe and substrate, were measured post facet-facet measurements. The DMAN and LGA substrate crystals were measured prior to any force measurements.

Both set of crystals had undergone cleaning regimes. Para substrate crystals were cleaned using the protocol outlined in Chapter 5, whereas the Para probes, and excipient substrates were cleaned using N_2 to remove surface debris.

The cantilever to which the probing crystal was attached, consisted of a high spring constant ($\bar{4}8N/m$). By using a cantilever with lower spring constant, it was possible to image the probe crystal without deflecting the stiffer cantilever and impacting the height measurements. Thus allowing for the surface of the crystal to be imaged post-mounting. The lack of deflection, on the probe cantilever, is due to the large difference in spring constants (48 to $0.03N/m$).

Cantilevers were calibrated by measuring the deflection sensitivity against a sapphire calibration sample followed by thermal tuning to obtain the spring constant.

Data was analysed using Nano Scope Analysis v1.9. The images were flattened using either first or second-order polynomial to remove either tilt or bow in the measurement. Surface roughness analysis was carried out using the roughness module in Nano Scope, which measures an array of surface roughness parameters, where a sample size of 15x15 μm was selected from each image and the full set of roughness descriptors were collected for both the sampled area and the whole image.

The collated data set was analysed using a bespoke python script using the same libraries stated in Section 5.2.2.3.

6.3 Crystal Growth and Characterisation

This section focuses on the prepared crystals of Para, DMAN, and LGA as both probes and substrates. In order to gain reliable information regarding the facet of substrate crystal, PXRD was used to identify the Miller plane of the facet. Using diffraction data over techniques such as goniometric observations eliminates the uncertainty that can be caused by the crystal having different morphologies based on the solvent used. Polymorph determination was carried out using PXRD, giving reliable crystalline information which was then compared to simulated powder diffraction from known crystals structures. Facet determination was only carried out on substrate crystals due to the probing crystals being too small for PXRD.

Previous studies have used the morphology of the crystals and predictive models to determine possible facets; however, due to the large impact of growth conditions on Para, model informed facet determination would not be sufficiently reliable. Three probes have been used in order to gain a range of data, of those facets, their geometries differ drastically enough to suggest different facets are used and thus surface termination.

Surface characterisation was carried out using AFM in order to measure the roughness and image the surface at high resolution. Optical and confocal microscopy was utilised in order to check the surface topography at the microscale and the true surface area.

As the samples form part of future work, no scanning electron microscopy was used due to the beam damage to the samples and thus modifications of surface chemistry and topography.

6.3.1 Polymorph and Facet Determination

The desired polymorphs were grown and confirmed with PXRD: Para Form I, α-LGA, and β-DMAN. These match the polymorphs used in Chapter 4.

Facet determination was partially successful, with the Para and LGA substrates successfully identified. However, due to the growth morphology of the DMAN crystal, a clear determination could not be made.

6.3.1.1 Paracetamol Form I

The substrate crystal used for the force measurements and which was subsequently characterised is shown in Figure 6.6. Due to the prismatic nature of Para, unique facets were studied from the same crystal particle which reduced effects caused by growth batches and identified changes only present due to surface termination.

The acquired powder patterns are shown in Figure 6.7 (depicted as solid lines),
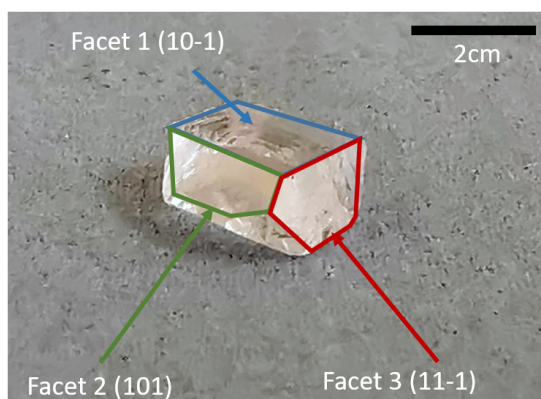
Figure 6.6: Paracetamol Form I substrate crystal with the three facets of interests.
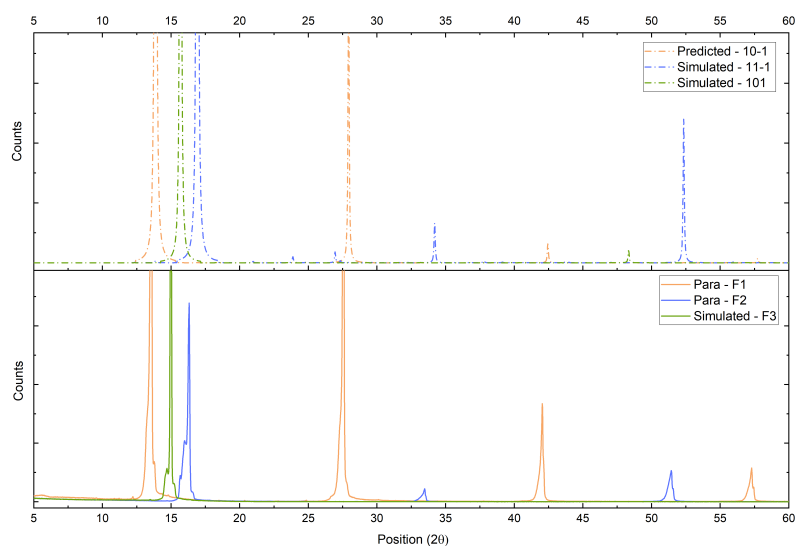
Figure 6.7: Paracetamol powder diffraction pattern (solid lines) for the three individually studied facets and their simulated (dashed lines) counter parts

along side the simulated powder patterns (dashed lines) from a predetermined single crystal (CSD Ref: HXACAN28)[113].

Facet 1 was identified as $10\bar{1}$ as there is alignment between all four peaks (13, 27, 42, and 57 2θ) and the simulated powder pattern for $10\bar{1}$. The two data sets are offset by ≈ 0.5 2θ, which can be associated with the temperature differences at which the crystals were measured. A higher temperature causes the lattice to expand due to the increase in vibration; thus differences in temperatures can cause discrepancies in peak positions. The powder pattern was measured at ambient (298 K) whereas the published single crystal data used for simulating the pattern was measured at 80 K [113].

Facets 2 and 3 were identified as 101 and $11\bar{1}$, respectively in a similar manner. However, the peak shifts were greater for the $11\bar{1}$ and some smaller peaks did not match the simulate patterns for both 101 and $10\bar{1}$. However, it is important to note that these crystals were manually mounted parallel in putty, as such a perfectly flat

facet would only be indexed with the use of a goniometric stage.

Due to the correct identification of the three facets related to form I, it was confidently assumed that the substrate crystal was the stable Para form I.

The polymorphism of the probe Para crystals was determined using a sample of the original powder form which the probe crystals were mounted. Figure 6.8 confirms the probing crystals to be Para form I with a good agreement to the simulated powder diffraction. As seen previously, some peak offset does exist due to the difference at which the measurements were made. Differences in peak ratios exist due to preferential orientation in the powder bulk as the crystals were not micronised.
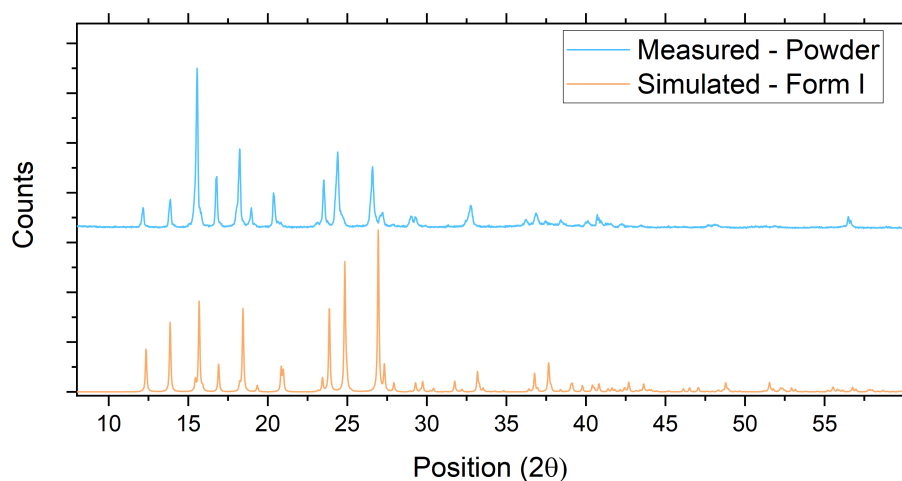
Figure 6.8: Powder pattern for Paracetamol probe crystals (blue - measured) compared to the simulated powder pattern for Paracetamol Form I (orange)

6.3.1.2   L-Glutamic Acid

From the batch of LGA grown crystals, two were used for analysis. The LGA substrate crystal was measured at $\approx 1mm$ in length, and only one facet was used for force-force measurements with the Para probes. The secondary LGA crystals from the same batch were crushed in order to determine the polymorphism of the batch. Due to the stark difference between the α - prismatic and β- needle, it was clear that the α form was crystallised.

The blue trace in the bottom of Figure 6.9 confirms the substrate crystal to be the α form by batch association. Due to the small sample size, the powder pattern has a high noise to signal ratio, but the main peaks are visible and are in good agreement with those predicted using a pre-determined crystal structure of α - LGA (CSD Ref: LGLUAC03 [115]).

The powder pattern from the single substrate crystals shows the facet parallel to the sample holder to be the [111] facet of α-LGA as seen by the matching orange

traces of Figure 6.9. Both peaks at $\approx$ 18 and 36 2θ from the simulation, of the preferred [111] orientation, are found in the measured pattern, with the latter peak being significantly smaller.
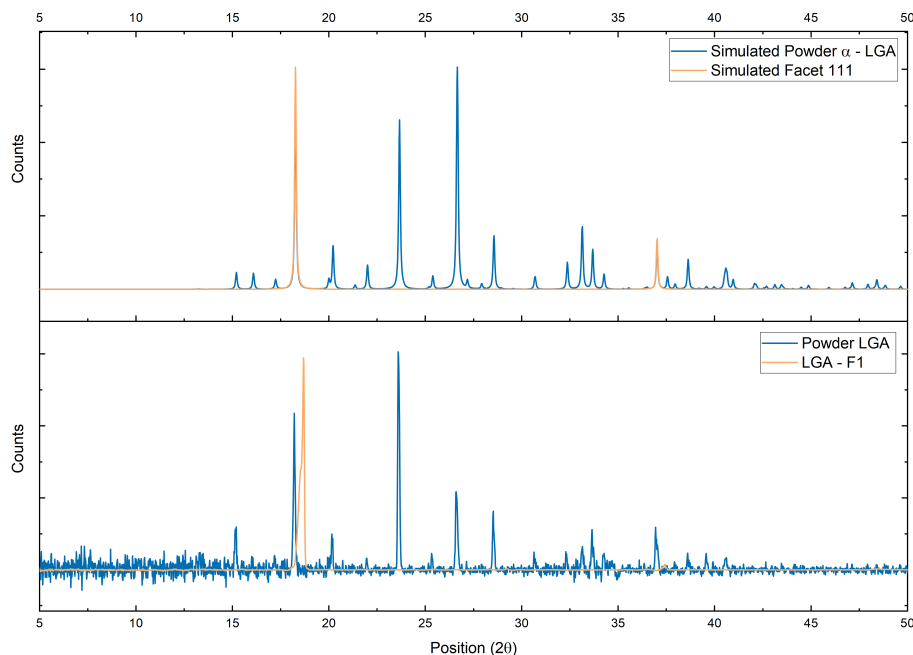
Figure 6.9: Simulated and measured powder patterns for α-LGA powder and LGA facet 111. Top) Blue line shows the powder pattern from LGLUAC03 [115] crystal structure whilst the orange line shows the prefered orientation of facet [111]. Bottom) Measured PXRD pattern of a single crushed crystal (blue) of LGA and the LGA substrate with one facet (orange) parallel to the sample holder surface.

6.3.1.3 D-Mannitol

Polymorph and facet determination of D-mannitol(DMAN) proved to be more challenging due to the size and shape of the substrate crystals. Similarly to LGA, a crystal grown from the same batch was crushed in order to determine the polymorphism.

The desired β-DMAN has a blade-like morphology which is similar to a wider three-dimensional needle. The substrate crystal grown was measured with an approximate length of 1 mm and width of 0.5 mm. Manually orienting such a small crystal in order to align the desired facet parallel with the sample holder was challenging, and the final determined facet is inconclusive.

Comparing the powder patterns, the measured (bottom-blue) and simulated (top-green) in Figure 6.10, majority of the peaks match with those for the β form. However, towards the higher 2θ positions, the overlap between the two is reduced due to an increase in peak shift. It is possible that two facets are being measured simultaneously, or the sample is angled at an edge, thus giving a mixture of preferred orientations and thus facets, which will be discussed in future sections. For

example, the orange peak at $\approx$ 11.42 2θ can be associated with either the (020) or (110). However, it is more probable that it is the (110) as the higher-order peaks appear but are greatly shifted.
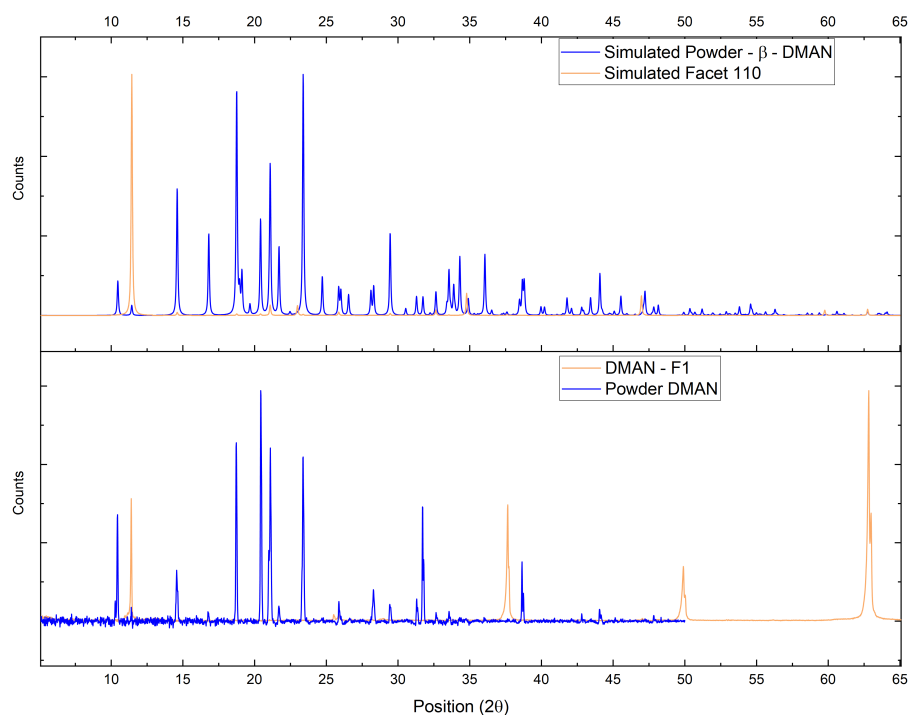
Figure 6.10: Simulated and measured powder patterns for β-DMAN powder and a possible single facet of 110-DMAN. Top) Blue line shows the powder pattern from DMANTL07 [114] crystal structure whilst the orange line shows the prefered orientation of facet (110). Bottom) Measured PXRD pattern of a single crushed crystal (blue) of DMAN and the DMAN substrate with a facet (orange) parallel to the sample holder surface.

In conclusion, the DMAN substrate crystal is the β polymorph, but there is very little confidence to state which probing facet. However, analysing the surface of the crystals does yield an explanation as to why it appears to be multiple facets.

6.3.2 Surface Characterisation

This section will focus on the surface characterisation of the Para probes (P_1, P_2, and P_3), Para substrate with the three individual facets ($F_{10\bar{1}}$,F_{101} and $F_{11\bar{1}}$), and the excipient substrates (DMAN and LGA). The surfaces of these crystals have been imaged using optical, confocal and atomic force microscopy in order to ascertain the surface roughness at different length scales.

Confocal images were taken of the probe crystals to determine their true surface area and thus accurately calculate the force per surface area. AFM measurements were taken of all crystals in order to measure their roughness at different length scales. Optical images were initially used to determine if the sample was flat and free of debris before force measurements were taken.

6.3.2.1 Probes

Whilst the probing facets used could not be determined using PXRD, and it is clear from their shapes that they are different facets. Understanding what the surface looks like at different length scales can offer an insight into what might cause changes in forces.

P_1 was the largest probe crystal. Figure 6.11 shows the large facet missing one edge of the main facet. In Figures 6.11a and 6.11c it is possible to see that the surface is relatively flat at the micron scale. Even in the deepest part of the surface, the depth of the surface does not exceed 400nm as further supported by the AFM images in Figures 6.11b and 6.11d.

(a) 3D Confocal

(b) 3D AFM

(c) Confocal Height

(d) AFM Deflection Error
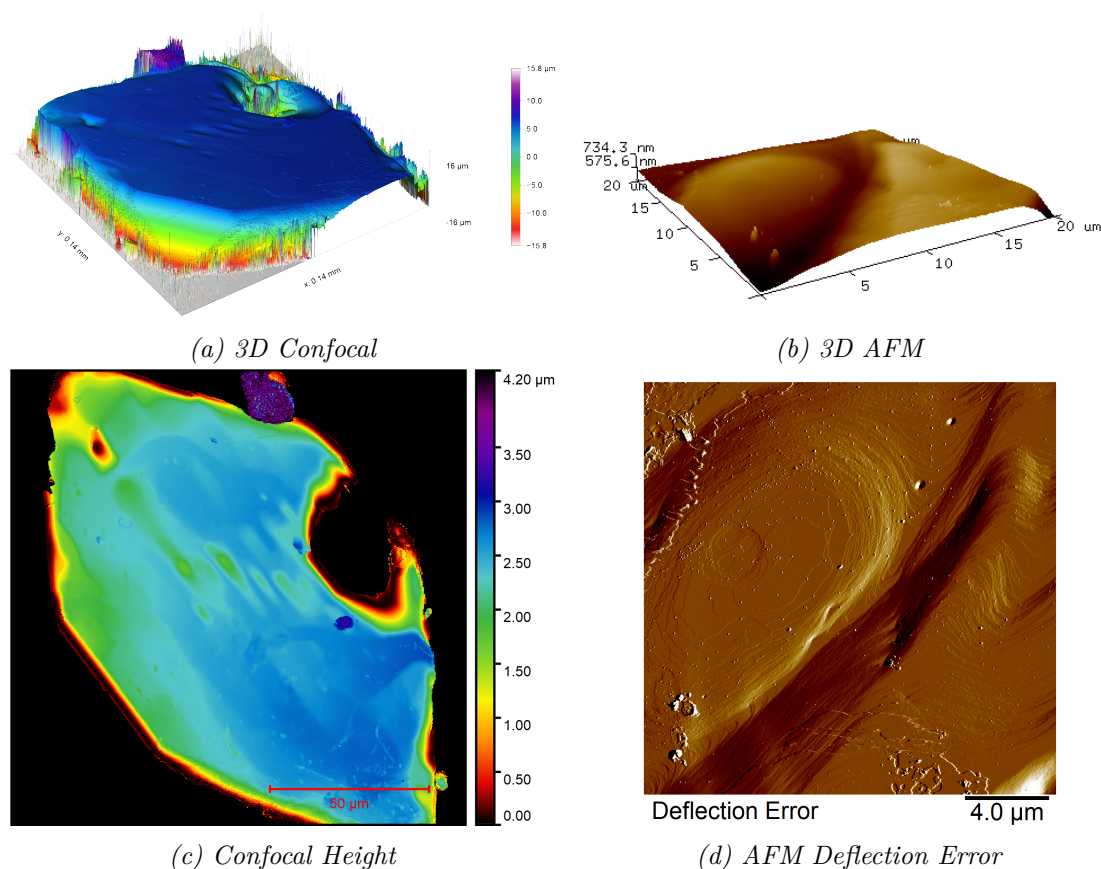
Figure 6.11: Surface images of P_1 probe.a) 3D projection of confocal measured image. b) 3D projection of AFM height measurement. c) False coloured image of the P_1 surface showing the flatness of the sample. d) AFM deflection error showing the smaller length scale features.

The deflection error shows the cantilever movement on the surface once contact has been made, as detailed in Section 3.2.2. In brief, once the cantilever makes contact with the surface it starts to bend as the force is being applied, this causes the deflection of the cantilever and triggers the feedback look between the piezo and cantilever. Thus measuring the error informs us of the texture of the surface and thus yields an image that allows us to assess the roughness of a surface. Displaying

this with the 3D height map in Figure 6.11b allows for an appreciation of the surface roughness both on the large high features and smaller deviations which would not be clear in the 3D height map alone. The z-range resolution of these measurements are in the *pm* range.

The AFM images show the terraces of the crystals with very few surface defects present. Small spherical asperities can be seen covering the surface. However, their height is measured at $\approx$ 12 nm, thus having a reduced impact on the facet-facet force measurements. Figure 6.11c shows two larger objects on the surface with a measured maximum height of 1 μm.

The surface geometry of P_2 was found to be more challenging to measure. As one of the smallest probing facets, a smaller area is available for face-facet contact. The purple region seen in Figure 6.12a was the region used for carrying out the force measurements. The tilt in the confocal images is associated with the AFM chip holder not being flat when mounted on the confocal microscope.

Figure 6.12 shows a relatively flat surface with surface defects being present. The left edge of the facet appears to have raised parts which could interfere with the total accessible contact area for the P_2 probe. However, evaluating the AFM

(a) 3D Confocal

(b) 3D AFM

(c) Confocal Height

(d) AFM Deflection Error
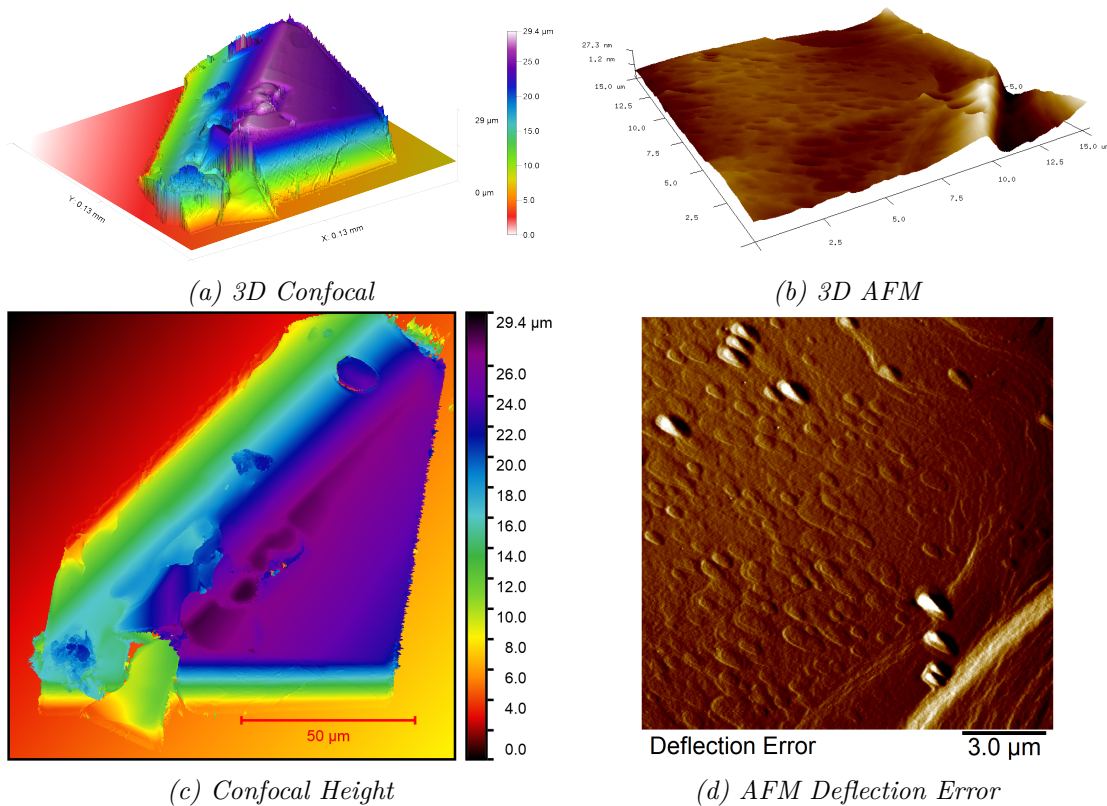
Figure 6.12: Surface images of P_2 probe.a) 3D projection of confocal measured image showing the tilt of the sample. b) 3D projection of AFM height measurement. c) False coloured image of the P_2 surface showing the flatness of the sample. d) AFM deflection error showing the smaller length scale features.

images it is clear the surface is not smooth at smaller length scale with only a couple of terraces visible. The highest asperities are still recorded at $\approx 14nm$.

The asperities seen in the deflection error plot are caused by the cantilever tip not being able to trace across the asperity surface caused the tip geometry and asperity. Regions of that appear to be protruding are in fact valleys with an average depth of ≈ 4 nm thus increasing the small scale surface roughness.

The final probe, P_3, appears to have the smoothest surface on both macro and nanoscale. Figure 6.13a shows the lack of large features protruding from the surface. Figure 6.13b shows the AFM height measurement in 3D, illustrating the lack of features at the nanometer length scale. This is further supported by Figure 6.13d showing a distinct lack of surface debris and asperities. Surface valleys do appear quite prominently, with an average depth ≈ 16 nm.

Based on the previously described confocal and AFM images, the surface roughness was calculated for two length scales. A sample of three separate sites was used for each probe to ensure a representative area was covered. Confocal images offered a macro scale descriptor of roughness and an accurate measurement of the true surface area of the probes. AFM based surface roughness identified nanoscale

(a) 3D Confocal

(b) 3D AFM

(c) Confocal Height

(d) AFM Deflection Error
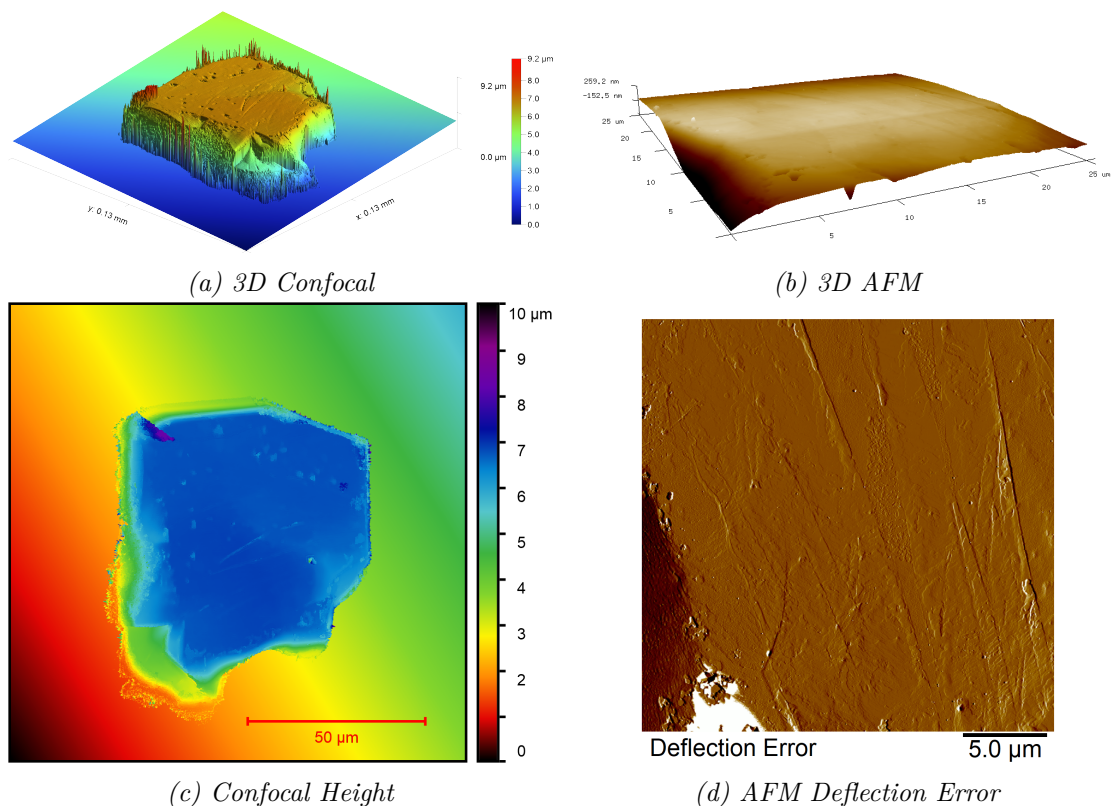
Figure 6.13: Surface images of P_3 probe.a) 3D projection of confocal measured image. b) 3D projection of AFM height measurement. c) False coloured image of the P_3 surface showing the flatness of the sample. d) AFM deflection error showing the smaller length scale features.

Table 6.1: Surface roughness parameters of paracetamol probes. Average values are determined from multiple AFM scans and thus represent nano scale measurements.

Probe	Projected Facet Area μm^2	True Facet Area μm^2	Facet Rugosity	Facet Rq nm	Average Rugosity	Average Rq nm
P_1	10424	10620	1.018	310	1.015	23
P_2	3524	4780	1.356	1145	1.016	45
P_3	3839	4118	1.073	253	1.002	15

differences which would impact the final adhesion force.

Table 6.1 shows the macro-scale measurements, carried out via confocal, as facet descriptors, whereas the nano-scale surface roughness descriptors are identified as averages due to the multiple samples taken to calculate them. Rugosity is defined as the ratio between the true area and projected area, thus accounting for the three-dimensional aspect of the roughness.

Correlating the surface roughness data with the images previously described it possible to conclude that the order of facet area is $P_1 > P_3 > P_2$. Whilst P_2 appears to be as large as P_1 in the confocal images, only the purple section of the facet in Figure 6.12c is available for probing as such resulting in a smaller surface area.

P_2 appears to have the highest macro-scale roughness with a facet rugosity of 1.356 and Rq of 1145 nm, which is further confirmed by the confocal images showing large features on the surface. However, when comparing the nano-scale roughness from the AFM data, the average rugosity between P_1 and P_2 are 1.015 and 1.016 respectively, but their Rq 23 nm and 45 nm. This suggests that on average they have a similar roughness, but P_2 has taller asperities.

Comparing P_1 and P_3 it is possible to see from both the images and nano-scale surface roughness data that P_3 is smoother at the smaller scale. However, multiple macro-scale features make it rougher at a larger scale.

It is expected that the macro-scale roughness would have a greater reduction of adhesive force between the two layers as less of the area would be in contact due to the asperities, as previously mentioned in other studies[180, 181].

6.3.2.2   Substrates

Substrate facets were characterised by AFM as the region of interest was very small due to constrained surface accessibility caused by the geometry of crystal and cantilever (as the substrate was angled towards the cantilever see Figure 6.18). Similarly to the probes, three samples were taken from each facet in a similar region to where the facet-facet force measurements were taken. Para substrate facets were characterised after face-facet measurements, whereas as LGA and DMAN were characterised prior.

(a) $F_{10\bar{1}}$ *3D projected height map*

(b) $F_{10\bar{1}}$ *deflection error*

(c) F_{101} *3D projected height map*

(d) F_{101} *deflection error*

(e) $F_{11\bar{1}}$ *3D projected height map*

(f) $F_{11\bar{1}}$ *deflection error*
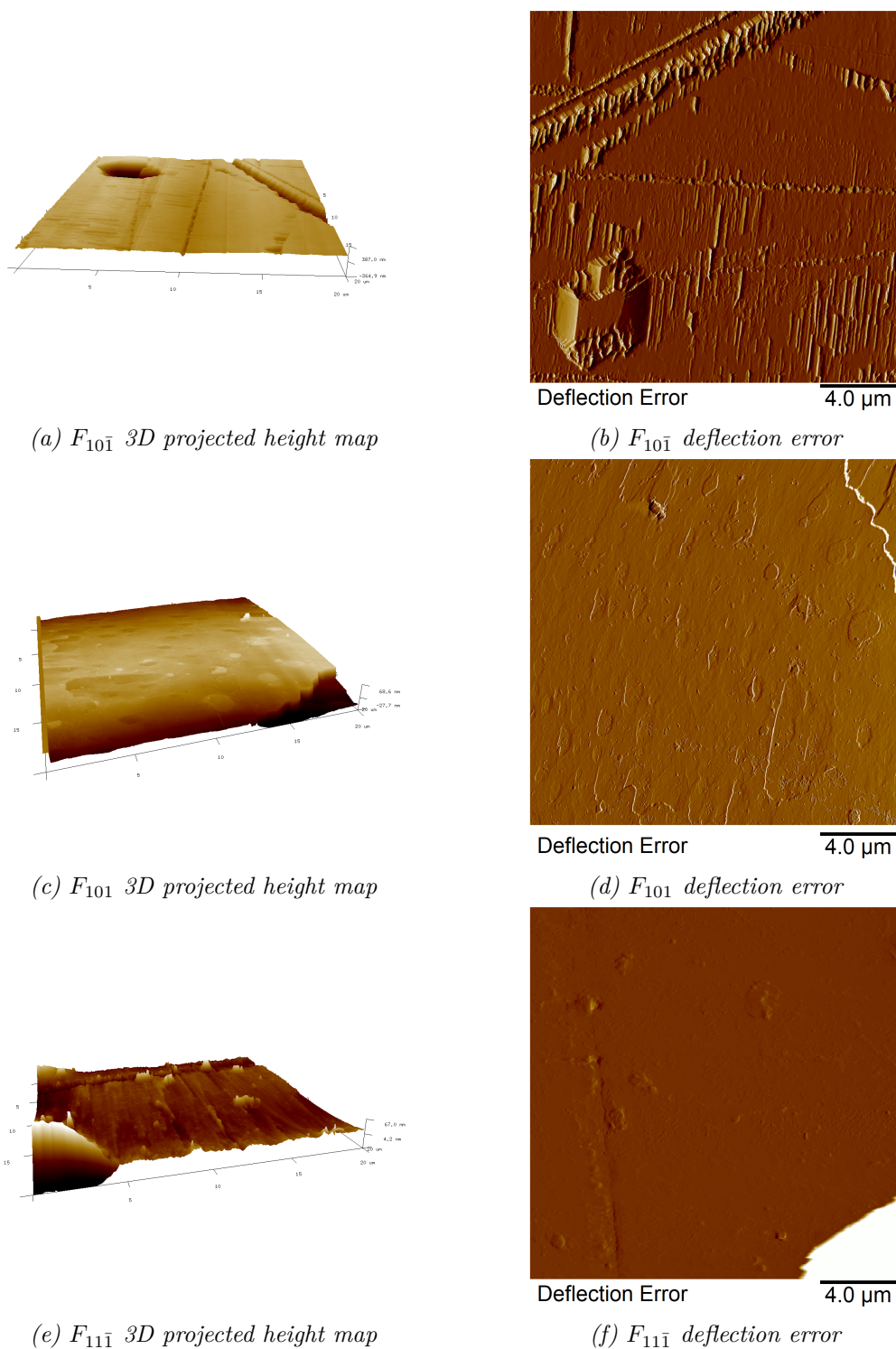
Figure 6.14: Example images from AFM scans of the paracetamol substrate facets $F_{10\bar{1}}$,F_{101} and $F_{11\bar{1}}$. 3D projected height map illustrate roughness of the facet overall surface geometry. Deflection error plots are used to show the surface features to support the evidence of surface roughness.

Figure 6.14 shows representative scans from each of the three Para facets. The 3D projected height maps illustrate the height of peaks and valleys in the surface, i.e. presence of scratches or asperities, while the deflection error provides texture

information to understand the overall topography.
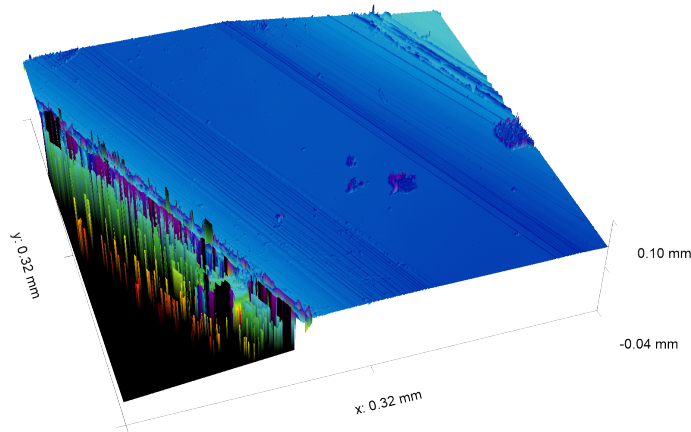
(a) 3D projected confocal image of DMAN facet
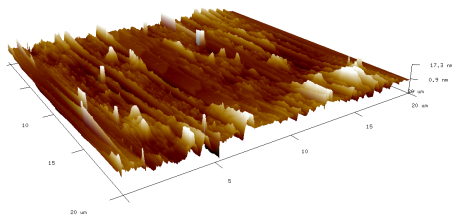
(b) DMAN 3D projected height map
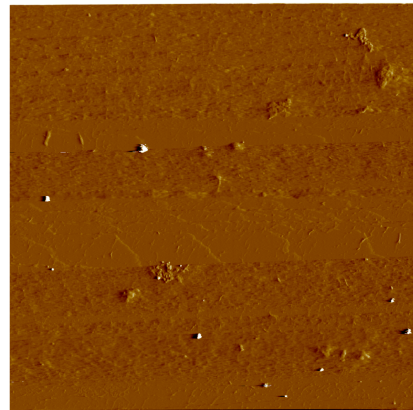
(c) DMAN deflection error
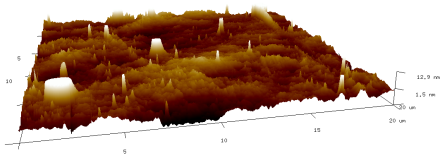
(d) LGA 3D projected height map
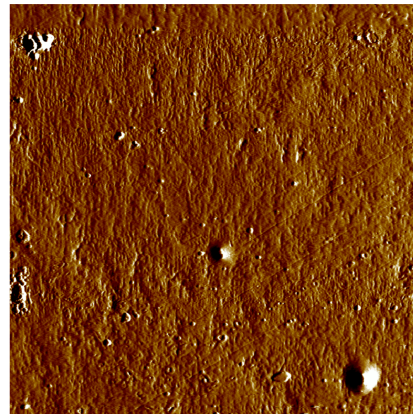
(e) LGA deflection error

Figure 6.15: Example images from AFM scans of the DMAN and LGA substrate facets. 3D projected height map illustrate roughness of the facet overall surface geometry. Deflection error plots are used to show the surface features to support the evidence of surface roughness. a) 3D projected image from confocal microscope showing the gowth of the DMAN facet at larger scale, b,d) Show a the smoothness of the surface with only 10nm deviation of the whole data range.

Facet $F_{10\bar{1}}$ is shown to be the facet with the largest surface roughness. From the

3D height map in Figure 6.14a, it is possible to identify large linear scratches with a depth of $\approx 450 nm$ and smaller scratches with a depth of $\approx 80 nm$. These are more visible in the deflection error scan (Figure 6.14b)showing the surface to have small scratches but a lack of asperities.

Facets F_{101} and $F_{11\bar{1}}$ share similar smooth topographies with $F_{11\bar{1}}$ having fewer pits that appear to be more shallow. Neither of these surfaces suffers from surface scratches, indicating that those on $F_{10\bar{1}}$ could have been introduced after harvesting and not during growth, this could have been caused when the crystals were transported between indexing and mounting.

During the AFM surface characterisation of the excipient substrates, it became apparent the DMAN facet had an interesting topography as a very small section of the facet appeared to be in focus on the optical images. As such, the sample was scanned with a confocal microscope to gain a better overview. Figure 6.15a shows the topography to be of one main smooth facet with larger asperities and diverging stacked facet edges towards the edges resulting in the middle of the sample being the only viable measurement site.

AFM scans were taken at several sites, including the boundaries between the large smooth section of DMAN and the edges. Figure 6.15b and 6.15c show the surface to be relatively smooth with a few asperities across the surface. Regions of increased roughness can be seen in Figure 6.15b, however, it is worth noting the Z-scale bar being very small and thus describing small deviations in height.

Similarly, LGA (Figure 6.15d and 6.15e) appears to be relatively smooth with a few asperities protruding from the surface.

Table 6.2: Surface roughness parameters of the substrates used for facet-facet measurements.

Substrate	Average Rugosity	Rq nm
$F_{10\bar{1}}$	1.098	101
F_{101}	1.024	10
$F_{11\bar{1}}$	1.007	13
DMAN	1.002	5
LGA	1.002	5

Quantifying the surface roughness of these substrates confirms the qualitative analysis. From the Para substrate, the roughness (based on rugosity), are ranked as follows: $F_{10\bar{1}} > F_{101} > F_{11\bar{1}}$. The difference between $F_{10\bar{1}}$ and $F_{11\bar{1}}$ is significant with 1.098 and 1.007 respectively.

However, the Rq identifies F_{101} as the smoothest facet. This is caused by the difference in how the surface roughness is characterised. Rq is the root mean squared deviations which in essence describes the deviation of each height point from the

mean plane of a 2D line profile. On the other hand, the rugosity is sensitive to the frequency of the peaks and pits as well as the height. As it was apparent in Figures 6.14d and 6.14f, facet F_{101} appeared to have more pits thus resulting in a higher rugosity, however $F_{11\bar{1}}$ showed deeper pits and thus higher Rq.

Interestingly DMAN and LGA appear to have the same surface roughness with an average rugosity of 1.002 and a small difference in Rq between 5 nm and 5 nm, respectively. As both surfaces appeared to have smooth surfaces with a lack of pits or scratches, only a few surface asperities were apparent. As expected, LGA has a higher Rq due to the larger asperities visible in Figure 6.15e.

The cause of this similar roughness is not clear. It is worth noting that the excipients did not undergo the same cleaning regime as the Para substrate. As DMAN and LGA were only cleaned with compressed N_2, it could be that they were not damaged by any cleaning regime. Understanding the impact of cleaning on the excipient particles would require a similar cleaning study to the one conducted for Para in Chapter 5.

These surface characterisations could be improved by measuring the surface roughness before and after facet-facet measurements, showing the effect of carrying out the force measurements on both the probe and substrate.

All tabulated values for the characterisation of probe and substrate facets were used in the normalisation of the facet-facet forces.

6.4 Methodology Facet-Facet Measurements

Within this methodology section, a description will be given of how the crystals were mounted to the cantilever and how the AFM was set up in order to achieve plane-plane force measurements.

Crystal probes were made using small Para crystals, whilst the substrates were Para, LGA and DMAN large ($> 1mm$) single crystals.

In order to carry out the crystal mounting and force measurements, a side-mounted camera was installed onto the Multimode 8 AFM. Figure 6.16 shows the two 10x objectives aligned onto the AFM sample chamber. Both objectives were set up to image reflected light.
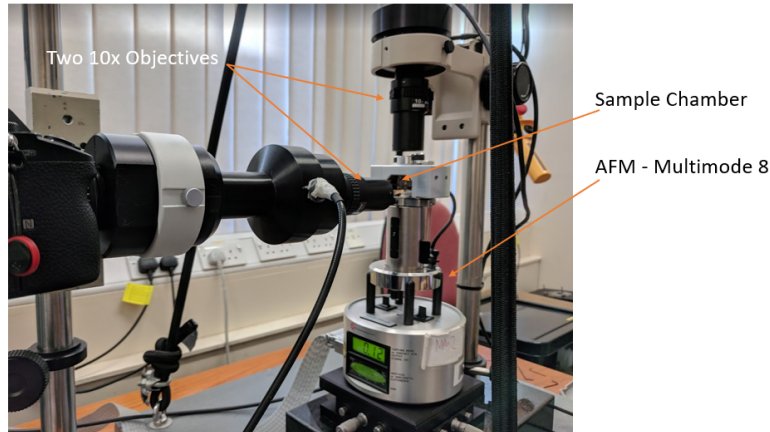
Figure 6.16: Photograph showing the two cameras set up allowing for side view images of the AFM cantilever. Two Nikon 10x objective were used with large working distances. These were mounted around the AFM (Bruker Multimode 8).

Preliminary experiments with softer cantilevers ($< 1N/m$) were unsuccessful in measuring a reliable force curve, caused by a lack of consistent separation between the surfaces. Due to the magnitude of forces measured, a stiff cantilever was selected for the crystal mounting, this not only allowed for reliable force measurements but also allowed the cantilever to be used for aligning the correct facet during the probe mounting phase.

The TL-NCL (TipLess - Non-Contact/tapping mode - Long cantilever) was used due to its spring constant ($\bar{4}8$ N/m), length (225 μm), and tipless design. The cantilever length allowed for larger crystals to be mounted without interference from the chip colliding with the crystal, the longer length also reduced the proportion of the cantilever that was covered in glue and subsequently fixing it whilst the tipless design allowed for the crystal to be mounted parallel to the cantilever.

6.4.1   Crystal-Cantilever Mounting

Harvested crystals, grown by the cooling method detailed above, were dispersed onto a ParaFilm covered AFM magnetic stub. Using a stereo optical microscope with an x10 magnification, adequate crystals were isolated from the rest of the powder. The criteria used for identifying suitable crystals were as follows:

- Crystal size - $< 100 \mu m$

- Crystal shape - Prismatic (in the case of Para)

- No visible defects - Cracks, breakage, or twinning

- No agglomeration

- Smooth surfaces
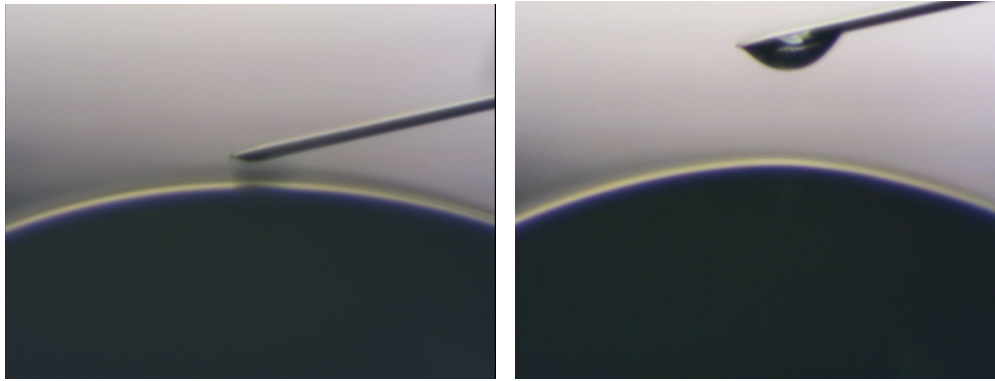
(a) Applying adhesive
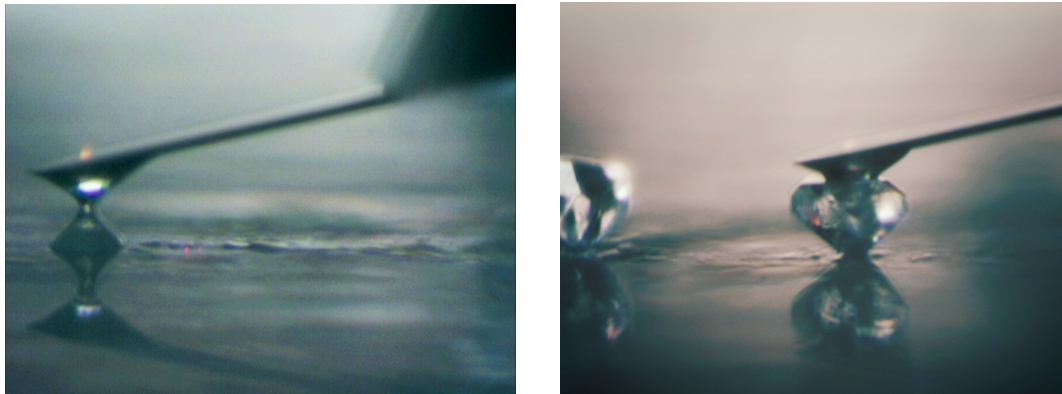
(b) Removing excess adhesive

(c) Attaching probe crystal

Figure 6.17: Process of mounting probe crystal to cantilever.

Using the two cameras and the stiff cantilever, the crystal was moved into position through the use of the AFM stage control (XY) and step motor(Z). The desired facet was placed face down onto the stub surface.

Nearby a small amount of two-part epoxy-resin adhesive (Araldite Original) was placed on the stub using a fine needle. The chosen adhesive had a semi-viscous

curing time of 10 minutes, and a full curing time of 24 hours. The cantilever was brought into contact with the adhesive and withdrawn, leaving behind a small drop of adhesive(Figure 6.17a).

Due to the capillary forces, the adhesive amount was too great and in some instances would engulf the whole crystal. As such, the excess adhesive was removed when the droplet was brought into contact with the stub surface (Figure 6.17b).

Using the minimum amount of adhesive required to achieve complete coverage of the top of the crystal, the cantilever was aligned over the crystals and brought into contact. Pressure was applied to the crystal to ensure the desired facet was parallel to the cantilever (Figure 6.17c).

The crystal-cantilever probe was left for 10 minutes undisturbed and then removed from the chamber and allowed to cure for 48 hours.

6.4.2 Force Measurements

Force measurements were carried out between single crystals of Para, LGA, and DMAN. Para was used as the probing crystal, with three different facets being selected. Due to the angle of the cantilever, the substrate had to be re-orientated in order to ensure flat contact between the substrate probe facet.

Figure 6.18 illustrates how the substrate crystal was placed in a putty-like substance (Rodico) with the chosen facet angled (α) to the approximate angle of the cantilever (θ), relative to the horizontal plane. To achieve the correct alignment, the side-mounted camera was used to image the two crystals. Angles were measured using ImageJ [166].

The crystal was adjusted using soft-tipped tweezers and force was only applied on the side opposite to the analysis region.

Figure 6.19a shows the angle of Para substrate to match that of the probe at 14.4^o, relative to the horizontal. By rotating the camera to ensure the probe was parallel to the horizontal, it allowed for an easier initial inspection between the two facets, as shown in Figure 6.19b.

Force volume (FV) scans were carried out six times across each facet with all three probes. In total, three Para, one DMAN and LGA facets were probed. The parameters of the FV scans are tabulated in Table 6.3.

Using a combination of the side-mounted and top-down images, it was possible to identify suitable sites for measurements. Multiple sites were chosen based on their lack of large surface features or variation of surface texture. Overall, 12288 force curves were collected for the cohesive measurements (Para/Para) between the three probes and facets. For the adhesive components (Para/DMAN, Para/LGA) 9216 total force curves were collected, the difference between the two is due to only

one facet being considered for both LGA and DMAN.

A relative trigger of 1 μN (approx 20 nm deflection)) was chosen in order to ensure contact between the two surfaces. With the smallest projected surface area of $\approx 1,370 \ \mu m^2$ the highest compression force was $0.7 \ nN/\mu m^2$ thus not being strong enough to cause the crystals to break or significantly damage the surface.

A ramp size of 550 nm was used in order to provide enough clearance between the probe and substrate, as well as account for the larger adhesion forces as the adhesion force is proportional to the distance required for the probe to move away
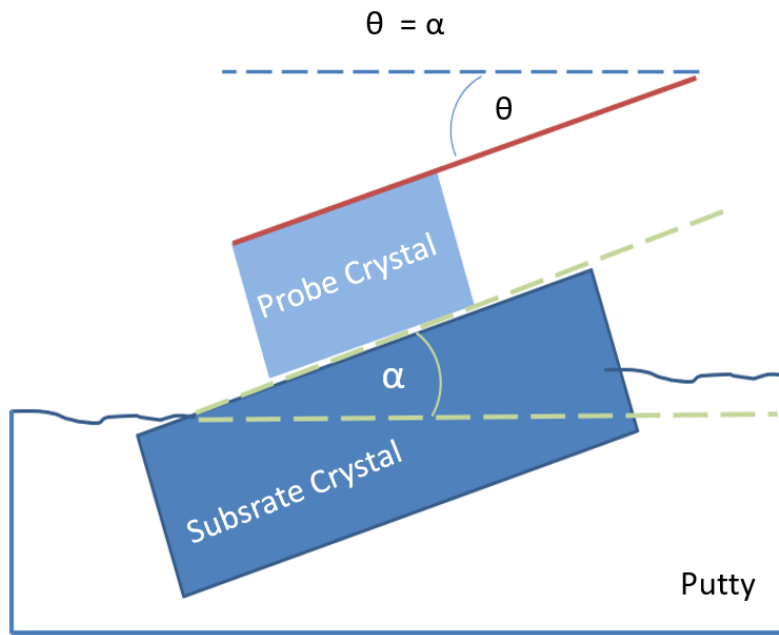
Figure 6.18: *Illustration showing the geometrical set up for the face-facet force measurements. The substrate crystal is mounted at the same angle as the probing crystal relative to the horizontal plane ($\alpha \approx \theta$).*
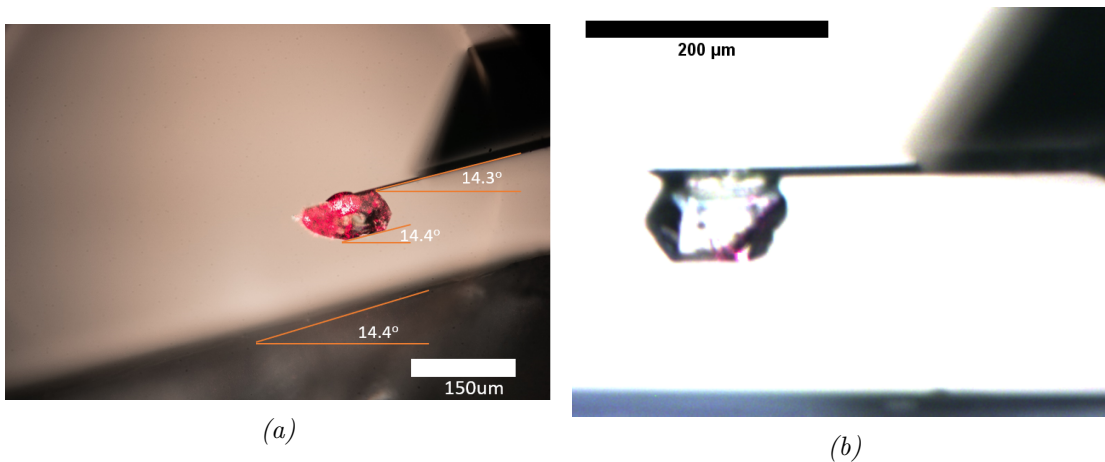
Figure 6.19: *Side mounted camera images showing the alignment between the probe and substrate surfaces. a) Para substrate aligned to 14.4º, matching the probe angle. b) Image with the camera rotated to match the angle of the probe, making angle differences quicker to identify.*

150

Table 6.3: Typical parameters for FV scans when measuring facet-facet forces

Scan size	20.00 μm	Ramp size	550.00 μm
Ramps/lines	16	FV Speed	40.00 $\mu m/s$
Trigger Threshold	1.00 μN	Forward Velocity	240 nm/s
XY Rotation	0°	Reverse Velocity	40 nm/s

from the surface.

The velocity was kept constant during all measurements. A relatively low reverse velocity (40 nm/s) was chosen to allow for more consistent adhesion forces to be measured, and reduce the likelihood of measuring a tapping force due to the higher forward velocity (240 nm/s) combined with the high mass of the crystal on the end of the cantilever, which was selected to reduce the duration of each force measurement and allow a full scan to be completed in a timely manner.

6.5 Results Facet-Facet Force Measurements

This section focuses on the measured forces between adhered facets of Paracetamol (Para), L-Glutamic Acid (LGA) and D-Mannitol (DMAN). Due to the large data set size, a couple of examples have been selected to illustrate typical force curves and scans. The analysis has been divided between cohesive and adhesive to allow for adequate discussions regarding system-specific properties.

For clarity, a general discussions section regarding the validity of the method, further analysis, impact of surface roughness, and limitations will be presented.

6.5.1 Paracetamol/Excipient - Adhesive Forces

The typical force curve shapes for Para/DMAN and Para/LGA are shown in Figure 6.20. When referencing the force curve described in Section 3.2.2 Figure 3.5 the tip displacement describes the tip-surface separation. Thus the adhesive peak is on the left of the plot, and however, typically the data is shown as the tip displacement towards the surface with zero, meaning the tip is above the surface with an increase in Z movement towards the surface, as shown below. The typical force curve is shown in Figure 6.20a still exist in both Para/DMAN and Para/LGA. However, as it can be seen a variation of these are also exhibited.

Figure 6.20a shows an ideal force curve with a clean pull off and a high magnitude of force where surface contact had been made. However, when analysing Figure 6.20b, a difference in the shape of the curve can be noticed around the pull-off section. A curved retraction trace (blue line) indicates the presence of capillary forces. The capillary forces are caused by a liquid bridge between the two surfaces as described in Section 2.4.1. Due to the formation of a liquid bridge the surface tension of solvent-solid increases the adhesive forces between the two surface, this is characterised by the long range reduction in adhesive force over a longer range. As the separation between the two surfaces is increased the radius of the liquid bridge is reduced and thus so is the adhesive force.

The formation of a liquid bridge between two surfaces is associated with the % relative humidity (% RH). As both Para/DMAN and Para/Para measurements were carried out at similar % RH, the surface properties of DMAN are the only changing factors. Para/Para measurements indicated no presence of capillary forces below the measured RH of 45%, as no curved retraction plots were observed. The hydrophilicity of a surface also governs how much solvent adsorbs to the surface. DMAN is typically more hydrophilic than Para. The contact angle (θ_C) of DMAN has been previously measured between $12 - 56^o$ ($\bar{\theta}_C = 33^o$) [182], depending on the facet of interest, compared to Para being measured at $16 - 68^o$ ($\bar{\theta}_C = 40^o$)[164]. The lower contact angle is indicative of better wetting and thus a more hydrophilic

surface.

A relative humidity study, where the % RH in the sample chamber is changed whilst sampling the same region, would allow for the deconvolution of the force components between capillary and adhesive forces. Unfortunately due to time restrictions such as study was not carried out but would be a high consideration for future work.

While Para/LGA share the same normal force curves, as seen in Figure 6.20a, the LGA substrate does not suffer from any noticeable capillary forces. However, due to the larger asperities, as identified in Section 6.3.2.2, breakages/deformation of asperities can be seen in the approach trace (red line) in Figure 6.20c. It can be seen in the contact region of the force curve, where a secondary "jump" is made. The force required to break/deform the asperity is related to the overall height of the peak.

While only a few force curves, from the Para/LGA data-set, showed this asperity

(a) P_1/DMAN - Normal force curve

(b) P_3/DMAN - Presence of capillary forces

(c) P_3/LGA - Asperities breaking

(d) P_3/LGA - Poor contact
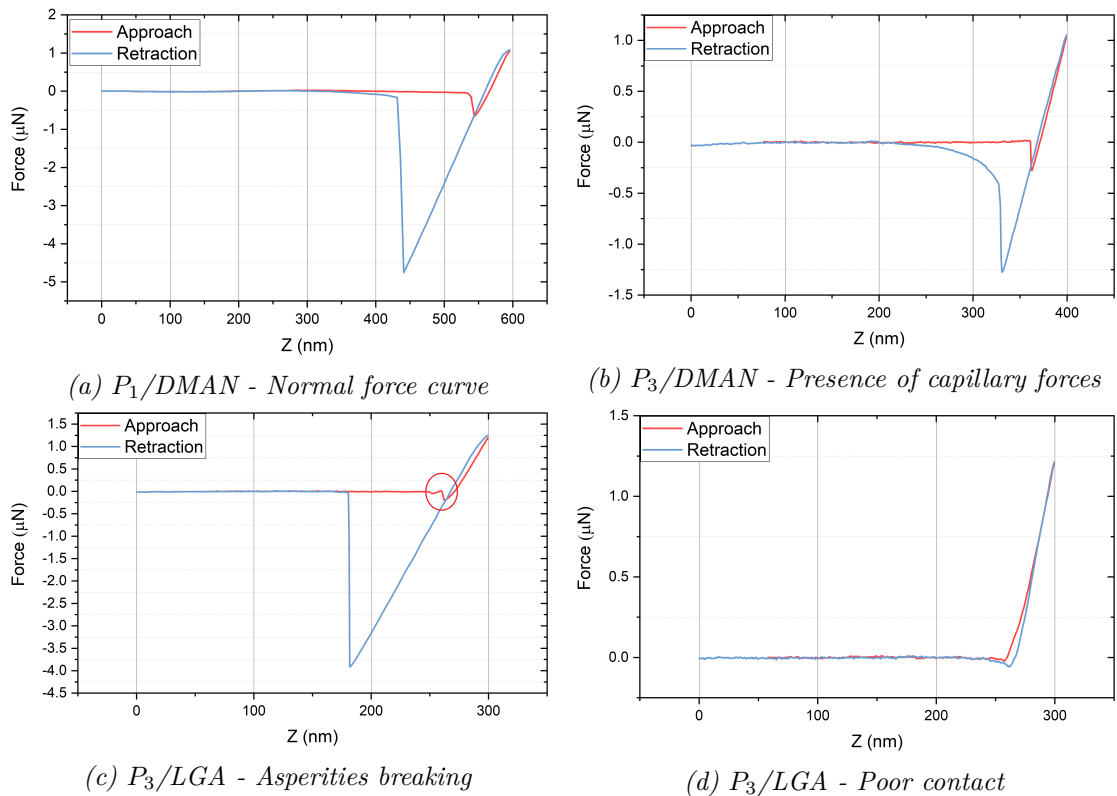
Figure 6.20: Examples force curves describing the typical magnitude and shapes between facets of Para and DMAN. a) A normal force curve with the Z(nm) along the x-axis describing the ramp of the tip towards the surface. The adhesive force is captured in the retraction (blue) plot where the difference between the baseline and lowest point is measured against the y-axis describing the force. b) Illustrates the presence of capillary forces by the curved retraction plot around the baseline. c) Illustrates the breakage of surface asperities, found only on LGA surfaces, by the small peak measured on the approach plot (red) highlighted by the red circle. d) Poor contact that where surface geometries restricted the interlocking of surfaces.

induced feature; the magnitude of the force is negligible compared to the overall adhesion value. However, it is worth considering the impact of asperity deformation, on both the probe and substrate, as it could alter the overall structure of the surface. An assessment to such a degree would require further investigation and normalisation of probe geometry as seen in previous studies [173, 171].

Finally, Figure 6.20d shows the force curve between P_3/LGA, where poor contact is made between the surfaces. A small adhesion force is recorded and is due to a false contact being made with the surface, most probably due to the collision between two asperities on the opposing surfaces resulting in a negligible pull-off force. These type of poor contact force curves were present amongst all facet-facet measurements, and are reflected in the adhesion distributions, which will be described later.

Para/LGA force curves did not exhibit capillary forces in the adhesion forces. Unfortunately, at the time of writing, no contact angle data was found within the literature for α-L-Glutamic acid and grown crystals were not adequately large enough for carrying out contact angle measurements. Therefore no comparison could be made regarding the hydrophilic nature of the material and its associated propensity for water adsorption.

A sample of Force Volume (FV) scans has been presented in Figure 6.21. FV scans are rasterised force curves across a surface with a given lateral resolution. These show the adhesion and height map for the interaction of P_1/DMAN, P_2/DMAN, P_1/LGA, and P_3/LGA. Pairs of scans are presented to show the consistency of data across multiple sites and probes.

Analysing the DMAN substrate data, similarly to Para/Para, the adhesion force is inversely proportional to the height. However, surface features are more prominent within all excipient FV scans. Surface features seen in Figures 6.21a and 6.21b are larger than those seen for the LGA system in Figures 6.21c and 6.21d. It is thought these are caused by the large asperities on the surfaces, whereas those on DMAN are caused by surface features such as peaks and valleys. The distribution of forces across all Para/Excipient systems have been presented in Figure 6.22. Each graph describes how each probe adheres to the substrate of LGA and DMAN. All values have been normalised to probe size. Average adhesions and standard deviation have not been presented for these measurements due to the nature of the distribution, some being bimodal, or heavily asymmetric. A quantitative comparison would be very difficult due to other effects such as humidity. Further work would allow for the quantification of the data.

Figure 6.22a shows the distribution for Para/DMAN. Data for P_1/DMAN contains an asymmetric distribution with majority of the forces being very low (0.02 kN/m^2) while P_2 and P_3 probes show a split in the distribution. Lower adhesion values can be associated with either poor contact or the measurement of capillary
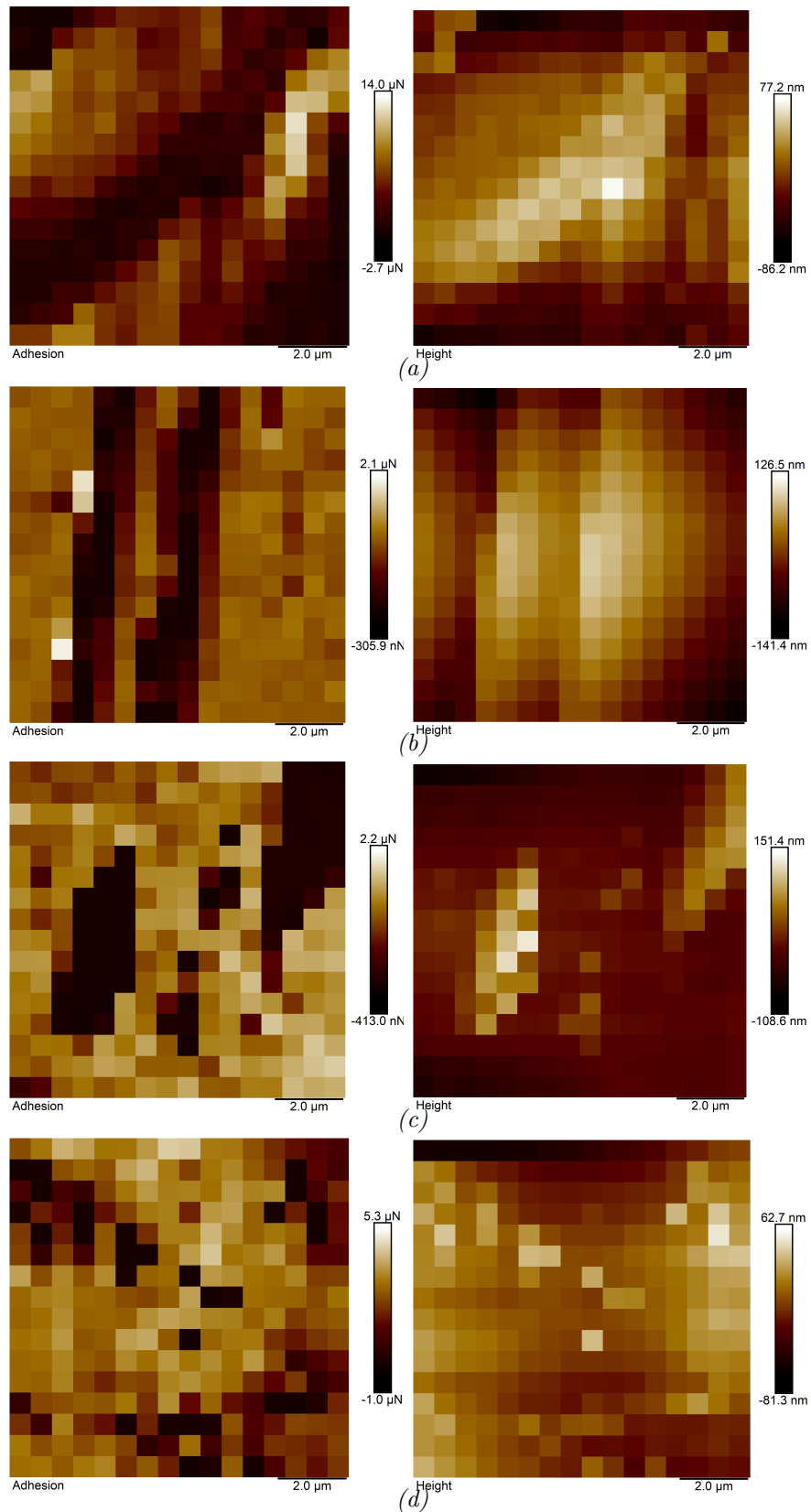
Figure 6.21: Example FV scans of P_1/DMAN (a), P_2/DMAN (b), P_1/LGA (c), P_3/LGA (d) showing adhesion and height maps. Adhesive plots (left) shows the region of substrate surface where adhesion is high (lighter pixels) which are inversely correlated with lowest points on the surface, shown in the height(right) plots where the pixels are darker.
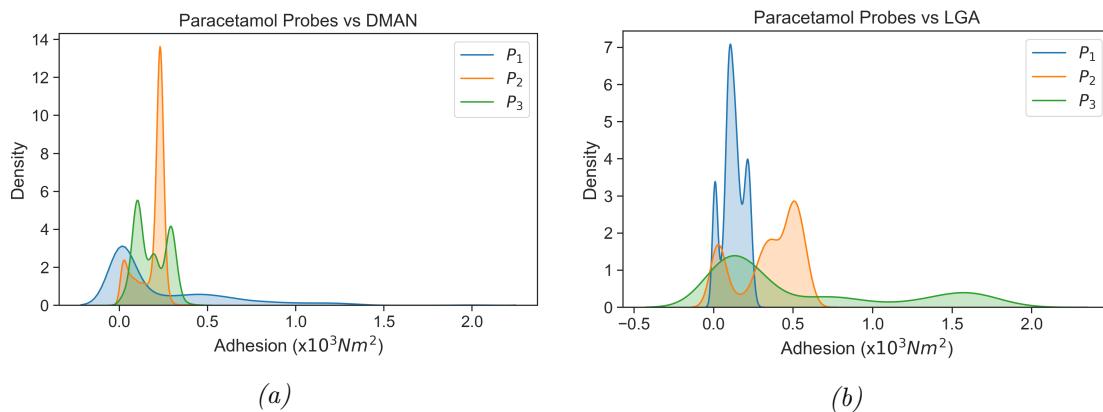
Figure 6.22: Adhesion force distributions for Paracetamol measured against L-Glutamic Acid and D-Mannitol. Each distribution is composed of 1536 force curves taken across multiple substrate sites, in total there are 10240 force curves for Para/DMAN and Para/LGA combined.

forces. However, based on the distributions the ranking of probes, from strongest adhesive forces to least, is as follows:

$$Para/DMAN : P_2 \approx P_3 >> P_1$$

The LGA data-set appears to have more features with a higher proportion of forces above 0.2 kN/m^2. Similarly, split distributions are prominent, and the lower forces can be associated with poor contact as shown in previous force curves. Overall LGA has globally, and locally higher adhesion forces compare to DMAN. The ranking of probes is as follows:

$$Para/LGA : P_3 > P_2 >> P_1$$

Further analysis is required in order to understand how the surface chemistry, roughness and geometry could impact the forces measured. These points will be discussed in the following sections.

6.5.2   Paracetamol/Paracetamol - Cohesive Forces

Cohesive forces were measured between the three Para probes, characterised in Section 6.3.2, P_1,P_2 and P_3. These were measured against the three facets of a single Para crystal ($F_{10\bar{1}},F_{101}$ and $F_{11\bar{1}}$). The crystal was subjected to the cleaning protocol outlined in Chapter 5 to ensure a reduction in surface debris and contaminations.

Typically most force curves between Para/Para displayed normal behaviour as previously seen in Figure 6.20a. The shape of the curves resembles that described in Section 3.2.2 when describing an ideal system, indicating hard contact between the two surfaces, no capillary forces and no surface damages.
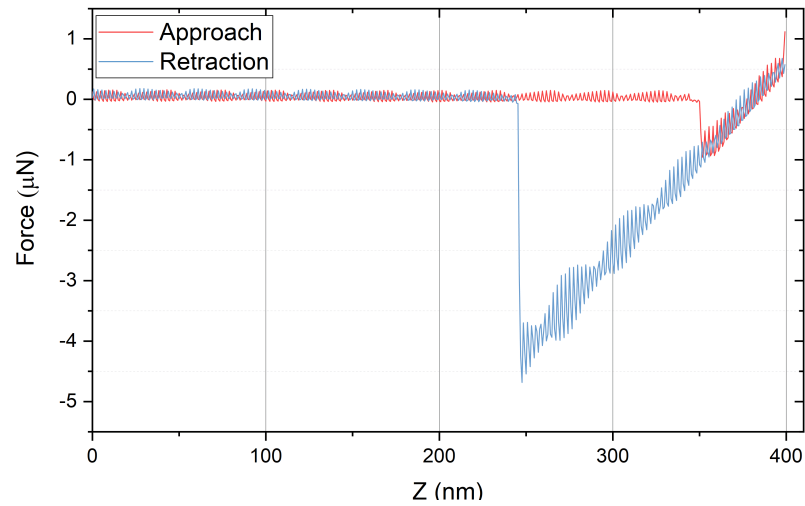
Figure 6.23: *Typical Para/Para force curve where adequate facet-facet contact was made. The oscillating noise is caused by an instrumental defect in the AFM controller.*

(a) $P_2/F_{10\bar{1}}$ - Adhesion map

(b) $P_2/F_{10\bar{1}}$ - Real height map

(c) P_2/F_{101} - Adhesion map

(d) P_2/F_{101} - Real height map
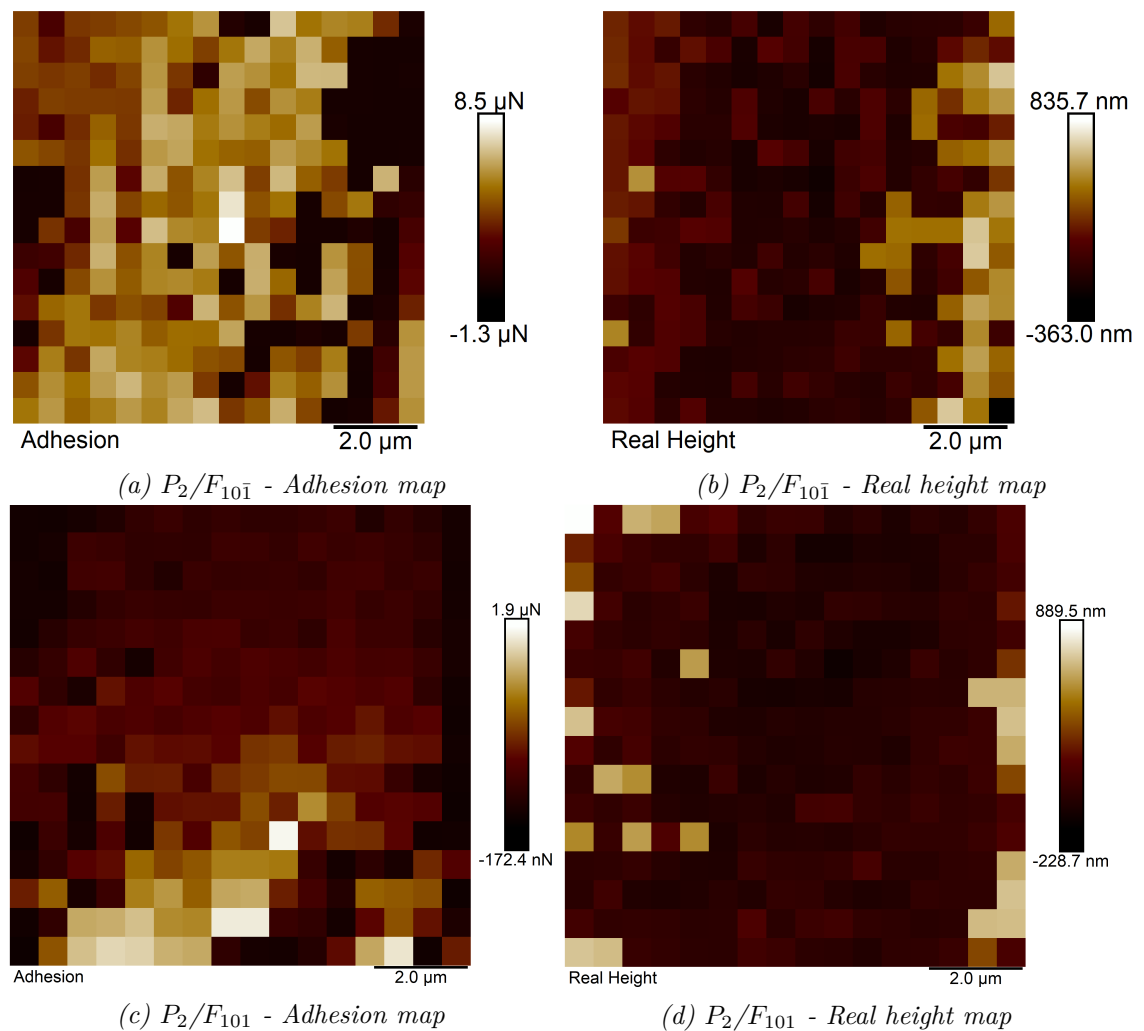
Figure 6.24: *Example force volume (FV) scans of $P_2/F_{10\bar{1}}$(a), b)) and P_2/F_{101}(c), d)), showing the change of adhesion and how it correlates to the change in height at which contact is made.*

The noise in Figure 6.23 is due to an instrumental defect that was incurred during the experimental study. Whilst not affecting the scanner, the fluctuations in voltage did generate noise levels up to 5% of the signal. Due to the size of the measured force and number of data points, it was deemed an acceptable error.

Force Volume (FV) scans were taken, in order to ascertain a statistically significant amount of data and ensure a proportion of the variable surface was sampled. These are a set of force curves that have been measured rasterising the surface of given scan size. In this case, 256 force curves were captured per FV scan. Figure 6.24 shows two examples of typical FV scans for Para/Para measurements and allows for certain differences to be highlighted and what causes those differences.

Figures 6.24a and 6.24b show an example FV scan of $P_2/F_{10\bar{1}}$, with the adhesion and height values being displayed respectively. Based on the adhesion scan, it is clear a range of forces are present across an area, as it would be expected. Areas of high adhesion are associated with regions of low height, this suggests the surfaces are gaining a higher degree of contact as the probing surface is allowed to reach lower concave areas. Regions of low adhesion typically appear as surface features in both adhesion and heightmap. This is caused by asperities on the substrate or probing surface reducing the accessible space. In some FV scans where surface roughness is relatively high at the nanoscale, low forces dominate due to the high presence of asperities.
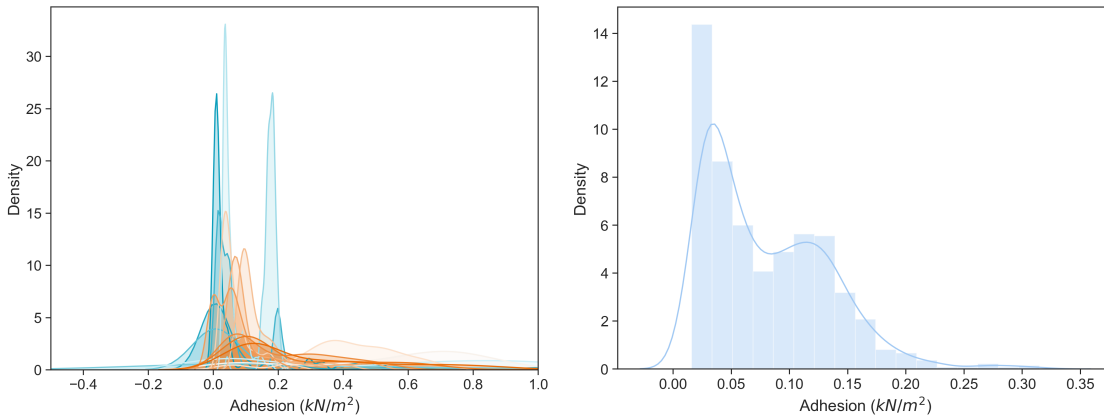
(a) Individual adhesion values for P1 probe across all the different sites

(b) Multiple data points fitted with a KDE for F_{101} substrate

Figure 6.25: Examples of adhesion distributions from multiple sites and how the data is fitted using a kernel density estimate. a) Each distribution represents 256 data force curves. b) The distribution is composed of 3584 force curves.

Another surface effect can be seen in Figures 6.24c and 6.24d, showing the FV scans of P_2/F_{101}. A force gradient appears in the adhesion map showing the bottom of the scan to have a higher adhesion force than the top. Comparing to the heightmap, which shows little change across the scan, indicates the presence of a

smooth "cliff edge" structure on the substrate. As the probe initially moves across flat surface forces are normal, as it approaches the edge of the "cliff" it still makes contact with the top due to the size of the probe, but less of the surface is in contact with the substrate.

(a) Facet grouped data set for Para/Para measurements

(b) Adhesion distributions for all Para probes with $F_{10\bar{1}}$ substrate
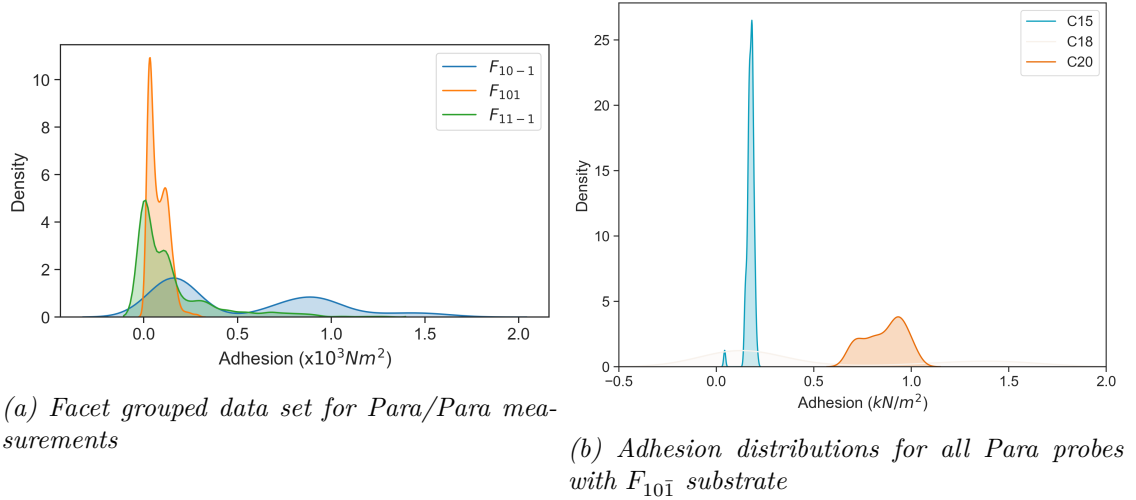
Figure 6.26: Adhesion force distributions of Para/Para facets. a) Shows the force distributions grouped based on substrate facet, thus showing which facet is most interacting. b) Shows force distribution grouped based on Para probes used for measuring substrate $F_{10\bar{1}}$

As it was seen in the surface characterisation section, whilst the surface was smooth at the macro scale, nanoscale roughness has an impact on the measured force of adhesion. This has been documented and studied previously in literature [183, 29, 171], however, these were typically for colloidal probes of spherical geometry; therefore roughness would have a smaller impact compared to flat plane samples.

Figure 6.25a illustrates how different scans contain a range of energy distributions. This is inherent with the nature of the varying surfaces.

By taking multiple FV scans for every probe substrate combinations, it was possible to analyse the distribution of adhesion force across each individual scans. Figure 6.25a shows the force distributions for all P_1 scans. All FV scans have been normalised by the true surface area measured with confocal microscopy in Section 6.3.2.1.

Grouping the data and aggregating into facet based distributions, it is possible to compare how different substrates adhere to the same set of probes. Figure 6.26a shows the adhesion force distribution of all Para facets.

Based on these distributions it is possible to rank which facets are most interactive when in the presence of other Para crystals. The facet ranking based on all the distributions are as follows:

$$F_{10\bar{1}} >> F_{101} > F_{11\bar{1}}$$

159

Facet $F_{10\bar{1}}$ shows a bimodal distribution with both peaks having the largest adhesive force, 0.15 kN/m^2 and 0.87 kN/m^2, compared to those of F_{101} and $F_{11\bar{1}}$ of 0.06 kN/m^2 and 0.03 kN/m^2 respectively. A bimodal distributions indicates two data sets exist within the one distribution. Plotting the component forces from the probes, it is possible to see in Figure 6.26b that P_1 and P_2 have similar low adhesive forces, whereas P_3 has a substantially higher adhesive force.

6.6 General Discussion

This section will focus on understanding the magnitude of the forces that occur between facets, the cohesive/adhesive balance, how the surface roughness affects the measured forces, and finally the limitations of the experiments and any further improvements that could be made in order to yield more robust and rich data.

6.6.1 Reality Check

Every force measurement has been processed with a specific cantilever calibration and normalised with a measured true surface area in order to determine the adhesive value from the deflection of a cantilever. A "reality check" has been carried out in order to check the feasibility of the average results determined from all facet-facet measurements.
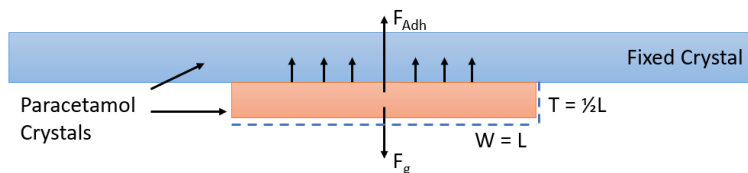
Figure 6.27: Diagram illustrating the gravitational(F_g) and adhesive (F_{Adh}) forces acting on a probe crystal (orange) adhered to a fixed crystal (blue). The dimensions of the probe crystals have been set to a plate like system where the length(L) is equal to the width(W) but the thickness(T) is half the length.

The model system set-up is shown in Figure 6.27, where two Para crystals are used. The substrate (blue) crystal is assumed to be fixed and infinite in size. The probe crystal (orange) has adhered to the bottom of the substrate. While suspended in the air, the force of gravity (F_g) is calculated and compared to the force of adhesion (F_{Adh}), which has been derived from the experimental data.

The size of the crystal is incrementally changed in order to determine the maximum size of the crystal before $F_g > F_{Adh}$, and thus the two crystals no longer adhere together under gravity ($a = 9.81 \ m/s^2$). The geometry of the crystal is set as a plate with length (L) and width (W) being equivalent, whereas the thickness (T) is half the size of the length ($T = \frac{1}{2}L$). The volume of a crystal is computed in order to calculate the mass of the crystal (m).

Compiling all Para/Para force curves and calculating an average value removes any facet variation and describes any Para/Para system. The density (ρ) of Para is given as 1.29 [184]. Equation 6.1 shows the equation used for calculating F_g and F_{Adh} where x is the changing length factor for the adhered crystal, and $\bar{F}_{ExpAdh}$ is the average experimentally determined force of adhesion between Para/Para facets.

$$F = ma$$
$$F_g = x(LWT)\rho a \qquad (6.1)$$
$$F_{Adh} = x(LW)\bar{F}_{ExpAdh}$$

The computed forces are shown in Figure 6.28 where $F_{Adh} > F_g$ while the length of the crystal sides are less than 1.1 cm and thickness less than 0.55 cm. After which, due to the mass of the crystal, the two crystals would no longer adhere. It is realistic to expect a crystal of > 1.2 cm length to not adhere to another fixed surface when suspended in air, as such the adhesion forces calculated for Para/Para systems are within a realistic range. Values for Para/DMAN and Para/LGA are of the same magnitude so can be reasonably concluded to be realistic.
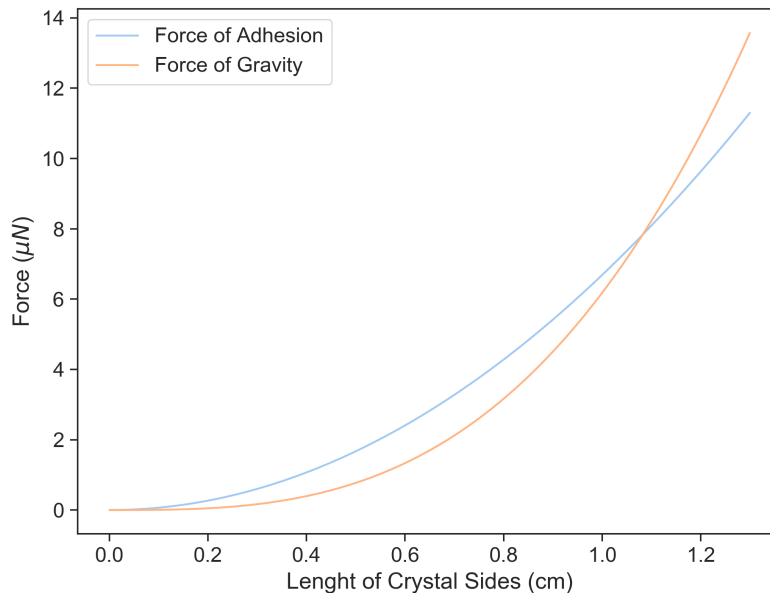
Figure 6.28: Computed values for the forces of adhesion and gravity where the size of the suspended crystal is changed in order to determine the minimum crystal size required for gravity to overcome the force of adhesion.

6.6.2 Cohesive/Adhesive Balance

In order to understand how Para would behave in the presence of either DMAN or LGA, the cohesive/adhesive balance (CAB) must be analysed. By comparing the average forces of adhesion measured for each probe in the presence of API or excipient, a system affinity is calculated.

Figure 6.29, shows the CAB plot for the given systems. As detailed in Section 4.3.4, values residing above the identity line (black) $F_{Coh} > F_{Adh}$, and conversely points below describe forces where $F_{Adh} > F_{Coh}$.

Based on the linear regression of all three probes, Para has a higher affinity to itself in the presence of DMAN than in the of LGA. However, with R^2 of -3.014 and -15.59 for Para/DMAN and Para/LGA, respectively, the linear regressions do not describe the systems adequately. The reason for calculating a negative R^2 are two-fold. Initially, a negative value is indicative of a null hypothesis (i.e. gradient = 0) being truer than the fitted data set; Secondly, as the fit is forced through $c = 0$, the linear regression fit is poor. However, whilst the linear regression does
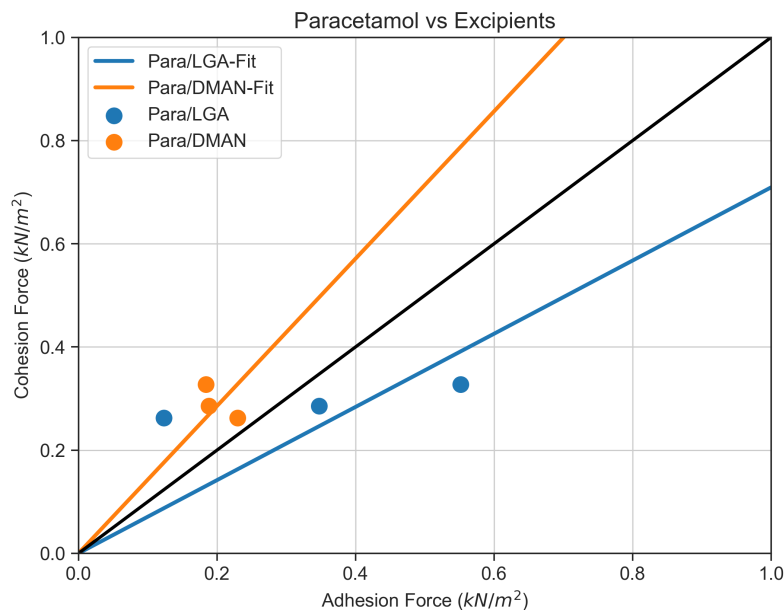
Figure 6.29: Cohesive/Adhesive Balance plot for the facet-facet measurements of Para/D-MAN (orange) and Para/LGA (blue). Para/LGA is predominantly dominated by adhesive forces (below the identity line). Para/DMAN shows a higher affinity for cohesive forces (above the identity line)

not properly describe the system, this suggests that each probe had a different interaction with the substrate compared to the rest of the system. Such an effect is more apparent within the Para/LGA force measurements. The most adhesive probe P_3 had an average adhesion force to LGA of 0.55 kN/m^2 compared to its cohesive force of 0.33 kN/m^2. On the other hand, P_1 measured the lowest average adhesive force for Para/LGA of 0.12= kN/m^2 and but a cohesive value of 0.26 kN/m^2. Concluding that P_1 is dominated by cohesive forces, whereas P_3 by adhesive forces. Such differences could be caused by either the surface roughness of the systems, impacting the contact between surfaces, or a manifestation of the surface chemistry from each facet. However, due to the surface roughness of both excipients being the same, in terms of rugosity and Rq, the differences can be associated with the surface chemistry.

In contrast, Para/DMAN exhibited a small variation adhesive forces of $0.19 - 0.25 kN/m^2$ between $P_3 - P_1$. However, the points presented are an average of all

measured force curves with a given probe. When comparing the CAB plot with values in Figure 6.22a, showing the individual probe force distribution, it becomes apparent that as DMAN exhibits bimodal distributions the average describes the midpoint of those two discreet data sets. As previously described, lower adhesive values are associated with poor contact between the two surfaces, thus reducing possible adhesion sites.

This raises an interesting dilemma. Are low forces, and thus facets that have not made full contact, relevant data points? Within a "real" system of facets interacting, non-full contact would be made between particles, and thus these values are relevant. However, in that situation, all facets would experience low forces to a certain cut-off force. Should the maximum forces be compared instead? In order to answer these, further experimentations must be carried out where multiple probes are used on a larger system variation. Within the scope of this project, the lower forces are deemed relevant as all possible interactions between facets are considered.

6.6.3 Effect of Surface Roughness

In order to determine the impact of surface roughness, a multivariate linear regression model was used to predict the forces for facet-facet measurements. The nanoscale surface roughness measured in Section 6.3.2 has been used as the descriptors.

Figure 6.30a shows how describing all facet-facet measurements with only Rq and rugosity shows no linear correlation ($R^2 = 0.17$). With both the probe and substrate, rugosity_x and rugosity_y, having an equally large impact on the predicted force. With the substrate having a slightly larger impact in the overall force.

The model can be improved by adding the peak and valley counts. These describe the number of pits and asperities on the surface. When in combination with the Rq and rugosity, it better describes the 3D aspect of the surface. Figure 6.30b shows an improvement in the correlation ($R^2 = 0.72$). The associated contributions still show rugosity to have the largest impact, more specifically the substrate rugosity (rugosity_y). The contribution from Rq, peak and valley counts are all from the probe. This could be due to the fact that the same probe is used to sample several sites/systems, and as such, the variations of those values would have a higher impact on the target values. The proportion of these contributions indicates that the change in the height of the valleys has a higher impact on the forces measured. This could be due to the reduction in contact area available for interaction, as seen in previous studies assessing the impact of surface roughness on adhesive forces[167, 96, 175, 126].

Utilising the macroscale surface roughness for the probes yielded a worse linear
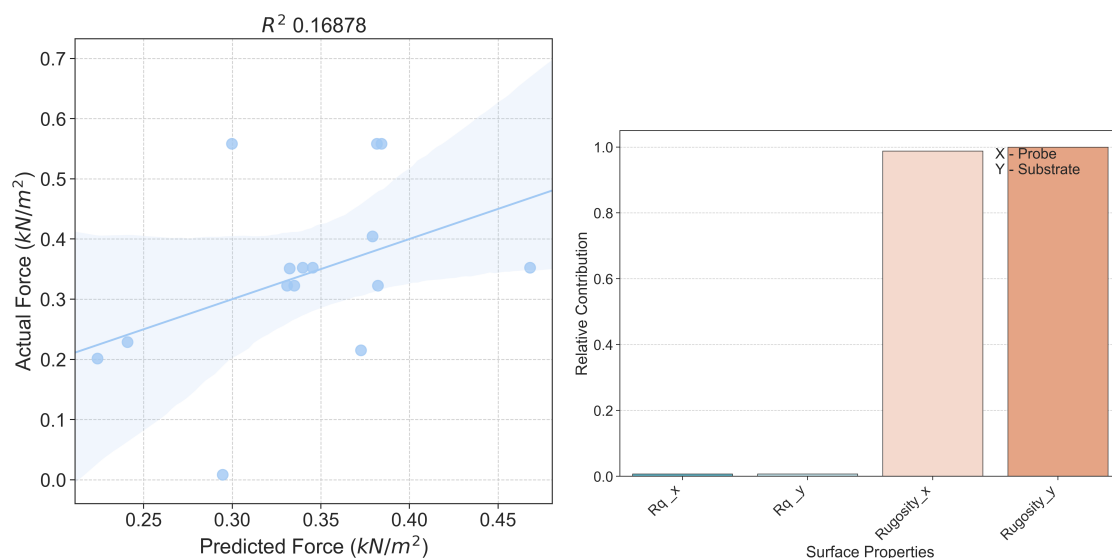
(a) Rq and rugosity
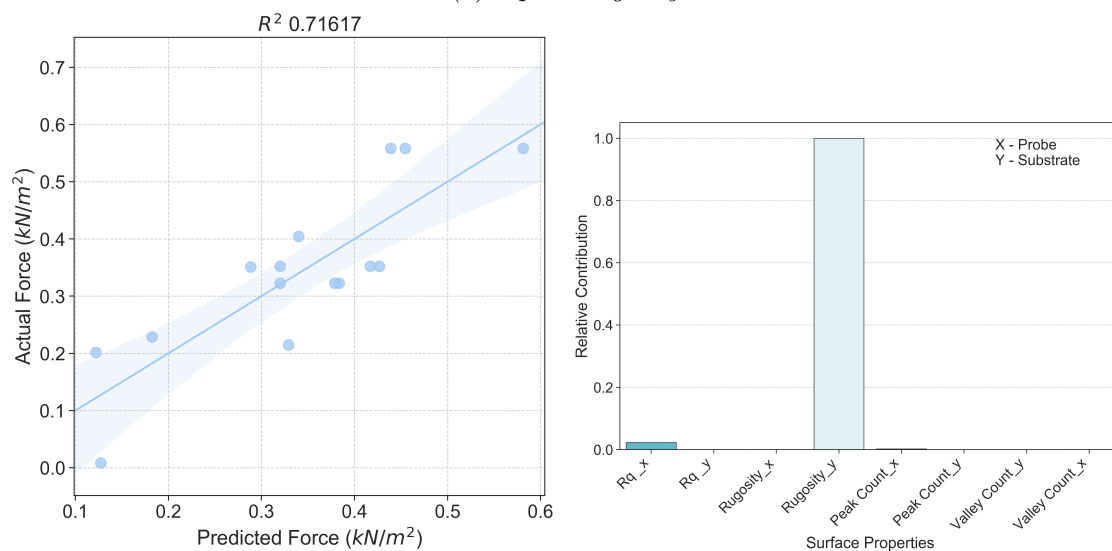
(b) Rq, rugosity, peak and valley counts

Figure 6.30: Multi variant linear regression models for correlating the surface roughness descriptors with all facet-facet force measurements. Model performance (left) is displayed alongside the relative contributions (right) from each surface descriptor

correlation of ($R^2 = 0.06$) when computed with the rugosity. However, when adding the peak and valley descriptors the model performed similarly ($R^2 = 0.72$) to the one outlined above with the nanoscale roughness. Whilst an improvement, the major contributing factor was still the substrate rugosity.

Whilst the roughness data suggests that facet-facet forces are predominantly determined by surface roughness and as such surface chemistry may not play any roles in the interactions, it is important to note that the models still do not account for 25% of the force. Moreover, differences measured between DMAN and LGA, as shown in the CAB plot highlight the impact of surface chemistry as both surfaces have the same roughness. As such, with the roughness normalised, it is possible to

measure discernible differences between systems.

6.6.4 Limitations and Future Work

Positive results have yielded insight into the measurable differences between facet-facet forces with a strong linear correlation. Whilst these are a step in the correct direction in order to understand the forces involved when faceted organic crystals come into contact, a few limitations must be explored and future work outlined in order to improve on this work.

Firstly, as it has been described many times, the surface contact has a significant impact on the forces measured. Any reduction in contact will result in a proportional reduction in force. Being able to image the true surface contact between faceted crystals, with a high enough resolution, is not currently feasible due to the geometrical set up of the planes and thus line of sight restrictions. It would not be possible to image the points that are in contact whilst also measuring the forces between them. The only feasible method of imaging the surfaces coming together would be with the use of a tomographic technique such as micro-CT. However, this would require developments to be made in both AFM and micro-CT to allow this. As such, an assumption is made that the measured surface area is an adequate approximation of the contact area.

During the experiments, the % RH was kept between 37 - 45 % and any changes to the force curves were noted and have been discussed. Keeping the % constant allows for comparative data to be collected, but does not give any insight into how the humidity impacts the measured forces. As it has been documented within the literature, the difference in % RH can have a significant impact not only the final force measurements but also the system it is measured on.

A study[71] examining the effects of surface geometry and RH on adhesion force observed that due to the increase of RH, causing an increase in capillary forces, the adhesion force was higher. The relationship between RH and adhesion force has been noted by many studies. However, the increase in RH can also reduce the interparticular interactions depending on the material properties, as shown by Young et al [185], where the interactions between triamcinolone acetonide particles decreased. This decrease was related to the reduced long-range electrostatic interactions that were quenched with the increase RH. Price et al[70] showed the impact material properties has on the capillary forces at a given RH. For a budesonide–lactose, the inter particulate forces were strong below 60% RH, while for salbutamol sulphate–lactose the forces were stronger above 60% RH.

As such, a humidity study would allow for the deconvolution of facet-facet forces and capillary forces, which may offer a greater insight into the causes of certain

forces. This would be carried out by measuring adhesive forces between surfaces whilst varying the % RH from 5-90 %.

While this study current has demonstrated the use of FV scans in order to capture a large data set of force curves (21,504), the physical sample size has been small. With three Para probes and one Para crystals for the cohesive measurements and one excipient facet per one excipient crystal for adhesive measurements. By increasing the sample size to more substrate crystals and multiple facets, the data set would become more representative of a powder mixture by the diversification of available surfaces. Furthermore, Para/Para measurements were taken with an instrument that was generating a noticeable amount of noise. Repeating those experiments would yield higher quality data for analysis.

6.7 Conclusions

This chapter presents a thorough account of the methodology required to measure facet-facet forces between organic crystals. The forces between paracetamol (Para), D-mannitol (DMAN), and L-glutamic acid (LGA) single crystals have been presented with an analysis of their surface roughness, and facet determination of the substrate crystals. A Cohesive/Adhesive Balance (CAB) plot has been used to identify preferential adherence between crystals. Three Para probes were used to measure the adherence to three Para, one DMAN, and one LGA facets.

The CAB plot highlighted that Para is more cohesive in the presence of DMAN and more adhesive in the presence of LGA. Whilst the linear regression describing the behaviour of the system did not correlate when compared to the null hypothesis, resulting in negative R^2-values (-15.59 and -3.01 for Para/DMAN and Para/LGA), indicating that Para has an affinity to particular facets against excipient crystals, it was possible to discriminate which system Para was more likely to adhere to.

As the facets of Para substrate crystals were successfully indexed, Para/Para measurements ranked the following facets in order of their cohesive forces:

$$F_{10\bar{1}} >> F_{101} > F_{11\bar{1}}$$

Excipient facets proved more difficult to index using powder X-ray diffraction due to their smaller size and facet geometry. LGA was successfully indexed as the [111] facet, whereas DMAN exhibited two different facets of [110] and [120] with the former being more probable based on the confocal images illustrating the presence of multiple facets on one plane. However, as only one facet of each excipient crystal was used the Para probes were ranked instead:

$$Para/DMAN : P_2 \approx P_3 >> P_1$$

$$Para/LGA : P_3 > P_2 >> P_1$$

The impact of surface roughness was assessed and confirmed that an increase in roughness reduces the adhesive force. A linear correlation was found with an R^2 of 0.7162 between the force of every facet-facet combination and the surface roughness when describes with the Rq, rugosity, valley count, and peak count, while the substrate rugosity was having the biggest impact. Whilst this suggests the majority of the force is dominated by the surface roughness when comparing forces between Para/LGA and Para/DMAN, the difference in force were substantial with the most adhesive Para/DMAN measured at an average of 0.2340 kN/m^2 compared to LGA of 0.5517 kN/m^2.

Analysis of individual force curves identified several mechanisms of adherence between facets. Firstly, normal contact between two hard surfaces, the forces where capillary forces are present and where asperities are deformed or crushed. While the RH was kept between 37-45 % throughout all measurements, an RH study would be required in order to deconvolute the capillary forces from the forces of adhesion between facets, based on surface chemistry accompanied by a repeat of the Para measurements to reduce the noise in the data. The addition of extra probes/substrates measurements and a dynamic study of surface roughness change due to face-facet collision would greatly benefit the robustness of the data and detail of analysis allowing for extra complexity to be accounted for.

In summary, facet-facet force measurements have been carried out using AFM. Surface characterisation has allowed for the correct identification of crystal facets and subsequently, the ranking of system and facets based on discreet facet interactions. The ranking offers a "real world" representation of inter-particular interactions that can be used to describe macro-scale interactions between relatively large facets. These results will be used to compare and contrast with the in-silico data, which offers an atomistic resolution of the same facet-facet interactions.

CHAPTER 7

General Discussion, Conclusions and Future Work

"Science is the acceptance of what works and the rejection of what does not. That needs more courage than we might think. - Jacob Bronowski"

The aim of this chapter is to synchronise the computational and experimental approaches into a discussion that assess the importance of specific surfaces properties, while co-currently summarising the work presented in subsequent chapters.

7.1 Overview

The compatibility between the active pharmaceutical ingredient (API) and the excipients used plays a critical role in the final drug product performance. The cohesive (API-API) and adhesive (API-Excipient) balance (CAB) between an API-excipient can be used to describe the likelihood of two powders sticking together.

With a validated model, it would be possible to predict the cohesive/adhesive balance between faceted crystals in formulations before carrying out experimental procedures, reducing the need for trial and error experiments. This would result in a reduction in wasted resources as well as time, thus helping to bring pharmaceutical drugs to market faster. In addition, the model provides mechanistic insight into why particular surfaces prefer to adhere, allowing the prospect of the more controlled formulation. Subsequently, a validated model could also be used to understand why some facets might exhibit a higher affinity to others in experimental measurements. Having an atomistic perspective allows the surface chemistry to be investigated.

The work presented has approached the challenge of understanding the interactions between specific facets of organic crystals using two separate methodologies, computational and experimental. The in-silico approach allowed for the probing of surfaces at an atomistic scale, providing the detail of the atom-atom interactions between surface, while the AFM directly measured the interactions between real indexed crystal surfaces, with all of their roughness, imperfections and general inhomogeneity. By assessing the interaction between faceted surfaces at different length scales, it has been possible to determine the magnitude to which surface chemistry or physical properties impact the inter-particular interactions, such as those seen in manufacturing processes (dry granulation) and inhalation formulations.

The simplest approach to predicting the facet interactions has been shown with the use of the anisotropy factor [85, 55], which describes the % of unsatisfied bonds on the surfaces of a facet, whilst describing only the energetics of the surface, it does reasonably predict most interactive facets, but does not describe how they might behave in the presence of other surfaces or quantify why they might be interactive.

Previous studies have attempted to computationally predict the inter-molecular interactions by modelling a single rigid molecule adhering to the surface [107] or by using nano-clusters of molecules [120] in order to identify the lowest interaction energy and relate it to the adherence of two surfaces. The logic behind this approach is to assume that the lowest interaction energy is the most likely one to occur as the system would move to minimise the energy. Whilst this true for mechanisms such as solvent/solute probes attaching or adsorbing to a surface, it is difficult to imagine a whole crystal moving in order to minimise the energy. Furthermore, as real surfaces are not atomically smooth nor void of defects, the movement in one

direction to minimise the energy would increase it in another section of the surfaces; therefore it is important to acknowledge every possible interaction that would occur between two surfaces.

This work has updated these methodologies by taking a holistic approach. By calculating all possible unique interactions between two facets coming into contact, it has allowed for the generation of statistically significant descriptions of probable interactions between surfaces, thus providing a more representative model. This approach has been validated by experimentally measuring the actual interaction forces between the same crystal facets.

From the model, it is possible to ascertain the contribution of the surface chemistry and topography towards the interactions energy, properties which have not been previously quantified against facet-facet interactions but are presented in this work. Moreover, with different chemistries accounted for and facets being probed, it has been demonstrated that the model improves on the anisotropy factor approach, by accounting for surface topography and functional group presence and positioning.

Experimentally, many studies have implemented inverted gas chromatography (IGC) in order to determine the adherence of particles[17, 20, 36, 95, 186]. However, bulk based measurements using IGC have shown inconsistencies between studies using the same materials, suggesting the methodology is unreliable [33]. A likely reason for this discrepancy is due to the physical limitations of the IGC experimental set-up, where the measurement of defined facet specific interactions is unfeasible, as a powder is used to pack the column and therefore no facet specificity can be inferred.

AFM studies of particle adhesion have shown a stronger correlation to product performance, most likely due to its direct relevance to real-world conditions [33], where particles come into contact with one another. However, particle characteristics and facet specificity were not taken into account when measuring particle-particle forces. Other studies collecting cohesive/adhesive balance information have done so using colloidal probes covered in micronised particles which again offer only random orientation and perhaps an unrealistic view due to the random packing of the surface. Furthermore, when considering the impact contact area has on the measured forces, it does not offer much confidence in the representative nature of the results.

The AFM methodology presented in this work has attempted to more carefully characterise the cohesive and adhesive inter-particle interactions of the most probable crystal facet interaction that might occur in the more complex mixtures of API and excipients. This was experimentally achieved by topographically characterising the surfaces, and aligning single individual facets of API/excipients in order to determine the differences in adherence between different combinations of particles.

The AFM data also offers a validation metric for the in-silico model. As both

methodologies quantify the differences in interfacial interactions between faceted organic crystals, it is possible to compare the ranking of preferential interaction between facets. If the rankings are in agreement, it strongly indicates the model is valid in predicting the interfacial interactions between faceted organic crystals.

7.2 General Discussion - Across Length Scales

Investigating the interfacial interactions across two drastically different length scales (macro and atomic), informs us of the impact different surface properties can have. Experimentally, complex behaviours are dominated by macro-scale features, and a full characterisation is required to ascertain the contributing interactions. Computationally, we start with the fundamental building blocks and describe the surface in a simplistic methodology in order to determine each surface characteristic based on the crystallographic structure.

The theoretical interactions between faceted crystals were simulated using pristine, defect-free surfaces, in a vacuum and without any temperature components. As such, any comparisons made to the "real world" ambient condition experimentally measured forces can only be done relatively, as absolute values are not directly comparable. However, steps have been taken in order to mitigate the differences between the two approaches and move the experiment closer to the computational approach. The cleaning study in Chapter 5 showed how it is possible to clean the surface of paracetamol crystals with the use of an anti-solvent such as DCM in order to reduce surface contamination debris that would impact measured adhesive forces. This approach was utilised throughout the study.

Comparisons have been made between most adhesive excipients measured and calculated, as well as the most cohesive paracetamol facets. Cohesive and adhesive balance (CAB) plots have been utilised in order to determine if the probing system, Para, in this case, has an affinity for itself (cohesive) or the excipient in question (adhesive). A description of how CAB plots are constructed has been given in Section 4.3.4. Briefly, all forces or interactions are averaged for a given probe. The cohesive component relates to the respective material (Para/Para) and is plotted on the Y-axis, whereas the adhesive component relates API to excipient interactions and is plotted on the X-axis.

7.2.1 Cohesive/Adhesive Balance - Model Validation

Comparing the CAB plots from the in-silico and AFM methodologies (Figure 7.1), the behaviour of Para to LGA and DMAN is examined. While the number of probes for the AFM measurements are smaller (n=3), the experiment accessed surface to surface interaction across a wide extent of the surfaces. The in-silico CAB results are largely in agreement with the experimentally measured forces, where Para has been predicted to be dominated by cohesive forces in the presence of DMAN and adhesive in the presence of LGA. In other words, Para has a higher affinity for itself than with D-Man, but it adheres to LGA more strongly than with itself. If the aim during formulation is to disperse particles of Para evenly throughout, then LGA
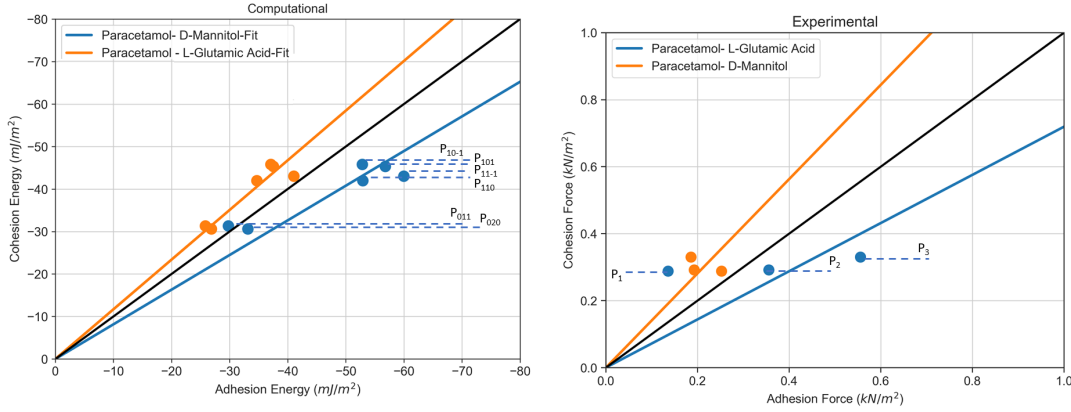
Figure 7.1: Cohesive-Adhesive Balance (CAB) plot of Paracetamol in the presence of excipients L-Glutamic Acid (blue) and D-Mannitol (orange) from in-silico and AFM data. Blackline illustrates the state of equilibrium between cohesion and adhesion. Lines of best fit are used to illustrate the overall system behaviour towards excipients.

would be the preferable excipient.

Both model and AFM data show Para/DMAN to have a higher consistency of cohesive affinity across facets compared to Para/LGA, where a broader spread of forces and interactions are seen. With some of the facets exhibiting an affinity for cohesive interactions in both model and AFM data as shown by the data point (blue) being above the black line.

Unfortunately, at the time of writing, no literature existed of studies quantifying the powder properties of Para, LGA and DMAN as formulations. However, auxiliary observations have been made for Para and DMAN. Vemavarapu *et al*[187] investigated the material properties of Para and DMAN (along with a range of other excipients) before and after granulation. The study determined that an increase in granular size lead to an improvement in flowability, Para showing a pre-blend Flodex flow number of 26 mm prior to granulation followed by 5 mm after granulation. Briefly, the Flodex flow number is determined by packing the powder in a cell and opening an aperture at the bottom till the powder flow. As such, a low number is indicative of better flow. The increase in granular size can be associated with the cohesive behaviour of the material. Szumilo *et al* found that granular size of Para was increased during granulation in the presence of DMAN [188] when normalised for other ingredients in the formulation. Thus indicating that Para is cohesive in the presence of DMAN as predicted by the in-silico model and measured by AFM.

Above, the overall affinities of the three test compounds were described. Breaking this down further to the specific facets of Para the average cohesive forces/interactions for Para/Para systems, the ranking of probes are the same:

$$P_{10\bar{1}} \approx P_{101} > P_{11\bar{1}}$$

Table 7.1: Table showing the average probe cohesive values

Para Probe	Model Data $E_{Coh}(mJ/m^2)$	AFM Data $F_{Coh}(kN/m^2)$
10-1	-45.78	0.1013
101	-45.32	0.1018
$11\bar{1}$	-43.055	0.0656
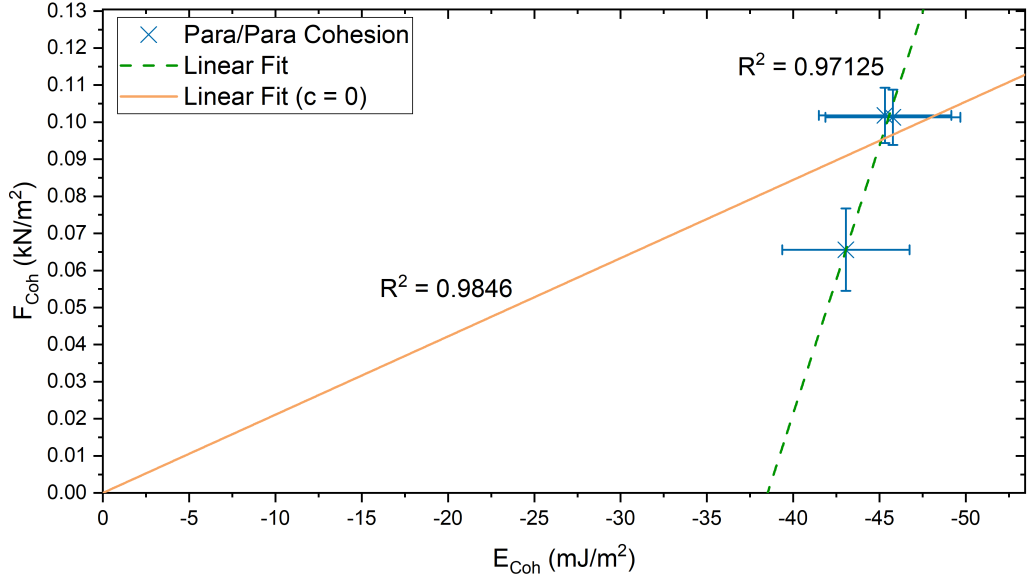
Figure 7.2: Linear correlation for Para/Para systems between in-silico calculated cohesive energy ($E_{Coh}(mJ/m^2)$) and AFM measured cohesive force ($E_{Coh}(mJ/m^2)$). Linear correlation with fixed intercept (orange) illustrates relationship when $E_{Coh}, F_{Coh} = 0$ and normal linear regression (dashed -green)

Values have been tabulated in Table 7.1 to illustrate the small difference between $(P_{10\bar{1}})$ and P_{101} when compared to $P_{11\bar{1}}$. This further illustrates a validation of the in-silico model utilising the AFM data.

Figure 7.2 highlights the existing relationship between the two data sets. A strong linear correlation ($R^2 = 0.984$) exists when the intercept is set to zero where $E_{Coh} = F_{Coh}$. However, fitting without fixed intercept yields a weaker, but still a high, correlation ($R^2 = 0.971$). Due to the low number of data points (three), it is worth noting that the R^2 is used as a correlation indication and its magnitude does not have high importance, they simply indicate a correlation between the data.

The intercept, in this case, is calculated to be -0.537 kN/m^2 for F_{Coh} when the cohesion energy (E_{Coh}) is equal to zero indicating the surfaces would be strongly repulsive. Such a scenario does not appear reasonable due to the properties of materials and lack of repulsive forces, for example, magnetic materials which would repel. This unexpected result could be explained by the small sample size and the assumption that the relationship between force and energy is linear within these

177

systems. As such, further work should be carried out to increase the sample size to better understand the relationship between the in-silico calculated energy of inter-action and the measured forces between faceted organic crystals, in order to account for the complexities of real-world interaction that are not currently resolved.

One property that has a large influence on the relationship between the angstroms scale calculations and macro-scale measurements is the surface roughness. The way in which roughness is described and measured can affect how the data is interpreted.

7.2.2 Impact of Surface Roughness

Many studies have shown the impact of surface roughness on the measured adhesion between particulates. Typically these are assessed for simple materials such as mica and glass where spherical probes are used and are easily quantified. Few studies have quantified the topography of functionalised colloidal probe, and none have done so for faceted organic crystals. The impact of surface roughness has been analysed for both the in-silico and experimental approaches.

In Section 6.6.3, it was shown using a multivariate linear regression (MLR) that the majority of the AFM measured forces could be attributed to the surface rough-ness of the opposing crystal surfaces. However, the computational model has a weaker linear correlation between the surface roughness and interaction energy, al-beit this roughness is at the molecular scale, meaning Å
hl deviations from the mean plane. Figure 7.3b illustrates this point as the linear fit for the MLR model show a correlation ($R^2 = 0.7543$) when comparing the Para/Para force measurements with rugosity and Rq being the descriptors for probe (X) and substrate (Y) surfaces. Both probe and substrate Rq had a minimal contribution to the predicted forces of the systems. This could be associated with the nature of how rugosity and Rq are described, where Rq describes the deviation of a point from the mean plane, whereas rugosity encompasses the 2D aspect of the roughness.

In any case, the in-silico model showed a weaker linear correlation ($R^2 = 0.512$), between the surface roughness and molecular interaction energy, as seen in Figure 7.3a. As the model is more sensitive to the angstroms levels of changes in the surface, the chemistry will have a more considerable impact. Moreover, the surfaces of Para were predicted to be relatively similar, as shown in Table 4.7 with a small variation in the rugosity or Rq. Interestingly, the higher contribution of the probe rugosity compared to the substrate supports the weak correlation (low R^2) as both substrate and probe should have similar contributions due to the same surfaces being calculated.

In contrast, the AFM data show a much stronger correlation as it is more sensitive to the macro-scale features and as such, the forces measured will be dictated by those

(a) In-silico linear model - Para/Para - Roughness only

(b) AFM linear model - Para/Para - Roughness only
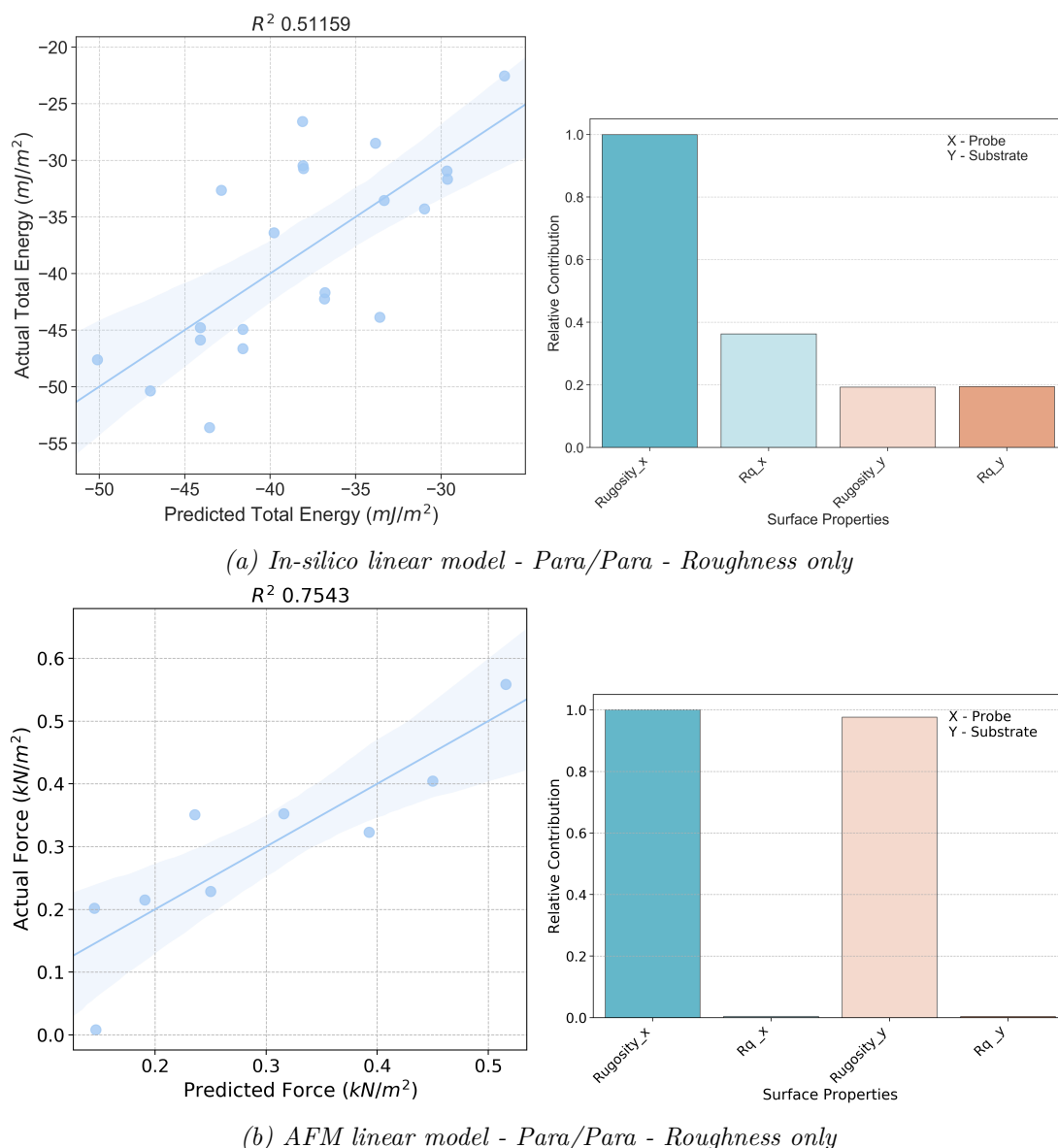
Figure 7.3: Multi-linear regression models illustrating the impact of roughness for the in-silico model compared to the AFM data.

features.

However, using the AFM in conjunction with the in-silico data it is possible to determine that whilst on the macro scale the roughness has a significant impact, the density of H-bond acceptor molecules on the surface of Para such as the C=O, NH, and OH have the greatest contribution to overall interaction of Para/Para surfaces as shown in Figure 7.4. When considering the surface chemistry and roughness, the MLR model shows a strong linear correlation ($R^2 = 0.94919$) between the descriptors and total interaction energy calculated.

It is also important to note that in some instances the surface roughness calculated with the in-silico approach showed that an increase in surface roughness yielded higher adhesive energy as was the case with Para/DMAN where facet DMAN(020)

179
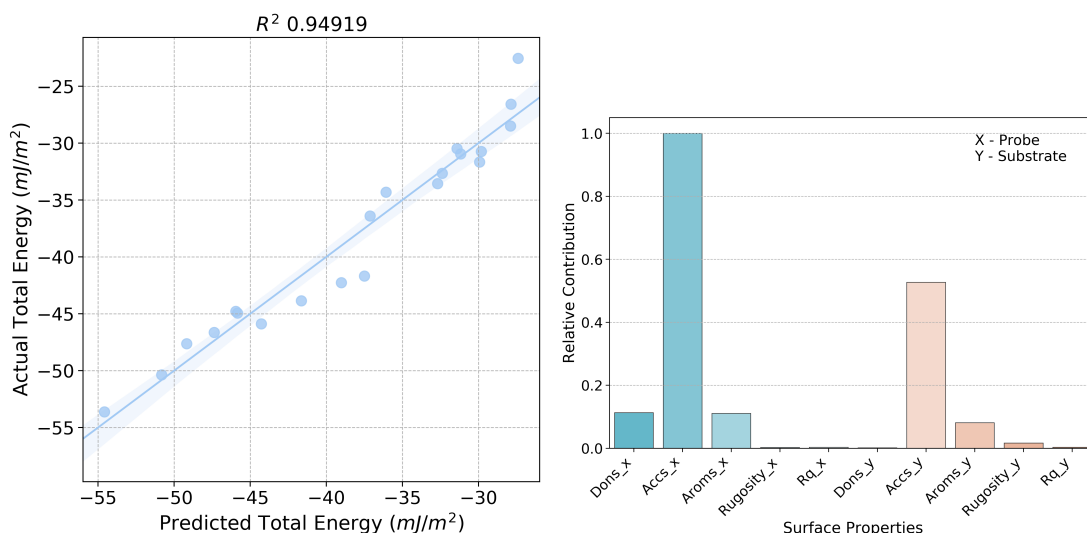
Figure 7.4: In-silico Para/Para - All descriptors

had a much higher Å roughness at 6.88 Å compared to 3.58 Å of DMAN(110). The energy measured was proportionally higher. A rougher surface on the atomistic scale can be correlated to a more energetically active surface due to the surface termination and thus unsatisfied intermolecular bonding present.

The current computational could be improved by extending the atomic roughness to a macro scale to bridge the gap between experimental and in-silico. As demonstrated in Section 4.4.5 the probability of interactions allows for the computational tool to have an experimental input to weigh the data towards the real-world systems. A similar approach could be taken for macro-scale roughness, where the measured roughness could be reproduced in simulations and used as a starting point for calculations.

7.3 Conclusions

This body of work was carried out in order to determine the behaviour between two faceted organic crystal particles as they come into contact within a powder-based formulation. An experimental and theoretical (using in-silico methods) approach has been undertaken to achieve a thorough understanding of the interactions that occur and the surface properties that might cause them. This Section concludes all the findings and postulates future impact this work may have for formulation and solid-state scientists, both in academic and industrial settings.

7.3.1 Determination of Morphology

In order to understand the impact of surface chemistry, facet determination and predictions were crucial in the characterisation stage of both in-silico and experimental procedures. Predicted morphologies were calculated utilising molecular mechanics whilst grown crystals were indexed using powder x-ray diffraction.

7.3.1.1 Morphology Prediction

The crystal structures of paracetamol Form I, α-L-Glutamic acid and β-D-mannitol were calculated and found to be in agreement to "real world" values, where the lattice energy was compared to the enthalpy of sublimation. With the only substantial difference being found for LGA where the lattice energy was calculated as -57.16 kcal/mol whilst the enthalpy of sublimation was found to be -63.68 kcal/mol.

Morphologies were then predicted using the attachment energy model and a generic force field (Dreiding), which showed good agreement with experimentally observed crystals with most major facets being correctly calculated. DMAN showed the only exception as experimentally the (120) facet was not present in the prediction. In its place the 110 resided. However, the rest of the morphology was correctly predicted.

The slight discrepancies are caused by the use of a generic model to predict the morphologies. However, by using a generic model, it allows for all systems to be described using the same "chemistry" which was critical for calculating the interactions between these systems.

7.3.1.2 Facet Indexing

By indexing the crystals of the substrates, it was possible to compare the ranking of most to least adhesive facets between the in-silico and experimental methodologies, allowing for conclusions to be drawn based on their surface chemistry.

Large substrate crystals were indexed by the use of powder x-ray diffraction. This was done by aligning the plane of the desired facet to that of the sample holder and carrying out a normal range scan for the given sample. By doing so, it was possible to isolate the peaks in the diffraction pattern that were caused by the given Miller plane. Experimentally measured diffractions were compared with simulated powder patterns from known single crystals deposited in the Cambridge Structural Database (CSD).

The Para substrate crystal was fully indexed on all three analysed facets. The facets used for the facet-facet measurements were ($10\bar{1}$), (101), and ($11\bar{1}$), which were predicted as observable in the theoretical model. Due to the large size ($\geq 1cm$) of the crystal, the diffraction patterns were clear and defined. The excipient crystals of DMAN and LGA were smaller in size ($\leq 2mm$) and posed greater challenges in successfully indexing using the same methodology. Due to their smaller size, only one facet from each crystal was index as the crystals could not be re-orientated as easily as the Para crystal. The LGA facet was measured as the (111) whilst the DMAN was (110), both of which were predicted in the morphology calculations.

7.3.2 Defining The Surface

Surfaces were computational defined based on the crystallographic data in order to simulate an approximation of a real facet. Notably, while the surfaces were calculated to be energetically favourable, they were not fully comparable with the experimentally measured ones due to their topological representation. In order to have comparable surfaces, the experimental crystals were also cleaned, i.e. surface contaminants were reduced, in order to probe the surface chemistry of the crystal.

7.3.2.1 In-Silico Surface Representation

Slabs of atomically smooth surfaces were generated with the use of optimised structures. The surfaces were simulated as pristine, defect-free, and at 0K with no surface features.

The surface properties of all three systems were calculated for each facet. Chemically, the density of H-Bond donors, acceptors and aromatic groups were quantified whilst physically the topological roughness of the surfaces were calculated as the rugosity, ratio between true area and projected area, and the Rq which can be described as the RMSD of the surface.

It was found that DMAN facet (020) had the highest surface roughness with and Rq and Rugosity of 6.88 Åand 1.76 rugosity, which is a large difference when compared to the smoothest facet (101) of Para with values of 2.43 Åand 1.20. The roughness was caused by the high protrusion of the functional groups and thus

increased in height from the mean of the plane.

Utilising such surface descriptors allowed for quantifiable measurements to be made which informed linear models that calculated the relationship between the chemical and physical descriptors, and the interaction energy between given facets.

7.3.2.2 Cleaning and roughness

Utilising cleaned Para surfaces allowed for more reliable comparisons to be drawn between the in-silico model and the experimentally measured interactions.

A cleaning study was carried out in order to determine the most efficient protocol for removing surface contamination from the Para facets. Multiple solvents and mechanical actions were screened, selecting the least aggressive method which has the highest efficacy.

Initially, atomic force (AFM) and optical microscopy were used to rule out all inadequate solvents and methods. Wiping the surface of a crystal with dichloromethane (DCM) wetted lens tissue was shown to have the least topological image on the surface of Para facets. Methods such as compressing, rolling or pressurised jet caused large macro-scale damage to the surface, which were visible with the optical microscope. Ethanol, methanol and water, both unsaturated and saturated, showed to roughen the surface topography, with damage from saturated water only being visible at the micron scale.

The adhesive forces between the AFM tip and surfaces were measured in order to determine the surface uniformity post-cleaning. It was found that all solvents, with the exception of DCM, reduced the uniformity of the surface, indicating the presence of contaminants or surface-bound solvent due to the solubility and volatility of the solvents. As DCM was found to remove surface debris and not damage the topography adequately, it was chosen as the cleaning solvent.

In order to ascertain the impact on the surface chemistry when cleaning with DCM, near ambient pressure x-ray photoelectron spectroscopy was carried out to determine the change in surface chemistry post-cleaning. This study was carried out in collaboration with the Schroeder group (University of Leeds)which found that 19 % of chemical contaminants were removed with the use of DCM and no traces of the solvent were left on the surface - indicating that the cleaning was physically removing particulate contaminants, visible with microscopy, but also removing chemical contamination such as hydrocarbons.

Surface roughness was measured using an AFM, and confocal microscopy for the substrates, whilst the probes were measured using just the AFM. Probes were measured with confocal in order to determine the surface area of the probe, which was then used to normalise the force measurements.

7.3.3 Inter-Particulate Interactions

For the in-silico approach, a molecular mechanics (MM) workflow has been developed to calculate the interfacial interactions between faceted organic crystals. The Surface-Surface Interaction Model (SSIM) was designed to calculate the interaction energy between two slabs of molecules at an atomistic scale. By focusing on facet-specific interactions, energetics associated with the surface chemistry can be identified. A surface compatibility ranking system allows relative comparisons to be made between adhesive and cohesive forces.

Previously, atomic force microscopy (AFM) studies have demonstrated the use of colloidal probes and coated cantilevers in order to gain insights into powder adhesive properties. However, the lack of fully faceted organic crystal adhesion data has made it difficult to relate these properties to the surface chemistry. This study has used AFM to measure the adhesive forces between defined crystal planes of paracetamol and a range of excipients (α-L-Glutamic Acid and β-D-Mannitol) to ascertain the impact surface chemistry and topography has on facet-facet interactions. Furthermore, the ranking of API-excipient interactions measured with AFM have shown good agreement with the in-silico results.

7.3.3.1 Surface-Surface Interaction Model

The implementation and theory of Surface-Surface Interaction Model (SSIM) has been outlined. Briefly, it calculates the interaction energy between two facets for all unique direct space positions in order to capture the energy landscape of two facets interacting. This is an improvement on existing methods which use the lowest energy point as an indicator of the interaction between two surfaces. Energy distribution showed the flaw of using the lowest energy as the singular point at which the energy is most attractive is typically where the facets interlock, sometimes replicating a continuation of the lattice. However, the energy differences compared to the mean of energy distributions could be an order of magnitude as seen for one set of facets (Para($10\bar{1}$)/Para($10\bar{1}$)) where the lowest energy point was $-300mJ/m^2$ where the mean was $-50mJ/m^2$.

Due to the large data set created from probing every single possible position between two facets, an analysis tool has been developed in conjunction with the model ssim_tool. The tool allows for the normalisation of data, categorisation into facet/facet interactions, calculation of cohesive/adhesive balance plots, the weighted probability to surface representation, generation of heat maps to determine positions of interactions, and the generation of energy-displacement density plots allowing the user to determine whether the interactions are dominated by topological or chemical features. Such a tool allows for multiple data sets to be analysed in minutes

compared to laborious extensive data generated by other computational methods such as molecular dynamics.

The data calculated and analysed for Para, DMAN, and LGA demonstrated the possibilities of using such tools. It was found that an increase in roughness on the atomistic scale typically resulted in higher interaction energy which is the opposite to the AFM data. This was due to a higher degree of contact being made between the in-silico surfaces and thus interlocking occurring which was exaggerated by the pseudo periodic nature of the surface. Furthermore, the rough surfaces exposing more of the molecules with more interactions therefore possibly giving a higher energy surface (much like where atomic defects and step edges/terraces are higher energy than the flat atomic plane).

Para showed to have the highest interaction energy with DMAN(020) possibly due to the high roughness found on the (020) facet. As expected for such neutrally charged systems, it was found that van der Waals (VdW) dominated for most interactions where they made up at least 85 % of the total interaction energy. Probe interactions were ranked for all Para probes in order of most to least interactive to all other substrate facets, and these are shown below:

$$Para/Para : (10\bar{1}), (101) > (11\bar{1}) > (110) >> (020) > (011)$$

$$Para/LGA : (11\bar{1}) > (101) > (110), (10\bar{1}) >> (011) > (020)$$

$$Para/DMAN : (11\bar{1}) > (101), (10\bar{1}) > (110) >> (011) > (020)$$

The ranking of these facets supports statements made in a few studies regarding the relationship between the anisotropy factor (% of satisfied intermolecular bonds on the surface), where the lower % is indicative of a more reactive surface[189, 55, 112, 85]. With an exception for facets such as Para(020) and (110) which are not in agreement with the anisotropy factor ranking, caused by the roughness and chemistry of the probing surface.

7.3.3.2 Facet-Facet Measurements

To reliably measure the surface properties contributions to an interaction between two facets, facet-facet adhesive forces were measured using AFM.The adhesion between faceted organic crystals was measured for the first time. Small crystals were mounted onto the end of AFM cantilevers, and with the orientation of the substrate crystals (also faceted) adjusted, the two crystals were brought into contact. Upon separation, the force required to "pull" them apart was measured and correlated to the adhesive force required per unit area.

Forces were measured for the fully indexed Para crystal allowing for three discreet

facets of the same crystal to be measured, giving a ranking of most interactive facets as shown below:

$$Para/Para : F_{10\bar{1}} >> F_{101} > F_{11\bar{1}}$$

Similarly to the in-silico results, the $(10\bar{1})$ was found to be the most adhesive for Para/Para systems followed by the (101) and $(11\bar{1})$. Showing good agreement between the computational and experimental methods.

The probes could not be indexed due to their small size; however, as they were all measured against a single facet of both excipient as such they can be ranked based on the probe number, shown below:

$$Para/DMAN : P_3 \approx P_2 >> P_1$$

$$Para/LGA : P_3 > P_2 >> P_1$$

Using the in-silico data it is possible to propose that P_3 and P_2 are the $(11\bar{1})$ and (101) facet respectively, whilst P_1 could be the (101) or (020) based on the overall low adhesive properties.

During AFM measurements, the quality of the data could be determined from the detailed characteristics of the force-spectroscopy curves. During data collection, it was identified that limited facet-facet contact, asperity presence, and capillary forces were impacting the adhesive forces measured. When capillary forces were detected the scans were repeated at a lower % RH, thus excluding them altogether. In regards to the asperities and limited contact, they were kept within the data set as they still represented real interactions between the two surfaces.

The capillary forces were seen, due to the generally low humidity in the laboratory, were caused by adsorbed water onto the surface of the crystal, these were seen only in DMAN. Asperity breakages were predominantly seen in LGA due to the higher quantity of asperity present on the surface, as identified by AFM imaging. Finally, limited contact occurs when two large asperities from both surfaces collide, prohibiting contact from being made between the surfaces, resulting in no adhesion force measurement being measured. The height and adhesion maps for a given facet-facet measurement showed an inverse correlation, similar to the in-silico approach describing that at a greater displacement of a probe facet the adhesion force was higher.

7.3.4   Cohesive-Adhesive balance

In order to compare the theoretical and experimental work in relative terms, the Cohesive/Adhesive Balance (CAB) was used to determine facet affinities for interactions. Computationally, more facets were calculated, leading to a larger data set

consisting of many different surface chemistries. With a larger dataset size, it was possible to predict more reliable system behaviours.

Computationally it was found that Para prefers to adhere to itself in the presence of DMAN, whereas in the presence of LGA it would rather adhere to it. In other words, Para is more cohesive with DMAN and more adhesive with LGA.

Experimentally, whilst fewer facets were measured, a similar trend emerged where Para was seen to be more cohesive with DMAN and adhesive with LGA, thus qualitatively validating the computational model. Furthermore, the Para probe data showed the same ranking of energy/force for the cohesive measurements (Para/-Para). In both cases the ranking of most interactive probes were $(10\bar{1}) \approx (101) >> (11\bar{1})$, indicating that the two approaches are within agreement.

Based on the theoretical calculations, the strong interactions were due to a higher density of H-Bond acceptor groups on the surface, as calculated by the multi-variant linear regression model.

By utilising the morphology data and weighting the interaction energies based on the surface area representation, it was possible to determine the expected interaction energy per area. This approach reduced the impact smaller, and higher energy facets had on the overall system calculations. However, the CAB then predicted both DMAN /LGA to be adhesive with Para. This approach could be used to include downstream processing and experimental data, where the morphology of the crystal and its facet representations are known and as such can simply be added to the model to predict average powder behaviour across the entire particle.

7.3.5 Impact of Surface Properties

Both theoretical and experimental approaches highlighted specific aspects of the surface properties that have a significant impact on the interfacial interactions between faceted crystals. In both instances, surface roughness had the largest contribution to the interaction energy and force of adhesion. As it was expected, the increase in roughness on the macro scale reduced the adhesion force recorded for all systems. However, instances where the surfaces were smooth on the macro scale but rough on the nanoscale, increased the experientially measured adhesive forces. Similarly, computationally measured interactions showed that certain types of roughness could increase the interaction energy between to facets as it allows for closer contact between the two surfaces with an increased contact area. This was seen for interactions between Para and DMAN, where the (020) facet showed a substantially larger average interaction energy compared to all other calculations.

From the large calculated data set, it was possible to identify specific surface features which have a higher impact on the interaction energy. It was demonstrated

when analysing the surface chemistry of Para-LGA using multivariate linear regression that the H-Bond acceptor groups on LGA such as C=O and COO$^-$ have a higher impact on the interaction energy than its H-bond donor groups (NH$_3^+$ and OH). Moreover, the orientation of functional groups on the surface was identified as one of the reasons for drastic changes in interaction energy as these can affect whether the functional groups are accessible for directionality driven by intermolecular interactions such as HB.

Experimentally, the forces measured did occasionally include the presence of capillary forces in the case of DMAN measured with Para. This was caused by the more hydrophilic nature surface of DMAN, which caused a layer of water to adsorb on the surface. This phenomenon was not constant throughout measurements as the % RH was kept below 45%, which appeared to be the boundary point between water being present or not on the surface of DMAN. In order to fully understand the impact of surface-bound water on the adhesion properties, a relative humidity study would be required, as detailed in future work. Similar measurements were not found for LGA and Para as both have been previously reported to have a lower higher contact angle and thus less hydrophilic.

7.3.6 Concluding Remarks

The presented body of work has demonstrated that we can begin to understand the interfacial interactions between faceted organic crystals. The novelty is demonstrated in the development of an in-silico methodology, the tool to analyse data from the surface-surface interaction model, experimentally measuring individual facet forces, studying the cleaning required for a sensitive organic crystal, and finally correlating the in-silico work with the experimental measurements on faceted crystals to gain a multi-scale perspective on the interactions.

The in-silico methodology that was developed calculated interaction of opposing crystal slabs, taking into account approach distance and atomic roughness induced steric repulsions, displacements and rotation. Full maps of the interaction space were produced allowing identification of the mechanism of surface interaction, all a marked improvement on single molecular probe methods and anisotropy factor.

AFM adhesion data has previously been shown to correlate well with actual formulation performance, as opposed to other techniques such as IGC. In this study, the facet specific interactions were measured for the first time and shown to be in agreement with the in silico method. It was found, not unexpectedly, that micro-surface roughness controlled surface adhesion, although in silico measurements showed conversely that atomic roughness increased surface adhesion.

With the use of these developed tools, it is possible for formulators and solid-

state scientists to better guide their decisions in formulating and understanding the powder and particle behaviour in future drug products. Due to the predictive nature of the in-silico model, resource-intensive experiments during drug development can be reduced, thus helping to bring medication to market sooner.

7.4 Future Work

In order to improve and further advance the understanding of interfacial interactions, a few developments need to be made. A note has been made on each of these and their impact on the existing and presented knowledge.

Firstly, the representation of surfaces within the in-silico model is idealistic, with zero defects or surface features. Implementing surface features to the model or macro-scale roughness would allow for the gap between the current model and AFM data to be better bridged, explaining macro-scale feature contributions. This would require the use of molecular mechanics due to the size requirements; however, with the current script implementation, the algorithms could be transferred to other programs.

In the process of calculating the interaction energy and quantifying the contributions from each surface, it would be very interesting to capture the % of surface bonds that are satisfied by the incoming surface interaction. Currently, the attachment energy (AE) is being calculated per unit of area giving a maximum to interaction energy between two surfaces (of the same plane), the percentage of interaction energy fulfilled would offer an interesting measurement of how satisfied a surface is. Currently, that calculation is possible for like surface but would be more useful when looking at heterogeneous surfaces.

The reliability of facet-facet contact area could be improved from the current methodology. The use of motorised goniometer should be implemented in order to align the substrate to the probe precisely. Furthermore, imaging of the two surfaces as the forces are being measured with an instrument such as micro-CT would allow for the exact contact area between the two surfaces to be measured thus providing the most accurate values to normalise the forces to as the contact area has a large impact on the measured force.

Subsequently, a dynamic roughness study should be carried out to measure the change in surface roughness, if any, before and after colliding the two surfaces together. This would enable us to determine whether the surface degrades during measurements, as such, improves our confidence in the measured adhesive forces.

Finally, the relative humidity has been mentioned many times to have an impact on the adhesion of two facets. As seen with DMAN, the presence of capillary forces were apparent below 45 % RH, not the case for Para and LGA. Conducting a relative humidity study would help identify the role surface-bound solvent has on the adhesive properties in varying amounts. Secondly, it would also allow for the simulation of a wet granulation process, and it would provide vital information on the surface hydrophilicity of surfaces.

Similarly, the impact of solvent/water should be studied for the in-silico method-

ology. Adding the presence of explicit solvents, such as water, in the model would replicate process conditions seen in the industry allowing for models to be a better representative of surfaces that have been wetted.

References

[1] David Taylor. The Pharmaceutical Industry and the Future of Drug Development. In R.E. Hester Harrison and R.M., editors, *Pharmaceuticals in the Environment*, pages 1–33. The Royal Society of Chemistry, 2015.

[2] California Biomedical Research Association. Fact Sheet New Drug Development Process. pages 1–2, 2012.

[3] A. H L Chow, H. H Y Tong, Pratibhash Chattopadhyay, and Boris Y. Shekunov. Particle engineering for pulmonary drug delivery. *Pharmaceutical Research*, 24(3):411–437, 2007.

[4] A.W. Miziolek, V. Palleschi, and I. (Eds.) Schechter. Laser Induced Breakdown Spectroscopy, 2006.

[5] Anahita Fathi-Azarbayjani, Abolghasem Jouyban, and Sui Yung Chan. Impact of Surface Tension in Pharmaceutical Sciences. *J Pharm Pharmaceut Sci (www.cspsCanada.org)*, 12(2):218–228, 2009.

[6] Sonali S Bharate, Sandip B Bharate, and Amrita N Bajaj. Interactions and incompatibilities of pharmaceutical excipients with active pharmaceutical ingredients : a comprehensive review. *Journal of excipients and food chemistry*, 1(3):3–26, 2010.

[7] Kwok Chow, Henry H.Y. Y Tong, Susan Lum, and Albert H.L. L Chow. Engineering of Pharmaceutical Materials: An Industrial Perspective. *Journal of Pharmaceutical Sciences*, 97(8):2855–2877, aug 2008.

[8] Sari Airaksinen, Milja Karjalainen, Niina Kivikero, Sari Westermarck, Anna Shevchenko, Jukka Rantanen, and Jouko Yliruusi. Excipient selection can significantly affect solid-state phase transformation in formulation during wet granulation. *AAPS PharmSciTech*, 6(2):E311–E322, 2005.

[9] Ulrich J. Griesser. The Importance of Solvates. In *Polymorphism: in the Pharmaceutical Industry*, pages 211–233. 2006.

[10] Rajendra K. Khankari and David J W Grant. Pharmaceutical hydrates. *Thermochimica Acta*, 248(C):61–79, 1995.

[11] SP Heinrich and CG Wermuth. Handbook of pharmaceutical salts; properties, selection, and use, 2008.

[12] Y A Abramov. *Computational Pharmaceutical Solid State Chemistry*. Wiley, 2016.

[13] Alfred Y Lee, Deniz Erdemir, and Allan S. Myerson. Crystal Polymorphism in Chemical Process Development. *Annu. Rev. Chem. Biomol. Eng*, 2:259–80, 2011.

[14] C. Sudha and K. Srinivasan. Nucleation control and separation of paracetamol polymorphs through swift cooling crystallization process. *Journal of Crystal Growth*, 401:248–251, 2014.

[15] Henry H Y Tong, Boris Y. Shekunov, John P. Chan, Cedric K F Mok, Henry C M Hung, and Albert H L Chow. An improved thermoanalytical approach to quantifying trace levels of polymorphic impurity in drug powders. *International Journal of Pharmaceutics*, 295(1-2):191–199, 2005.

[16] Siti Fatimah Binti Ibrahim. *Prediction of the Mechanical Properties of Molecular Crystals Based Upon Their Crystallographic Structure*. PhD thesis, University of Leeds, 2016.

[17] John F. Gamble, Michael Leane, Dolapo Olusanmi, Michael Tobyn, Eneš Enes Supuk, Jiyi Khoo, Majid Naderi, Eneš Enes Supuk, Jiyi Khoo, Majid Naderi, Enes Šupuk, Jiyi Khoo, and Majid Naderi. Surface energy analysis as a tool to probe the surface energy characteristics of micronized materials - A comparison with inverse gas chromatography. *International Journal of Pharmaceutics*, 422(1-2):238–244, 2012.

[18] Current Chemical and Engineering Challenges. *Pharmaceutical Process Development. Current Chemical and Engineering Challenges*. 2011.

[19] Darragh Murnane, Christopher Marriott, and Gary P. Martin. Polymorphic control of inhalation microparticles prepared by crystallization. *International Journal of Pharmaceutics*, 361(1-2):141–149, 2008.

[20] Raimundo Ho and Jerry Y Y Heng. A review of inverse gas chromatography and its development as a tool to characterize anisotropic surface properties of pharmaceutical solids, 2012.

[21] Renu Chadha and Swati Bhandari. Drug-excipient compatibility screening-Role of thermoanalytical and spectroscopic techniques. *Journal of Pharmaceutical and Biomedical Analysis*, 87:82–97, 2014.

[22] Nicholas Kevlahan. Principles of Multiscale Modeling. *Physics Today*, 65(6):56, 2012.

[23] Y A Abramov. *Computational Pharmaceutical Solid State Chemistry*. Wiley, 2016.

[24] Vasuki Ramachandran, Darragh Murnane, Robert B. Hammond, Jonathan Pickering, Kevin J. Roberts, Majeed Soufian, Ben Forbes, Sara Jaffari, Gary P. Martin, Elizabeth Collins, and Klimentina Pencheva. Formulation pre-screening of inhalation powders using computational atom-atom systematic search method. *Molecular Pharmaceutics*, 12(1):18–33, 2015.

[25] R. B. Hammond, K. Pencheva, V. Ramachandran, and Kevin J. Roberts. Application of Grid-Based Molecular Methods for Modeling Solvent-Dependent Crystal Growth Morphology: Aspirin Crystallized from Aqueous Ethanolic Solution. *Crystal Growth & Design*, 7(9):1571–1574, sep 2007.

[26] E. Hasselbrink. Capturing the Complexities of Molecule-Surface Interactions. *Science*, 326(5954):809–810, 2009.

[27] Joanna Bojarska and Waldemar Maniukiewicz. Investigation of intermolecular interactions in finasteride drug crystals in view of X-ray and Hirshfeld surface analysis. *Journal of Molecular Structure*, 1099:419–426, 2015.

[28] J. N. Israelachvili and D. Tabor. The Measurement of Van Der Waals Dispersion Forces in the Range 1.5 to 130 nm. *Proceedings of the Royal Society of London A: Mathematical, Physical and Engineering Sciences*, 331(1584), 1972.

[29] Hans-Jürgen Butt, Brunero Cappella, and Michael Kappl. Force measurements with the atomic force microscope: Technique, interpretation and applications. *Surface Science Reports*, 59(1-6):1–152, oct 2005.

[30] J. M. Montero, M. A. Isaacs, A. F. Lee, J. M. Lynam, and K. Wilson. The surface chemistry of nanocrystalline MgO catalysts for FAME production: An in situ XPS study of H2O, CH3OH and CH3OAc adsorption. *Surface Science*, 646:170–178, 2016.

[31] R Jones, H M Pollock, D Geldart, and A Verlinden. Inter-particle forces in cohesive powders studied by AFM: Effects of relative humidity, particle size and wall adhesion. *Powder Technology*, 132(2-3):196–210, 2003.

[32] Martin Götzinger and Wolfgang Peukert. Dispersive forces of particle-surface interactions: Direct AFM measurements and modelling. In *Powder Technology*, volume 130, pages 102–109, 2003.

[33] Matthew D. Jones and Graham Buckton. Comparison of the cohesion-adhesion balance approach to colloidal probe atomic force microscopy and the measurement of Hansen partial solubility parameters by inverse gas chromatography for the prediction of dry powder inhalation performance. *International Journal of Pharmaceutics*, 509(1-2):419–430, 2016.

[34] Hak Kim Chan. Dry powder aerosol drug delivery-Opportunities for colloid and surface scientists. *Colloids and Surfaces A: Physicochemical and Engineering Aspects*, 284-285:50–55, 2006.

[35] Robert B. Hammond, Vasuki Ramachandran, and Kevin J. Roberts. Molecular modelling of the incorporation of habit modifying additives: α-glycine in the presence of l-alanine. *CrystEngComm*, 13(15):4935, 2011.

[36] Umang V. Shah, Dolapo Olusanmi, Ajit S. Narang, Munir A. Hussain, John F. Gamble, Michael J. Tobyn, and Jerry Y Y Heng. Effect of crystal habits on the surface energy and cohesion of crystalline powders. *International Journal of Pharmaceutics*, 472(1-2):140–147, 2014.

[37] J. W. Mullin. *Crystallization, Fourth Edition*. Butterworth-Heinemann, Oxford, 4 edition, 2001.

[38] René-Just Haüy. Essai d'une théorie sur la structure des crystaux, appliquée à plusieurs genres de substances crystallisées. 1784.

[39] René Just Haüy. *Traité de minéralogie*. Paris : Louis, 1801.

[40] H Dorsett. *Overview of Molecular Modelling and Ab initio Molecular Orbital Methods Suitable for use with Energetic Materials*. 2000.

[41] J D Wright. *Molecular Crystals*. Cambridge University Press, 2nd editio edition, 1995.

[42] Catherine E. Housecroft and Edwin C E.C. Constable. *Chemistry: An Introduction to Organic, Inorganic and Physical Chemistry*. 2010.

[43] Jacob N. Israelachvili. *Intermolecular and surface forces.* Academic Press, 2011.

[44] R. Clydesdale, G.; Roberts, K.; Docherty. The crystal habit of molecular materials: a structural perspective. In Angelo. Gavezzotti, editor, *Theoretical Aspects and Computer Modeling of the Molecular Solid State*, chapter 7, page 204. John Wiey & Sons, 1997.

[45] Yasuo. Arai. *Chemistry of Powder Production*, volume 1 English. Springer Netherlands, Dordrecht, 1996.

[46] J. W. Gibbs. On the Equilibrium of Heterogeneous Substances. In *Transactions Of The Connecticut Academy of Arts and Science Vol III*, chapter 5, pages 97–198. The Academy, 1875.

[47] G. Wulff. Zur Frage der Geschwindigkeit des Wachsthums und der Auflösung der Krystallflächen. *Zeitschrift für Kristallographie - Crystalline Materials*, 34(1-6):499, 1901.

[48] Auguste Bravais. *Études crystallographiques.* Gauthier-Villars, Paris, 1866.

[49] M G Freidel. Etudes sur la loi de Bravais. *Bull. Soc. Franc. Miner.*, 9:326, 1907.

[50] D. Harker J.D.H. Donnay. A New Law of Crystal Morphology Extending The Law Of Bravais. *American Mineralogist*, 22:446, 1937.

[51] P. Hartman and W. G. Perdok. On the relations between structure and morphology of crystals. III. *Acta Crystallographica*, 8(9):525–529, sep 1955.

[52] IUPAC. *Compendium of Chemical Terminology.* 2014.

[53] H J Human, J P Van Der Eerden, L A M J Jetten, and J G M Odekerken. On the roughening transition of biphenyl: Transition of faceted to non-faceted growth of biphenyl for growth from different organic solvents and the melt. *Journal of Crystal Growth*, 51(3):589–600, 1981.

[54] L A M J Jetten, H J Human, P Bennema, and J P Van Der Eerden. On the observation of the roughening transition of organic crystals, growing from solution. *Journal of Crystal Growth*, 68(2):503–516, 1984.

[55] Alexandru A Moldovan, Ian Rosbottom, Vasuki Ramachandran, Christopher M Pask, Oboroghene Olomukhoro, and Kevin J Roberts. Crystallographic Structure, Intermolecular Packing Energetics, Crystal Morphology

and Surface Chemistry of Salmeterol Xinafoate (Form I). *Journal of Pharmaceutical Sciences*, 106(3):882–891, mar 2017.

[56] Ian M. Grimsey, Jane C. Feeley, and Peter York. Analysis of the surface energy of pharmaceutical powders by inverse gas chromatography. *Journal of pharmaceutical sciences*, 91(2):571–83, feb 2002.

[57] Gary. Attard and Colin. Barnes. *Surfaces*. Oxford University Press, 1998.

[58] Irving Langmuir. The constitution and fundamental proeprties of solids and liquids. Part 1. Solids. *Journal of the American Chemical Society*, 38(11):2221–2295, nov 1916.

[59] 1.6 Relaxation & Reconstruction of Surfaces.

[60] Zhiyong Gao, Chengwei Li, Wei Sun, and Yuehua Hu. Anisotropic surface properties of calcite: A consideration of surface broken bonds, 2017.

[61] A E Romanov, A L Kolesnikova, I S Yasnikov, A A Vikarchuk, M V Dorogov, A N Priezzheva, L M Dorogin, and E C Aifantis. Relaxation phenomena in disclinated microcrystal. *Rev. Adv. Mater. Sci*, 48:170–178, 2017.

[62] Thomas Young. An Essay on the Cohesion of Fluids. *Proceedings of the Royal Society of London*, 1(January):171–172, jan 1805.

[63] Jabez Chinnam, Debendra Das, Ravikanth Vajjha, and Jagannadha Satti. Measurements of the contact angle of nanofluids and development of a new correlation. *International Communications in Heat and Mass Transfer*, 62:1–12, 2015.

[64] Agnieszka Pozarska, Claudia Da Costa Mathews, Mei Wong, and Klimentina Pencheva. Application of COSMO-RS as an excipient ranking tool in early formulation development. *European Journal of Pharmaceutical Sciences*, 49(4):505–511, 2013.

[65] T Todorova and B Delley. Wetting of paracetamol surfaces studied by DMol3-COSMO calculations. *Molecular Simulation*, 34(10-15):1013–1017, 2008.

[66] B. Delley. The conductor-like screening model for polymers and surfaces. *Molecular Simulation*, 32(2):117–123, 2006.

[67] Jonathan P. K. Seville and Chuan-Yu Wu. *Particle Technology and Engineering. An Engineer's Guide to Particles and Powders: Fundamentals and Computational Approaches.* 2016.

[68] R. A. Fisher. On the capillary forces in an ideal soil; correction of formulae given by W. B. Haines. *The Journal of Agricultural Science*, 16(03):492, jul 1926.

[69] Jonathan Seville, Ugur Tuzun, and Roland Clift. *Processing of Particulate Solids*. Springer Netherlands, Dordrecht, 1997.

[70] R Price, P.M M Young, S Edge, and J.N N Staniforth. The influence of relative humidity on particulate interactions in carrier-based dry powder inhaler formulations. *International Journal of Pharmaceutics*, 246(1-2):47–59, oct 2002.

[71] Jennifer C Hooton, Caroline S German, Stephanie Allen, Martyn C Davies, Clive J Roberts, Saul J B Tendler, and Philip M Williams. of the Effect of Nanoscale Contact Geometry and Surface Chemistry on. 21(6), 2004.

[72] Tao Jiang and Yong Zhu. Measuring graphene adhesion using atomic force microscopy with a microsphere tip. *Nanoscale*, 7(24):10760–10766, 2015.

[73] J.A.S. Cleaver and J.W.G. Tyrrell. The Influence of Relative Humidity on Particle Adhesion. *Kona Powder and Particle*, 22(22):9, 2004.

[74] Jacob N. Israelachvili. Strong Intermolecular Forces: Covalent and Coulomb Interactions. *Intermolecular and Surface Forces*, pages 53–70, 2011.

[75] Jacob N. Israelachvili. Interactions Involving Polar Molecules. *Intermolecular and Surface Forces*, pages 71–90, 2011.

[76] Jacob N. Israelachvili. Interactions Involving the Polarization of Molecules. *Intermolecular and Surface Forces*, pages 91–106, 2011.

[77] Jacob N. Israelachvili. Van der Waals Forces. *Intermolecular and Surface Forces*, pages 107–132, 2011.

[78] Frank Jensen. *Introduction to Computational Chemistry*. 2007.

[79] Peter. Bladon, John E. Gorton, Robert B. Hammond, and Royal Society of Chemistry (Great Britain). *Molecular modelling : computational chemistry demystified*. RSC Publishing, nov 2012.

[80] Bhaskar Chilukuri and Thomas R Cundari. Surface interactions of Au(I) cyclotrimer with Au(111) and Al(111) surfaces: A computational study. *Surface Science*, 606(13-14):1100–1107, 2012.

[81] Petra M. Hansson, Agne Swerin, Joachim Schoelkopf, Patrick A C Gane, Esben Thormann, Patrick A C Gane, and Esben Thormann. Influence of surface topography on the interactions between nanostructured hydrophobic surfaces. *Langmuir*, 28(21):8026–8034, 2012.

[82] E. Chigo Anota, D Cortes Arriagada, A. Bautista Hernández, and M Castro. In silico characterization of nitric oxide adsorption on a magnetic [B_24N_36 fullerene/(TiO_2)_2] - nanocomposite. *Applied Surface Science*, 400:283–292, apr 2017.

[83] Michał Wera, Piotr Storoniak, Damian Trzybiński, and Beata Zadykowicz. Intermolecular interactions in multi-component crystals of acridinone/thioacridinone derivatives: Structural and energetics investigations. *Journal of Molecular Structure*, 1125:36–46, 2016.

[84] Yi Gao and Kenneth W Olsen. Molecular dynamics of drug crystal dissolution: Simulation of acetaminophen form I in water. *Molecular Pharmaceutics*, 10(3):905–917, 2013.

[85] I Rosbottom, K J Roberts, and Docherty R. The solid state, surface and morphological properties of p-aminobenzoic acid in terms of the strength and directionality of its intermolecular synthons. *CrystEngComm*, 17:5768–5788, 2015.

[86] Robert Hooke. *Lectures De Potentia Restitutiva, or of Spring Explaining the Power of Springing Bodies.* The Royal Society, 1678.

[87] J. H. Waite and C. C. Broomell. Changing environments and structure-property relationships in marine biomaterials. *Journal of Experimental Biology*, 215(6):873–883, 2012.

[88] Kazue Kurihara. Molecular Architecture Studied by the Surface Forces Measurement. *Langmuir*, 32(47):12290–12303, 2016.

[89] Dennis C. Prieve. Measurement of colloidal forces with TIRM. *Advances in Colloid and Interface Science*, 82:93–125, 1999.

[90] Xiangjun Gong, Zhaohui Wang, and To Ngai. Direct measurements of particle-surface interactions in aqueous solutions with total internal reflection microscopy. *Chemical communications (Cambridge, England)*, 50(50):6556–70, 2014.

[91] Laurent Helden, Kilian Dietrich, and Clemens Bechinger. Interactions of Colloidal Particles and Droplets with Water-Oil Interfaces Measured by Total Internal Reflection Microscopy. *Langmuir*, 32(51):13752–13758, dec 2016.

[92] Zhaohui Wang, Chuanxin He, Xiangjun Gong, Jianqi Wang, and To Ngai. Measuring the surface-surface interactions induced by serum proteins in a physiological environment. *Langmuir*, 32(46):12129–12136, nov 2016.

[93] Drug Patent International. IGC Diagram, 2014.

[94] Pirre P. Yla Maihaniemi, Jerry Y.Y. Y. Heng, Frank Thielmann, and Daryl R Williams. Inverse Gas Chromatographic Method for Measuring the Dispersive Surface Energy Distribution for Particulates. *Langmuir*, 24(17):9551–9557, sep 2008.

[95] Robert R Smith, Daryl R Williams, Daniel J Burnett, and Jerry Y Y Heng. A New Method to Determine Surface Energy Site Distributions by Inverse Gas Chromatography A New Method to Determine Dispersive Surface Energy Site Distributions by Inverse Gas Chromatography. 2014.

[96] David Cline and Richard Dalby. Predicting the quality of powders for inhalation from surface energy and area. *Pharmaceutical research*, 19(9):1274–7, sep 2002.

[97] Henry H.Y. Tong, Boris Y. Shekunov, Peter York, and Albert H.L. Chow. Predicting the aerosol performance of dry powder inhalation formulations by interparticulate interaction analysis using inverse gas chromatography. *Journal of Pharmaceutical Sciences*, 95(1):228–233, jan 2006.

[98] G. Binnig, C. F. Quate, and Ch. Gerber. Atomic force microscope. *Physical Review Letters*, 56(9):930–933, mar 1986.

[99] AFM (Atomic Force Microscope) - University of Greifswald.

[100] Jeffrey L. Hutter and John Bechhoefer. Calibration of atomic-force microscope tips. *Review of Scientific Instruments*, 64(7):1868–1873, jul 1993.

[101] William A. Ducker, Tim J. Senden, and Richard M. Pashley. Direct measurement of colloidal forces using an atomic force microscope. *Nature*, 353(6341):239–241, sep 1991.

[102] F Pouille. Enforcement of Temporal Fidelity in Pyramidal Cells by Somatic Feed-Forward Inhibition. *Science*, 293(5532):1159–1163, aug 2001.

[103] Heinrich Hertz. Ueber die Berührung fester elastischer Körper. *Journal für die reine und angewandte Mathematik (Crelle's Journal)*, 1882(92):156–171, 1882.

[104] Yu. D. Ivanov, T. O. Pleshakova, K. A. Malsagova, A. L. Kaysheva, A. T. Kopylov, A. A. Izotov, V. Yu. Tatur, S. G. Vesnin, N. D. Ivanova, V. S. Ziborov, and A. I. Archakov. AFM-based protein fishing in the pulsed electric field. *Biochemistry (Moscow) Supplement Series B: Biomedical Chemistry*, 9(2):121–129, apr 2015.

[105] B.V Derjaguin, V.M Muller, and Yu.P Toporov. Effect of contact deformations on the adhesion of particles. *Journal of Colloid and Interface Science*, 53(2):314–326, nov 1975.

[106] E.R. R Beach, G.W. W Tormoen, J Drelich, and R Han. Pull-off Force Measurements between Rough Surfaces by Atomic Force Microscopy. *Journal of Colloid and Interface Science*, 247(1):84–99, mar 2002.

[107] Robert B. Hammond, Caiyun Ma, Kevin J. Roberts, Phuong Y. Ghi, and Robin K. Harris. Application of Systematic Search Methods to Studies of the Structures of Urea-Dihydroxy Benzene Cocrystals. *The Journal of Physical Chemistry B*, 107(42):11820–11826, 2003.

[108] R B Hammond, K Pencheva, and K J Roberts. Molecular modeling of crystal-crystal interactions between the α- and β-polymorphic forms of L-glutamic acid using grid-based methods. *Crystal Growth and Design*, 7(5):875–884, 2007.

[109] R. B. Hammond, S. Jeck, C. Y. Ma, K. Pencheva, K. J. Roberts, and T. Auffret. An examination of binding motifs associated with inter-particle interactions between facetted nano-crystals of acetylsalicylic acid and ascorbic acid through the application of molecular grid-based search methods. *Journal of Pharmaceutical Sciences*, 98(12):4589–4602, 2009.

[110] Thai T H Nguyen, Ian Rosbottom, Ivan Marziano, Robert B Hammond, and Kevin J Roberts. Crystal Morphology and Interfacial Stability of RS-Ibuprofen in Relation to Its Molecular and Synthonic Structure. 2017.

[111] Steve Beach, David Latham, Colin Sidgwick, Mazen Hanna, and Peter York. Control of the Physical Form of Salmeterol Xinafoate. *Org. Process Res. Dev.*, 3(5):370–376, 1999.

[112] Mathew J. Bryant, Ian Rosbottom, Ian J. Bruno, Robert Docherty, Colin M. Edge, Robert B. Hammond, Robert Peeling, Jonathan Pickering, Kevin J. Roberts, and Andrew G. P. Maloney. "Particle Informatics": Advancing Our Understanding of Particle Properties through Digital Design. *Crystal Growth & Design*, 19(9):5258–5266, 2019.

[113] Joanna M. Bak, Paulina M. Dominiak, Chick C. Wilson, and Krzysźtof Woniak. Experimental charge-density study of paracetamol - Multipole refinement in the presence of a disordered methyl group. *Acta Crystallographica Section A: Foundations of Crystallography*, 65(6):490–500, 2009.

[114] W Kaminsky and A M Glazer. Crystal optics of D-mannitol, C 6 H 14 O 6 : crystal growth, structure, basic physical properties, birefringence, optical activity, Faraday effect, electro-optic effects and model calculations . *Zeitschrift für Kristallographie*, 212(4):283–296, 1997.

[115] M. S. Lehmann and A. C. Nunes. A short hydrogen bond between near identical carboxyl groups in the α-modification of L-glutamic acid. *Acta Crystallographica Section B Structural Crystallography and Crystal Chemistry*, 36(7):1621–1625, jul 1980.

[116] Ying Li, Hui Li, Frank C. Pickard, Badri Narayanan, Fatih G. Sen, Maria K.Y. Chan, Subramanian K.R.S. Sankaranarayanan, Bernard R. Brooks, and Benoît Roux. Machine Learning Force Field Parameters from Ab Initio Data. *Journal of Chemical Theory and Computation*, 13(9):4492–4503, sep 2017.

[117] Tran Doan Huan, Rohit Batra, James Chapman, Sridevi Krishnan, Lihua Chen, and Rampi Ramprasad. A universal strategy for the creation of machine learning-based atomistic force fields. *npj Computational Materials*, 3(1), 2017.

[118] Dassault Systèmes BIOVIA. Materials Studio, 2016.

[119] Mopac. Quantum Chemistry Program Exchange Program.

[120] Robert B Hammond, Klimentina Pencheva, and Kevin J Roberts. Structural variability within, and polymorphic stability of, nano-crystalline molecular clusters of l-glutamic acid and D-mannitol, modelled with respect to their size, shape and 'crystallisability'. *CrystEngComm*, 14(3):1069–1082, 2012.

[121] G. L. Perlovich, Tatyana V. Volkova, and Annette Bauer-Brandl. Polymorphism of paracetamol. *Journal of Thermal Analysis and Calorimetry*, 89(3):767–774, sep 2007.

[122] Guido Barone, Giuseppe Della Gatta, Daniela Ferro, and Vincenzo Piacente. Enthalpies and entropies of sublimation, vaporization and fusion of nine polyhydric alcohols. *Journal of the Chemical Society, Faraday Transactions*, 86(1):75–79, 1990.

[123] Olga V Dorofeeva and Oxana N Ryzhova. Gas-phase enthalpies of formation and enthalpies of sublimation of amino acids based on isodesmic reaction calculations. *Journal of Physical Chemistry A*, 118(19):3490–3502, 2014.

[124] Peter A Wood, Tjelvar S.G. Olsson, Jason C Cole, Simon J Cottrell, Neil Feeder, Peter T.A. Galek, Colin R Groom, and Elna Pidcock. Evaluation of molecular crystal structures using Full Interaction Maps. *CrystEngComm*, 15(1):65–72, 2013.

[125] Gary Nichols, Christopher S. Frampton, Gary Nicnols, Christopher S. Frampton, Gary Nichols, and Christopher S. Frampton. Physicochemical characterization of the orthorhombic polymorph of paracetamol crystallized from solution. *Journal of Pharmaceutical Sciences*, 87(6):684–693, jun 1998.

[126] T. Beyer, T. Beyer, G. M. Day, G. M. Day, S. L. Price, and S. L. Price. The prediction, morphology, and mechanical properties of the polymorphs of paracetamol. *Journal of the American Chemical Society*, 123(21):5086–5094, 2001.

[127] Raimundo Ho, David A Wilson, and Jerry Y Y Heng. Crystal habits and the variation in surface energy heterogeneity. *Crystal Growth and Design*, 9(11):4907–4911, 2009.

[128] M Kitamura and T Ishizu. Growth kinetics and morphological change of polymorphs of L-glutamic acid. *Journal of Crystal Growth*, 209(1):138–145, jan 2000.

[129] G Van Rossum. Python tutorial, Technical Report CS-R9526, 1995.

[130] Wes McKinney. Data Structures for Statistical Computing in Python. In *Proceedings of the 9th Python in Science Conference*, pages 51–56, 2010.

[131] John D. Hunter. Matplotlib: A 2D graphics environment. *Computing in Science and Engineering*, 9(3):99–104, 2007.

[132] Michael Waskom, Olga Botvinnik, Paul Hobson, John B. Cole, Yaroslav Halchenko, Stephan Hoyer, Alistair Miles, Tom Augspurger, Tal Yarkoni, Tobias Megies, Luis Pedro Coelho, Daniel Wehner, Cynddl, Erik Ziegler, Diego0020, Yury V. Zaytsev, Travis Hoppe, Skipper Seabold, Phillip Cloud,

Miikka Koskinen, Kyle Meyer, Adel Qalieh, and Dan Allan. seaborn: version 0.8.1, nov 2014.

[133] I. Rosbottom, K. J. Roberts, and R. Docherty. The solid state, surface and morphological properties of p-aminobenzoic acid in terms of the strength and directionality of its intermolecular synthons. *CrystEngComm*, 17(30):5768–5788, aug 2015.

[134] Barry K Lavine, Charles E Davidson, Curt Breneman, and William Katt. Electronic van der Waals Surface Property Descriptors and Genetic Algorithms for Developing Structure-Activity Correlations in Olfactory Databases. *Journal of Chemical Information and Computer Sciences*, 43(6):1890–1905, 2003.

[135] Timothy Clark. QSAR and QSPR based solely on surface properties? In *Journal of Molecular Graphics and Modelling*, volume 22, pages 519–525, jul 2004.

[136] N Al-Zoubi, I Nikolakakis, and S Malamataris. Crystallization conditions and formation of orthorhombic paracetamol from ethanolic solution. *The Journal of pharmacy and pharmacology*, 54(3):325–33, 2002.

[137] Jerry Y.Y. Heng, Alexander Bismarck, Adam F. Lee, Karen Wilson, and Daryl R. Williams. Anisotropic Surface Chemistry of Aspirin Crystals. *Journal of Pharmaceutical Sciences*, 96(8):2134–2144, aug 2007.

[138] Umang V. Shah, Dolapo Olusanmi, Ajit S. Narang, Munir A. Hussain, John F. Gamble, Michael J. Tobyn, and Jerry Y.Y. Heng. Effect of crystal habits on the surface energy and cohesion of crystalline powders. *International Journal of Pharmaceutics*, 472(1-2):140–147, sep 2014.

[139] W. Omar, S. Al-Sayed, A. Sultan, and J. Ulrich. Growth rate of single acetaminophen crystals in supersaturated aqueous solution under different operating conditions. *Crystal Research and Technology*, 43(1):22–27, 2008.

[140] E. W. Becker. On the history of cluster beams. *Zeitschrift für Physik D Atoms, Molecules and Clusters*, 3(2):101–107, jun 1986.

[141] Isao Yamada, Jiro Matsuo, Noriaki Toyoda, and Allen Kirkpatrick. Materials processing by gas cluster ion beams. *Materials Science and Engineering: R: Reports*, 34(6):231–295, oct 2001.

[142] E. Taglauer. Surface cleaning using sputtering. *Applied Physics A Solids and Surfaces*, 51(3):238–251, sep 1990.

[143] Andreas Momber. *Blast cleaning technology*. Springer Berlin Heidelberg, 2008.

[144] D. F. O'Kane and K. L. Mittal. Plasma Cleaning of Metal Surfaces. *J Vac Sci Technol*, 11(3):567–569, 1974.

[145] F. J. Vidal-Iglesias, J. Solla-Gullón, E. Herrero, V. Montiel, A. Aldaz, and J. M. Feliu. Evaluating the ozone cleaning treatment in shape-controlled Pt nanoparticles: Evidences of atomic surface disordering. *Electrochemistry Communications*, 13(5):502–505, may 2011.

[146] S. Lerouge. Sterilisation and cleaning of metallic biomaterials. In *Metals for Biomedical Devices*, pages 303–326. Woodhead Publishing, jan 2010.

[147] John B. Durkee. Cleaning with Solvents. In *Developments in Surface Contamination and Cleaning - Fundamentals and Applied Aspects*, pages 759–871. Elsevier, 2008.

[148] George B. Vos. Examination of cleaning materials, techniques, and evaluation processes on various material surfaces. In *SAE Technical Papers*. SAE International, 1963.

[149] Rajiv Kohli. Removal of Surface Contaminants Using Ionic Liquids. In *Developments in Surface Contamination and Cleaning*, volume 6, pages 1–63. Elsevier Inc., jun 2013.

[150] Jiwei Wang, Yong Mei, Xuemei Lu, Xiaoxing Fan, Dawei Kang, Panfeng Xu, and Tianya Tan. Effects of annealing pressure and Ar + sputtering cleaning on Al-doped ZnO films. *Applied Surface Science*, 387:779–783, nov 2016.

[151] J. Vig and J. LeBus. UV/Ozone Cleaning of Surfaces. *IEEE Transactions on Parts, Hybrids, and Packaging*, 12(4):365–370, dec 1976.

[152] D. M. Mattox. Surface cleaning in thin film technology. *Thin Solid Films*, 53(1):81–96, aug 1978.

[153] Tadahiro Ohmi. Total room temperature wet cleaning for Si substrate surface. *Journal of the Electrochemical Society*, 143(9):2957–2964, 1996.

[154] Emiliano Carretti, Massimo Bonini, Luigi Dei, Barbara H. Berrie, Lora V. Angelova, Piero Baglioni, and Richard G. Weiss. New frontiers in materials science for art conservation: Responsive gels and beyond. *Accounts of Chemical Research*, 43(6):751–760, jun 2010.

[155] Mariavitalia Tiddia, Martin P. Seah, Alex G. Shard, Guido Mula, Rasmus Havelund, and Ian S. Gilmore. Argon cluster cleaning of Ga+ FIB-milled sections of organic and hybrid materials. *Surface and Interface Analysis*, 2018.

[156] A. Kirkpatrick, S. Kirkpatrick, M. Walsh, S. Chau, M. Mack, S. Harrison, R. Svrluga, and J. Khoury. Investigation of accelerated neutral atom beams created from gas cluster ion beams. *Nuclear Instruments and Methods in Physics Research, Section B: Beam Interactions with Materials and Atoms*, 307:281–289, jul 2013.

[157] D. Takeuchi, K. Fukushima, J. Matsuo, and I. Yamada. Study of Ar cluster ion bombardment of a sapphire surface. *Nuclear Instruments and Methods in Physics Research, Section B: Beam Interactions with Materials and Atoms*, 121(1-4):493–497, jan 1997.

[158] Benjamin Tayler-Barret. *The Detection and Quantification of Nonyl Phenyl Ethoxylate Surfactant on Paracetamol Single Crystal Surfaces*. PhD thesis, University of Leeds, 2019.

[159] Joachim Schnadt, Jan Knudsen, Jesper N. Andersen, Hans Siegbahn, Annette Pietzsch, Franz Hennies, Niclas Johansson, Nils Mårtensson, Gunnar Öhrwall, Stephan Bahr, Sven Mähl, and Oliver Schaff. The new ambient-pressure X-ray photoelectron spectroscopy instrument at MAX-lab. *Journal of Synchrotron Radiation*, 19(5):701–704, sep 2012.

[160] Tulio C.R. Rocha, Andreas Oestereich, Demid V Demidov, Michael Hävecker, Spiros Zafeiratos, Gisela Weinberg, Valerii I Bukhtiyarov, Axel Knop-Gericke, and Robert Schlögl. The silver-oxygen system in catalysis: New insights by near ambient pressure X-ray photoelectron spectroscopy, 2012.

[161] Nora H. de Leeuw and Stephen C Parker. Surface Structure and Morphology of Calcium Carbonate Polymorphs Calcite, Aragonite, and Vaterite: An Atomistic Approach. *The Journal of Physical Chemistry B*, 102(16):2914–2922, 1998.

[162] Gabriela F. Moreira, Elaynne R. Peçanha, Marisa B.M. Monte, Laurindo S. Leal Filho, and Fernando Stavale. XPS study on the mechanism of starch-hematite surface chemical complexation. *Minerals Engineering*, 110:96–103, aug 2017.

[163] Dhananjay I. Patel, James O'Tani, Stephan Bahr, Paul Dietrich, Michael Meyer, Andreas Thißen, and Matthew R. Linford. Ethylene glycol, by near-ambient pressure XPS. *Surface Science Spectra*, 26(2):024007, dec 2019.

[164] Jerry Y.Y. Heng and Daryl R Williams. Wettability of paracetamol polymorphic forms i and II. *Langmuir*, 22(16):6905–6909, 2006.

[165] Roger A. Granberg and Åke C. Rasmuson. Solubility of paracetamol in pure solvents. *Journal of Chemical and Engineering Data*, 44(6):1391–1395, 1999.

[166] W.S. Rasband. ImageJ.

[167] Cordula Weiss, Peter McLoughlin, and Helen Cathcart. Characterisation of dry powder inhaler formulations using atomic force microscopy. *International Journal of Pharmaceutics*, 494(1):393–407, 2015.

[168] R. Merkel, P. Nassoy, A. Leung, K. Ritchie, and E. Evans. Energy landscapes of receptor–ligand bonds explored with dynamic force spectroscopy. *Nature*, 397(6714):50–53, jan 1999.

[169] Theodora S. Tsapikouni and Yannis F. Missirlis. Measuring the force of single protein molecule detachment from surfaces with AFM. *Colloids and Surfaces B: Biointerfaces*, 75(1):252–259, jan 2010.

[170] Aneta E. Sikora, James R. Smith, Sheelagh A. Campbell, and Keith Firman. AFM protein-protein interactions within the EcoR124I molecular motor. *Soft Matter*, 8(23):6358–6363, may 2012.

[171] Robert Jones, Hubert M Pollock, Jamie A.S. S Cleaver, and Christopher S Hodges. Adhesion Forces between Glass and Silicon Surfaces in Air Studied by AFM: Effects of Relative Humidity, Particle Size, Roughness, and Surface Treatment. *Langmuir*, 18(21):8045–8055, oct 2002.

[172] Eric Finot, Eric Lesniewska, Jean-Claude Mutin, and Jean-Pierre Goudonnet. Investigations of surface forces between gypsum crystals in electrolytic solutions using microcantilevers. *The Journal of Chemical Physics*, 111(14):6590–6598, oct 1999.

[173] Chris S Hodges, Jamie A.S. S Cleaver, Mojtaba Ghadiri, Robert Jones, and Hubert M Pollock. Forces between Polystyrene Particles in Water Using the AFM: Pull-Off Force vs Particle Size. *Langmuir*, 18(15):5741–5748, jul 2002.

[174] U Sindel and I Zimmermann. Measurement of interaction forces between individual powder particles using an atomic force microscope. *Powder Technology*, 117(3):247–254, jun 2001.

[175] Margaret D Louey, Paul Mulvaney, and Peter J Stewart. Characterisation of adhesional properties of lactose carriers using atomic force microscopy. *Journal of Pharmaceutical and Biomedical Analysis*, 25(3-4):559–567, jun 2001.

[176] Kalyana C. Pingali, Troy Shinbrot, Alberto Cuitino, Fernando J. Muzzio, Eric Garfunkel, Yevgeny Lifshitz, and Adrian B. Mann. AFM study of hydrophilicity on acetaminophen crystals. *International Journal of Pharmaceutics*, 438(1-2):184–190, nov 2012.

[177] Philippe Begat, David A V Morton, John N. Staniforth, and Robert Price. The cohesive-adhesive balances in dry powder inhaler formulations I: Direct quantification by atomic force microscopy. *Pharmaceutical Research*, 21(9):1591–1597, 2004.

[178] Jeffrey L. Hutter. Comment on Tilt of Atomic Force Microscopy Cantilevers. *Langmuir*, 21:2630–2632, 2005.

[179] Isao Yamada. Low-energy cluster ion beam modification of surfaces. *Nuclear Instruments and Methods in Physics Research, Section B: Beam Interactions with Materials and Atoms*, 148(1-4):1–11, jan 1999.

[180] Yakov I. Rabinovich, Joshua J. Adler, Ali Ata, Rajiv K. Singh, and Brij M. Moudgil. Adhesion between nanoscale rough surfaces. I. Role of asperity geometry. *Journal of Colloid and Interface Science*, 232(1):10–16, 2000.

[181] J. A.S. Cleaver and L Looi. AFM study of adhesion between polystyrene particles; - The influence of relative humidity and applied load. *Powder Technology*, 174(1-2):34–37, 2007.

[182] Raimundo Ho, Steven J. Hinder, John F. Watts, Sarah E. Dilworth, Daryl R. Williams, and Jerry Y.Y. Heng. Determination of surface heterogeneity of d-mannitol by sessile drop contact angle and finite concentration inverse gas chromatography. *International Journal of Pharmaceutics*, 387(1-2):79–86, mar 2010.

[183] Yuxuan Gong, Scott T Misture, Peng Gao, and Nathan P Mellott. Surface roughness measurements using power spectrum density analysis with enhanced spatial correlation length. *Journal of Physical Chemistry C*, 120(39):22358–22364, 2016.

[184] John R. Rumble, editor. *Physical Constants of Organic Compounds in CRC Handbook of Chemistry and Physics*. CRC Press/Taylor & Francis, Boca Raton, FL., 100th edit edition, 2019.

[185] Paul M Young, Robert Price, Michael J Tobyn, Mark Buttrum, and Fiona Dey. Investigation into the effect of humidity on drug-drug interactions using the atomic force microscope. *Journal of Pharmaceutical Sciences*, 92(4):815–822, 2003.

[186] M.G. Cares-Pacheco, G Vaca-Medina, R Calvet, F Espitalier, J.–J. Letourneau, A Rouilly, and E Rodier. Physicochemical characterization of d-mannitol polymorphs: The challenging surface energy determination by inverse gas chromatography in the infinite dilution region. *International Journal of Pharmaceutics*, 475(1-2):69–81, nov 2014.

[187] Chandra Vemavarapu, Madhu Surapaneni, Munir Hussain, and Sherif Badawy. Role of drug substance material properties in the processibility and performance of a wet granulated product. *International Journal of Pharmaceutics*, 374(1-2):96–105, jun 2009.

[188] Michal Szumilo, Piotr Belniak, Katarzyna Swiader, Ewelina Holody, and Ewa Poleszak. Assessment of physical properties of granules with paracetamol and caffeine. *Saudi Pharmaceutical Journal*, 25(6):900–905, sep 2017.

[189] I. Rosbottom, J. H. Pickering, B. Etbon, R. B. Hammond, and K. J. Roberts. Examination of inequivalent wetting on the crystal habit surfaces of RS-ibuprofen using grid-based molecular modelling. *Physical Chemistry Chemical Physics*, 20(17):11622–11633, 2018.

APPENDIX A

Appendix

(a) $Para(10\bar{1})/Para(11\bar{1})$

(b) $Para(011)/Para(10\bar{1})$

(c) $Para(020)/Para(020)$

(d) $Para(110)/Para(110)$

(e) $Para(101)/Para(110)$

(f) $Para(020)/Para(110)$
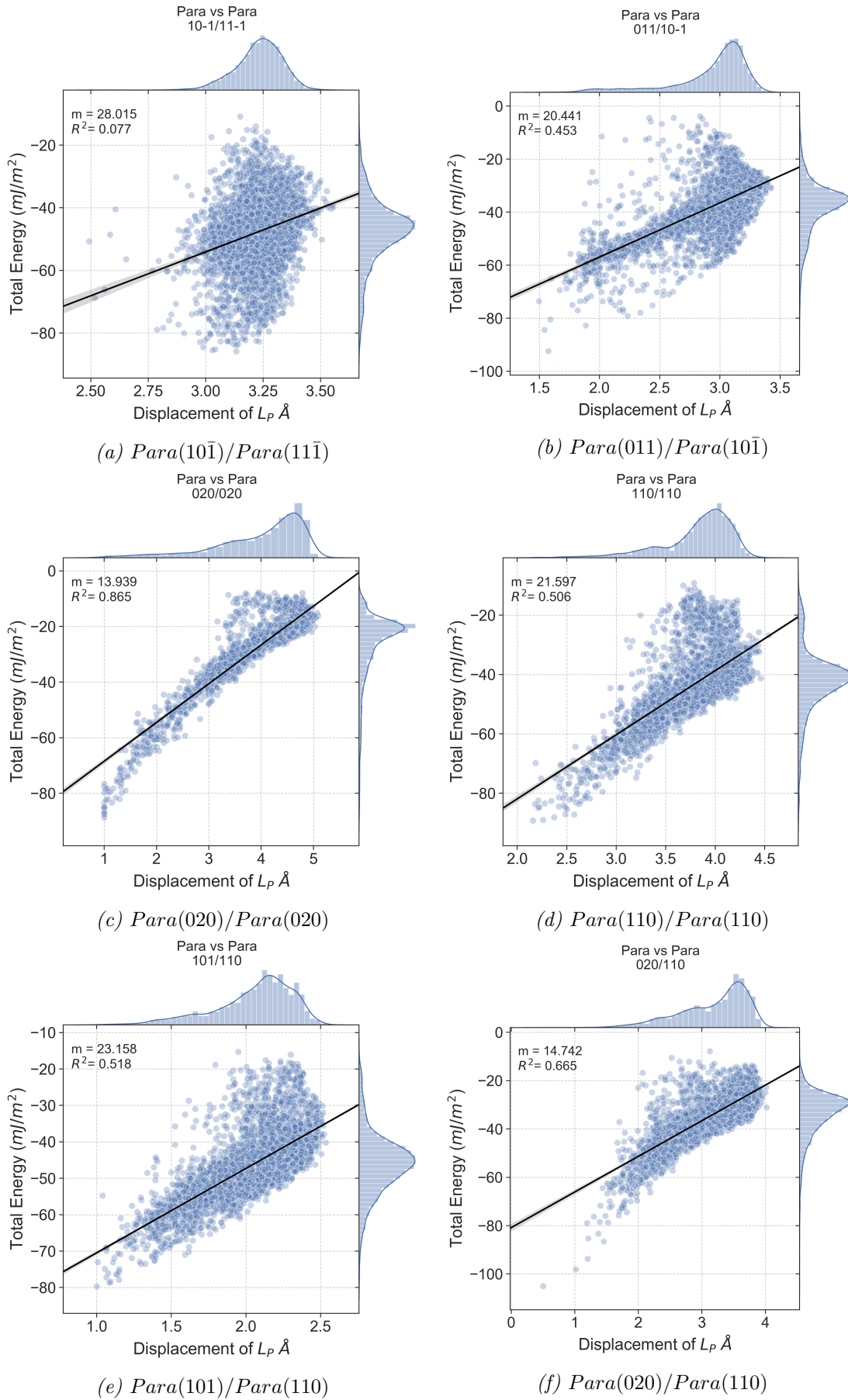
Figure A.1: Energy-displacement density plots for Para/Para homogenous and heterogenous facets

```perl
1
2 #!perl
3 ##### 11.00.pl Changed the way the minimum is found it no longer
     goes from an
4 ##### approach point of view but from a retraction.
5 ##### Speed up on the switching between fixed and unfiex.
6 ##### Reset parameter put in place for dealing with overran jobs on
      HPCs.
7 #####
8 #####
9 ##### 10.06.pl Changed to allow for both areas to be tabulated in
     the final table###
10 ##### 10.05.pl Changed the requirement for size'####
11 #use MatServer; # Please enable if running on Linux system
12 use strict;
13 use Getopt::Long qw(GetOptions);
14 use MaterialsScript qw(:all);   # Can be used in Material Studio
15 use List::Util qw(reduce);    # Allows the use of lists
16 use warnings 'all';
17 use Math::Trig;
18 use Data::Dumper;
19 use POSIX; # Used for rounding up.
20 use Time::HiRes qw( time );
21
22 my $start = time();
23 my $linux = 0;
24 my $reset = 0;
25 my (@input,@size,@thick,@rot,@dT,$sep);
26 my (@Length,@min,@area,@atoms,@lim,@longest,@mol);
27 my (@range,@set,@cent_set,@xytime,@ztime);
28 my ($zStack,$FZStack);
29 ### Development Only##
30 my @trackedAtoms; #Used for keeping track of 2 atoms from the
     layers
31 our ($bug ,$del,$ani,$timer)=(0,0,0,1);
32 my $spacer = "###############";
33 #### Options for linux systems
34 GetOptions(
35       'linux=i' => \$linux,);
36 if ($linux == 1 ) {
37   use MatServer;
38   GetOptions(
39       'size=i{1}'    => \$size[0],
40       'thick=f{2}'      => \@thick,
41       'sep=i{1}'   => \$sep,
42       'rot=i{3}'        => \@rot,
```

```perl
43          'inp=s{2}'    =>\@input,
44          'deb=i'       =>\$bug,
45          'del=i'        => \$del,
46          'ds=i{2}'         => \@dT,
47              'reset=i{1}'      => \$reset,
48          'ani=i'               => \$ani);
49
50 }else{
51 # Commands required to pass through the script from command line
52 GetOptions(
53          'Area_L2=i'      => \$size[0],
54          'Thickness_L1=f'  => \$thick[0],
55          'Thickness_L2=f'  => \$thick[1],
56          'Separation=i'    => \$sep,
57          'Rotation_Step=i' => \$rot[2],
58          'Rotation_Start=i'=> \$rot[0],
59          'Rotation_End=i'  => \$rot[1],
60          'Layer_1=s'      =>\$input[0],
61          'Layer_2=s'      =>\$input[1],
62          'Debug=i'       =>\$bug,
63          'Delete=i'      => \$del,
64          'Animation=i'    => \$ani,
65          'D_Spacing_L1=i'    => \$dT[0],
66          'D_Spacing_L2=i'    => \$dT[1]);
67 }
68
69
70
71 print "\n\n";
72 print "$spacer  $spacer $spacer\n";
73 print "#       Calculation Set up \n";
74 print "$spacer  $spacer $spacer\n";
75 print "   Size_L2 = $size[0]\n";
76
77 print "    Thickness_L1 = $thick[0]\n";
78 print "    Thickness_L2 = $thick[1]\n";
79 print "   Input 1 = $input[0]\n";
80 print "   Input 2 = $input[1]\n";
81 print "  Rotation_start = $rot[0]\n";
82 print "    Rotation_end = $rot[1]\n";
83 print "   Rotation_step = $rot[2]\n";
84 print "       Seperation = $sep\n";
85 print "$spacer  $spacer $spacer\n";
86 print "\n\n";
87
88 ####Error Handling Methods
89 my $fail=0; ## If the input file/GUI interface doesn't have all the
```

```perl
        values it will exit the code.
for my $var (1..2){
  defined ($input[$var-1]) || print "Error ",$fail=1,"\n","No input
      set for L_$var \n";
  defined ($size[0])     || print "Error ",$fail=2,"\n","No size
      set for L_$var \n";
  defined ($thick[$var-1]) || print "Error ",$fail=3,"\n","No
      thickness set for L_$var \n";
  defined ($rot[$var-1])   || print "Error ",$fail=3,"\n","Missing
      Rotational setting- Check Start,End,Step \n";
  defined ($rot[$var])    || print "Error ",$fail=3,"\n","Missing
      Rotational setting- Check Start,End,Step \n";
  defined ($sep)         || print "Error ",$fail=4,"\n","Missing
      Seperation \n";
}
if ($fail != 0){ die "Error Found: Please check input files or
    typos\n";}
####

my $fh1 = $Documents{"$input[0]".".xsd"}; # Pulls input files from
    active folder
my $fh2 = $Documents{"$input[1]".".xsd"};
my $Compo = Documents->New("Comp_"."$input[0]"."$input[1]".".xsd");
    # Creates new file that will hold
                                    # the two layers in one structure
my @L = Documents->New("Layer1".".xsd");
push (@L,Documents->New("Layer2".".xsd"));
$L[0]->CopyFrom($fh1); # Creates copies of the structural files to
    make sure it doesn't alter the originals
$L[1]->CopyFrom($fh2);
$fh1->Close;
$fh2->Close;

my $no_rot = ($rot[1] - $rot[0])/$rot[2]; # Calculates number of
    steps required for rotation

#Calculating Separation between slabs
#Using half the d-spacing to figure out the separation between the
    two centroids required

my $cen_sep = $sep + ((($thick[0]/$dT[0])/2)+(($thick[1]/$dT[1])/2)
    ); # Calculates a separation between L1 and L2
print "$spacer  $spacer $spacer\n";
print "#      Building Slabs \n";
print "$spacer  $spacer $spacer\n";


```

215

```perl
123  # This section attempts to reduce any high aspect ratio shapes from
          taking place.
124  # WHERE @min[0][1][2][3] = L1minU , L1minV,L2minU, L2minV
125  # WHERE @Length[0][1][2][3] = LengthU_A , LengthV_A,LengthU_B,
      LengthV_B
126  # Where @area[0][1][2][3]  = Unit cell Area of L1, Area of Slab L1,
          Unit Cell Area of L2, , Area of Slab L2
127  # Area of the unit cell is taken into account.
128
129  my $req_len = sqrt($size[0]);
130  my %tracked = ( "Atom_2" => ,
131          "Atom_2" => );
132  for (my $l = 0; $l <2;$l++){
133    if ($bug > 2) {
134      my $trackedatom = $L[$l]->UnitCell->Atoms(0); # Selects first
        atom from the layer
135      $tracked{"Atom_$l"} = [sprintf("%.6f",$trackedatom->X),
136                    sprintf("%.6f",$trackedatom->Y),
137                    sprintf("%.6f",$trackedatom->Z)];
138      printf "\nTracked Atom Set $l = x: %f, y: %f,z:%f\n",$tracked{"
        Atom_$l"}[0],
139                              $tracked{"Atom_$l"}[1],
140                              $tracked{"Atom_$l"}[2];
141    }
142    #Sets the atom coordinates to the hash.
143    $L[$l] = orientation($l);        # Checks The orientation of the
         cell
144    push(@mol,atoms($L[$l]));         # Passes layers and find the
          number of molecules in unit cell.
145    push(@Length, getLattice($l,1));    # Extracts Lengths of Unit
          cells
146    push(@area,$L[$l]->Lattice2D->CellArea);    # Passes the Area of
          the Cell
147    #printf "\nLattice dimensions L%f %f %f\n",($l+1),$Length[$l*2],
        $Length[$l*2+1];
148    if ($bug>0){print "Calculating the area\n";}
149    push(@min,(ceil($req_len/$Length[$l*2+1])),   # Divides the
        required length for a square by the length of the
150        (ceil($req_len/$Length[$l*2+2])));    # length lattice for
        the two layers.
151    #if ($bug>0){printf "The min value is %i and %i",$min[$l*2+1],
        $min[$l*2+2];}
152  # push (@min, getDims($Length[$l*2],$Length[$l*2+1]));
153    $min[0] = 3;
154    $min[1] = 3;               # Starts subroutine to reduce the aspect
        ratio of the unit cell.
155  # $_ *= $size[$l] for $min[$l*2],$min[$l*2+1];    # Multiplies the
```

216

```perl
     min value to crate a square
156                              # by the desired size of the surface

158   $L[$l]->BuildSuperCell($min[$l*2],$min[$l*2+1]);  # Builds
        SuperCell
159   push(@atoms,$L[$l]->UnitCell->Atoms->Count);  # Counts how many
        atoms have been fixed in the Unitcell.
160   push(@area,$L[$l]->Lattice2D->CellArea);       # Adds the area of
        the Slab to the array
161 }

162

163

164 if ($bug >= 1){
165   print "Number of molecules in the Unit cell of L1 = $mol[0]\n";
166   print "Number of molecules in the Unit cell of L2 = $mol[1]\n";
167   print "Area of L1 & L2 unit cells = $area[0] , $area[2]\n";
168   print "Area of L1 & L2 Slabs = $area[1] , $area[3] \n";
169 }                                        # minVA and minVB
170 print "L1 must be mutiplied by $min[0] x $min[1] along UxV \n";
171 print "L2 must be mutiplied by $min[2] x $min[3] along UxV \n\n";
172 print "$spacer  $spacer $spacer\n";
173 print "#    Building Complete \n";
174 print "$spacer  $spacer $spacer\n";

176 print "\n";
177 print "$spacer  $spacer $spacer\n";
178 print "#  Calculating Centroids and Middle Cell \n";
179 print "$spacer  $spacer $spacer\n";
180 print "\n\n";

182 my $sup_lat = $L[0]->SymmetryDefinition;
183 #This section looks at finding the lower and upper boundary of the
        middle cell
184 #In the array @range the indexes are as follows
185 #range[0,1,2,3]= U_lower,V_lower,U_upper,V_upper
186 my @L2_range;
187 push(@lim,int(3/2),int(3/2),int(($min[2]/2)-1),int(($min[3]/2))-1);
         # Minus 1 to ensure that the middle cell is selected over the
        middle
188 push(@range,$Length[0],$Length[1]);

190 push(@L2_range,$Length[3],$Length[4]);

192 @range = map {$lim[$_] * $range[$_]} 0..$#range;
193 @L2_range = map {$lim[$_] * $L2_range[$_]} 0..$#L2_range; #
        Calculates the lower boundary of the L2 units cell

194
```

```perl
195  push(@range,($range[0]+$Length[0]),($range[1]+($Length[1]*sin(
         $Length[2]))));
196
197  @range = map (sprintf("%.6f",$_),@range);    # Ensures all floats
         are round to 6 sig figures.
198  #@range = map {$range[$_]+0.8}0..$#range; # Fixes issues with atoms
          lying on the unit cell
199
200  #%lines_prop hold the line properties for the two edges of the
         parallelogram.
201  my %lines_prop;
202
203  my $u = tan($Length[2]);
204
205  $lines_prop{'mean'} = tan($Length[2]);
206  $lines_prop{'C1'} =   - ($lines_prop{'mean'}*$range[0]) ;
207  $lines_prop{'C2'} =   - ($lines_prop{'mean'}*$range[2]) ;
208  if ($bug > 3 ){
209    printf "The Mean : %f\n C1 : %f \n C2: %f\n", $lines_prop{'mean'
         },$lines_prop{'C1'},$lines_prop{'C2'};
210    print "Unit multipliers        : @lim\n";
211    print "Length and Angles     : @Length\n";
212    print "Ranges (U_L,V_L,U_U,V_U)\n: @range\n";
213    print "Range for L2          : @L2_range\n";
214  }
215
216  #Copies Layers into Composite Layers and sets up the sets for the
         layers.
217  # $set[0,1,2,3,4,5] = Set_1,Set_2,Set_3,Set_4,Set_5,Set_6
218  # Which translates to : L1, L2, FlagsOfL1, ColumnOfL1,
         AlignmentLayerOfL1,AlignmentLayerOfL2
219  for (my $i = 0; $i < 2; $i++) {
220    push(@set,$Compo->CopyFrom($L[$i]->UnitCell->Atoms));
221    my $ii = $i+1;
222    my $str = "Set_$ii";
223    $Compo->CreateSet($str,$set[$i]);
224    #push(@cent_set,$Compo->CreateCentroid($Compo->Sets("$str")->
         Atoms));
225    #$cent_set[$i]->IsWeighted = "No";
226    #$cent_set[$i]->IsVisible = "No";
227  }
228
229  my $cAtoms = $set[0]->Atoms; # Capture all atoms from current Layer
         .
230  my @atom_count;
231  my ($xyz_table,$xyzsheet);
232  if ($bug >= 1){
```

218

```perl
233  # Keeps track of all saved atoms
234    $xyzsheet=Documents->New("XYZ_coordinates_of_atoms.std");
235    $xyz_table=$xyzsheet->ActiveSheet;
236    $xyz_table->ColumnHeading(0)="All_x";
237    $xyz_table->ColumnHeading(1)="All_y";
238    $xyz_table->ColumnHeading(2)="x_1";
239    $xyz_table->ColumnHeading(3)="y_1";
240    $xyz_table->ColumnHeading(4)="x_2";
241    $xyz_table->ColumnHeading(5)="y_2";
242  }

243
244  ## Prepares surface for column set up
245  my (@flags,@column,@display,@alignCent); #Creates arrays for
         storing atom positions that will be fixed and unfixed.
246  foreach my $atom (@$cAtoms){
247    my $y = sprintf ("%.6f",$atom->Y);
248    my $x = sprintf ("%.6f",$atom->X);
249    my $z = sprintf ("%.6f",$atom->Z);
250    $atom_count[2] += 1 ;

251
252    if($bug >2){
253      #printf "Looking for X: %f Y: %f Z: %f\n", $tracked{"Atom_0
         "}[0],$tracked{"Atom_0"}[1],$tracked{"Atom_0"}[2];
254      #printf "Atom Coor   X: %f Y: %f Z: %f\n", $x , $y , $z;
255      if ($x == $tracked{"Atom_0"}[0] and $y == $tracked{"Atom_0"}[1]
          and $z == $tracked{"Atom_0"}[2]){
256        push(@trackedAtoms,$atom);
257        printf "First Tracked Atom found x: %f, y: %f,z:%f\n",$x,$y,
         $z;
258      }
259    }
260    if ($bug == 1 ){
261      $xyz_table->Cell($atom_count[2],0) = "$x";
262      $xyz_table->Cell($atom_count[2],1) = "$y";
263    }
264    # Creates AlligmentCentroids for the top layer
265    if ($z >= (-($thick[0]/$dT[0]))){
266      push(@alignCent,$atom);
267    }

268
269    if ($z >= (-($thick[0]/($dT[0])))){
270      push(@flags,$atom);
271    }

272
273    # Checks the for atoms within the boundary of the unit cell
         equivalent
274    if ($y >= $range[1] and $y <= $range[3]){
```

```perl
275      $atom_count [0] += 1;
276      if ( checkPosition ($x ,$y) == 1){
277        push (@column ,$atom );
278        if($bug >= 1){
279          $xyz_table ->Cell($atom_count[0],4) = "$x";
280          $xyz_table ->Cell($atom_count[0],5) = "$y";
281        }
282      }else{
283        #if ($z >= (-($thick[0]/($dT[0]*2)))){
284        # push (@flags ,$atom );
285        #}
286      }
287
288    }else{
289      ## Creates Flags for sensing any additional interactions which
       will only pick up half the unit cell thickness worth of atoms
290      #if ($z >= (-($thick[0]/($dT[0]*2)))){
291      # push (@flags ,$atom );
292      #}
293      $atom_count [1] += 1;
294      if ($del == 1) {
295        $atom ->Delete ;
296        #next ;
297            #Deletes XYZ atoms in all cells that are not in the
     middle cell.
298      }else{
299        $atom ->Fix('XYZ');
300        if ($bug >= 1){
301          $xyz_table ->Cell($atom_count[1],2) = "$x";
302          $xyz_table ->Cell($atom_count[1],3) = "$y";
303        }
304        #next ;
305        #if ($bug ==1){printf "Number of Atoms FIXED in L1 =
     $atom_count[1] \n\n";}
306        #print "    $x    $y  \n";
307                #Fixes XYZ atoms in all cells that are not in the
     middle cell.
308      }
309    }
310    if ($bug ==1){
311      printf "Number of Atoms NOT FIXED in L1 = $atom_count[0] \n\n";
312      printf "Number of Atoms FIXED in L1 = $atom_count[1] \n\n"
313    }
314 }
315 $Compo ->CreateSet("Set_3",\@flags );
316 $Compo ->CreateSet("Set_4",\@column );
317 $Compo ->CreateSet("Set_5",\@alignCent );
```

```perl
318
319  if($bug >= 2){
320      $xyzsheet->Export("Xyz_coordinates.csv");
321      $xyzsheet->Discard;
322  }
323  printf "Number of Atoms in L1 = %i \n\n",($set[0]->Atoms->Count);
324  printf "Number of Atoms in L2 = %i \n\n",($set[1]->Atoms->Count);
325
326  ## Finds the top D-spacing for the LS
327  my $cAtoms_2 = $set[1]->Atoms;
328  my @alignCent_2;
329  foreach my $atom_2 (@$cAtoms_2){
330      $atom_count[3] += 1;
331      my $y = sprintf ("%.6f",$atom_2->Y);
332      my $x = sprintf ("%.6f",$atom_2->X);
333      my $z = sprintf ("%.6f",$atom_2->Z);
334      if ($bug>2){
335          if ($x == $tracked{"Atom_1"}[0] and $y == $tracked{"Atom_1"}[1]
              and $z == $tracked{"Atom_1"}[2]){
336              push(@trackedAtoms,$atom_2);
337              printf "Second Tracked Atom found x: %f, y: %f,z:%f\n",$x,$y,
          $z;
338          }
339      }
340      if ($z > (-($thick[1]/$dT[1]))){
341          push(@alignCent_2,$atom_2);}
342      }
343  $Compo->CreateSet("Set_6",\@alignCent_2);
344  $set[1]->Fix('XYZ');
345
346  if ($bug > 2){
347      #Creates tracker set for the first atoms in both layers.
348      $Compo->CreateSet("Atom_i",$trackedAtoms[0]);
349      $Compo->CreateSet("Atom_j",$trackedAtoms[1]);
350  }
351  push(@cent_set,$Compo->CreateCentroid($Compo->Sets("Set_5")->Atoms)
      ); ## Layer 1 bottom sets
352  $cent_set[0]->IsWeighted = "No";
353  $cent_set[0]->IsVisible = "No";
354  push(@cent_set,$Compo->CreateCentroid($Compo->Sets("Set_6")->Atoms)
      ); ## Layer 2 Bottom sets
355  $cent_set[1]->IsWeighted = "No";
356  $cent_set[1]->IsVisible = "No";
357
358
359  ## VERSION 11.00 Update Set_1 & Set_2 have had centroids removed
360  # Thus:
```

```perl
361 # @xyz array holds the XYZ coordinates for the centroids to the
        equivalent sets:
362 # @xyz[0,1,2,3,4,5]=x5,y5,z5,x6,y6,z6
363 #Extracts the XYZ coordinates from the Sets to gain the centroids.
364 # @xyz array holds the XYZ coordinates for the centroids to the
        equivalent sets:
365 # @xyz[0,1,2,3,4,5,6,7,8,9,10,11]=x1,y1,z1,x2,y2,z2,x5,y5,z5,x6,y6,
        z6
366
367 # diffXYZ function takes the XYZ and finds the difference in the
        XYZ directions
368 # Cen_dif array is as follows @Cen_dif[0,1,2] = x5-x6, y5-y6 , z5-
        z6
369 my (@xyz,@cen_dif);
370
371 #Flips top layer 180 on x axis around the centroid.
372 my $Top_Layer = $Compo->DisplayRange->Sets("Set_1")->Atoms;
373 $Top_Layer->RotateAboutPoint(180, Point(X => 1.0, Y => 0.0, Z =>
        0.0),$cent_set[0]->CentroidXYZ);
374 $L[0]->Discard;
375 $L[1]->Discard;
376
377 push(@xyz,cenXYZ(@cent_set));
378 push(@cen_dif,diffXYZ(@xyz));
379
380 $Top_Layer->Translate(Point(Z=>(200)));
381 $Compo->CalculateBonds;
382 $Top_Layer->Translate(Point(Z=>(-200)));
383
384 if ($bug>3){
385   print "Var Values are as follows:\n
386   Length[0]:$Length[0]\n
387   Length[1]:$Length[1]\n
388   Length[2]:$Length[2]\n
389   Length[3]:$Length[3]\n
390   Length[4]:$Length[4]\n
391   Length[5]:$Length[5]\n
392   lim[0]:$lim[0]\n
393   lim[1]:$lim[1]\n
394   lim[2]:$lim[2]\n
395   lim[3]:$lim[3]\n";
396
397   printf "Movement of Layer 1 has been made by:\n
398   X: %f \n
399   Y: %f \n
400   Z: %f \n", (((cos($Length[5])*$Length[4])+$Length[3])*$lim[2]), (
        sin($Length[5])*$Length[4])*$lim[3],($cen_sep-abs($cen_dif[2]));
```

```perl
401 }
402 $Top_Layer->Translate(Point(Z=>(1+$cen_sep-abs($cen_dif[2])), Y=>
        abs($cen_dif[1]), X=> abs($cen_dif[0])));
403
404 if ($bug >= 2){
405   my @xyz_new = cenXYZ(@cent_set);
406   print "Positions of centroids before moving : @xyz\n";
407   print "Positions of centroids after moving : @xyz_new\n";
408 }
409
410
411 print "\n$spacer  $spacer $spacer\n";
412 print "#  Centroids Aligned and Unit cell Selection Complete\n";
413 print "$spacer  $spacer $spacer\n";
414 print "\n\n";
415
416
417 #################################### Engine Set-up
        #########################################################
418 our $forcite=Modules->Forcite;
419 $forcite->ChangeSettings(Settings(CurrentForcefield=>"Dreiding",
420   ChargeAssignment => "Use current",
421   NonPeriodicvdWAtomCubicSplineCutOff => 80,
422   WriteLevel => "Silent"));
423
424 print "$spacer  $spacer $spacer\n";
425 print "#     Grid And Tables Set-up \n";
426 print "$spacer  $spacer $spacer\n";
427
428
429 #################################### Step Set-up
        #########################################################
430 my $grid_spacing=1;   # Grid spacing in Angstroms
431 my (@energy,@es_energy,@hb_energy,@vdw_energy,@displaceArray,
        @collisionEnergy,@MINIMA);  # Array to hold energy values at
        different Z positions
432 my @frame=();
433
434 my $doc = $Compo;
435 my $newStudyTable=Documents->New("InteractionEnergy.std");
436 my $calcSheet=$newStudyTable->ActiveSheet;
437
438 $calcSheet->ColumnHeading(0)="Cell";
439 $calcSheet->ColumnHeading(1)="Layer1";
440 $calcSheet->ColumnHeading(2)="Isolated Energy of Flags";
441 $calcSheet->ColumnHeading(3)="Layer2";
442 $calcSheet->ColumnHeading(4)="Energy of Layer1";
```

```
443 $calcSheet ->ColumnHeading(5)="Interaction Energy";
444 $calcSheet ->ColumnHeading(6)="ES Layer1";
445 $calcSheet ->ColumnHeading(7)="ES Layer2";
446 $calcSheet ->ColumnHeading(8)="HB Layer1";
447 $calcSheet ->ColumnHeading(9)="HB Layer2";
448 $calcSheet ->ColumnHeading(10)="VDW Layer1";
449 $calcSheet ->ColumnHeading(11)="VDW Layer2";
450 $calcSheet ->ColumnHeading(12)="Total ES Energy";
451 $calcSheet ->ColumnHeading(13)="Total HB Energy";
452 $calcSheet ->ColumnHeading(14)="Total VDW Energy";
453 $calcSheet ->ColumnHeading(15)="X axis Displacement";
454 $calcSheet ->ColumnHeading(16)="Y axis Displacement";
455 $calcSheet ->ColumnHeading(17)="Area of Layer 1 ";
456 $calcSheet ->ColumnHeading(18)="Area of Layer 2 ";
457 $calcSheet ->ColumnHeading(19)="Displacement of Layer 1 ";
458 $calcSheet ->ColumnHeading(20)="Rotation";
459 $calcSheet ->ColumnHeading(21)="Total No. Of Atoms Layer 1";
460 $calcSheet ->ColumnHeading(22)="Total No. Of Atoms Layer 2";
461 $calcSheet ->ColumnHeading(23)="Collision Energy";
462
463 my ($Debug,$DebugTable);
464 if ($bug >= 1 ){
465   $DebugTable = Documents ->New("DebugTable.std");
466   $Debug = $DebugTable ->ActiveSheet;
467   $Debug ->ColumnHeading(0)="Position";
468   $Debug ->ColumnHeading(1)="X Axis Displacement";
469   $Debug ->ColumnHeading(2)="Y Axis Displacement";
470   $Debug ->ColumnHeading(3)="Z Axis Displacement";
471   $Debug ->ColumnHeading(4)="Degrees of Rotation around Z Axis";
472   $Debug ->ColumnHeading(5)="Interaction Energy";
473   $Debug ->ColumnHeading(6)="Total ES Energy";
474   $Debug ->ColumnHeading(7)="Total HB Energy";
475   $Debug ->ColumnHeading(8)="Total VDW Energy";
476   $Debug ->ColumnHeading(9)="Step Size";
477   $Debug ->ColumnHeading(10)="Collision Energy";
478
479 }
480
481 ############################################# Set up Grid
      ############################################
482 $calcSheet ->Cell(0,17)=$area[1];
483 $calcSheet ->Cell(0,18)=$area[3]; #Inputs the area of the Layer
484 $calcSheet ->Cell(0,21)=$atoms[0];
485 $calcSheet ->Cell(0,22)=$atoms[1];
486
487 my (@num_steps,@step_size,@grid_length);
488 for (my $i = 0; $i < 2; $i++) {
```

```perl
489    $grid_length[0] = $Length[0];
490    $grid_length[1] = $Length[1] * sin($Length[2]);
491    $grid_length[2] = $Length[3];
492    $grid_length[3] = $Length[4] * sin($Length[5])   ;
493
494    #This section finds the longest side of the unit cells
495    if ($grid_length[$i]<$grid_length[$i+2]) {
496      push(@longest,$grid_length[$i+2]);
497    }else{
498      push(@longest,$grid_length[$i]);
499    }
500    push(@num_steps, int($longest[$i]/$grid_spacing));
501    push(@step_size, $longest[$i]/$num_steps[$i]);
502 }
503
504 print "The number of steps in U direction is $num_steps[0]\n";
505 print "The step size in U direction is $step_size[0]\n";
506
507 print "The number of steps in V direction is $num_steps[1]\n";
508 print "The step size in V direction is $step_size[1]\n";
509
510 #################################### In
511 my $layer1_Doc=Documents->New("layer1.xsd");
512 #Set up for the Trajectory File.
513 if ($ani >= 1){
514    $FZStack = Documents->New("FinalZStack.xtd");
515    $FZStack->Trajectory->AppendFramesFrom($doc);
516 }
517
518 #Set energies of Layer 2 as all zero due to the atoms all being
        fixed.
519 # Copy Layer2 in new document, calculate energy and save in the
        table
520 $layer1_Doc->CopyFrom($doc);
521 $layer1_Doc->UnitCell->Sets("Set_2")->Atoms->Delete;
522 $calcSheet->Cell(0,3)=$layer1_Doc;
523 # Calculate energy of Layer1 and save in table
524 #####################################################
525 #This section calculates the energy of the bottom attoms of layer 1
        that are not in the unit cell.
526 #print "About to Calculate the Isolated energies \n";
527 my $l1_flag = getEnergy($layer1_Doc,$layer1_Doc->DisplayRange->Sets
    ("Set_4")->Atoms,
528             $layer1_Doc->DisplayRange->Sets("Set_3")->Atoms,
    $forcite,"collision",0);
529
530 $calcSheet->Cell(0,2) = $l1_flag;
```

```perl
531 $layer1_Doc = getEnergy($layer1_Doc,$layer1_Doc->DisplayRange->Sets
      ("Set_4")->Atoms,
532             $layer1_Doc->DisplayRange->Sets("Set_3")->Atoms,
      $forcite,"unit",0);
533
534 $calcSheet->Cell(0,4)=($layer1_Doc->PotentialEnergy);
535 $calcSheet->Cell(0,7)=($layer1_Doc->ElectrostaticEnergy);
536 $calcSheet->Cell(0,9)=($layer1_Doc->HydrogenBondEnergy);
537 $calcSheet->Cell(0,11)=($layer1_Doc->VanDerWaalsEnergy);
538 ##################################### SystematicCalculations
      ##########
539 my $Setupduration = time() - $start;
540 print "Time to setup structure: $Setupduration s \n";
541 print "$spacer  $spacer $spacer\n";
542 print "#    Grid And Tables Set-up Complete\n";
543 print "$spacer  $spacer $spacer\n";
544 print "\n\n";
545 print "\n\n";
546
547 print "$spacer  $spacer $spacer\n";
548 print "#    Starting Calculations \n";
549 print "$spacer  $spacer $spacer\n\n";
550 #($num_steps[0],$num_steps[1])=(2,2);
551 $Compo->Centroids->Delete;
552 $Compo->Sets("Set_2")->Delete;
553 $Compo->Sets("Set_6")->Delete;
554 $Compo->Sets("Set_5")->Delete;
555 my ($counter,$frame,$newtime,$counter2,$tick,$progress) =
      (0,0,0,0,0,0);
556 if ($bug >=2) {
557   my $layerSet=Documents->New("layerSetUP.xsd");
558   $layerSet ->CopyFrom($doc);
559 }
560
561 #$num_steps[0]= 1;
562 #$num_steps[1]= 1;
563 my $switchTrigger;
564 my $tablePosition = 0;
565 my $total_num_steps = ($num_steps[0] * $num_steps[1] * (($rot[1]-
      $rot[0])/$rot[2]));
566 for (my $r = $rot[0]; $r < $rot[1]; $r += $rot[2]){
567   undef @MINIMA;
568   my ($alldoc,$tempLayer,$flag,$unit)=copyStructure($input[0],
      $input[1],$r);
569   $tempLayer->RotateAbout($r,Point(Z => 1.0, Y => 0.0, X => 0.0));
570   $tempLayer->Translate(Point(X=>-($longest[0]/2),Y=>-($longest
      [1]/2)));
```

```perl
571
572  for (my $x = 0; $x < ($num_steps[0]); $x++) {
573    for (my $y = 0; $y < ($num_steps[1]); $y++) {
574      $tempLayer->Translate(Point(X=>$step_size[0]*$x,Y=>$step_size
  [1]*$y));
575      my $copytime = time() - $newtime;
576      if ($ani>1){
577      eval{
578        our $zStack = Documents->New("Temp_ZStack.xtd");
579        $zStack->Trajectory->AppendFramesFrom($alldoc);
580        1;}or do{
581        print "Tried to create animation but could not\n";
582      };
583      }
584      #my $mytemp = Documents->New("Temp_Structure_"."$x _ $y".".
  xsd");
585      #$mytemp->CopyFrom($alldoc);
586      $calcSheet->Cell($counter,0)="Position"."_$x"."_$y";
587      $calcSheet->Cell($counter,15)="$x";
588      $calcSheet->Cell($counter,16)="$y";
589      $calcSheet->Cell($counter,20)="$r";
590      print "#Current Position: $x , $y\n ";
591      my $progressPerCent = ((++$progress)/ $total_num_steps)* 100;
592      print "#Progressed: $progressPerCent % \n";
593
594      my $dZ = 0.1;
595      my $constant = 0.05;
596      my ($interaction_Energy,$vdw_energy,$es_energy,$hb_energy);
597      my ($collisionEnergy_temp,$dCollisionEnergy);
598      my ($overshot, $displacement, $move) = (0,0,0,0,0,0);
599      my $z_limit = 100;
600      undef @energy;       # Empty the array
601      undef @es_energy;
602      undef @hb_energy;
603      undef @vdw_energy;
604      undef @displaceArray;
605      undef @collisionEnergy;
606      $xytime[0] = time();
607      for (my $k = 0; $k < 100; ++$k) {
608
609        print"$spacer\n";
610        $frame += 1;
611        print "\n#        Counter_$frame        \n";
612        $ztime[0] = time();
613        if ($k == 0){
614          $dZ = 0.5
615        }
```

```
616        if ($x == 0 and $y==0 and $k == 0){
617          $switchTrigger = 0;
618        }else{
619          $switchTrigger = 1;
620        }
621        $tempLayer->Translate(Point(Z=>$dZ));
622        $displacement += $dZ;
623        $ztime[1] = time();
624        my $collisionAtoms = getEnergy($alldoc,$unit,$flag,$forcite
       ,"collision",$switchTrigger);
625
626        my $unitAtoms;
627        $ztime[2]=time();
628        $collisionEnergy_temp = ($collisionAtoms - ($calcSheet->
       Cell(0,2)));
629
630        #printf "Calculated the Collision Energy : %f\n",
       $collisionEnergy_temp;
631
632        push(@collisionEnergy,$collisionEnergy_temp);
633        push(@displaceArray,$displacement);
634        # If bug 10 is enabled the separation will also be
       calculated for the Unit cell
635        #during the steepest descent method.
636        $ztime[10] = time();
637
638        if ($bug >= 9){
639          printf "Debug with Extra interaction Energy is on, Bug =
       %i",$bug;
640          my $unitAtoms = getEnergy($alldoc,$unit,$flag,$forcite,"
       unit");
641          saveToDebug($alldoc,
642              $Debug,$x,$y,$r,$displacement,
643              $dZ,$collisionEnergy_temp,$counter2,$bug);
644        }elsif($bug < 5 and $bug >=1){
645          saveToDebug(0,$Debug,$x,$y,$r,$displacement,
646          $dZ,$collisionEnergy_temp,$counter2,$bug);
647        }
648        $ztime[11] = time();
649        #Calculates the energy difference between different points
       based on the overshot
650        #$overshot:index -- 0:k-1; 1:k-2; 2:k-4;
651        $dCollisionEnergy = $collisionEnergy_temp -
       $collisionEnergy[$k-2**$overshot];
652        $ztime[3]=time();
653        if ($bug >= 1) {
654          if ($bug >= 10){
```

```perl
655             printf "#Interaction Energy = %f \n",($alldoc->
    PotentialEnergy - ($calcSheet->Cell(0,4)));
656          }
657          print "##Position"."_$x"."_$y \n";
658          print "#Collision Energy            =
    $collisionEnergy_temp \n";
659          printf "#Difference in Energy between %f and %f =
    $dCollisionEnergy\n" , $displacement , $displaceArray[$k-2**
    $overshot];
660          print "#Step Size                 = $dZ \n";
661          print "#Displacement is           = $displacement \n";
662       }
663       $frame[$k]=$frame;
664       ++$counter2;
665       $ztime[5] = time();
666       if ($timer == 1){
667        printf "Time taken to record data to debug file and
    calculate unit cell %f \n", $ztime[11]-$ztime[10];
668          printf "Time taken to push Data to Array = %f\n",$ztime
    [10]-$ztime[2];
669          printf "Time taken to move slab     = %f\n", ($ztime[1]-
    $ztime[0]);
670          printf "Time Taken to carry out calculation = %f\n",(
    $ztime[2]-$ztime[1]);
671          printf "Time Taken to prepare steps sizes = %f\n",($ztime
    [4]-$ztime[3]);
672       }
673       print "OS : $overshot \n";
674       print "$spacer\n";
675
676       if ($dZ < 0.001 and $dCollisionEnergy < 0.01 and
    $dCollisionEnergy > -0.01){
677         last;
678       }
679
680
681       #If the graident is Positive overshot is triggered.
682       if ($dCollisionEnergy >= 0.000001 and $dZ != 0.5){
683         $overshot +=1;
684       }else{
685         $overshot = 0;
686       }
687       if ($overshot > 3){
688         last;
689       }
690       if($overshot == 0 and $dCollisionEnergy < 1000 and $k > 2
    and $collisionEnergy_temp < 1000){
```

```perl
691            $dZ = calculateDZ($dZ,$dCollisionEnergy,$constant);
692         }elsif($dCollisionEnergy < 1000 and $k>2 and
    $collisionEnergy_temp < 1000){
693            ($dZ,$constant,$displacement) = moveLayerBack($overshot,
    $tempLayer,$displacement,$dZ,
694                                  \@displaceArray,$k,$constant);
695         }
696         $ztime[4]=time();
697         if ($dCollisionEnergy > 1000){
698            $dZ = 0.5;
699         }
700         #Conditions for reaching convergence
701         #if ($overshot > 2){
702         # $dZ = 0.001;
703         #}
704      }
705      #print "About to run the last position calculation\n";
706      #print "Energy Array : @collisionEnergy\n";
707      #print "Diplacement Array : @displaceArray\n";
708      my $n = reduce { $collisionEnergy[$a] < $collisionEnergy[$b]
    ? $a : $b } 0..$#collisionEnergy; # Finds Lowest Interaction
    Energy Step
709      #printf "Index Value calculated : %i\n", $n;
710      #$tempLayer->Translate(Point(Z=>($displaceArray[$n] -
    $displacement)));
711      #my $unitAtoms = getEnergy($alldoc,$unit,$flag,$forcite,"unit
    ",1);
712      #($interaction_Energy,$es_energy,$hb_energy,$vdw_energy) =
    componentEnergies($unitAtoms,$calcSheet);
713
714      #printf "Interaction Calculations    = %f\n",
    $interaction_Energy;
715      #printf "HB _ Energy             = %f\n",$hb_energy;
716      #printf "ES_Energy               = %f\n",$es_energy;
717      #printf "VdW_Energy              = %f\n",$vdw_energy;
718      my @Array = ($x,$y,$displaceArray[$n]);
719      #printf "Array of the Positions = @Array \n";
720      push (@MINIMA, \@Array);
721      print "\n $spacer $spacer $spacer\n";
722      #print "#Lowest Energy         = $interaction_Energy \n";
723      print "$spacer $spacer $spacer\n";
724      print "\n";
725      print "$spacer Approach Scan Complete $spacer \n";
726      print "\n";
727
728      #$calcSheet->Cell($counter,5)=$interaction_Energy;  #Based on
     the lowest value it uses that index value.
```

```perl
        #$calcSheet->Cell($counter,12)=$es_energy;
        #$calcSheet->Cell($counter,13)=$hb_energy;
        #$calcSheet->Cell($counter,14)=$vdw_energy;
        #$calcSheet->Cell($counter,19)=$displaceArray[$n];
        #$calcSheet->Cell($counter,23)=$collisionEnergy[$n];
        $newtime = time();
        ++$counter;

        if ($ani >= 1){
          my $to = $FZStack;
          my $from = $zStack;
          my $trjTo = $to->Trajectory;
          $FZStack ->CurrentFrame = $tick;
          if ($ani >= 2){
            $trjTo->InsertFramesFrom($from);
          }else{
            $trjTo->InsertFramesFrom($from, Frames(Start => ($frame[
    $n]), End => $frame[$n]));
          }
          $zStack->Discard;

        }
        if ($timer==1){
          printf "Time taken to do Z-Stack      =%f  \n", (time() -
    $xytime[0]);
        }
        $tempLayer->Translate(Point(X=>-$step_size[0]*$x, Y=>-
    $step_size[1]*$y, Z=>-$displacement));

        ++$tick;
        if ($displacement > 50){
          last;
        }
      }
    }
    print "$spacer  $spacer $spacer\n";
    print "#  Rotation $r Complete \n";
    print "$spacer  $spacer $spacer\n";

    print "Table postion = $tablePosition \n";
    getEnergyMinima(\@MINIMA, $alldoc,$tempLayer,$flag,$unit,
     $calcSheet,$forcite,\@step_size,$tablePosition);
    $tablePosition += ($num_steps[0]* $num_steps[1]);
    $alldoc->Discard;
    if ($bug > 0){
      $DebugTable-> Export("Debug of"."$input[1]"."".csv");
    }
```

```perl
772    $area[0] = int($area[0]);
773    $area[2] = int($area[2]);
774    $newStudyTable->Export("$input[0]"."_"."$area[0]"."vs"."_$input
         [1]"."_$area[2]"."_$reset".".csv");
775 }
776 print "\n\n";
777 print "$spacer  $spacer $spacer\n";
778 #$layer1_Doc->Discard;
779 if ($bug > 0){
780    $DebugTable->Discard;
781 }
782 $newStudyTable->Discard;
783 my $time1=localtime;
784 print "#  Calculation ended $time1 \n";
785 my $duration = time() - $start;
786 print "Execution time(): $duration s\n";
787 print "Done!!\n";
788 print "$spacer  $spacer $spacer\n";
789
790 reset;
791
792 my $rand = int(rand(100));
793
794 sub copyStructure {
795 #Copy the original structure and define the layer to move
796    my ($i,$j,$r)=@_;
797
798    my $all_doc=Documents->New("Start_Structure_of"."_$i"."_$j"."_$r.
         xsd"); # Names all positions with File name.
799
800    $all_doc->CopyFrom($Compo);# Copy the whole cell (both layers) to
          another document
801
802    my $tempLayer= $all_doc->DisplayRange->Sets("Set_1")->Atoms;#
         Define the layer to move
803    my $flags= $all_doc->DisplayRange->Sets("Set_3")->Atoms;# Define
         the layer to move
804    my $unit= $all_doc->DisplayRange->Sets("Set_4")->Atoms;# Define
         the layer to move
805
806    return ($all_doc, $tempLayer,$flags,$unit);
807 }
808
809 sub diffXYZ {
810    my @xyz = @_;
811    my @numbers = (0,1,2);
812    my @dif;
```

```perl
813    foreach my $i (@numbers){
814      push(@dif,($xyz[$i]-$xyz[$i+3]));
815    }
816    return(@dif);
817 }
818
819 sub cenXYZ {
820    my @set =@_;
821    my @center;
822    if ($bug ==1){
823      print "Set used are...";
824      print "@set\n";
825    }
826    foreach my $set_i (@set){
827      push(@center,($set_i->CentroidXYZ->X,
828              $set_i->CentroidXYZ->Y,
829              $set_i->CentroidXYZ->Z));
830    }
831    if ($bug >= 1 ){print "The XYZ for centroid as ARRAYS for @set
      are @center\n";}
832    return(@center);
833 }
834
835 sub getDims {
836    my @lat = @_;
837    my $dif = $lat[0] / $lat[1];
838    if ($bug >= 1){
839    print "\n Array passed to get_dims2 = @lat\n";
840    print "\n $lat[0] $lat[1]\n";
841    print "\n Difference is  $dif\n";
842    }
843    if ($dif < 1){
844    return (round(1 / $dif,0), 1);
845    }else{
846    return (1, round($dif,0));
847    }
848 }
849
850 sub getLattice {
851    #### Function used to gather lattice parameters of surface and
      return UV.
852    #### Function will resolve for V vector using the angle of the
      cell.
853    my $i = $_[0];
854    my $triger = $_[1];
855    my $lat = $L[$i]->SymmetryDefinition;
856    my $angle = deg2rad($L[$i]->Lattice2D->AngleTheta);
```

```perl
857    my @len = $lat->LengthU;
858    push (@len,(sin($angle)*$lat->LengthV));
859    if ($triger == 1){           # If the orientation is being reset
        it will return the original
860      return($len[0],$lat->LengthV,$angle);          # Length of U as
          opposed to the resolved.
861    }else{
862    return($len[0],$len[1]);
863    }
864 }

865
866 sub orientation {
867    my $l = $_[0];
868
869    my $orientation = $L[$l]->SymmetryDefinition->
        OrientationConvention;
870    if ($orientation eq "U along X, V in XY plane") {
871        print "Lattice uses U along X , V in XY plane\n";
872    }else{
873    my ($L_U,$L_V,$angle) = getLattice($l,1);
874    $L[$l]->UnbuildSurface;
875    my $buildSurface = Tools->SurfaceBuilder->Surface;
876    $buildSurface->SetPlaneGroup("p 1");
877    $buildSurface->SetMeshParameters($L_U, $L_V, $angle);
878    $buildSurface->Build($L[$l], Settings(
879    OrientationConvention => "U along X, V in XY plane"));
880    }
881    return($L[$l]);
882 }
883 sub atoms {
884    my $layer = $_[0];
885    my $atom = $layer->UnitCell->Atoms(0);
886    my $fragment = $atom->Fragment->Atoms;
887    my $pattern = Documents->New("Pattern.xsd");
888    $pattern->CopyFrom($fragment);
889    $pattern->CalculateBonds;
890    my $mol = Tools->Patterns->FindPatterns->Find($layer,$pattern);
891    $pattern->Discard;
892
893 return ($mol->Count);
894
895 }
896
897 sub atomDistances {
898 # Measures the distance between two atoms. UNDER DEVELOPMENT
899    my $atom_1 = $_[0];
900    my $atom_2 = $_[1];
```

```perl
901 }
902
903 sub getCoordinates {
904 #Finds XYZ Coordinates for atom provided.
905   my $atom = $_[0];
906   my $y = sprintf ("%.6f",$atom->Y);
907   my $x = sprintf ("%.6f",$atom->X);
908   my $z = sprintf ("%.6f",$atom->Z);
909   return ($x , $y, $z);
910 }
911
912 sub round {
913     my ($x) = @_;
914     my $a = 10**0;
915
916     return (int($x / $a + (($x < 0) ? -0.5 : 0.5)) * $a);
917 }
918
919 sub checkPosition {
920   my $x = $_[0];
921   my $y = $_[1];
922   my $mx = $lines_prop{'mean'} * $x;
923   my @equation;
924   $equation[0] = $mx + $lines_prop{'C1'} - $y;
925   $equation[1] = $mx + $lines_prop{'C2'} - $y;
926   if ($bug>2){
927   #printf "\nEquation1 value : %f \n", $equation[0];
928   #printf "\nEquation1 value : %f \n", $equation[1];
929   }
930   if ($lines_prop{'mean'} < 0){
931     if ($equation[1]>= 0 and $equation[0] <= 0){
932       return (1);
933     }else{
934       return (0);
935     }
936   }
937   if ($equation[0]>= 0 and $equation[1] <= 0){
938     return (1);
939   }else{
940     return (0);
941   }
942 }
943
944 sub getEnergy {
945   my ($alldoc,$unit,$flags,$forcites,$case,$k) = @_;
946   #printf "FUNCTION getEnergy\n";
947   #printf "In this situation the case is %s\n",$case;
```

```perl
948    my @time;
949    if ($case eq "collision"){
950        $time[0] = time();
951        if ($bug <= 9){
952          if ($k == 0){
953             #print "\nCollision Mode - Flags unfixed\n";
954             $unit->Fix('XYZ');
955             $flags->Unfix('XYZ');
956          }
957        }else{
958           #print "\n Collision Mode - flags unfixed \n";
959           $unit->Fix('XYZ');
960           $flags->Unfix('XYZ');
961        }
962        $time[1] = time();
963        $forcite->Energy->Run($alldoc);
964        $time[2] = time();
965        printf "Time taken to run Forcite = %f\n ", $time[2] - $time
      [1];
966        #printf "Time taken to fix and Unfix atoms = %f \n", $time[1]
        - $time[0];
967        #printf "Energy of The collision = %f",$alldoc->
      PotentialEnergy;
968        return ($alldoc->PotentialEnergy);
969    }elsif ($case eq "unit"){
970        if ($k == 0 ){
971          print " Atoms have been switched \n";
972          $flags->Fix('XYZ');
973          $unit->Unfix('XYZ');
974        }
975        $time[3] = time();
976        $forcite->Energy->Run($alldoc);
977        $time[4] = time();
978        printf "Time taken to run Forcite - $case mode = %f\n ",
      $time[4] - $time[3];
979        #printf "Energy of the Unit = %f\n",$alldoc->PotentialEnergy;
980        return($alldoc);
981    }
982 }
983
984
985 sub calculateDZ {
986     my $dZ = $_[0];
987     my $dCollisionEnergy = $_[1];
988     my $constant = $_[2];
989
990    #print "FUNCTION calculateDZ\n";
```

```perl
    #printf "Values passed = %f,%f,%f\n",$dZ,$dCollisionEnergy,
     $constant;
     eval{
          $dZ = abs(log(abs($dCollisionEnergy/$dZ)*100))*$constant;
     return ($dZ);
          1;
     }or do{
          print "Check Collision Energy, dZ forced to 0.001\n";
          return (0.001);
     }
}

sub moveLayerBack {
  # Finds the distance it needs to move based on the overshot value
     passed to it.
     my ($case,$tempLayer,$displacement,$dZ,$displaceArray,$k,
     $constant) = @_;
  #print "FUNCTION  moveLayerBack\n";
  #print "\nInputs for moveLayerBack @_\n";
     my $move = $displacement - @{$displaceArray}[$k-($case*2-1)];
     # Case = 1 = k-1 , 2 = k - 3;
     $displacement += -$move;
  $tempLayer->Translate(Point(Z=>-$move));
     $dZ= $dZ*0.25;
  $constant = $constant/2;
  #printf "Function return: dZ = %f, constant = %f, displacement =
     %f, move = %f",$dZ, $constant,$displacement,$move;
  return ($dZ,$constant,$displacement);
}

sub lowestValueIndex {
  my @array = @{$_[0]};
  my $index = reduce { $array[$a] < $array[$b] ? $a : $b } 0..$#
     array;
  return ($index);
}

sub componentEnergies {
  my ($alldoc,$calcSheet) = @_;
  #print "Started componentEnergies\n";
  my $interaction_Energy=($alldoc->PotentialEnergy - ($calcSheet->
     Cell(0,4)));
  my $es_energy=($alldoc->ElectrostaticEnergy - ($calcSheet->Cell
     (0,7)));
  my $hb_energy=($alldoc->HydrogenBondEnergy - ($calcSheet->Cell
     (0,9)));
  my $vdw_energy=($alldoc->VanDerWaalsEnergy - ($calcSheet->Cell
```

```perl
       (0,11)));
1029   printf "\nEnergy : %f \n",$interaction_Energy;
1030   return($interaction_Energy,$es_energy,$hb_energy,$vdw_energy);
1031 }


1032

1033

1034 sub saveToDebug {
1035   my ($alldoc,$Debug,$x,$y,$r,$displacement,$dZ,
      $collisionEnergy_temp,$counter2,$bug) = @_;
1036   my ($interaction_Energy,$es_energy,$hb_energy,$vdw_energy) = ("
      NaN","NaN","NaN","NaN");
1037   #print "FUNCTION : SavetoDebug\n";
1038   #print "bug $bug\n";
1039   if ($bug == 10){
1040     ($interaction_Energy,$es_energy,$hb_energy,$vdw_energy) =
      componentEnergies($alldoc,$calcSheet);
1041     #printf "Component Energies = %f , %f ,%f , %f\n",
      $interaction_Energy,$es_energy,$hb_energy,$vdw_energy;
1042   }
1043   $Debug->Cell($counter2,0) = "Position"."_$x"."_$y";
1044   $Debug->Cell($counter2,1) = "$x";
1045   $Debug->Cell($counter2,2) = "$y";
1046   $Debug->Cell($counter2,3) = "$displacement";
1047   $Debug->Cell($counter2,4) = "$r";
1048   $Debug->Cell($counter2,5) = "$interaction_Energy";
1049   $Debug->Cell($counter2,6) = "$es_energy";
1050   $Debug->Cell($counter2,7) = "$hb_energy";
1051   $Debug->Cell($counter2,8) = "$vdw_energy";
1052   $Debug->Cell($counter2,9) = "$dZ";
1053   $Debug->Cell($counter2,10) = "$collisionEnergy_temp";
1054 }

1055

1056 sub getEnergyMinima {
1057   my ($MINIMA, $alldoc,$tempLayer,$flag,$unit,$calcSheet,$forcite,
      $step_size,$tablePosition) = @_;

1058

1059   my @init;
1060   my @movement;
1061   my $counter = 0;
1062   print "Counter = $counter\n";
1063   foreach my $x (@MINIMA){
1064     if (!@init){
1065       @movement = ($x->[0], $x->[1], $x->[2]);
1066     }else{
1067       @movement = map { $x->[$_] - $init[$_]} 0..$#init;
1068     }
1069     @init = ($x->[0], $x->[1], $x->[2]);
```

```perl
      print "Current Position = @init \n";
      print "Move by = @movement\n";
      print "Step Size = @step_size\n";
      $tempLayer ->Translate (Point (
                    X=>$step_size [0]*$movement [0],
                    Y=>$step_size [1]*$movement [1],
                    Z=>$movement [2]));

      my $unitAtoms = getEnergy ($alldoc ,$unit ,$flag ,$forcite ,"unit",
      $counter);
      saveToMainTable ($calcSheet ,$tablePosition , componentEnergies (
      $unitAtoms ,$calcSheet),$x ->[2]);
      ++$counter;
      ++$tablePosition;
   }
   $tempLayer ->Translate (Point (
                    X=>-$step_size [0]*$init [0],
                    Y=>-$step_size [1]*$init [1],
                    Z=>-$init [2]));
}


sub saveToMainTable {
   my ($calcSheet ,$counter ,$interaction_Energy ,$es_energy ,$hb_energy
     ,$vdw_energy ,$displacement) = @_;
   $calcSheet ->Cell ($counter ,5)=$interaction_Energy; #Based on the
     lowest value it uses that index value.
   $calcSheet ->Cell ($counter ,12)=$es_energy;
   $calcSheet ->Cell ($counter ,13)=$hb_energy;
   $calcSheet ->Cell ($counter ,14)=$vdw_energy;
   $calcSheet ->Cell ($counter ,19)=$displacement;
   #$calcSheet ->Cell ($counter ,23)=$collisionEnergy [$n];
   }

my @qoute = ("Two things are infinite: the universe and human
    stupidity; and I'm not sure about the universe. - Albert
    Einstein",
       "There is no law except the law that there is no law. - John
    Archibald Wheeler",
       "Falsity in intellectual action is intellectual immorality. -
     Thomas Chrowder Chamberlin",
       "The saddest aspect of life right now is that gathers
    knowledge faster than society gathers wisdom. - Isaac Asimov",
       "Science without religion is lame, religion without science
    is blind. - Albert Einstein",
       "A man who dares to waste one hour of time has not discovered
     the value of life. - Charles Darwin",
```

```
1106        "The good thing about science is that it's true whether or
      not you believe in it. - Neil deGrasse Tyson",
1107        "Nothing in life is to be feared, it is only to be understood
      . Now is the time() to understand more, so that we may fear less
      . - Marie Curie",
1108        "You cannot teach a man anything; you can only help him
      discover it in himself. - Galileo",
1109        "Imagination is more important than knowledge. - Albert
      Einstein",
1110        "Shall I refuse my dinner because I do not fully understand
      the process of digestion? - Oliver Heaviside",
1111        "If I have seen further it is by standing on the shoulders of
       Giants. - Isaac Newton",
1112        "One, remember to look up at the stars and not down at your
      feet. Two, never give up work. Work gives you meaning and
      purpose and life is empty without it. Three, if you are lucky
      enough to find love, remember it is there and don't throw it
      away. - Stephen Hawking",
1113        "The science of today is the technology of tomorrow - Edward
      Teller",
1114        "Scientists have become the bearers of the torch of discovery
       in our quest for knowledge - Stephen Hawking",
1115        "Our scientific power has outrun our spiritual power. We have
       guided missiles and misguided men -Martin Luther King, Jr.",
1116        "Medicine is a science of uncertainty and an art of
      probability - William Osler",
1117        "Research is what I'm doing when I don't know what I'm doing
      -Wernher von Braun ",
1118        "Science is about knowing; engineering is about doing - Henry
       Petroski",
1119        "No amount of experimentation can ever prove me right; a
      single experiment can prove me wrong - Albert Einstein");
1120
1121
1122 print "\n",$qoute[int(rand(20))];
```